

**Adding Value to Waste from the Aquaculture Industry: The  
Development of Green Processing Technologies, Characterization, and  
Applications of Waste Blue Mussel Shells**

By

Jennifer Nicole Murphy

A thesis submitted to the School of Graduate Studies

in partial fulfillment of the requirements for the degree of

**Doctor of Philosophy**

**Department of Chemistry**

Memorial University of Newfoundland

**July 2019**

St. John's

Newfoundland

## **Abstract**

Mussels (*Mytilus edulis*) are a high protein food grown using aquacultural methods around the world. By-product streams from this industry include raw discards (small or damaged product) and cooked shells that retain their posterior adductor muscle. The shell by-product streams from aquaculture could be used in a range of applications but shell storage without protein removal is problematic. An environmentally friendly shell cleaning protocol was developed using two industrial available food grade enzymes (Multifect PR 6L and PR 7L) to remove protein from mussel shells and is described in **Chapter 2**. This process was optimized using a Design of Experiments approach and could be performed in seawater or tap water using raw or cooked mussels. This method provides two product streams: a biorenewable calcium carbonate and protein hydrolysate.

Characterization of the shells, including by  $^1\text{H}$  MAS NMR spectroscopy, is described in **Chapter 3**. Heat treatment of blue mussel shells yields four  $\text{CaCO}_3$  materials with differing ratios of aragonite and calcite. Heat treatment (220 °C, 48 h) of the shells caused a large decrease in organic matrix levels as shown by  $^1\text{H}$  MAS NMR spectroscopy and this reduction in matrix content leads to a simple way to separate the prismatic calcite layer from the nacreous layer, allowing easy isolation of natural platelets of nacre. Using mussel protein hydrolysate from the shell cleaning protocol as an additive, synthetic nacre was prepared using a  $\text{CaCl}_2$  and  $\text{Na}_2\text{CO}_3$  mixing method.

The preparation of calcium acetate from mussel shell materials and acetic acid is described in **Chapter 4**. An exploratory central composite design compared the yield of  $\text{Ca}(\text{CH}_3\text{COO})_2$  with respect to shell material used, concentration of  $\text{CH}_3\text{COOH}$ , and time.

The yield of  $\text{Ca}(\text{CH}_3\text{COO})_2 \cdot \text{H}_2\text{O}$  was optimized further using heated, crushed shells using a custom optimal design. A maximum yield of 93% was reached after 32 h using 9%  $\text{CH}_3\text{COOH}$  and food-grade white vinegar gave an 85% yield of  $\text{Ca}(\text{CH}_3\text{COO})_2 \cdot \text{H}_2\text{O}$  after 24 h. De-icing experiments showed that the  $\text{Ca}(\text{CH}_3\text{COO})_2 \cdot \text{H}_2\text{O}$  produced from waste blue mussel shells melted 10-13 wt.% of ice in 15 min at concentrations of 20-30% (m/v) at  $-16\text{ }^\circ\text{C}$ .

During the synthesis of calcium acetate, a new material was discovered (**Chapter 5**), which was formed by the reassembly of calcite prisms held together by the organic matrix ‘glue’ as evidenced by NMR spectroscopy. This self-assembled calcite (SAC) material has a nest-like morphology and can absorb 10 times its mass in water. This inorganic sponge was used to adsorb dyes from aqueous solution (24 wt% of fabric dye) and absorb crude oil. SAC had an average crude oil absorption capacity of 978%  $\pm$  84.3% with no consequence on crude oil absorption over 10 cycles of re-use. The SAC material was also used as an inorganic filler in ionic liquid gel polymer electrolytes (**Chapter 6**). The addition of SAC resulted in mechanically and thermally stable films with good conductivity and large electrochemical window. Cell capacitors fabricated using this material had very good capacitance, 110 F/g at a current density of 2 A/g. The maximum energy density and power density of the device containing SAC was 28 Wh/kg and 8.1 kW/kg at 0.5 and 10 A/g, respectively.

## **Acknowledgements**

Firstly, I would like to thank my supervisor Dr. Fran Kerton for all her support throughout my program. I am deeply grateful for all that she has done for me; from help with writing to pep talks and life lessons. I am very appreciative that she let me continue learning crystallography by attending workshops and meetings. I would also like to thank my co-supervisor Dr. Kelly Hawboldt for her support and helpful discussions. I am happy to have had a co-supervisor whom I learned so much from, it was always nice to hear her perspective. I would like to thank Dr. Doug MacFarlane for agreeing to supervise me and allowing me to visit Monash University. It was one of the best experiences of my life. I am grateful to Dr. Tiago Mendes for training me and scientific discussion about my project. I would like to express deep gratitude to the MacFarlane group for making me feel at home, especially Dr. Karolina Matuszek, Dr. Mega Kar, Dr. Jacinta Bakker, and Dr. Tamás Oncsik for a truly unforgettable experience.

A special thank you to Dr. Chris Kozak for blowing shit up. It was a pleasure to learn from him in his natural environment; I hope to be just as enthusiastic as him if I am ever so lucky to teach. I would also like to thank my crystallography mentor, Dr. Louise Dawe, for countless hours of support and teaching.

I would like to thank my committee member Dr. Christina Bottaro for critique and advice at my committee meetings, Dr. Céline Schneider for NMR training and experiments, Nick Ryan for IR training, Adam Beaton for TGA training, Dr. David Grant and Dylan Goudie for SEM training, Wanda Aylward for powder XRD, Dr. Chris Parrish for helpful

discussions, Dr. Penny Morrill for help with my acid mine drainage work, Dr. Michael Katz for surface area measurements and help with single crystal issues, and the administrative staff of the Chemistry Department for helping with travel arrangements at conference times.

A very special thank you to the Newfoundland Aquaculture Industry Association, Darrell Green, and Jennifer and Mark Green of Green Seafoods for waste mussels and teaching me about mussel aquaculture in Newfoundland. I would also like to thank RDC (Ocean Industries Student Research Award), NSERC (Alexander Graham Bell Canada Graduate Scholarship, Michael Smith Foreign Study Supplement, and Dr. Kerton's research grant), Department of Chemistry, School of Graduate Studies (SGS), Graduate Students' Union (GSU) and Memorial University for funding, which was a huge contribution to the successful completion of my PhD studies.

A very heart felt thank you goes to the Green Chemistry and Catalysis Group members, past and present, who have made this a very memorable experience. I am thankful to have had a great group of colleagues to share this adventure with. I am grateful for charades, beer drinking, conferences, dance parties, screech-ins, bed sharing, laughter, tears, Halloween parties, camping trips, and picnics. These things could not have been shared with a better group of people.

The biggest thank you of all goes to my husband, Dr. Kenson Ambrose. I am grateful to have met him on the very first day of my PhD. I can't imagine what it would have been like without him. I am thankful that he put up with my giant piles of laundry for weeks at a time, but I am most thankful for his love, kindness, encouragement, and hugs before conference talks.

## Table of Contents

<b>Abstract</b> .....	<b>ii</b>
<b>Acknowledgements</b> .....	<b>iv</b>
<b>List of Figures</b> .....	<b>x</b>
<b>List of Tables</b> .....	<b>xvii</b>
<b>List of Abbreviations</b> .....	<b>xix</b>
<b>Chapter 1 Introduction</b> .....	<b>1</b>
1.1 Green Chemistry .....	1
1.1.1 Renewable Resources and the Ocean Based Biorefinery .....	2
1.1.2 The Ocean-Based Biorefinery .....	3
1.1.3 Mollusc Production .....	4
1.2 Processing and Characterization of Mollusc Shells .....	8
1.2.1 Shell Cleaning Technologies.....	8
1.2.1.1 Thermal Treatment and Physical Separation .....	9
1.2.1.2 Bio-cleaning .....	9
1.2.2 Characterization of Mollusc Shells .....	11
1.2.2.1 Powder X-ray Diffraction and Polymorphs of Calcium Carbonate .....	11
1.2.2.2 Morphology of Shells using Microscopy .....	13
1.2.2.3 Solid-state NMR spectra of Mollusc Shells .....	14
1.2.2.4 Infrared Spectra of Mollusc Shells.....	17
1.2.2.5 Surface Areas of Ground Mollusc Shells .....	19
1.3 Applications of Mollusc Shells .....	20
1.3.1 High Purity Calcium Carbonate .....	20
1.3.2 Soil Amendment.....	21
1.3.3 Acid Mine Drainage .....	27
1.3.4 Phosphate Removal and Water Purification.....	29
1.3.5 Building Materials.....	32
1.4 De-icers .....	34
1.4.1 Calcium Acetate .....	35
1.4.2 Ice Control in North America.....	36
1.5 Mollusc-derived Calcium Oxide in Catalysis .....	38
1.6 Design of Experiments .....	44
1.7 Mollusc-inspired materials .....	49
1.8 Building Bridges in Sustainable Science .....	50
1.8.1 Supercapacitors .....	51
1.8.1.1 Energy Density and Electrolytes .....	51
1.8.1.2 Renewable Resources for Electrodes .....	53
1.9 Summary .....	53
1.10 Objectives.....	54

1.11 Co-authorship Statement .....	56
1.12 References .....	62
<b>Chapter 2 Enzymatic processing of mussel shells to produce biorenewable calcium carbonate in seawater .....</b>	<b>74</b>
2.1 Introduction .....	74
2.2 Results and Discussion .....	77
2.2.1 Initial Screening of Biocatalytic Process Conditions .....	79
2.2.2 Experimental Designs for Optimization of Shell Cleaning .....	84
2.2.2.1 Optimization of shell cleaning process for raw, shell-on mussels using Multifect PR 6L .....	85
2.2.2.2 Optimization of shell cleaning process for cooked, shell-on mussels using Multifect PR 7L .....	87
2.3 Conclusions .....	90
2.4 Experimental .....	91
2.4.1 General Considerations .....	91
2.4.2 Enzymatic Treatment of Whole Raw Mussels .....	92
2.4.3 Enzymatic Treatment of Whole Cooked Mussel Meat and Shell .....	93
2.4.4 Enzymatic Treatment of Cooked Mussel Meat .....	93
2.5 References .....	93
<b>Chapter 3 Wealth from waste: Blue mussels (<i>Mytilus edulis</i>) offer up a sustainable source of natural and synthetic nacre .....</b>	<b>97</b>
3.1 Introduction .....	97
3.2 Results and Discussion .....	100
3.2.1 Preliminary Studies Towards Synthetic Nacre .....	114
3.3 Conclusions .....	117
3.4 Experimental .....	119
3.4.1 Materials .....	119
3.4.2 Instrumentation .....	119
3.4.3 Synthetic Nacre .....	120
3.4.4 Nail Enhancements .....	121
3.5 References .....	121
<b>Chapter 4 The synthesis of calcium acetate from raw and heat-treated blue mussel shell and its use as a de-icer .....</b>	<b>126</b>
4.1 Introduction .....	126
4.2 Results .....	129
4.2.1 Ground Mussel Shell Contamination .....	129
4.2.2 Exploratory Experimental Design for the Synthesis of Calcium Acetate .....	130
4.2.3 Optimization of Calcium Acetate Yield using HTC shells .....	136
4.2.4 Characterization of Calcium Acetate .....	139
4.2.5 De-icing Experiments .....	145

4.3 Conclusions .....	147
4.4 Experimental .....	148
4.4.1 General Considerations .....	148
4.4.2 Synthesis of Calcium Acetate .....	149
4.4.3 De-icing Experimental Procedure .....	150
4.5 References .....	150
<b>Chapter 5 Absorbent self-assembling calcite material from the prismatic layer of waste <i>Mytilus edulis</i> shells.....</b>	<b>154</b>
5.1 Introduction .....	154
5.2 Results .....	156
5.2.1 Preparation of SAC .....	156
5.2.2 Characterization of SAC .....	159
5.2.3 <sup>1</sup> H MAS NMR of SAC .....	161
5.2.4 Dye Adsorption Studies .....	162
5.2.5 Oil Recovery .....	164
5.3 Conclusions .....	167
5.4 Experimental .....	168
5.4.1 Materials .....	168
5.4.2 Characterization .....	168
5.4.3 Preparation of Self Assembled Calcite (SAC) .....	169
5.4.4 Isolation of insoluble organic matrix .....	170
5.4.5 Dye Adsorption/Desorption .....	170
5.4.6 Oil Recovery .....	171
5.5 References .....	172
<b>Chapter 6 Bio-renewable calcite as an inorganic filler in ionic liquid gel polymer electrolytes for supercapacitors .....</b>	<b>178</b>
6.1 Introduction .....	178
6.2 Results and Discussion .....	181
6.2.1 Ionic Conductivity .....	181
6.2.2 ILGPE Characterization .....	182
6.2.3 Electrochemical Measurements.....	184
6.2.4 Impedance Spectroscopy .....	187
6.3 Conclusions .....	191
6.4 Experimental .....	192
6.4.1 Materials .....	192
6.4.2 Preparation of ILGPEs .....	192
6.4.3 Preparation of Electrodes .....	193
6.4.4 Electrochemical Measurements.....	193
6.4.5 Characterization of ILGPEs .....	195
6.5 References .....	195

<b>Chapter 7 Conclusions and Future Work .....</b>	<b>197</b>
7.1 Conclusions .....	198
7.2 Future Work .....	203
7.3 References .....	207
<b>Appendix A .....</b>	<b>208</b>
<b>Appendix B .....</b>	<b>217</b>
<b>Appendix C .....</b>	<b>240</b>
<b>Appendix D .....</b>	<b>249</b>
<b>Appendix E .....</b>	<b>259</b>

## List of Figures

<b>Figure 1.1</b> The 12 principles of green chemistry. ....	2
<b>Figure 1.2</b> An overview of products and material that can be derived from waste mussel shells and residual meat. ....	8
<b>Figure 1.3</b> a) Whole cooked blue mussels and b) an example of residual meat left on the shell after meat is removed. (Copyright J. N. Murphy) .....	9
<b>Figure 1.4</b> Powder XRD spectra for showing the presence of calcite and aragonite in raw mussel shell and after calcination of mussel shells at 1050 °C for 2h. (Reprinted with permission from Tekin K. Hydrothermal Conversion of Russian Olive Seeds into Crude Bio-oil Using a CaO Catalyst Derived from Waste Mussel Shells. Energy & Fuels. 2015;29(7):4382-92. Copyright 2016 American Chemical Society.).....	12
<b>Figure 1.5</b> SEM of the fracture layer through <i>Mytilus californianus</i> showing the prismatic calcite layer (top) and the aragonite layer (bottom), Source: Weiner and Addadi 1997, Figure 4, p.692. Reproduced with permission of Royal Society of Chemistry. ....	14
<b>Figure 1.6</b> <sup>13</sup> C CP MAS spectra of the aragonitic shell of untreated <i>P. canaliculus</i> with contact time of (a) 1 and (b) 8 ms. The spectra expose the bioorganic content, mainly proteinaceous, and partially resolve the ~171 ppm peak of the interfacial carbonates. (c) Expansion of the carbonate-peak region of the <sup>13</sup> C MAS spectra with DE with 2400 s relaxation delay, red; DE with 15 s relaxation delay, blue; and CP with 8 ms contact time and 2 s relaxation delay, black. (DE=direct excitation, CP=cross polarization) Reprinted with permission from (Ben Shir I, Kababya S, Katz I, Pokroy B, Schmidt A. Exposed and Buried Biomineral Interfaces in the Aragonitic Shell of <i>Perna canaliculus</i> Revealed by	

Solid-State NMR. Chemistry of Materials. 2013;25(22):4595-602.). Copyright 2016 American Chemical Society.....	16
<b>Figure 1.7</b> FTIR spectra of (a) calcium carbonate with 99.5% purity, (b) raw green lipped mussel shells and (c) green lipped mussel shells pyrolysed at 800°C. (Source: Shariffuddin <i>et al.</i> Chemical Engineering and Research Design, 2013, Fig. 3, p.1696. Reproduced with permission of Elsevier) .....	18
<b>Figure 1.8</b> Organic and alkaline substrates used in bioreactors. (Source: McCauley <i>et al.</i> Water Research, 2009, Fig. 1, p.963. Reproduced with permission of Elsevier.) .....	28
<b>Figure 1.9</b> SEM images of (A) q-CaCO <sub>3</sub> and (B) m-CaCO <sub>3</sub> . (Source: P. Ballester <i>et al.</i> 2007, Cement and Concrete Research, Fig.2, p.561. Reproduced with permission of Elsevier.) .....	33
<b>Figure 1.10</b> One factor plots for a) Calcination temperature, b) Catalyst concentration and c) MeOH:oil ratio as functions of yield and purity (Source: Rezaei <i>et al.</i> 2013, Fuel, Fig. 5, p. 540. Reproduced with permission of Elsevier.).....	41
<b>Figure 1.11</b> Mussel shell catalysts reusability under optimal conditions of (a) purity, (b) yield. (Source: Rezaei <i>et al.</i> 2013, Fuel, Fig. 6, p. 540. Reproduced with permission of Elsevier.) .....	42
<b>Figure 1.12</b> Design Space for a central composite circumscribed (CCC) design.....	48
<b>Figure 2.1</b> Calibration curve for TGA analysis of mussel shells after enzymatic cleaning. One standard deviation shown with error bars. $y=0.6511x + 3.7592$ . $R^2=0.9975$ .....	79
<b>Figure 2.2</b> Response surface of wt% meat remaining based on temperature and time for removal of raw protein from mussel shells using Multifect PR 6L.....	87

**Figure 2.3** Response surface of wt% meat remaining based on the amount of enzyme solution and time for the removal of cooked protein from mussel shells using Multifect PR 7L. ....89

**Figure 3.1** a) Appearance of i) untreated blue mussel shells and shells heated at ii) 120 °C, iii) 160 °C, and iv) 200 °C for 48 h. b) Infrared spectra of i) untreated blue mussel shells and shells heated to ii) 160 °C iii) 200 °C and iv) 220 °C for 48 h. c) SEM micrographs (back-scatter detection) of blue mussel after heat treatment for 48 h at the noted temperature. Schematic of the inner and outer layer of mussel depicts where the region where the micrographs were taken. The outer layer, i)-iii), after heating at 220 °C, 160 °C and 220 °C, respectively. The inner layer, iv)- vi), after heating at 220 °C, 160 °C and 160 °C, respectively. ....103

**Figure 3.2** a) Appearance of blue mussels after drying at 220 °C for 48 h. b) Powder XRD diffractograms for i) whole mussel shells treated at 220 °C for 48 h and the resulting ii) outer and iii) inner layer shell of the mussel. c) Normalized 600 MHz <sup>1</sup>H NMR spectra (20 kHz, relaxation delay 2 s, 16 scans) of i) whole mussel shells treated at 220 °C and the resulting ii) outer and iii) inner shell layer. Intensities of the signals are increased from the original spectra to show the peak at 13.8 ppm. ....107

**Figure 3.3** Digital images of a) crushed nacre isolated from the inner layer of blue mussel shells and b) small flakes of nacre as a result of gentle grinding of nacre with a mortar and pestle. ....110

**Figure 3.4** a) IR spectra of synthetic CaCO<sub>3</sub> products from the direct mixing method using reaction conditions i) 0.8 M CaCl<sub>2</sub> and Na<sub>2</sub>CO<sub>3</sub> ii) 0.8 M CaCl<sub>2</sub> and Na<sub>2</sub>CO<sub>3</sub> with the addition of mussel protein hydrolysate and iii) 0.8 M CaCl<sub>2</sub> and Na<sub>2</sub>CO<sub>3</sub> with the addition

of mussel protein hydrolysate and mussel shells for seeding nacre. b) SEM micrographs (back-scatter detector) of i) product from 0.8 M $\text{CaCl}_2$ and $\text{Na}_2\text{CO}_3$ with the addition of mussel protein hydrolysate and mussel shells for seeding and ii) the shell surface after the reaction of i).	116
<b>Figure 4.1</b> Digital images of (a) the synthesis of $\text{Ca}(\text{CH}_3\text{COO})_2$ using mussel shells that were ground in a stainless steel vial and (b) the resulting $\text{Ca}(\text{CH}_3\text{COO})_2$ product after filtering.	130
<b>Figure 4.2</b> The response surface plot of yield of $\text{Ca}(\text{CH}_3\text{COO})_2$ based on concentration of acetic acid and time using calcined mussel shells (CC).	133
<b>Figure 4.3</b> The response surface plot of yield of calcium acetate based on concentration of acetic acid and time using raw mussel shells (RTC).	134
<b>Figure 4.4</b> The response surface plot of yield of $\text{Ca}(\text{CH}_3\text{COO})_2$ based on concentration of acetic acid and time using heated mussel shells (HTC).	136
<b>Figure 4.5</b> The response surface plot of the optimization of $\text{Ca}(\text{CH}_3\text{COO})_2$ yield based on concentration of acetic acid and time using heated mussel shells (HTC).	138
<b>Figure 4.6</b> Infrared spectra for $\text{Ca}(\text{CH}_3\text{COO})_2$ products made using CC, RTC, HTC and optical calcite in the the $400\text{-}1800\text{ cm}^{-1}$ region.	140
<b>Figure 4.7</b> Infrared spectra for $\text{Ca}(\text{CH}_3\text{COO})_2$ products made using CC, RTC, HTC, and optical calcite showing the $2500\text{-}4000\text{ cm}^{-1}$ region where there are clear differences in bands from water.	140
<b>Figure 4.8</b> Thermogravimetric analysis for calcium acetate monohydrate ( $\text{Ca}(\text{CH}_3\text{COO})_2\cdot\text{H}_2\text{O}$ ) made using optical calcite.	142

<b>Figure 4.9</b> Thermogravimetric analysis for calcium acetate monohydrate ( $\text{Ca}(\text{CH}_3\text{COO})_2 \cdot \text{H}_2\text{O}$ ) made using HTC shells. ....	142
<b>Figure 4.10</b> Digital images of $\text{Ca}(\text{CH}_3\text{COO})_2 \cdot \text{H}_2\text{O}$ made from BM shells that show its needle growth and fluffiness. ....	143
<b>Figure 4.11</b> Scanning electron micrographs (back-scattered) of calcium acetate monohydrate made from HTC shells at various magnifications. ....	144
<b>Figure 4.12</b> Powder X-ray diffractograms of $\text{Ca}(\text{CH}_3\text{COO})_2 \cdot \text{H}_2\text{O}$ made from optical calcite and HTC shells plotted with the simulated diffractogram from the crystallographic information file (CIF). CCDC 1122640. ....	145
<b>Figure 5.1</b> Overview of the preparation and purification of SAC. Digital images of BMH shells (a), the appearance of BMH shells after being treated with 5% $\text{CH}_3\text{COOH}$ , washed with distilled water and dried (b), the result of treating b with 5% $\text{CH}_3\text{COOH}$ is a mixture of SAC, residual BMH shells and calcium acetate (c), SAC is collected via simple decantation (d) and washed in ethanol (e) before being dried in a vacuum oven to get pure SAC (free of residual calcium acetate) (f). Some SAC is very spherical (g) and it is produced alongside calcium acetate monohydrate (h). ....	159
<b>Figure 5.2</b> Comparison of prismatic calcite from BMH shells and SAC. a) FESEM (BSED) image of the outer prismatic calcite layer of BMH shells after heating the shells at 220 °C for 48 h b-c Select FESEM images of SAC showing the microstructure composed of calcite crystals in a nest-like formation at different scales. Scale bars: 30 $\mu\text{m}$ (a), 100 $\mu\text{m}$ (b), 20 $\mu\text{m}$ (c). ....	160
<b>Figure 5.3</b> Visual comparison between BMH shells and SAC. Digital images of (a) 0.5 g of powdered BMH shells and (b) 0.5 g of SAC. ....	161

<b>Figure 5.4</b> Aqueous dye adsorption by SAC. Digital images of crystal violet (0.1 mg/mL) before and after adsorption for 48 h (a) and SAC stained with fuschia fabric dye after 24 h and before and after heat treatment at 500 °C for 10 minutes to desorb the dye (b). Dyes can also be desorbed in a MeOH/H <sub>2</sub> O solution. ....	164
<b>Figure 5.5</b> Typical cycle of SAC crude oil absorption. Digital images of SAC added to a thin film of crude oil (a) is easily separated by a simple filtration (b) and collected for weighing (c) and finally cleaned with small volumes of CHCl <sub>3</sub> before drying and repeating the cycle. SAC absorbs crude oil consistently over 10 cycles (e) as the oil absorption capacity is statistically the same over ten cycles. Error bars represent one standard deviation of each cycle.....	166
<b>Figure 6.1</b> a) FTIR spectra of ILGPEs to show the incorporation of calcite. i) ILGPE-I, ii) ILGPE-II, and iii) ILGPE-III. b) Thermogravimetric analysis of ILGPE-I and ILGPE-II. ....	183
<b>Figure 6.2</b> SEM micrographs of a) porous region and b) edge region of ILGPE-II and digital images of c) ILGPE-III and d) ILGPE-II.....	184
<b>Figure 6.3</b> Cyclic voltammograms of Cell II at a) different scan rates and b) different operating potentials at a scan rate of 100 mV/s. ....	185
<b>Figure 6.4</b> a) Galvanostatic discharge curves for Cell II at various current densities and b) specific capacitance of Cell I (black) and Cell II (blue) as a function of current densities. ....	186
<b>Figure 6.5</b> a) Nyquist plot for Cell I (black) and Cell II (blue). Inset: Magnified high frequency region. b) Cyclic stability of Cell I and Cell II at a current density of 2 A/g. Data in black and blue shows the respective cells charging to 2.5 V and data in pink shows Cell	

I charging to 3.0 V. Secondary axis shows Coulombic efficiency (purple) for Cell II over 5000 cycles.....188

**Figure 6.6** Ragone plot for Cell I (black) and Cell II (blue) charging from 0-2.5 V. Charge/discharge current density is 0.5-10 A/g.....190

**Figure 7.1** Digital image of different loadings of HTG shells added to the AMD solution after 1 h of stirring. Left 5 g/L, middle 15 g/L, and right 25 g/L. ....204

## List of Tables

<b>Table 1.1</b> World aquaculture and capture production of mollusc species <sup>a</sup> .....	5
<b>Table 1.2</b> Summary of <sup>1</sup> H NMR Data for Nacreous Molluscs.....	17
<b>Table 1.3</b> Soil enzyme activities for treatments T1-T5. All values are in $\mu\text{mol product g dry soil}^{-1} \text{ h}^{-1}$ . Mean values and standard deviations are obtained from $n = 4$ samples. (Source: Paz-Ferreiro <i>et al.</i> Chemosphere, 2012, Tab.3, p.1119. Reproduced with permission of Elsevier.) .....	24
<b>Table 1.4</b> Heavy metal desorption of Cu, Cd, Ni, and Zinc, expressed as percentage of the previously retained, in the various shell treated (6, 12 or 24 $\text{g kg}^{-1}$ ) and untreated (0 $\text{g kg}^{-1}$ ) mine soil samples as function of metal added. (Source: Ramírez Pérez <i>et al.</i> , Journal of Hazardous Materials, 2013, Tab. 5, p.127. Reproduced with permission of Elsevier.) ....	27
<b>Table 1.5</b> Working temperatures for chloride and acetate-based de-icers. ....	38
<b>Table 1.6</b> Variables studied and their values. (Source: Rezaei <i>et al.</i> 2013, Fuel, Tab. 1, p. 536. Reproduced with permission of Elsevier.).....	39
<b>Table 1.7</b> All experiments performed and the responses, Purity (Y1) and Yield (Y2). (Source: Rezaei <i>et al.</i> 2013, Fuel, Tab. 2, p. 537. Reproduced with permission of Elsevier.) .....	40
<b>Table 1.8:</b> Algebraic Signs for Calculating Effects in the 2 <sup>3</sup> Design. ....	46
<b>Table 2.1</b> Data for exploratory experiments on biocatalytic cleaning of raw shell-on blue mussels.....	82
<b>Table 2.2</b> Data for exploratory experiments on biocatalytic digestion of cooked blue mussel meat, removed shells. <sup>a</sup> .....	83

<b>Table 2.3</b> Factors and levels studied for optimization of shell cleaning process using Multifect PR 6L to remove meat from raw mussels .....	85
<b>Table 3.1</b> Summary of <sup>1</sup> H NMR data for nacreous molluscs.....	108
<b>Table 4.1</b> Exploratory central composite circumscribed design factors and levels for the synthesis of calcium acetate from mussel shell materials.....	131
<b>Table 4.2</b> Custom RSM design factors and levels for the optimization of yield of calcium acetate using HTC shells.....	136
<b>Table 4.3</b> Data for de-icing experiments performed at different concentrations of calcium acetate brine applied to ice and reported as mass losses and gains at -16°C. ....	146
<b>Table 7.1</b> Concentration of elements present in AMD solution before and after being treated with 15 g/L RTG and HTG shells. ....	205

## **List of Abbreviations**

6L: Multifect PR 6L

7L: Multifect PR 7L

ACC: Amorphous Calcium Carbonate

AMD: Acid Mine Drainage

ANOVA: ANalysis Of VAriance

BBD: Box-Behnken Design

BET: Brunauer-Emmett-Teller

BM: Blue Mussel

BMH: Heat-treated BM shells

BMR: Untreated BM shells

BSED: Backscattered Electron Detector

CAD: Canadian Dollars

CC: Calcined Crushed BM shells

CCC: Central Composite Circumscribed

CCD: Central Composite Design

CCF: Central Composite Face-centered

CCI: Central Composite Inscribed

CP: Cross Polarization

CV: Cyclic Voltammetry

DE: Direct Excitation

DI: Deionized Water

DIN: Dissolved Inorganic Nitrogen

DMA: Dynamic Mechanical Analysis

DOC: Dissolved Organic Carbon

DoE: Design of Experiments

DON: Dissolved Organic Nitrogen

DSC: Differential Scanning Calorimetry

e.g.: for example (Latin *exemplie gratia*)

ECs: Electrochemical Capacitors

EIS: Electrochemical Impedance Spectroscopy

ELU: 1  $\mu\text{mol}$  lactic acid released per minute / g immobilized enzyme at 25°C and pH 6.8

ESR: Equivalent Series Resistance

*et al.*: and others (Latin *et alii*)

FAO: Food and Agriculture Organization of the United Nations

FTIR: Fourier-transform Infrared

HAP: Hydroxyapatite

HTC: BM shells heated at 220 C for 48 h

i.e.: that is (Latin *id est*)

ICP-MS: Inductively Coupled Plasma Mass Spectrometry

ILGPEs: Ionic Liquid Gel Polymer Electrolytes

ILs: Ionic Liquids

IR: Infrared

MAS: Magic Angle Spinning

MSPD: Matrix Solid-Phase Dispersion

NAIA: Newfoundland Aquaculture Industry Association

NMR: Nuclear Magnetic Resonance

NS: Natural Seawater

RSM: Response Surface Methodology

RTC: Room Temperature Crushed BM shells

SAC: Self-Assembling Calcite

SAMs: Self-Assembled Monolayers

SDD: Silicon Drift Detector

SDG: Sustainable Development Goals

SEM: Scanning Electron Microscopy

SS: Synthetic Seawater

TGA: Thermogravimetric Analysis

USD: US Dollar

UV: Ultraviolet

UV-vis: Ultraviolet-visible

VOCs: Volatile Organic Compounds

XRD: X-ray Diffraction

$\delta$ : chemical shift

$\nu$ : IR frequency

## **Chapter 1 Introduction**

Sections 1.2-1.3 and 1.5 are published in a book chapter by J. N. Murphy and F. M. Kerton entitled 'Characterization and utilization of waste streams from mollusc aquaculture and fishing industries.' in Kerton, F. M. and Yan, N. eds. *Fuels, Chemicals and Materials from the Oceans and Aquatic Sources*. Wiley, pp. 189-225.

### **1.1 Green Chemistry**

Green chemistry is an approach to carrying out chemistry and engineering in a safe and sustainable way.<sup>1</sup> The 12 principles of green chemistry, shown in **Figure 1.1**, were created by Paul Anastas and John Warner.<sup>2</sup> These principles can be applied as a methodology to enable scientists and engineers to protect or benefit people, the environment, and the economy by finding ways to limit waste, conserve energy, and replace hazardous chemicals. The principles address much more than the hazards of chemical toxicity concerns and include life cycle analysis considerations such as the use of renewable feedstocks and the end life of a product or material.<sup>2</sup>

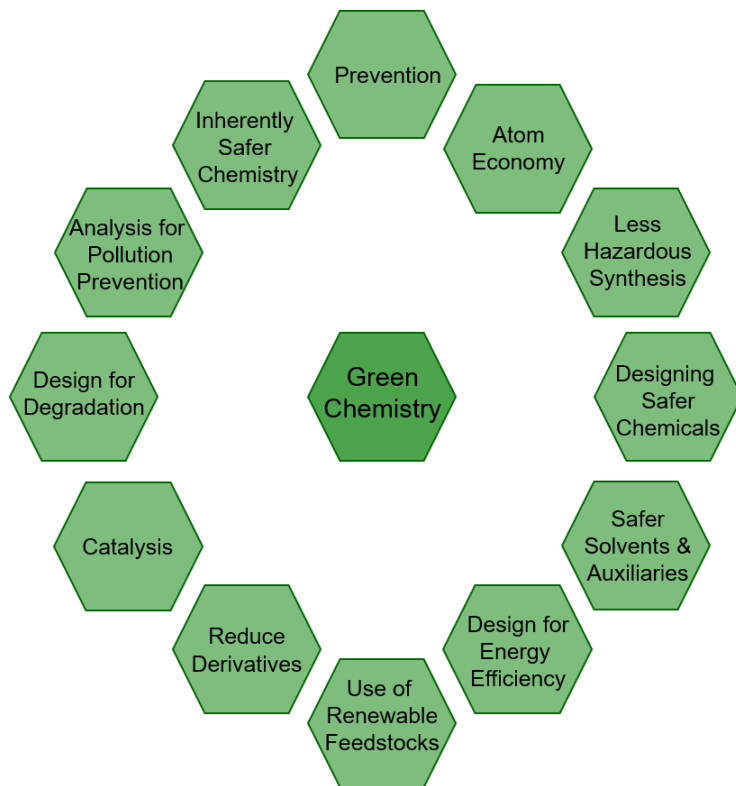


**Figure 1.1** The 12 principles of green chemistry.

### **1.1.1 Renewable Resources and the Ocean Based Biorefinery**

The use of renewable feedstocks is one of the principles of green chemistry where resources that are non-depleting are used preferentially over resources that are finite. Biomass, which is any material that comes from a living organism<sup>3</sup>, is an example of a renewable resource. Many researchers are interested in using biomass and renewable resources to produce chemicals, fuels and materials via a range of tools, which could lead to the development of biorefineries.<sup>4</sup> Such approaches often involve either chemical or biological catalysis<sup>5,6</sup>, and thermochemical processing.<sup>7,8</sup>

If the by-product or waste stream from a process can be used as the starting material for another product this enhances the overall sustainability of the process. Recently, researchers have begun exploring such options in the food industry.<sup>9-12</sup> However, such research has mainly been focused on biomass and food waste that originated on land with aquatic and ocean-sourced biomass being overlooked.<sup>13-15</sup> This poses issues for the World as oceans cover 71% of the surface of our planet and there is a strain on land space to provide food for billions of people and we are running out of fertile soil to grow crops.

As described by Tilman and Clark, what we eat is directly linked to human health and environmental sustainability.<sup>16</sup> Therefore, our diets must transition away from agricultural protein dependence and shift towards pescatarian or Mediterranean diets to reduce greenhouse gas emissions and improve our overall health. Due to cultural aspects, proximity to the oceans and financial status, it is unrealistic to expect everyone to transition their diets. In terms of emissions, fed-fish produce significant levels of emissions because there is a need to feed them. This takes grains and therefore terrestrial space and fresh water. Un-fed fish, such as molluscs and other bivalves require very little land-based inputs and fresh water for growth and processing in comparison.

### **1.1.2 The Ocean-Based Biorefinery**

Currently, more than 50% of all fish consumed by humans globally comes from aquaculture. When the capture fisheries began to plateau in the late 1980s, aquaculture production increased to fill the demand for fish and seafood. Today, the capture fishery is struggling to recover with some scientists reporting it will never recover fully, while the

aquaculture industries sharp increase of 31% in production from 2004 to 2014 and a further 64% increase projected by 2030, makes aquaculture the fastest growing food sector in the world.<sup>17</sup> Currently many coastal regions around the world have not availed of marine aquaculture. The untapped potential for aquaculture development in underutilized coastal regions was assessed by Halpern *et al.* Mapping of coastal regions suitable for marine aquaculture and calculations revealed that it takes only 0.015% of the oceans surface to produce the same amount of seafood from all capture fisheries.<sup>18</sup> Additionally, they estimate that more than 100 times the current global seafood consumption in finfish could be grown each year if just 1% of areas in their study were developed.

Therefore, a large increase in seafood production is imminent and a big part of our social responsibility that will result from this is waste management. As increased fish consumption and fish product commercialization leads to increased waste, utilization of fish by-products has been gaining attention because they can represent a significant additional source of nutrition and valuable chemicals including oils, platform chemicals, chitin, and calcium carbonate.<sup>13, 15, 19</sup> However, this area has been dominated by fin fish waste as a source of high value fish oils and nutraceuticals.<sup>20</sup> Many other areas of seafood processing are increasing, including molluscs, which present a valuable source of protein and calcium carbonate.

### **1.1.3 Mollusc Production**

The FAO (Food and Agriculture Organization of the United Nations) Fisheries and Aquaculture Department is a valuable source of statistics relevant to this field. In 2016,

total world fisheries production from wild capture and aquaculture sources was close to 108 million tonnes including 19 million tonnes of molluscs, **Table 1.1.**<sup>21</sup>

**Table 1.1** World aquaculture and capture production of mollusc species<sup>a</sup>

Species group	2007		2016	
	Aquaculture	Capture	Aquaculture	Capture
Freshwater molluscs	139 643 (83 309)	389 840	285 894 (419 435)	338 224
Abalones, winkles, conchs	342 576 (460 618)	134 118	400 230 (1 933 726)	167 427
Oysters	4 312 197 (2 965 131)	153 137	5 594 822 (6 628 893)	135 435
Mussels	1 659 132 (1 195 219)	113 843	2 007 507 (3 847 331)	128 453
Scallops, pectens	1 303 341 (2 005 061)	733 151	2 126 930 (5 607 886)	569 239
Clams, cockles, arkshells	4 202 076 (3 978 859)	806 542	5 570 141 (9 610 646)	591 265
Miscellaneous marine molluscs	849 829 (530 734)	877 916	1 536 615 (1 153 804)	421 633
<b>Totals</b>	<b>12 808 794 (11 218 931)</b>	<b>3 208 547</b>	<b>17 139 139 (29 201 721)</b>	<b>2 351 676</b>

<sup>a</sup>Data obtained from FAO<sup>21</sup> (<http://www.fao.org/fishery/statistics/en>). Quantities in tonnes with the value in 1 000 USD in parentheses if available.

Molluscs accounted for approximately 16% of world fisheries production in 2016 and those produced via aquaculture significantly outweighed those captured from the wild. This harvest primarily consists of marine species with oysters and clams dominating world production followed by scallops and mussels. Aquacultural production of molluscs grew by close to 31% in weight-terms during the nine-year period 2007-2016 and by nearly 140% in terms of economic value in the same timeframe. The continued growth in this sector globally will lead to significant quantities of bio-renewable calcium carbonate

becoming available and waste protein streams too. The aim of this chapter is to highlight and review the processing and applications of by-products from mollusc aquaculture.

The species that are harvested (either from wild or via aquacultural practices) are dependent on local climates and customs. In terms of molluscs, the three main aquaculture mollusc products farmed in Canada are mussels (including Eastern Blue mussel – *Mytilus edulis*, Western Blue mussel – *Mytilus trossulus* and Gallo mussel – *Mytilus galloprovincialis*), oysters (including American oyster – *Crassostrea virginica* and Pacific oyster – *Crassostrea gigas*) and clams (including Manila clam – *Venerupis philippinarum*, Littleneck clam – *Protothaca staminea* and Geoduck – *Panopea generosa*).<sup>22</sup> Of these, in Canada, mussels are the top shellfish aquaculture product and had a farm-gate value of \$44.7 million CAD in 2015.

Fish processing and aquaculture industries can be a large part of the economy in rural coastal regions of the world. Therefore, valorization of waste-streams from such industries could lead to increased rural employment opportunities. Up to 70% by weight of a mussel accounts for the shell, leaving a very large mass of waste. Waste mollusc shells are currently dumped at sea or sent to landfill, which both add a cost to the food processor due to fees that must be paid. The shells cannot be stored because of residual meat on them, which attracts vermin and can cause an unpleasant stench due to decomposition. Therefore, ways to process the shells are being pursued by many researchers around the world. The development of truly sustainable fishing and aquaculture industries requires a cradle to grave approach to processing, where the maximum value is extracted from the seafood product and by-products. This approach not only creates a viable revenue stream from

material that was previously a ‘cost’ but also ensures any technology/process/product developed will either have a minimal or positive impact with respect to environmental, social and economic effects. In order to make the mollusc aquaculture industry truly sustainable, we need to use all of the waste; not just the shell or protein hydrolysate. **Figure 1.2** describes the broad range of possible chemical-based products or uses for waste from mollusc aquaculture. Instead of thinking of the mollusc shells as waste, we should think of them as a by-product of processing and utilize them to the best of their potential as a ‘new’ raw material. In my opinion, the calcium carbonate rich shells have the potential to become high value, low volume products such as a component in cosmetics or medicine (e.g. filler/diluent in tablets) or low value, high volume products such as a component in building materials. Some of these opportunities are described later in this chapter, but first, an overview of processes for cleaning shells and methods to characterize them are summarized.

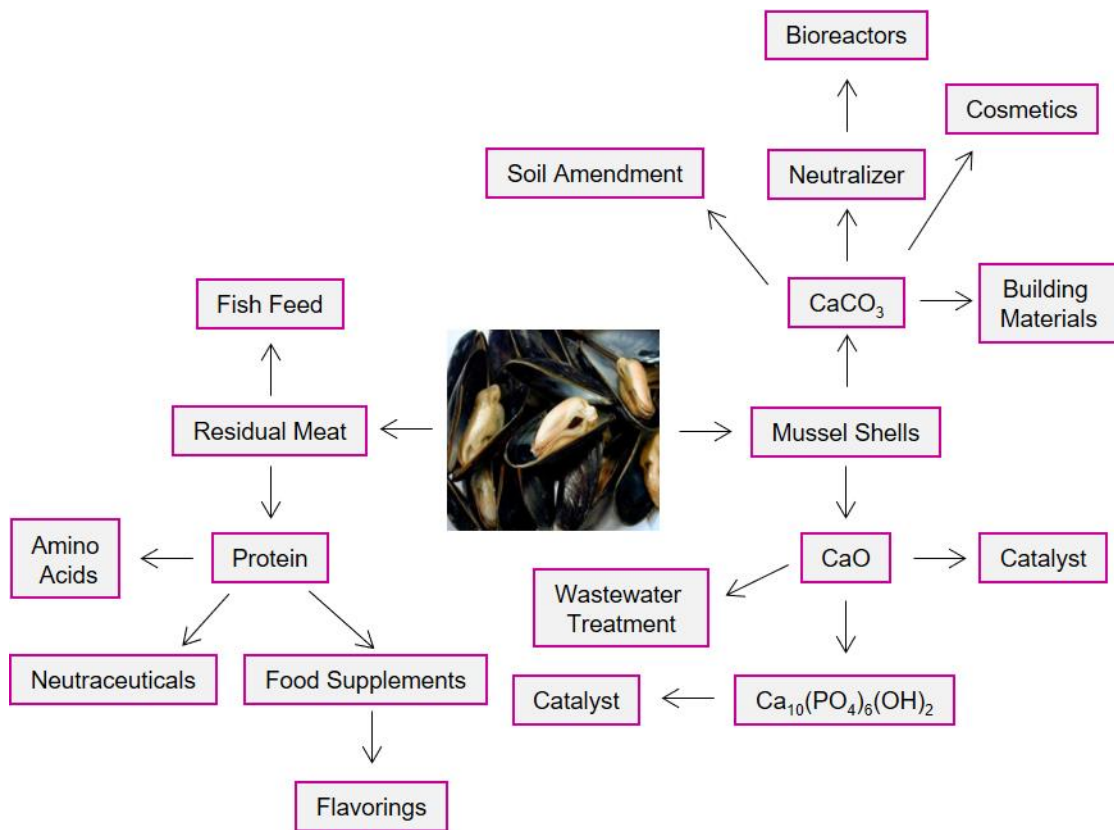


**Figure 1.2** An overview of products and material that can be derived from waste mussel shells and residual meat.

## 1.2 Processing and Characterization of Mollusc Shells

### 1.2.1 Shell Cleaning Technologies

In order to utilize waste mussel shells as a source of calcium carbonate, the shells must be cleaned because any organic contents would decrease the purity of  $\text{CaCO}_3$  and makes the materials challenging to store i.e. residual protein decomposes and produces a stench. There are two types of mussel waste; whole mussels and mussels with the meat removed and adductor attached, **Figure 1.3**. Some mussels are rendered unsellable due to their size or are damaged shells during mussel processing. In these cases, there is a considerable amount

of protein to remove, up to 50 wt.% of the mussel. In the mussel cannery industry, mussels are first cooked, and their meat removed, leaving behind a small amount of meat. The remaining residual meat must be removed; however, very little research has been done on the actual cleaning of the shells to rid them of residual meat.



**Figure 1.3** a) Whole cooked blue mussels and b) an example of residual meat left on the shell after meat is removed. (Copyright J. N. Murphy)

#### **1.2.1.1 Thermal Treatment and Physical Separation**

The primary process to ‘clean’ mollusc shells is to heat to high temperatures to ‘burn’ off the organic contents.<sup>23, 24</sup> Other processes include separating the meat from the shell via dissection or other means<sup>25, 26</sup>, and washing with large amounts of water.<sup>23, 27</sup> Additionally, many papers describing uses of mussel shells do not describe the mussel shell cleaning process. In manuscripts where CaO (lime) production was the main goal, the shells, as they are being calcined, are typically just heated to the required high temperature without cleaning.

#### **1.2.1.2 Bio-cleaning**

The application of enzyme technology in seafood processing has brought about many possibilities for the protein recovered as food supplements including flavorings and protein

supplements.<sup>28</sup> Enzymes are highly active biocatalysts that have several advantages in that they perform very specific reactions under mild reaction conditions with high turnovers, are biodegradable and are natural products. However, enzymes are often expensive and are very complex molecules.<sup>29</sup> Hydrolases are a class of enzymes that catalyze hydrolysis reactions. There are 12 subgroups of hydrolases named according to the type of bond that is hydrolyzed. Of these 12, esterases, proteases and glycosidases are the most well-known.<sup>29</sup> Enzymatic proteolysis of cod by-products and shrimp processing waste have been studied extensively.<sup>28</sup> However, there are few reports of enzymatic hydrolysis of mussel meat. Of these reports, Optimase and Protamex were used but they do not describe the hydrolysis as a way of cleaning mussel shells of residual meat, instead they hydrolyze detached mussel meat to produce protein hydrolysate. This is because mussels are high in protein and low in fat and calories. Therefore, their protein hydrolysate is a good source of protein and amino acids, and can be used for flavoring and supplements in the food industry.<sup>28</sup> Using Protamex optimal conditions for the hydrolysis of mussel meat (emaciated with water) were pH 6.85, an enzyme: substrate ratio of 4.5 % at 51 °C for 3 h. These conditions resulted in a degree of hydrolysis of 26.5 % and 65 % protein recovery with glutamate, aspartate and tryptophan being the main amino acid components.

One report that does use enzymatic hydrolysis for cleaning mussel shells is in a patent from New Zealand. The patent describes the cleaning of waste mollusc shells using enzyme solutions of alcalase, pepsin, and papain. The pH was adjusted to acidic or basic depending on which enzyme was used with a reaction time maximum of 2 hours at temperatures ranging from 45-70 °C.<sup>30</sup> The optimization method was not described, nor was there an

interest in the protein hydrolysate. Protein hydrolysate is rich in nitrogen and can affect local bodies of water by possible eutrophication risks, so it needs to be ideally used for a new product or treated before being released into the environment.

## **1.2.2 Characterization of Mollusc Shells**

Coastal regions in countries such as Spain and New Zealand have been utilizing waste mussel shells as a source of  $\text{CaCO}_3$  and  $\text{CaO}$  for a number of years. In turn mollusc shells, including types of mussels, have been studied using many analytical techniques including Thermogravimetric Analysis (TGA), Scanning Electron Microscopy (SEM), Powder X-ray Diffraction (XRD), Infrared spectroscopy (IR), Solid State NMR spectroscopy and Brunauer-Emmett-Teller (BET) surface area analysis, among others.

### **1.2.2.1 Powder X-ray Diffraction and Polymorphs of Calcium Carbonate**

Thermogravimetric Analysis TGA is an analytical technique whereby the solid sample undergoes thermal decomposition. The thermal decomposition products for  $\text{CaCO}_3$  are  $\text{CaO}$  and  $\text{CO}_2$ . This decomposition occurs at approximately 600 °C. It can be used to calculate the mass of volatile or less thermally stable compounds present. The extent of conversion to  $\text{CaO}$  via calcination can be studied using powder XRD. This is a useful technique as  $\text{CaO}$  is an active catalyst that can be obtained from mollusc shells.<sup>26, 31</sup> The different polymorphs of  $\text{CaCO}_3$  can be determined and optimal calcination temperatures can be identified when all of the  $\text{CaCO}_3$  is gone. Raw mussel shells are often composed of calcite and aragonite as shown in **Figure 1.4**, but sometimes they are composed of just one or the other.<sup>26</sup> For example, Jones and co-workers showed using powder XRD that raw

green lipped mussels do not contain any calcite at ambient temperature.<sup>32</sup> CaO has a unique powder XRD spectrum and can be easily distinguished from aragonite and calcite as shown in **Figure 1.4**.

Powder XRD can be used to identify crystalline compounds in a sample. Calcite and aragonite have different unit cell parameters and space groups and therefore have different powder XRD diffractograms, making them distinguishable from one another. If there are multiple compounds (i.e. polymorphs), the relative amounts can be determined based on the relative intensities of the peaks.<sup>33</sup> Powder XRD can be a very useful tool in determining whether shells are composed of aragonite, calcite, or both as shown for mussel shells in **Figure 1.4**.

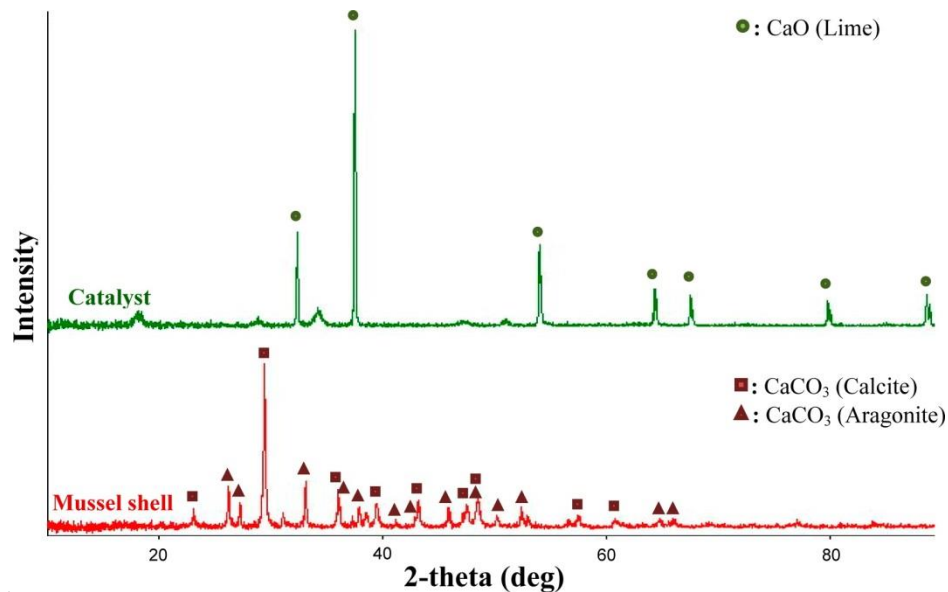


**Figure 1.4** Powder XRD spectra for showing the presence of calcite and aragonite in raw mussel shell and after calcination of mussel shells at 1050 °C for 2h. (Reprinted with permission from Tekin K. Hydrothermal Conversion of Russian Olive Seeds into Crude Bio-oil Using a CaO Catalyst Derived from Waste Mussel Shells. *Energy & Fuels*. 2015;29(7):4382-92. Copyright 2016 American Chemical Society.)

### 1.2.2.2 Morphology of Shells using Microscopy

The morphologies and microstructure of materials like mollusc shells can be determined using a scanning electron microscope (SEM). Images are produced by scanning the surface of a sample with a focused beam of electrons.<sup>34</sup> These electrons interact with atoms in sample. There are several types of detectors that can be used; back-scatter electron detector (BSED), secondary electron detector and energy dispersive X-rays (EDX). Images that use back-scattered electron detection may have brighter and darker regions. Areas of lighter regions contain more electrons. Secondary electron detection gives better topology imaging than BSED. EDX gives information about the elements in a sample based on the characteristic radiation that is emitted by the sample.<sup>34</sup>

Mollusc shells are 95-99.9%  $\text{CaCO}_3$ , with the remaining percentages made of other minerals and an organic matrix composed of silk-fibroin like proteins,  $\beta$ -chitin and glycoproteins that act as a glue to hold crystals of  $\text{CaCO}_3$  in place as well as controlling nucleation and polymorph type.<sup>35, 36</sup> Mollusc shells can consist of calcite, aragonite or a mixture of both polymorphs. If both calcite and aragonite are present in the mollusc shell, they are always separated into layers.<sup>37</sup> This has been shown using SEM of *Mytilus californianus* as shown in **Figure 1.5**. Calcite prisms that make up the outer layer can be  $>100 \mu\text{m}$  long and up to  $50 \mu\text{m}$  in diameter that are surrounded in a layer of organic matrix.<sup>38</sup> The inner aragonite layer of mollusc shells, also known as nacre or ‘mother of pearl’, are generally composed of polygonal aragonite platelets that are  $5\text{-}15 \mu\text{m}$  in diameter and  $0.5 \mu\text{m}$  thick. The platelets are arranged in parallel laminae and stacked on top of each layer separated by a small layer of the interlamellar organic matrix.<sup>39</sup> Biogenic aragonite of

the nacreous layer has been seen in many other molluscs including *Unio treminalis*, *Haliotis rufescens*, and *Pinctada fucata*.<sup>40-42</sup>

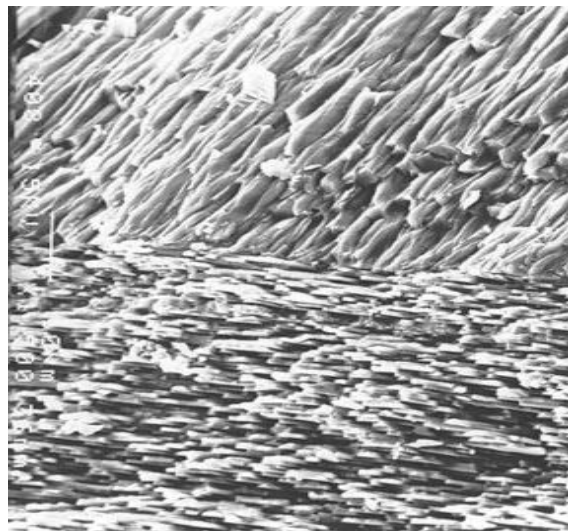


**Figure 1.5** SEM of the fracture layer through *Mytilus californianus* showing the prismatic calcite layer (top) and the aragonite layer (bottom), Source: Weiner and Addadi 1997, Figure 4, p.692. Reproduced with permission of Royal Society of Chemistry.

### 1.2.2.3 Solid-state NMR spectra of Mollusc Shells

NMR spectroscopy is a sensitive technique that has been used to study the organic matrix of mollusc shells. For solid-state NMR to yield meaningful data, artificial motions are introduced to average out anisotropic dipolar interactions in the solid. These motions cause the line shape to be sharper (i.e. more like solution NMR) than the broad line shape of a static (no artificial motion) spectrum.<sup>43</sup> This experiment is called magic angle spinning (MAS). In MAS, the sample (in a rotor) is spun at a high frequency at an angle of  $54.74^\circ$  with respect to the external magnetic field. Another important experiment in solid-state NMR is cross polarization (CP). In CP experiments, polarization from abundant spins such as  $^1\text{H}$  is transferred to dilute spins such as  $^{13}\text{C}$ . Here, a  $90^\circ$  pulse is made on the  $^1\text{H}$  only

and the polarization is transferred during the spin locking period (the contact time). CP enhances signal from dilute spins by a factor of  $\gamma_I/\gamma_S$  where  $\gamma_I$  is the gyromagnetic ratio of the abundant nuclei and  $\gamma_S$  is the gyromagnetic ratio of the dilute nuclei. The contact time must be considered carefully.<sup>43</sup> For example, larger molecules relax more quickly in comparison to small molecules. In the case of the organic matrix in molluscs, which are macromolecules, their signal will relax fast. Therefore, if the contact time is too long, by the time the data acquisition begins, they may be relaxed and there may not be any signal. A solid-state NMR spectroscopy study into the shell of *Perna canaliculus* exposed a small number of disordered carbonates. This was unusual as the main polymorph of the shell aragonite has highly ordered carbonates. The disordered carbonates were interacting with bioorganics, carbonates and water molecules. The <sup>13</sup>C CP-MAS NMR (**Figure 1.6**) reveals the proteinaceous content of the shells mentioned above. Again, based on the study of aragonite rich *Perna canaliculus* shells these carbon peaks are not just from the calcium carbonate in the shells, but also from the biopolymers between the layers. The peaks at 53 and 45 ppm are likely from Glycine and Alanine side chains which are consistent with silk fibroin protein content.<sup>44</sup> Peaks from 100-160 ppm are from proteins with aromatic side chains. The carbonyl peak at 171 ppm is from the calcium carbonate as well as carboxylic acids and amides.<sup>44</sup> Because of all of the disorder arising from small amounts of biopolymer the carbonate peak is much broader than what one would see in a pure calcite (168.21 ppm) or aragonite (170.49) sample using similar parameters. This is a result of their high crystallinity. The carbonate peak for amorphous CaCO<sub>3</sub>, for example, is very broad.<sup>45</sup>

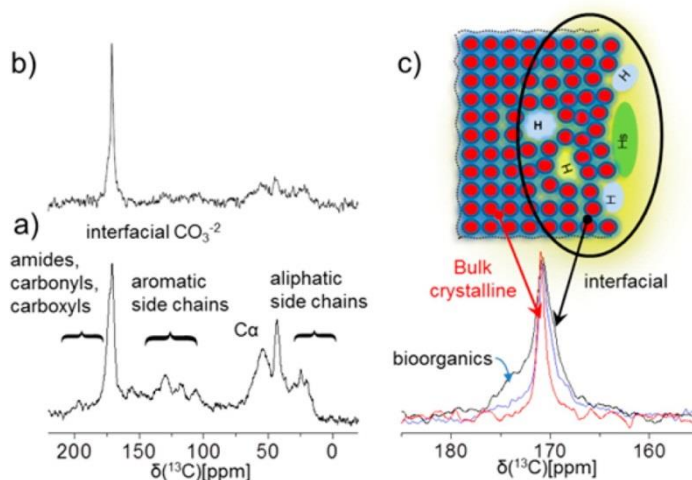


**Figure 1.6**  $^{13}\text{C}$  CP MAS spectra of the aragonitic shell of untreated *P. canaliculus* with contact time of (a) 1 and (b) 8 ms. The spectra expose the bioorganic content, mainly proteinaceous, and partially resolve the  $\sim 171$  ppm peak of the interfacial carbonates. (c) Expansion of the carbonate-peak region of the  $^{13}\text{C}$  MAS spectra with DE with 2400 s relaxation delay, red; DE with 15 s relaxation delay, blue; and CP with 8 ms contact time and 2 s relaxation delay, black. (DE=direct excitation, CP=cross polarization) Reprinted with permission from (Ben Shir I, Kababya S, Katz I, Pokroy B, Schmidt A. Exposed and Buried Biomineral Interfaces in the Aragonitic Shell of *Perna canaliculus* Revealed by Solid-State NMR. *Chemistry of Materials*. 2013;25(22):4595-602.). Copyright 2016 American Chemical Society.

$^1\text{H}$  NMR resonances of nacreous mollusc are summarized in **Table 1.2**.  $^1\text{H}$  MAS NMR spectra of molluscs *Perna canaliculus* and *Haliotis laevis* are broad and contain up to 2 proton environments, none of which are from the organic matrix. Jager *et al.* observed a resonance at 13.8 ppm in spectra of mollusc shells and assigned this to acidic bicarbonate hydrogens that result from an amorphous surface layer about 10 nm thick that coat the aragonite tablets in nacre in *Haliotis laevis*.<sup>46, 47</sup> This signal was also observed in annealed *Perna canaliculus* (New Zealand green-lipped mussel).<sup>44</sup>  $^1\text{H}$  NMR spectra of amorphous calcium carbonate (ACC) did not reveal any acidic bicarbonate protons.<sup>45</sup> However, due to the similarity of the chemical shift of these protons compared with those of  $\text{KHCO}_3$  and  $\text{NaHCO}_3$  it is believed that the resonances in this region of  $^1\text{H}$  NMR spectra

result from small amounts of  $\text{Ca}(\text{HCO}_3)_2$ .<sup>45,47</sup> The other proton environment near 5 ppm is from water. A resonance ~1-1.5 ppm was observed in both of these shell samples, Jager *et al.* claimed these proton resonances result from mobile  $\text{CH}_3$  units of chitin in the organic matrix while Shir *et al.*<sup>44</sup> reports them as an instrument artifact.

**Table 1.2** Summary of  $^1\text{H}$  NMR Data for Nacreous Molluscs

Shell Type	Nature of Shell	Heat Treatment	Water $\delta$	$\text{HCO}_3^-$ $\delta$	Reference
Perna canaliculus <sup>a</sup>	Calcite/nacre	None	~5 ppm	14.5	41
	Calcite/nacre	250 °C, overnight	~5 ppm	None	
Haliotis laevigata <sup>b</sup>	nacre	None	5.2 ppm	14.4	44

<sup>a</sup>Shells were ground to a fine powder before heat treatment <sup>b</sup>Nacre separated from the prismatic layer by sand blasting.

#### 1.2.2.4 Infrared Spectra of Mollusc Shells

Studies on the different polymorphs and hydrates of  $\text{CaCO}_3$  have shown that each polymorph has a unique IR spectrum<sup>45,48</sup> which helps to distinguish between polymorphs present in mollusc shells. Carbonate ions,  $\text{CO}_3^{2-}$ , have four fundamental modes of stretching;  $\nu_1$ , symmetric C-O stretch,  $\nu_2$ ,  $\text{CO}_3^{2-}$  out of plane bending,  $\nu_3$ , C-O asymmetric stretch (doubly degenerate) and  $\nu_4$ , O-C-O planar bending (doubly degenerate).<sup>48</sup> The symmetry of the  $\text{CO}_3^{2-}$  in the solid phase of calcite and aragonite dictates which of these fundamental modes are active in the infrared, allowing us to distinguish easily between aragonite and calcite. The site symmetry of the  $\text{CO}_3^{2-}$  ion based on crystal data is  $D_3$  and  $C_s$  in calcite and aragonite respectively.<sup>49</sup> Therefore, based on the selection rules for the  $D_3$  and  $C_s$  point groups, three of the fundamental modes,  $\nu_2$ ,  $\nu_3$ , and  $\nu_4$  for calcite and all fundamental modes for aragonite are expected to be observable.

Though not used extensively to study biogenic  $\text{CaCO}_3$ , the IR spectra for aragonite and calcite in mussel shells are nearly identical to spectra of those from geological origin. An example of calcium carbonate with 99.5% purity, raw mussel shells and mussel shells pyrolyzed at  $800^\circ\text{C}$ , **Figure 1.7**, shows that the calcium carbonate IR spectra and mussel shell IR spectra are identical.<sup>50</sup>

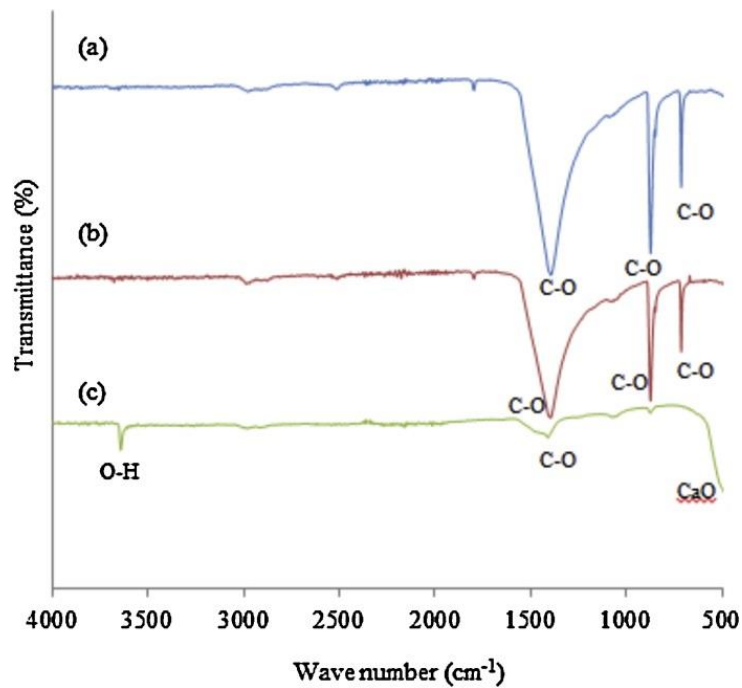


**Figure 1.7** FTIR spectra of (a) calcium carbonate with 99.5% purity, (b) raw green lipped mussel shells and (c) green lipped mussel shells pyrolysed at  $800^\circ\text{C}$ . (Source: Shariffuddin *et al.* Chemical Engineering and Research Design, 2013, Fig. 3, p.1696. Reproduced with permission of Elsevier)

Fourier transform IR (FT-IR) spectrophotometers measure the percent transmittance of a material which is the ratio of intensity of the sample beam relative to the reference beam, expressed as a percentage.<sup>43</sup> This type of spectrum results in the absorptions pointing down, as shown in **Figure 1.7**, which allows differences in spectra to be noticed easily. Sample

prep for FT-IR measurements can be cumbersome. For example, grinding of the material of interest with an IR inactive compounds such as KBr or mineral oil. Modern FT-IR instruments have an attenuated total reflectance (ATR) attachment which measures absorbance rather than transmittance where the resulting absorptions point up. It requires little to no sample prep. In this method, the material of interest is pressed against a material of higher refractive index (i.e. diamond) and an absorption spectrum is recorded. Absorption can be converted to transmittance by using the following  $A = -\log(\%T/100\%)$ , where A is absorbance and %T is the percent transmittance.<sup>43</sup> This mathematical transformation does not affect the positions of the absorption bands in a spectrum or the shape of the bands. Therefore, it is common to display spectra as percent transmittance even if they were collected in absorbance mode (ATR) because it is easier to compare several spectra this way.

#### **1.2.2.5 Surface Areas of Ground Mollusc Shells**

The surface area and particle size of ground mollusc shells can be very important depending on the application. For example, a higher surface area is often beneficial for catalysis and adsorption applications. Many of the surface areas for ground raw mollusc shells have been low. The surface areas of ground short-necked clam, green mussel, oyster, and cockle shells have been reported as 0.83, 0.62, 1.43 and 0.83 m<sup>2</sup>/g, respectively.<sup>51</sup> Calcining mussel shells increased the surface area from 0.92 m<sup>2</sup>/g to 11.89 m<sup>2</sup>/g as reported by Tekin.<sup>26</sup> However, in another study where shells were calcined, particles in the 53-106 μm range had a surface area of 1.22 m<sup>2</sup>/g and particles in the 212-250 μm range had a surface area of just 0.43 m<sup>2</sup>/g,<sup>52</sup> which is much lower than the aforementioned 12 m<sup>2</sup>/g. The highest surface

area found in literature to date was 5.01 m<sup>2</sup>/g for raw ground golden mussel shell used as a solid support in vortex-assisted matrix solid-phase dispersion (MSPD).<sup>53</sup>

### **1.3 Applications of Mollusc Shells**

Mollusc shells can be used in a diverse range of areas. Morris *et al.* and Hou *et al.* have recently reviewed the applications of mollusc waste where the shells remain CaCO<sub>3</sub> and are used for health promoting applications.<sup>54, 55</sup> This list below is not meant to be exhaustive. For example, the use of mollusc shells as an antimicrobial agent or livestock feed additive are not described, nor are the use of scallop and other shells in art and other decorative areas.

#### **1.3.1 High Purity Calcium Carbonate**

CaCO<sub>3</sub> is the most heavily exploited mineral on Earth<sup>56</sup> and used in many industrial areas including building materials, limestone and precipitated CaCO<sub>3</sub>. In Galicia, Spain, a mussel cannery generates 80,000 tons per year of mussel waste. To valorise the waste and create a value-added product from mussel aquaculture, a pilot plant for the generation of high purity CaCO<sub>3</sub> by eliminating water, salt, mud, and any organic matter, was opened.<sup>23</sup>

Shells (organic residue attached) were washed with large amounts of fresh water to remove salt and then shells were heated to 500 °C to burn off the residual organic matter. This method uses a lot of freshwater, 0.8 m<sup>3</sup> per t of shells, and required a large amount of energy.<sup>23</sup> Some of the water in this process is recycled at a wastewater treatment plant onsite. In 2006, over 1300 t of high purity (>95 %) CaCO<sub>3</sub> was produced for three different particle sized products from this plant. The first product was fine powder (20 μm) CaCO<sub>3</sub>

aimed at being a liming agent to neutralize acidic wastewater from a local power plant. The second and third products were flaked sized particles (<4 mm, <2 mm) that were mainly used for additives to mulch for soil amendment in the area and for agricultural uses such as a food additive for laying hens and broilers.

One of the main issues encountered by operating a plant that used waste mussel shells as a feedstock was the odour from storage of the waste prior to cleaning and the VOCs produced from the decomposition of residual meat. The smell of the processing plant bothered people living in the neighbourhood. It was addressed by ensuring the raw mussel shell waste was fresh, with minimal amounts of decomposition. This was achieved by cutting down the storage time to a maximum of three days from the time received. Another issue was the fine particle size of powdered product, which generated particulate matter during calcination and packaging. This problem was solved by installing bag filters in the already existing air extraction system. To reduce the amount of contaminants in emissions (SO<sub>2</sub>, NO<sub>2</sub>) Barros *et al.* switched to propane from oil as a fuel source for many parts of the process. This plant and the struggles encountered with respect to greening of a process is a perfect example of how using a renewable feedstock is not always green initially but making adjustments can lead to a more environmentally friendly process.

### **1.3.2 Soil Amendment**

Soils near Galicia, Spain are acidic in nature. Amendment of the soil is performed using cow slurry, which contributes to soil acidification. However, with Galicia being a large producer of mussels, there is a lot of mussel shell residue. They have combined liming

agents from mussel shell with cow slurry to increase nutrient levels and increase the pH.<sup>57</sup> Kwon *et al.* showed using oyster shells as a liming agent in combination with other amendments can improve soil fertility.<sup>58</sup> The soil was a Humic Cambisol with a pH of 5.5 with high organic content and a silty loam texture. The high amount of aluminum in the soil is the main reason for the low fertility. Mussel shells, provided by Calizas Marinas S. A. Shells, were washed with freshwater to remove salt and heated to 500 °C to remove any organic contents. The shells were ground to an unspecified particle size.

Biological properties of soil have been used as indicators for soil quality because of their quick response to changes in the soil. The soils were monitored based on 6 biological properties; Microbial biomass C and N, dissolved organic C (DOC), dissolved organic N (DON), dissolved inorganic N (DIN), and net N mineralization; and activity of 4 soil enzymes; dehydrogenase, acid phosphomonoesterase, B-glucosidase and urease. All of the amendments were incorporated on top of the soil in 5 plots measuring 6 × 6 m with 2 m separating each plot. T1 was a control plot without amendment; T2 had 80 Kg Nha<sup>-1</sup> of cow slurry spread in the Spring and 60 Kg Nha<sup>-1</sup> in the Fall, T3, T4 and T5 had the same amount of cow slurry as T2 with the addition of 0.5, 1.0 and 1.5 t ha<sup>-1</sup> of ground mussel shells, respectively.<sup>57</sup> Incorporation of the amendment began in April 2010 and the sampling was in December 2010. As expected, with the addition of the mussel shell liming agent the pH of the soils increased from 5.40 in T1 to 5.96 in T5. There was no effect for the exchangeable Mg, Na, P or K but there was an increase in the exchangeable Ca in T3, T4, and T5. The total amount of Al in the exchange complex and the Al saturation was significantly reduced for T3, T4, and T5, independent of the amount of mussel shell added.

Microbial biomass C and N increased for T4 and T5, a sign of higher soil fertility. It has been shown that in general, DOC and DON increase after liming. Dissolved organic matter is known to play a crucial role in C and N terrestrial cycles, namely supplying N, P and S to plants. DON was higher at T5, likely due to an increased pH and exchangeable Ca. There was no change in DIN. There was also not a clear effect on the N mineralization by the combination of cow slurry and mussel shell liming agent. The soil enzyme dehydrogenase does not occur on stable soil complexes, it only occurs in viable cells. Therefore, an increase in dehydrogenase shows an increase in microbial activity. Such is true for the soil samples treated with higher mussel shell amounts, T4 and T5, as shown in **Table 1.3**. This general increase in microbial population was also supported by an increase in microbial C and N. Urease catalyzes the conversion of urea into CO<sub>2</sub> and NH<sub>3</sub>. The activity of urease increased with large amounts of liming agent, T4 and T5. The degradation of organic materials such as crop residue and manure from animals is correlated to the activity of β-glucosidase. The activity of β-glucosidase is also a good indicator of pH changes, the largest of which were T4 and T5, respectively. Lastly, the largest amounts of liming agent, T4 and T5, inhibited the activity of phosphomonoesterase. These results were a similar finding to Lee et al. who had completed a similar study using oyster shells.<sup>59</sup> The excretion of phosphomonoesterase by microorganisms and plants is dependent on their need for orthophosphate, which is also affected by soil pH.

**Table 1.3** Soil enzyme activities for treatments T1-T5. All values are in  $\mu\text{mol product g dry soil}^{-1} \text{ h}^{-1}$ . Mean values and standard deviations are obtained from  $n = 4$  samples. (Source: Paz-Ferreiro *et al.* Chemosphere, 2012, Tab.3, p.1119. Reproduced with permission of Elsevier.)

	Dehydrogenase	$\beta$ -glucosidase	Urease	Phosphomonoesterase
T1	$0.44 \pm 0.05$	$1.25 \pm 0.22$	$8.6 \pm 0.9$	$4.6 \pm 0.9$
T2	$0.47 \pm 0.10$	$1.38 \pm 0.60$	$9.5 \pm 1.5$	$3.9 \pm 0.2$
T3	$0.41 \pm 0.09$	$1.29 \pm 0.14$	$8.0 \pm 2.4$	$4.3 \pm 0.2$
T4	$0.70 \pm 0.05$	$1.87 \pm 0.27$	$14.7 \pm 0.7$	$3.1 \pm 0.8$
T5	$0.72 \pm 0.05$	$1.88 \pm 0.29$	$16.7 \pm 0.9$	$2.5 \pm 0.8$

Dumps from old mining operations pose pollution risks. After a Cu shut down operations in the 1980s after the ore quality became too poor, the dump site continued to contaminate the region in Touro, Spain. High concentration of metal sulfides, including pyrite, caused acidification to the surrounding environment. With Galicia being the second largest mussel producer in the world, Ramírez-Pérez *et al.*<sup>60</sup> used naturally basic mussel shells as part of a soil amendment project to increase the pH of the sump site so that plant life could grow again. Previous studies on this region revealed Cd, Pb, Cr, Zn, Ni and Cu in the soil samples and found that the presence organic matter, Fe and Mn oxides and cation exchange capacity affect the degree of heavy metal sorption and retention. Through analysis of sorption and desorption curves Vega *et al.* determined that heavy metals were weakly binding to the soil and desorbing them causes alarm for pollution risks.<sup>61</sup> After testing mussel shell in conjunction with barley straw and sewage sludge he showed that amendments can increase the capacity for sorption and retention of heavy metals because of an increase of soil pH. Heavy metal sorption occurs mainly by displacing the dominant cation in the cation

exchange complex. The dominant cation in amended and non-amended soils are  $\text{Ca}^{2+}$  and  $\text{Al}^{3+}$ , respectively.<sup>62</sup>

To test the effect of three different concentrations of ground mussel shell amendment on contaminated acidic Cu mine soil to attempt to increase the retention of four heavy metal cations; Cu, Zn, Cd, and Ni. By increasing the retention time, the mobility of the ions would decrease and so too would their availability for uptake by plants.<sup>60</sup> The risk for soil and water pollution would be significantly reduced. Mussel shells (pH 9.4) were from a facility in Galicia, where they have been mass produced since 1989, they arrived washed, dried and ground to a particle size of  $< 1$  mm. Soil samples were collected from non-amended areas around the Touro Cu mine dump. 10 soil sub-samples (0-20cm) were collected, air dried and sieved (2 mm).<sup>60</sup> Batch experiments were conducted with varying amounts from 80-1570  $\mu\text{mol}$  of each metal cation studied and varying the mussel shell amendment from 0-24  $\text{g kg}^{-1}$ . The retention of Cu at the lowest metal concentration, 80  $\mu\text{m}$ , was 86 % without any shell added. Cd, Ni, and Zn were much poorly retained under these conditions with 37, 40, and 29 % retention, respectively. The retention of the metals increases as mussel shell amounts are increased, reaching  $>95$  % retention for all metals when the shell dose is 24  $\text{g kg}^{-1}$ . In all cases Cu was the most retained metal. The order of Zn, Cd, and Ni varied a lot over the doses of amendment and metal concentrations. In general, the percentage of retained metal decreased as the metal concentration increased. At the highest dosage of shell and concentration of metal the retention percentages for Cu, Cd, Ni, and Zn were 100, 87, 77, and 98 %, respectively.<sup>60</sup> The pH of the mine soil increased from 3.8-4.8 with the highest dose of mussel shell amendment, which also increased the adsorption of the metals. The metal retention was affected differently depending on metal concentration and dosage.

However, it was not pH alone that affected the retention of  $\text{Cd}^{2+}$  and  $\text{Zn}^{2+}$ . The retention of these divalent cations is known to be greater for mussel shells that have a higher aragonite content.<sup>63</sup> The results of desorption studies are shown in **Table 1.4**. In non-amended soils the percentage desorbed ranged from 24-40% for Ni and Cd, ranged from 7-39% for Zn and stayed below 12% for Cu. For Cu, Cd, and Ni desorption increased as the amount of metal held in the soil increased. The opposite was true for Zn. The trend for metal desorption percentage of non-amended soils was  $\text{Cd} > \text{Ni} > \text{Zn} > \text{Cu}$ .<sup>60</sup> This trend suggests that Cd and Ni are more reversibly retained than Zn and Cu. For the highest amount of amendment at the greatest metal concentrations, the desorption percentages were all less than 1%. In general, mussel shell diminished metal desorption, most specifically at high mussel shell amounts.

**Table 1.4** Heavy metal desorption of Cu, Cd, Ni, and Zinc, expressed as percentage of the previously retained, in the various shell treated (6, 12 or 24 g kg<sup>-1</sup>) and untreated (0 g kg<sup>-1</sup>) mine soil samples as function of metal added. (Source: Ramírez Pérez *et al.*, Journal of Hazardous Materials, 2013, Tab. 5, p.127. Reproduced with permission of Elsevier.)

Shell dose (g kg <sup>-1</sup> )		Added metal (mmol)					
		0.08	0.16	0.31	0.79	1.26	1.57
Cu	0	6.1	7	9.8	7	9.2	11.7
	6	0.3	0.2	0.2	<0.1	0.4	0.3
	12	0.1	<0.1	<0.1	<0.1	<0.1	<0.1
	24	0.3	<0.1	<0.1	0.2	<0.1	<0.1
Cd	0	27.5	33.3	34.8	24.5	26.8	40
	6	10.7	8.7	9.2	9.6	9	10.7
	12	0.3	1.8	2.1	1.4	3.8	4.1
	24	<0.1	<0.1	<0.1	0.1	1.4	0.9
Ni	0	28.6	27.4	25.1	27.3	30.2	33.9
	6	16.4	11.8	11.3	7.8	12.8	14.2
	12	2	1.4	4.2	3.2	4.6	3.8
	24	0.2	0.1	<0.1	<0.1	<0.1	0.9
Zn	0	25.3	39.4	15.3	7.5	14.6	7.6
	6	4.6	6.4	7.1	6.5	9.5	9.3
	12	0.3	0.3	0.4	0.2	1.3	2.5
	24	0.3	0.1	<0.1	<0.1	<0.1	<0.1

### 1.3.3 Acid Mine Drainage

Acid mine drainage (AMD) often arises from coal mining when pyrite from coal mining is exposed to water and oxygen. The sulfide becomes oxidized to sulfuric acid, decreasing stream water pH and catalyzing leaching of metal materials.<sup>64</sup> Mussel shells have been used as potential treatments in environmental remediation of AMD sites.<sup>64-67</sup>

Sulfate reducing bioreactors have been used recently to treat AMD. They remove contaminants of acidity, metals and sulfate from AMD. These bioreactors have low maintenance and energy costs and can use natural organic waste as substrates. Typically,

the reactors have organic and alkaline substrates. The use of mussel shells that would normally go to landfill is a more economical and sustainable than using limestone from a quarry.<sup>67</sup>

One study examined the efficacy of the removal of metals with various sized and shaped reactors using various substrates from an AMD seep at Stockton Coal Mine in New Zealand that was made up of greater than 98% Fe and Al.<sup>64</sup>



**Figure 1.8** Organic and alkaline substrates used in bioreactors. (Source: McCauley *et al.* Water Research, 2009, Fig. 1, p.963. Reproduced with permission of Elsevier.)

The substrates were mainly waste materials from industrially processing. Mussel shells from mussel farm waster and limestone were the alkaline substrates. Post peel from untreated fence manufacturing, *Pinus radiata* bark, and compost containing predominantly delignified bark were the organic substrates. **Figure 1.8** shows the substrates with a ruler to get an idea for their size.

Bioreactors with the highest mussel shell content had the most effective metal and sulfate removal. The dissolution of the alkaline substrate was dependent on grain size, shape,  $\text{CaCO}_3$  and mineralogy. Limestone is mainly calcite whereas mussel shells can contain calcite and aragonite. The enhanced performance of reactors with mussel shells is attributed

to faster acid dissolution and was confirmed as effluent Ca concentrations were higher in bioreactors with mussel shells.<sup>64</sup>

Bioreactors that contained 20% mussel shell and had Ca concentrations 39% higher in the effluent than reactors that contained 12.5% limestone. Sulfate removal was also very good for reactors with mussel shells; however, it was not all attributed to the increase in pH. Other ways sulfur could have been removed are through H<sub>2</sub>S degassing and gypsum (CaSO<sub>4</sub>) precipitation.<sup>64</sup>

A comparative study of limestone with mussel shell as alkaline substrates in upward flow bioreactors was performed and found similar results with Al, Mn, Fe, Ni, Cu, Zn, and Cd present.<sup>67</sup> Metal removal was satisfactory in all bioreactors. The trend for dissolved metal removal was: Al>Cd>Zn>Fe>Cu>Ni>>Mn. Bioreactors with mussel shells as the alkaline substrate removed more dissolved metals than those that had limestone. Sulfate reducing bioreactors using mussel shells and limestone significantly reduced metal concentration in AMD. The reactors were more efficient and displayed higher alkalinity with mussel shell as opposed to limestone. The differences in alkalinity between mussel shell and limestone bioreactors were once again attributed to the differences in mineralogy. In 2005 Cubillas *et al.* showed that mussel shell (calcite and aragonite) BET surface increased by 80 % during dissolution whereas limestone (calcite) only increased by 30 %.<sup>68</sup>

### **1.3.4 Phosphate Removal and Water Purification**

Phosphate removal from waste water is of growing concern because high levels of phosphorus, nitrogen, and other nutrients are resulting in eutrophication and causing unfortunate consequences such as algae blooms.<sup>32</sup> Although eutrophication is the result of

high levels of phosphorus, nitrogen, and other nutrients in water, the severity of eutrophication is mainly phosphorus dependent. Orthophosphate is the most common form of phosphorus that pollutes wastewater.<sup>69</sup> The abundance of algae from algal blooms reduces the oxygen content in the water and has devastating effects on aquatic life.<sup>52</sup>

The amount of phosphates can be controlled through chemical precipitation, biological treatment or adsorption.<sup>70</sup> Chemical treatment is typically achieved by precipitating phosphate with Al, Ca, or Fe but the disposal of the effluent can come at a high cost. Biological treatment is tedious because it relies heavily on temperature, environment and time. Adsorption is simplest and economically favorable depending on the source of the adsorbent. With particular attention on renewable materials from waste by-product streams a number of adsorbents including eggshell, crab shells, calcite, kaolinite, fly ash, red mud and steel slag have been investigated.<sup>69, 70</sup> This application is important in countries that have large agricultural sectors. The idea is to help remove phosphates from agricultural and industrial wastewater and stop it from entering surrounding ecosystems.

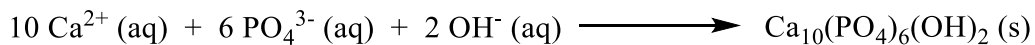
Lime (CaO) is a very common adsorbent used to capture phosphates. The source of lime is typically limestone which must be heated to 650 °C to yield lime.<sup>52</sup> However, limestone is a non-renewable resource and can be replaced by renewable CaCO<sub>3</sub> rich mollusc shells from mussels and oysters and by calcination of the shells lime is produced just as with fossil fuel derived limestone. Both CaCO<sub>3</sub> and CaO from mussel or oyster shells have been studied for their efficacy to remove phosphate from aqueous test solutions. In general, raw shells (CaCO<sub>3</sub>) have proven to be less effective at phosphate removal as compared to calcined shells (CaO).<sup>52</sup> The most important factors with respect to how well the shell-

sourced CaCO<sub>3</sub>/CaO adsorb phosphate are time, concentration of adsorbent/adsorbate, particle size and pH.

There are three generally accepted mechanisms for phosphate removal from water using calcined mussel and oyster shells; (1) homogeneous precipitation of calcium phosphate in solution, (2) heterogeneous precipitation of calcium phosphate on the shell surface and (3) adsorption or absorption of phosphate onto the surface of the shell.<sup>52</sup>

Hydroxyapatite (HAP), similar to the mineral phase of calcium phosphate in bones has been used bone regrowth tissue engineering<sup>55</sup> and dental materials. The most ideal outcome of this process is to produce HAP, an insoluble form of calcium phosphate that has other uses. The precipitation of HAP, shown in **Equation 1.1**, only occurs at pH > 10 because a sufficient concentration of OH<sup>-</sup> is needed and the correct phosphate species, PO<sub>4</sub><sup>3-</sup>. This was observed experimentally by J. Xiong *et al.* as in their work uptake of phosphate was slow at a pH of 1.5.<sup>69</sup> Under such conditions, the hydroxide ions that form from dissolution of lime are being used up in neutralisation reactions.

### **Equation 1.1**



The lack of solubility of CaCO<sub>3</sub> as compared to lime makes it unlikely that precipitation of calcium phosphate is the main mechanism when raw mussel or oyster shells are used, instead it must proceed via an adsorption or absorption process. However, if calcination or pyrolysis of raw shells is incomplete then both precipitation and adsorption/absorption can occur.<sup>52</sup> A challenge when using CaCO<sub>3</sub> directly for adsorption of orthophosphates is its

lack of stability in an acidic environment. It decomposes to form a sludge, making it difficult to remove.<sup>70</sup> An ongoing aim in research is to produce a more robust material towards adsorption of phosphates that can be easily collected. Calcined oyster shells have been used in conjunction with another by-product (fumed silica from smelting processes in Australia) to make a phosphate removal material that tackle the sludge issue.<sup>70</sup>

### **1.3.5 Building Materials**

A binder, an aggregate and additives are the main components in a dry mortar. Research for the development of new mortar formulations investigated how new additives can improve the mortars by enhancing mechanical properties such as workability, compressive strength and durability. The binder component, cement, is the most expensive component of dry mortars.<sup>71</sup> Therefore, replacement is appealing financially to reduce costs as long as standards for mechanical properties are met. Waste materials such as tire rubber ash and fumed silica, among other have been tested and have shown to be advantageous. Limestone from waste mussel shells and other molluscs from aquacultural processing have been tested as a filler material to partially replace Portland cement, a very common binder, therefore, further research and developments for new formulations of mortar based on mollusc shells will likely continue in the future.<sup>24, 51</sup>

In Galicia, Spain, over 80 000 tonnes of limestone have been produced from mussel cannery waste each year.<sup>24</sup> A study from 2007 showed a direct comparison of using limestone from waste mussel shells, m-CaCO<sub>3</sub>, and limestone from a quarry, q-CaCO<sub>3</sub>. The test mortars were prepared as shown from Portland CEM II/A-V 42.5R type cement, silica sand and limestone. Some mortars used just q-CaCO<sub>3</sub> or m-CaCO<sub>3</sub>, others are a

combination of the two sources of limestone and lastly mortars where limestone replaced some of the cement. This was to test whether a mortar could be produced with a decreased production cost and maintain mechanical properties.

It was concluded that strength values increased with curing time. After 7 days of curing, the mortar that contained m-CaCO<sub>3</sub> had less strength than that containing q-CaCO<sub>3</sub>, but after 90 days of curing it was the opposite. The mortar with the most m-CaCO<sub>3</sub> had the highest strengths, likely from the differences in microstructure between q-CaCO<sub>3</sub> and m-CaCO<sub>3</sub>.<sup>24</sup> The two sources of CaCO<sub>3</sub> have very distinct, differently shaped and sized particles. **Figure 1.9** shows SEM images of q-CaCO<sub>3</sub> and m-CaCO<sub>3</sub>; q-limestone has spherical shaped particles between 2 and 6 μm in size, m-limestone has many morphologies but is dominated by prismatic particles up to 14 μm in size. It was speculated that large prismatic particles could have formed a network that binds strongly with cement as it solidified, owing to its enhanced strength.<sup>24</sup>

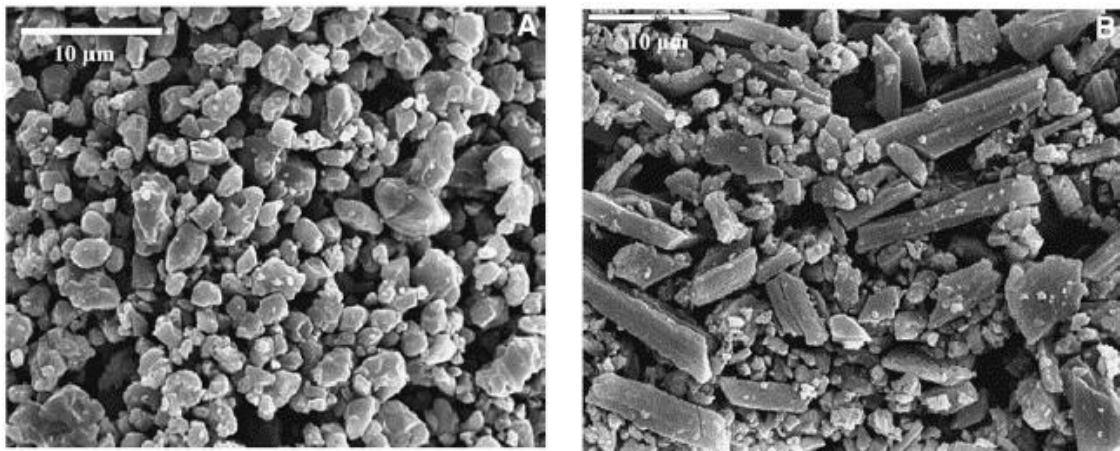


**Figure 1.9** SEM images of (A) q-CaCO<sub>3</sub> and (B) m-CaCO<sub>3</sub>. (Source: P. Ballester *et al.* 2007, *Cement and Concrete Research*, Fig.2, p.561. Reproduced with permission of Elsevier.)

The compressive strength of mortars prepared by replacing some of the Portland cement with m-CaCO<sub>3</sub> showed similar and better strengths in comparison to the control mortar. The amount of cement was reduced by 10% and showed no adverse effects on the mechanical properties of the mortar.<sup>24</sup> The replacement of q-CaCO<sub>3</sub> of m-CaCO<sub>3</sub> demonstrated an excellent way to manage industrial waste, reduce costs for mortar production, and reducing the need to mine CaCO<sub>3</sub> from the quarries, making it a more environmentally friendly process.

A study by Lertwattanakul *et al.* showed the incorporation of ground mollusc shells can lessen the demand on water in mortar when compared with Portland cement.<sup>51</sup> Test mortars were prepared by replacing Portland cement Type 1 with increasing amounts of seashell powder. The amounts were 5, 10, 15, and 20 % by weight replacement. The water demand, setting time, compressive strength and drying shrinkage of the test mortars were determined and compared to the control mortar, Portland cement. Particle size analysis showed that the particles of ground sea shells were smaller than the particles of Portland cement.<sup>51</sup> The presence of seashells reduced the amount of water needed and the higher the content of the shells, the less water required. This was likely because particles from seashells are flatter than the Portland cement particles and have a lower porosity so there is less water retained in the mortar.<sup>51</sup> These two studies are examples of how the source of CaCO<sub>3</sub> has an affect on the mortar. In both cases it is due to morphology of CaCO<sub>3</sub> particles in the mortar.

#### **1.4 De-icers**

Mussel shells are a valuable source of CaCO<sub>3</sub> (> 95%) and as such have been valorized in many areas where CaCO<sub>3</sub> is used.<sup>54, 55, 72</sup> One area that mollusc shells have been

underutilized is as a starting material for synthesis. This may be due to purity issues. For example, while molluscs contain silk fibroin-like proteins, glycoproteins and  $\beta$ -chitin, studies have shown that there are small amounts of metals and minerals present. For example, ground *Mytilus galloprovincialis* shells have ions of Na, K, Mg, Mn, Fe, Zn, P and Al as determined by atomic emission and absorption spectroscopy.<sup>60</sup> As discussed in **1.3.1**, Barros *et al.* developed a plant in Spain to make high purity (>95% )  $\text{CaCO}_3$ . The remaining <5% is composed of  $\text{MgCO}_3$ ,  $\text{Fe}_2\text{O}_3$ ,  $\text{K}_2\text{O}$ ,  $\text{SiO}_2$ ,  $\text{Al}_2\text{O}_3$ ,  $\text{NaCl}$  and organic carbon.<sup>23</sup>

#### **1.4.1 Calcium Acetate**

Calcium acetate ( $\text{Ca}(\text{CH}_3\text{COO})_2$ ) can be prepared by simple means from the reaction  $\text{CaCO}_3$  with  $\text{CH}_3\text{COOH}$ .  $\text{Ca}(\text{CH}_3\text{COO})_2$  can be used medicinally as a dietary supplement to supplement calcium and can also be used to treat high levels of phosphate in dialysis patients.  $\text{Ca}(\text{CH}_3\text{COO})_2$  can also be used in the preparation of hydroxyapatite, used for biomedical applications such as bone and coatings of metal implants and is an approved food additive in Canada.<sup>73, 74</sup> Little research has been reported on the use of  $\text{Ca}(\text{CH}_3\text{COO})_2$  as a de-icer.<sup>75</sup> However, it has been shown that  $\text{Ca}(\text{CH}_3\text{COO})_2$  has a lower freezing point than  $\text{NaCl}$  (based on same molarity solutions), is an effective de-icer and is less corrosive than  $\text{NaCl}$ .<sup>75</sup> The use of mussel shells as a starting material to make  $\text{Ca}(\text{CH}_3\text{COO})_2$  for de-icing roads in Canada is attractive because it is a non-corrosive and more environmentally friendly alternative to  $\text{NaCl}$ .

### 1.4.2 Ice Control in North America

In Canada and much of North America, the use of de-icing agents is critical to keep roadways safe and open during the winter months. Their use minimizes traffic accidents, injuries and deaths during ice and snow conditions.<sup>76</sup> Road salt (mainly NaCl) has been used as a de-icing agent in Canada since the 1940s.<sup>77</sup> On average, 5 million tonnes of road salt is used each winter to keep roadways across the country safe. While Canada has no plans to end the use of road salt, in 1995 due to the large quantities of chlorides being release in the environment, road salts underwent a 4-year comprehensive study under the Environmental Protection Act and was deemed a toxic substance.<sup>76</sup> In Canada, the average loading of NaCl was 100-200 kg of salt per kilometre of two-lane highway in 2000. CaCl<sub>2</sub> is the second most common road salt used in Canada and is mainly administered as a brine. MgCl<sub>2</sub> and KCl are also used but to a lesser extent. The use of organic salts was not presented in the study because they are not in use or only used in select scenarios (i.e. airports). This study showed that while natural background chloride concentrations are typically just a few milligrams per litre, except for regions that naturally have a higher salinity, during spring thaw chloride concentrations spike. For example, chloride concentrations as a result of runoff from roadways and salt storage sites have been measured as high as 18 000 mg/L and 82 000 mg/L, respectively. Ground water near storage areas had chloride concentrations as high as 2 800 mg/L. Rural lakes even see an increase of chloride concentrations of 150-300 mg/L.<sup>76</sup>

Rock salt is cheap (\$40 USD per ton) but the repairs to highways and vehicles due to its acceleration of corrosion puts its estimated cost much higher (at \$1200-2400 USD per ton,

per year).<sup>78</sup> Calcium magnesium acetate ( $\text{CaMg}_2(\text{CH}_3\text{COO})_6$ ) is produced from acetic acid and limestone and is 30 times the cost of NaCl (\$1100 UDS per ton). Because of its cost,  $\text{CaMg}_2(\text{CH}_3\text{COO})_6$  is less commonly used on highways and limited use to environmentally sensitive regions and bridges.<sup>78</sup> However, the use of renewable feedstocks, such as by-products from the food industry, can potentially make acetate based de-icers cheaper. De-icers have been made from renewable feedstocks via a renewable source of organic and inorganic materials.  $\text{CaMg}_2(\text{CH}_3\text{COO})_6$  and calcium magnesium propionate ( $\text{CaMg}(\text{CH}_3\text{CH}_2\text{COO})_4$ ) have been prepared from fermentation<sup>78</sup>,  $\text{Ca}(\text{CH}_3\text{COO})_2$  has been made using bamboo vinegar,<sup>75</sup> and a variety of organic de-icers have been made from degradation products from corn steep water.<sup>79</sup> These show organic materials can be sourced from fermentation of biomass and does not need to be sourced from oil-based resources.  $\text{Ca}(\text{CH}_3\text{COO})_2$  has previously been prepared using mollusc shells.<sup>80</sup> It has been synthesized using waste oyster shells for food-grade applications,<sup>81</sup> but in other studies it was not made clear what the end product would be used for,<sup>80</sup> others, including a patent from South Korea using waste oyster shells, were for de-icing applications.<sup>82, 83</sup>

The effective working temperature or lowest effective de-icing temperature of the most common chloride and acetate-based de-icers are summarized in **Table 1.5**.<sup>76, 84</sup> The working temperatures can be very important depending on the climate.

**Table 1.5** Working temperatures for chloride and acetate-based de-icers.

<b>Salt</b>	<b>Working Temperature (°C)</b>
NaCl	0 to -15
CaCl <sub>2</sub>	< -23
MgCl <sub>2</sub>	-15
KCl	-4
Calcium Magnesium Acetate	-15
Potassium Acetate	-32
Sodium Acetate	-18

Calcium and magnesium from  $\text{CaMg}_2(\text{CH}_3\text{COO})_6$  have been found to be beneficial to soil properties. High concentrations of calcium cause clay to form aggregates which overall enhances water drainage and aeration.<sup>85</sup> Acetate-type de-icers are biodegradable. The biggest risks associated with acetate-based de-icers is the breakdown of the acetate ion by microorganisms. The acetate ion is a nutrient that is readily utilized by microorganisms which leads to oxygen deficient conditions in soil and water.

### **1.5 Mollusc-derived Calcium Oxide in Catalysis**

Biodiesel is an alternative to fossil fuel derived diesel. It is derived from biomass, the fatty acid components of vegetable oils. Fatty acids are converted into fatty acid methyl esters using known transesterification procedures, in the presence of a catalyst and low molecular weight alcohol. Many heterogeneous basic catalysts have been studied for this reaction, mainly group II metal oxides, calcium oxide, magnesium oxide, strontium oxide, mixed oxides as well as hydrotalcites. Calcium oxide is the most popular of these solid basic catalysts because of its high reactivity, moderate reaction conditions, low cost, accessibility, non-corrosiveness and high reusability. Additionally, it is more abundant due

to natural sources of calcium such as egg and mollusc shells.<sup>31</sup> A recent study by Rezaei *et al.* showed that CaO from mussel shells had good catalytic activity toward transesterification of soybean oil using methanol. In this study, Rezaei *et al.* use a response surface methodology (RSM) to optimize the yield of biodiesel. More details on these methods and how they are useful are described in section **1.6 Design of Experiments**. A Box-Behnken design was used to optimize the purity and yield of biodiesel based on three factors; calcination temperature (X1), catalyst concentration (X2) and molar ration of methanol to oil (X3). The factors and their respective values are summarized in **Table 1.6**.<sup>31</sup>

**Table 1.6** Variables studied and their values. (Source: Rezaei *et al.* 2013, Fuel, Tab. 1, p. 536. Reproduced with permission of Elsevier.)

Factors	Symbol	Range and levels		
		-1	0	1
Calcination temperature (°C)	X1	950	1000	1050
Catalyst concentration (wt.%)	X2	6	9	12
Molar ratio (MeOH:oil)	X3	12:01	18:01	24:01:00

Mussel shells were collected along the Persian Gulf coast. The details of how shells were cleaned was not given. They were ground and sieved before being calcined at 950, 1000 and 1050 °C. Powder XRD analysis showed that only CaO was present after 2 h. Soybean oil which is mainly linoleic and oleic acid was purchased. All reactions were carried out at 60 °C for 8 h. The CaO catalyst was removed by centrifugation and the glycerol was removed by a simple separation. The purity and yield of biodiesel were determined using gas chromatography with a flame ionization detector. Methyl laurate was added to crude biodiesel samples as a standard reference. The results of the Box-Behnken design experiments are summarized in **Table 1.7**.

**Table 1.7** All experiments performed and the responses, Purity (Y1) and Yield (Y2). (Source: Rezaei *et al.* 2013, Fuel, Tab. 2, p. 537. Reproduced with permission of Elsevier.)

Manipulated variables			Responses	
Calcination temperature (°C) (X1)	Catalyst concentration (wt.%) (X2)	MeOH:oil (X3)	Purity (%) (Y1)	Yield (%) (Y2)
1050	9	12:01	79.45	66.18
1050	6	18:01	88.67	61.00
1000	6	12:01	51.85	44.85
1050	12	12:01	84.79	73.60
950	12	18:01	73.22	53.82
1050	9	24:01:00	95.20	87.35
1000	9	18:01	67.40	54.39
1000	9	18:01	67.28	54.29
950	9	18:01	66.30	40.58
1000	9	18:01	67.20	53.52
1000	12	18:01	79.85	65.42
950	6	12:01	11.37	8.15
950	6	24:01:00	59.42	42.15
1000	6	24:01:00	72.12	61.66
1050	12	24:01:00	100	94.10

Analysis of variance of the model showed that X1, X2 and, X3 were all highly significant. Their effects are shown in **Figure 1.10**. These figures all show that increasing the calcination temperature, catalyst concentration and methanol to oil ratio all had positive effects on the purity and yield of the biodiesel produced from soybean oil. At the highest value of each factor the highest yield and purity was reached. Therefore, the optimized conditions for biodiesel production using CaO from mussel shells was a calcination temperature of 1050 °C, a catalyst concentration of 12 wt% and a MeOH:oil ratio of 24:1. A prediction model gave values of 99.68% purity and 94.17% yield which are consistent with values from **Table 1.7** under these conditions, 100% purity and 94.1% yield. <sup>31</sup>

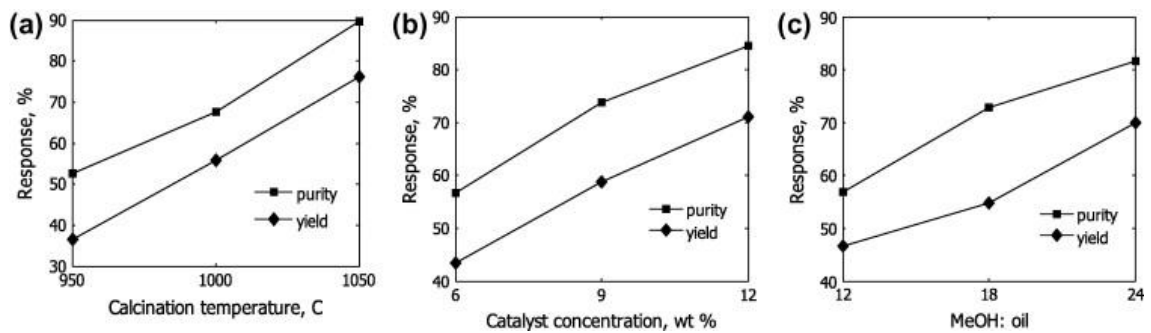


**Figure 1.10** One factor plots for a) Calcination temperature, b) Catalyst concentration and c) MeOH:oil ratio as functions of yield and purity (Source: Rezaei *et al.* 2013, *Fuel*, Fig. 5, p. 540. Reproduced with permission of Elsevier.)

Catalyst reusability was tested at optimal conditions in two ways. One, the catalyst was calcined at 1050 °C after each use and two, the catalyst was washed with methanol after each use, without calcination. **Figure 1.11** shows the purity and yield results of the mussel shell catalyst after being used five times. The calcination of the reused mussel shell catalyst reduces the activity of the catalyst. The purity and yield after five uses with the uncalcined catalyst were 85.22% and 59.10%, respectively; much higher than that of the calcined catalyst after five uses where the purity and yield were 73.67% and 37.13%, respectively. The reduction in catalytic activity was attributed to a suspected decrease in surface area upon re-calcination.<sup>31</sup>

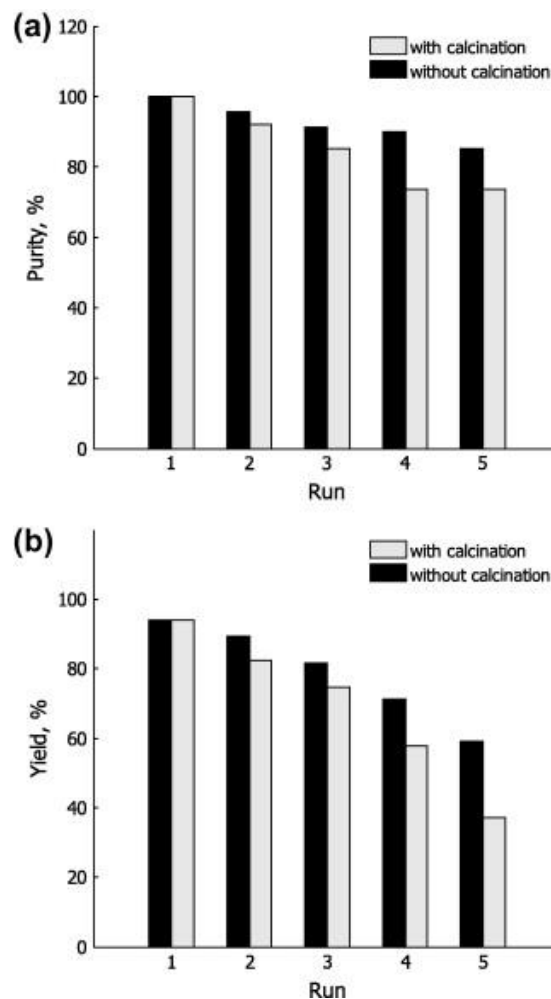


**Figure 1.11** Mussel shell catalysts reusability under optimal conditions of (a) purity, (b) yield. (Source: Rezaei *et al.* 2013, *Fuel*, Fig. 6, p. 540. Reproduced with permission of Elsevier.)

Another way to get biofuel from biomass is by hydrothermal processing. It is an ideal way to process biomass with high water content and it uses temperatures much lower than pyrolysis. Lignocellulosic biomass waste is a promising feedstock for the production of fuels because it is abundant and cheap. Catalysts are used to increase the bio-oil yield (decreasing waste), reduce energy and increase selectivity. Russian olive seeds are waste after the flesh of the Russian olive is consumed. The olive seeds are source of

lignocellulosic biomass studied for the hydrothermal conversion to bio-oil using a CaO catalyst from mussel shells.<sup>26</sup> Biomass conversion was carried out in a 500 mL high temperature and high pressure Parr reactor. 10 g of biomass along with 100 mL of distilled water are pressurized to 1 MPa with N<sub>2</sub> and heated to the desired temperature. During heating from 240-340 °C the vessel pressures increased to between 3.2 and 15.0 MPa. The mussel shells were collected from the Gulf of Izmit, Turkey. Shells were rinsed with water, air dried, and ground. Particle sizes were < 200 µm. The ground shell was calcined at 1050 °C for 2 h. Again, powder XRD was used to confirm the catalyst was CaO, no CaCO<sub>3</sub> remained.<sup>26</sup> The yield of bio-oil was optimized very differently in comparison to the bio-diesel previously discussed. First, the optimal temperature and residence times were determined without the use of mussel shell catalyst. Then, catalyst was added, and optimal catalyst loading was determined. The temperature plays an important role in thermally treated processes because it can dictate to a certain degree which product to expect; bio-oil, bio-gas or solid residue. For example, heating at low temperatures for a longer period of time produces mainly solid residue (torrefaction) and heating to high temperatures rapidly produces mainly gas (gasification). The highest bio-oil yield was 12.9% at 280 °C, the yield decreased at higher temperatures and therefore, 280 °C was chosen as the optimal temperature for hydrothermal conversion of Russian olives seeds to bio-oil. The optimal residence time was determined at 280 °C to be 5 min, with a bio-oil yield of 14.1%. Increasing the residence time past 5 min led to a decrease in bio-oil yields, likely due to bio-oil being converted into gaseous or charred products.<sup>26</sup> Studies of the effect on catalyst concentration at 280 °C for 5 min showed that mussel shell derived CaO at 5 wt % gave a bio-oil yield of 20.7%, nearly a 50% increase in yield. The catalyst increased the

hydrothermal conversion to bio-oil. Increasing the catalyst loading caused a decrease in bio-oil and solid residue yields. This suggests that high catalyst loading could be useful for biomass gasification.

## **1.6 Design of Experiments**

Design of Experiments (DoE) is a methodology whereby statistics is applied to experimentation. It is essentially a process of planning experiments so that the right data is analyzed by statistical methods that results in objective and meaningful inferences from the data. It simplifies learning about the process that is being investigated by screening for important factors and building a mathematical model to obtain prediction equations and optimize the response, if necessary.<sup>86</sup> Statistical DoE allows processes with multiple parameters (or factors) to be optimized more efficiently and for any beneficial or inhibitory interactions between parameters to be identified. It is commonly used in engineering and scientific research.

There are three basic principles of DoE; replication, randomization, and blocking. Replicating experiments allows the experimenter to more precisely estimate the sample mean, thereby allowing for a better estimate of experimental error. Doing experiments in a random order reduces bias and systematic errors and blocking increases the precision of experiments by factoring out variables that are not studied.<sup>86</sup>

Factorial designs are the most efficient experimental design when it comes to experiments with two or more factors. In factorial designs every possible combination of levels for every factor is studied. For example, in a basic  $2^k$  factorial design there are two levels,

generally coded '+' and '-' for high and low level, and k factors.  $2^k$  also denoted the number of experiments needed for each replicate, for example if  $k=3$ , there are three factors (A, B, and C) so every replicate has 8 runs or experiments. Treatment combinations, denoted by lowercase letters, are the combination of factors for an experimental run. They are often written in standard order such that one factor is introduced at a time and each new factor is successively combined with the combinations before it. For example, the standard order of treatment combinations is (1), a, b, ab, c, ac, bc, and abc for a  $2^3$  design. For (1) all factors are at low levels, for ab factors A and B are at high levels and factor C at low level and so on. The response is measured for each treatment combination in order to calculate the estimate of effects for each factor. Estimates of effects are denoted by capital letters. For a  $2^3$  design there are 7 effects; A, B, AB, C, AC, BC, and ABC. Of these 7 effects, A and B are called main effects, AB, AC, and BC are two-factor interactions and ABC is a three-factor interaction. A main effect of a factor is described as the change in response that is caused by a change in the level of the factor. An interaction effect occurs when the difference in the response between levels of one factor is different at all levels of the other factors.<sup>86</sup>

**Table 1.8:** Algebraic Signs for Calculating Effects in the  $2^3$  Design.

Treatment Combination	Factorial Effect						
	A	B	AB	C	AC	BC	ABC
(1)	-	-	+	-	+	+	-
a	+	-	-	-	-	+	+
b	-	+	-	-	+	-	+
ab	+	+	+	-	-	-	-
c	-	-	+	+	-	-	+
ac	+	-	-	+	+	-	-
bc	-	+	-	+	-	+	-
abc	+	+	+	+	+	+	+

Using a sign table is a quick and easy way to estimate effects, **Table 1.8**. The estimates of effects are calculated easily by calculating the average of the highs and subtracting the average of the lows. With the sign table the estimate of the effect A for a  $2^3$  design is calculated using **Equation 1.2**, where n is the number of replicates.

**Equation 1.2**

$$A = \frac{[(a + ab + ac + bc) - ((1) + b + c + bc)]}{4n}$$

Statistical significance of the estimates of effects is tested by the ANalysis Of VAriance (ANOVA) and the model for prediction is developed using regression analysis. A  $2^3$  prediction model where every effect is significant is described by **Equation 1.3** where coded variables  $x_1$  and  $x_2$  represent A and B, and  $\beta$  represents the regression coefficient. It is fairly straight forward to do ANOVA and build a regression model for small factorial

designs, however, for bigger designs and higher order models it is common to use software such as Minitab® Statistical Software and Design Expert®.

### Equation 1.3

$$y = \beta_0 + \beta_1x_1 + \beta_2x_2 + \beta_3x_3 + \beta_{12}x_1x_2 + \beta_{13}x_1x_3 + \beta_{23}x_2x_3 + \beta_{123}x_1x_2x_3$$

Two-level factorial and fractional factorial designs are often used as exploratory experiments. They are only capable of fitting first order models. To investigate whether or not a model may have curvature, center points,  $n_c$ , must be added. If the test for curvature is positive, it is common to follow the path of steepest ascent or descent until a minimum or maximum is reached and then build a Central Composite Design (CCD) by adding axial points to optimize the response. There are three types of CCDs; Central Composite Circumscribed (CCC) which requires 5 levels, Central Composite Inscribed (CCI) which requires 5 levels, and Central Composite Face-centered (CCF) that requires three levels. CCC designs provide the highest quality prediction over the design space but require factor ranges outside the range of the factorial part. **Figure 1.12** shows the design space for a CCC design and how easy it is to build beginning with a simple 2-level factorial with two factors, A and B, depicted by blue circles. These points represent the four experiments of a  $2^2$  factorial design, 1, a, b, and ab. With just two levels, one can only get a linear model. To test for curvature, center points are tested, depicted by the pink circle. To fully develop the CCC design, axial points ( $+\alpha$  and  $-\alpha$ ) denoted by yellow stars are added. These axial points go beyond the design space. It is important to plan for these points when beginning the factorial part of the experimental design so that one can ensure the  $\pm \alpha$  corresponds to a feasible level. In order for the CCC to be rotatable, that is the for the measure of error to be

equal through all of design space,  $\alpha$  is the fourth root of  $2^k$  where  $k$  is number of factors. This can lead  $\alpha$  to be an awkward factor level to work with. With the addition of the axial points, there are now 5 levels of each factor, which completes the CCC design.

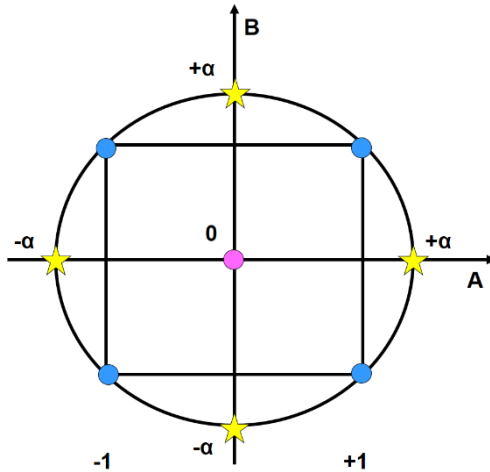


**Figure 1.12** Design Space for a central composite circumscribed (CCC) design.

CCDs are one of many types of Response Surface Methods (RSMs). Another common RSM is called a Box-Behnken Design (BBD). It is similar to a CCD in that it can predict a quadratic model and similar to a factorial design with three levels. One major drawback is that the BBD cannot be built upon the way you can build upon a factorial design and keep adding experiments to make a CCD. BBDs do, however, require less treatment combinations in cases involving 3 or 4 factors. Design-Expert® software from Stat-Ease® is commonly used for DoE and hosts a large spread of optimal designs that can be built on command. For example, a custom design can be created using 3 factors but with the minimum amount of experiments needed to optimize a yield.

DoE is a proven fast and cost-effective way to optimize a process that has been extended to renewable feedstocks. For example, Rezaei and co-workers optimized their process of using calcined mussel shells (CaO) as a catalyst for biodiesel production in just 15 experiments using a BBD.<sup>31</sup>

## **1.7 Mollusc-inspired materials**

Nature's ability to create sophisticated structures with impressive mechanical properties drives a broad field of biomimetic materials research.<sup>87</sup> CaCO<sub>3</sub> is the most abundant mineral found in nature where it serves a number of structural, protection, and mechanical functions in freshwater and marine organisms.<sup>88, 89</sup> Biomineralized crystals are different from regular surface and structure of geological/artificial crystals and are difficult to simulate.<sup>90</sup> The morphology and growth of CaCO<sub>3</sub> materials can be controlled biomimetically<sup>91-94</sup> and by other anthropogenic means.<sup>95-97</sup>

While mollusc shells can contain prismatic calcite and nacre (aragonite), nacre is by far the more studied structural motif with many researchers dedicated to deciphering the biomineralization of nacre molluscs.<sup>36, 89, 98-100</sup> The formation of nacre is complicated and new research is constantly being conducted to understand it better. Unlike man-made composites that contain fibres,<sup>101</sup> nacre is a natural composite material that has platelet reinforcement,<sup>35</sup> a microstructure that gives nacre a 3000-fold higher fracture resistance than geological aragonite.<sup>102, 103</sup> In addition, nacre has interesting bulk material properties such as tensile strength, Young's modulus and fracture toughness.<sup>35, 36</sup> Because nacre is mechanically strong with high bioactivity and biocompatible, it has been explored in bone implantation applications including drug delivery, bone cement and artificial bone

substitute, including dental implants.<sup>36, 39, 104</sup> Over the last three decades, nacre-inspired materials research has come a long way<sup>105</sup> and there are now many methods to synthesize nacre-layer materials for use as biomaterial for orthopedic and tissue engineering applications<sup>39</sup>, as well as armour<sup>106</sup>, and electronics.<sup>107</sup>

The study of prismatic calcite in molluscs is becoming more popular and understanding its formation is valuable.<sup>38</sup> For example, prismatic-type CaCO<sub>3</sub> thin films<sup>108</sup> like the prismatic calcite layer of molluscs and flexible calcite needles that resemble spicules from *Sycon* sp., a calcareous sponge<sup>94</sup> have recently been reported. The morphology and growth of calcite has been controlled to large extent by proteins and peptoids<sup>109</sup> like molluscs. Other ways to tailor calcite morphologies include using functionalized self-assembled monolayers (SAMs) as templates where amorphous calcium carbonate (ACC) is converted into calcite<sup>96,97</sup> and forcing the crystallization of CaCO<sub>3</sub> in constrained volumes to get a desired crystal shape and size.<sup>95, 107</sup>

## **1.8 Building Bridges in Sustainable Science**

The United Nations has identified 17 Sustainable Development Goals (SDG) to be achieved by the year 2030.<sup>110</sup> The research in this thesis is closely aligned with SDG 2 'Zero Hunger' as described earlier in **Chapter 1**. Finding uses for by-products of increasing food production can help increase economic feasibility (SDG 8). However, in addition to renewable feedstocks for fuels, chemicals and materials production (the primary objective of this thesis), renewable energy is of critical importance in sustainable development. In many cases, new energy storage methods need to be developed and these should be achieved in a sustainable and economic fashion that align with SDG 7, 'Affordable and

Clean Energy'. There are several forms of clean energy including wind, solar and electric. Batteries and supercapacitors play an important role in our day to lives, making up components in our smart phones and laptops. More safe, sustainable, and affordable electrochemical devices could benefit everyone.

### **1.8.1 Supercapacitors**

Electrochemical capacitors (ECs) or supercapacitors are low energy, high power charge storage devices with a longer cycle life compared to rechargeable batteries that stems from the electrostatic reaction at the electrode-electrolyte interface rather than reduction and oxidation that takes place in batteries.<sup>111, 112</sup> They are used in applications ranging from portable electronics to electric vehicles and even heavy machinery. ECs are safer during rapid charging and discharging compared to batteries. While often used in a circuit accompanying a battery, ECs can replace batteries in applications where high delivery or uptake, or power is required.<sup>113</sup>

#### **1.8.1.1 Energy Density and Electrolytes**

In order to improve the performance of ECs there are two components of the device one can alter, the electrode material and the electrolyte. Increase energy density is highly sought after because the energy density of commercial ECs is much lower than batteries. Energy density is directly proportional to the square of the potential,  $E = \frac{1}{2} CV^2$ , where C is capacitance and V is potential. Aqueous electrolytes are limited to a potential of approximately 2 V.<sup>114</sup> While the maximum potential of 2.7 V for organic electrolytes is much higher than aqueous electrolytes, the flammability and toxicity make organic

electrolytes hazardous.<sup>115</sup> Therefore, investigating electrolytes with higher operating potentials while also being inherently more safe is attractive for clean energy.

Ionic Liquids (ILs) have high conductivities and wider electrochemical windows than organic and aqueous electrolytes and have been explored as electrolytes in supercapacitors to increase the maximum cell voltage, thereby increasing the maximum energy density.<sup>115-</sup>

<sup>118</sup> ILs are chemically and thermally stable and their non-flammability and negligible volatility make them inherently safer than organic electrolytes. Several ILs have been investigated as electrolytes in ECs. The two most commonly used ILs are based on imidazolium or pyrrolidinium cations. These cations have properties that are useful in ECs. Imidazolium cation based ILs have relatively lower viscosity and higher ionic conductivity whereas pyrrolidinium based ILs have larger electrochemical windows and therefore, higher energy density.<sup>119</sup> Even though ILs are much more viscous than organic and aqueous electrolytes, a leakage risk still exists for ECs. Solid electrolytes can be used to remove the risk of leakage.

ILs have been used to make gel polymer electrolytes, a combination of polymer and IL where the IL is entrapped in the polymer, making a solid-state electrolyte/separator with additional mechanical and interfacial stability than typical electrolytes.<sup>120-124</sup> Solid electrolytes reduce leaking of ECs.<sup>125, 126</sup> Ionic liquid gel polymer electrolytes (ILGPEs) have been synthesized using a plethora of ionic liquids and polymer combinations and used in lithium batteries and electrochemical supercapacitors.<sup>118, 127-129</sup>

Research has shown the chemical, mechanical stability and conductivity of ILGPEs can be improved further with the addition of passive inorganic fillers (one that is not involved in the conduction process) such as ceramics (ie. SiO<sub>2</sub>) and zeolites.<sup>121, 127, 130-132</sup> As far as I

am aware, renewable inorganic fillers have not been reported to date. It is important to research energy storage devices that are efficient, sustainable and cheap. This can include how they are fabricated (i.e components they contain or are made up of) and how they are powered (i.e wind and solar). While ILGPEs have large electrochemical windows and increased safety over traditional electrolytes, the drawback of ILGPEs is their decreased ionic conductivity and poor interfacial properties.<sup>119</sup>

### **1.8.1.2 Renewable Resources for Electrodes**

Electrodes of ECs are made up of high surface area carbon materials. Many have focused on the renewability of the carbon electrode material through the conversion of biomass to porous carbon for electrodes of supercapacitors. They include waste soybean root, bamboo, peanut shells and many others with various surface areas.<sup>117, 133, 134</sup> These highly porous materials were tested in ECs with aqueous, IL, and IL gel polymer electrolytes, have high specific capacitances ranging from 75-421 F/g.

## **1.9 Summary**

Aquaculture operations have increased substantially over the last three decades and we rely on the sustainability of aquaculture to provide food for the growing global population. It is our responsibility to manage waste from mussel aquaculture. As such, mussel waste is a valuable source of biomass which can lead to two streams; a protein stream and a shell ( $\text{CaCO}_3$ ) stream. The primary way to clean waste shells is to burn off the organic material and use large volumes of fresh water. These methods are energy intensive and require the use of valuable resources. Mussel shells are mainly  $\text{CaCO}_3$  and can contain two

polymorphs, calcite and aragonite. These shells have been valorized in many applications where the material remains  $\text{CaCO}_3$  or is thermally degraded to  $\text{CaO}$ . Applications of mussel shell include amending acidic soils, building materials and water treatment.  $\text{CaO}$  from mollusc shells has been showed to be an effective catalyst for biofuel synthesis. In some applications, the use of Design of Experiments (DoE) is helpful for optimization of a process or yield. Calcium acetate is a de-icer that is not currently on the market. It can be prepared using mollusc shells and renewably sourced acetic acid. Furthermore, research areas where inert renewable inorganic materials are used as fillers, e.g. ECs, has largely been unexplored.

$\text{CaCO}_3$  in molluscs has a very interesting structure; they contain prismatic calcite or aragonite and nacre or mother of pearl. These materials have unique properties that drive a broad field of research to understand the biomineralization of  $\text{CaCO}_3$  and inspire the creation of biomimetic composite materials.

### **1.10 Objectives**

The objective of this thesis was to valorize waste from mussel aquaculture in order to increase the economic viability and reduce the environmental impacts of mussel processing. To achieve this goal, in **Chapters 2 to 6** the following objectives were targeted; (1) Develop an environmentally friendly shell cleaning protocol to clean mussel shells of their residual protein so that shell and protein biomass streams are separated, (2) Study the effect of heat treatment on blue mussel shells, fully characterize the shells before and after heat treatment, and draw conclusions based on the results, (3) Use the mussel shells as a source of  $\text{CaCO}_3$  starting material to prepare calcium acetate, a non-corrosive and bio-

degradable de-icer, (4) Understand the production of an unusual  $\text{CaCO}_3$  material that was produced during calcium acetate synthesis and study its potential applications, and (5) Employ the new  $\text{CaCO}_3$  material as a filler in solid electrolytes in supercapacitors.

### **1.11 Co-authorship Statement**

This PhD thesis includes results of joint research that have been published in or submitted to peer reviewed journals in the form of a book chapter and three full papers, as follows:

#### **Chapter 1** Introduction

A large portion of Chapter 1 is published as a book chapter entitled ‘Characterization and utilization of waste streams from mollusc aquaculture and fishing industries.’

**Authors** Jennifer N. Murphy and Francesca M. Kerton

**Book** Kerton, F. M. and Yan, N. eds. Fuels, Chemicals and Materials from the Oceans and Aquatic Sources. Wiley, pp. 189-225.

The principle author (Jennifer N. Murphy) contributed to all areas of the project as the main researcher including literature review, collecting and organizing data, writing the book chapter (first and final drafts) and securing permissions

The corresponding author (Dr. Francesca M. Kerton) proposed the topic of the book chapter and contributed to several aspects of the chapter including: statistics of global mollusc production and mussel farming, as well as editing each draft of the chapter including the final draft, and supervision of the principal author (J. N. M)

**Chapter 2** Enzymatic processing of mussel shells to produce biorenewable calcium carbonate in seawater

**Authors** Jennifer N. Murphy, Kelly Hawboldt and Francesca M. Kerton

**Article** *Green Chemistry*, **2018**, 20, 2913-2920

The principle author (Jennifer N. Murphy) contributed to all aspects of the project as the main researcher including literature review, collecting and analyzing the data, presenting and discussing the data with the corresponding author, writing the manuscript (first and final drafts) and preparing answers to the questions and comments of the peer reviewers.

The corresponding author (Dr. Kelly Hawboldt) contributed to the revision of the manuscript and supervised the principal author (J. N. M.)

The corresponding author (Dr. Francesca M. Kerton) proposed the initial topic of the project and contributed to several aspects of the project including the revision of the draft manuscript and submission to the journal, and supervision of the principal author (J. N. M.).

**Chapter 3** Wealth from waste: Blue mussels (*Mytilus edulis*) offer up a sustainable source of natural and synthetic nacre.

**Authors** Jennifer N. Murphy, Céline M. Schneider, Lilo K. Mailänder, Quentin Lepillet, Kelly Hawboldt and Francesca M. Kerton

**Article** *Green Chemistry*, **2019**, 21, 3920-3929.

The principle author (Jennifer N. Murphy) contributed to all aspects of the project as the main researcher including literature review, collecting and analyzing the data, presenting and discussing the data with the corresponding author and co-second author C. M. S., writing the manuscript (first and final drafts) and preparing answers to the questions and comments of the peer reviewers.

The co-second author (Dr. Céline M. Schneider) ran the NMR experiments and assisted J. N. M. in preparing the NMR discussion of the manuscript. This work accounts for approximately 10% of the research

The co-second authors (Lilo K. Mailänder and Quentin Lepillet) ran the synthetic nacre experiments and collected characterization data on the products. Combined, these two contributed about 20% of the total experiments.

The corresponding author (Dr. Kelly Hawboldt) supervised the principal author (J. N. M.)

The corresponding author (Dr. Francesca M. Kerton) proposed the initial topic of the research and contributed to several aspects of the project including the revision of the draft manuscript and submission to the journal, and supervision of the principal author (J. N. M.).

## **Chapter 4 The synthesis of calcium acetate from blue mussel shells and its use as a de-icer**

**Authors** Jennifer N. Murphy, Kelly Hawboldt and Francesca M. Kerton

**Article** A manuscript is in preparation to submit to *Can. J. Chem.*

The principle author (Jennifer N. Murphy) contributed to all aspects of the project as the main researcher including literature review, collecting and analyzing the data, presenting and discussing the data with the corresponding author, and writing the manuscript (first and final drafts).

The corresponding author (Dr. Kelly Hawboldt) supervised the principal author (J. N. M.)

The corresponding author (Dr. Francesca M. Kerton) proposed the initial topic of the research and contributed to several aspects of the project including the revision of the draft manuscript and supervision of the principal author (J. N. M.).

## **Chapter 5 Absorbent self-assembling calcite material from the prismatic layer of waste *Mytilus edulis* shells**

**Authors** Jennifer N. Murphy, Céline M. Schneider, Kelly Hawboldt and Francesca M.

Kerton

**Article** In preparation to submit to *Matter*.

The principle author (Jennifer N. Murphy) contributed to all aspects of the project as the main researcher including literature review, collecting and analyzing the data, presenting and discussing the data with the corresponding author and co-second author C. M. S., writing the manuscript (first and final drafts) and preparing answers to the questions and comments of the peer reviewers.

The co-second author (Dr. Céline M. Schneider) ran the NMR experiments and assisted J. N. M. in preparing the NMR discussion of the manuscript. This work accounts for approximately 10% of the research

The corresponding author (Dr. Kelly Hawboldt) supervised the principal author (J. N. M.)

The corresponding author (Dr. Francesca M. Kerton) proposed the initial topic of the research and contributed to several aspects of the project including the revision of the draft manuscript and submission to the journal, and supervision of the principal author (J. N. M.).

## **Chapter 6 Bio-renewable calcite as an inorganic filler in ionic liquid gel polymer electrolytes for supercapacitors**

**Authors** Jennifer N. Murphy Tiago C. Mendes, Mega Kar, Francesca M. Kerton and Douglas R. MacFarlane

**Article** A manuscript is in preparation for submission to *Adv. Energy Mat.*

The principle author (Jennifer N. Murphy) contributed to all aspects of the project as the main researcher including literature review, collecting and analyzing the data, presenting and discussing the data with the corresponding author, writing the manuscript (first and final drafts). The co-second authors (Dr. Tiago Mendes and Dr. Mega Kar) proposed initial conditions for galvanostatic cycling and cyclic voltammetry and revised the manuscript. This work accounts for approximately 10% of the research

The corresponding author (Dr. Francesca M. Kerton) supervised the principal author (J.N.M) at Memorial University where some SEM was conducted.

The corresponding author (Dr. Doug R. MacFarlane) proposed the initial topic of the research and contributed to several aspects of the project including the revision of the draft manuscript, and supervision of the principal author (J. N. M.).

## 1.12 References

1. M. Lancaster, *Green Chemistry An Introductory Text*, Royal Society of Chemistry, Cambridge, UK, 2 edn., 2010.
2. P. T. Anastas and C. J. Warner, *Green Chemistry: Theory and Practice*, Oxford University Press, Oxford, 1998.
3. J.-L. Wertz and O. Bédué, *Lignocellulosic Biorefineries*, EPFL Press, New York, 2013.
4. M. Aresta, Dibenedetto, A., & Dumeignil, F, *Biorefinery From Biomass to Chemicals and Fuels*, De Gruyter, Berlin, Germany, 2012.
5. M. Besson, P. Gallezot and C. Pinel, *Chem. Rev.*, 2014, **114**, 1827-1870.
6. A. J. J. Straathof, *Chem. Rev.*, 2014, **114**, 1871-1908.
7. I. I. Enagi, K. A. Al-attab and Z. A. Zainal, *Renewable Sustainable Energy Rev.*, 2018, **90**, 43-55.
8. R. C. Brown, *Thermochemical Processing of Biomass: Conversion into Fuels, Chemicals and Power*, Wiley, 2019.
9. C. S. K. Lin, L. A. Pfaltzgraff, L. Herrero-Davila, E. B. Mubofu, S. Abderrahim, J. H. Clark, A. A. Koutinas, N. Kopsahelis, K. Stamatelatou, F. Dickson, S. Thankappan, Z. Mohamed, R. Brocklesby and R. Luque, *Energ. Environ. Sci.*, 2013, **6**, 426-464.
10. A. S. Matharu, E. M. de Melo and J. A. Houghton, *Bioresource Technol.*, 2016, **215**, 123-130.
11. S. Dahiya, A. N. Kumar, J. Shanthi Sravan, S. Chatterjee, O. Sarkar and S. V. Mohan, *Bioresource Technol.*, 2018, **248**, 2-12.

12. A. Nayak and B. Bhushan, *J. Environ. Manage.*, 2019, **233**, 352-370.
13. F. M. Kerton, Y. Liu, K. W. Omari and K. Hawboldt, *Green Chem.*, 2013, **15**, 860-871.
14. F. M. Kerton, in *Chemical Process Technology For A Sustainable Future*, eds. T. M. Letcher, J. L. Scott and D. A. Patterson, Royal Society of Chemistry Publishing, Cambridge, UK, 2014.
15. I. S. Arvanitoyannis and A. Kassaveti, *Int. J. Food Sci. Tech.*, 2008, **43**, 726-745.
16. D. Tilman and M. Clark, *Nature*, 2014, **515**, 518-522.
17. Food and Agriculture Organization of the United Nations. *The State of World Fisheries and Aquaculture 2016. Contributing to food security and nutrition for all.*, Rome, 2016.
18. R. R. Gentry, S. D. Gaines, B. S. Halpern, H. E. Froehlich, B. S. Halpern, D. Grimm, P. Kareiva, M. Parke, M. Rust and B. S. Halpern, *Nat. Ecol. Evol.*, 2017, **1**, 1317-1324.
19. N. Yan and X. Chen, *Nature*, 2015, **524**, 155-157.
20. R. L. Olsen, J. Toppe and I. Karunasagar, *Trends Food Sci. Technol.*, 2014, **36**, 144-151.
21. Food and Agriculture Organization of the United Nations, [www.fao.org/fishery/statistics/en](http://www.fao.org/fishery/statistics/en), January 18, 2019).
22. Fisheries and Oceans Canada, <http://www.dfo-mpo.gc.ca/aquaculture/index-eng.htm>, (accessed February 26, 2016).

23. M. C. Barros, P. M. Bello, M. Bao and J. J. Torrado, *J. Clean Prod.*, 2009, **17**, 400-407.
24. P. Ballester, I. Mármol, J. Morales and L. Sánchez, *Cement Concrete Res.*, 2007, **37**, 559-564.
25. D. Gallardi, K. Hobbs, T. Mills, C. Couturier, C. Parrish and H. Murray, *Aquaculture*, 2014, **430**, 149–158.
26. K. Tekin, *Energy & Fuels*, 2015, **29**, 4382-4392.
27. A. Shavandi, A. E.-D. A. Bekhit, A. Ali and Z. Sun, *Mater. Chem. Phys.*, 2015, **149-150**, 607-616.
28. V. M. Silva, K. J. Park and M. D. Hubinger, *J. Food Sci.*, 2010, **75**, C36-C42.
29. A. Illanes, *Enzyme Biocatalysis: Principles and Applications*, Springer Science + Business Media B.V, 2008.
30. M. J. Frude, *Method for removing excess meat from whole of crushed mollusk shellfish waste*. New Zealand Pat., 555418, 2008.
31. R. Rezaei, M. Mohadesi and G. R. Moradi, *Fuel*, 2013, **109**, 534-541.
32. M. I. Jones, L. Y. Wang, A. Abeynaike and D. A. Patterson, *Adv. App. Ceram.*, 2011, **110**, 280-286.
33. G. S. Girolami, *X-Ray Crystallography*, University Science Books, 2016.
34. N. Brodusch, H. Demers and R. Gauvin, *Field Emission Scanning Electron Microscopy: New Perspectives for Materials Characterization*, Singapore: Springer Singapore, Singapore, 2018.
35. A. P. Jackson, J. F. V. Vincent and R. M. Turner, *Proc. R. Soc. Lond., B, Biol. Sci.*, 1988, **234**, 415-440.

36. F. Nudelman, *Semin. Cell Dev. Biol.*, 2015, **46**, 2-10.
37. S. Weiner and L. Addadi, *J. Mater. Chem.*, 1997, **7**, 689-702.
38. F. Nudelman, H. H. Chen, H. A. Goldberg, S. Weiner and L. Addadi, *Faraday Discuss.*, 2007, **136**, 9-25.
39. E. M. Gerhard, W. Wang, C. Li, J. Guo, I. T. Ozbolat, K. M. Rahn, A. D. Armstrong, J. Xia, G. Qian and J. Yang, *Acta Biomater.*, 2017, **54**, 21-34.
40. B. Pokroy, A. N. Fitch and E. Zolotoyabko, *Cryst. Growth Des.*, 2007, **7**, 1580-1583.
41. X. Li, W.-C. Chang, Y. J. Chao, R. Wang and M. Chang, *Nano Lett.*, 2004, **4**, 613-617.
42. K. Takahashi, H. Yamamoto, A. Onoda, M. Doi, T. Inaba, M. Chiba, A. Kobayashi, T. Taguchi, T.-a. Okamura and N. Ueyama, *ChemComm*, 2004, DOI: 10.1039/B315478E, 996-997.
43. D. L. Pavia, *Introduction to spectroscopy*, Australia Belmont, CA : Brooks/Cole, Cengage Learning, 4th edn., 2009.
44. I. Ben Shir, S. Kababya, I. Katz, B. Pokroy and A. Schmidt, *Chem. Mater.*, 2013, **25**, 4595-4602.
45. H. Nebel, M. Neumann, C. Mayer and M. Epple, *Inorg. Chem.*, 2008, **47**, 7874-7879.
46. N. Nassif, N. Pinna, N. Gehrke, M. Antonietti, C. Jäger and H. Colfen, *Proc. Natl. Acad. Sci. U.S A.*, 2005, **102**, 12653-12655.
47. C. Jäger and H. Colfen, *CrystEngComm*, 2007, **9**, 1237-1244.

48. C. E. Weir and E. R. Lippincott, *J. Re. Nat. Stand. Sec. A*, 1961, **65A**, 173-183.
49. R. S. Halford, *J. Chem. Phys.*, 1946, **14**, 8-15.
50. J. H. Shariffuddin, M. I. Jones and D. A. Patterson, *Chem. Eng. Res. Des.*, 2013, **91**, 1693-1704.
51. P. Lertwattanakul, N. Makul and C. Siripattaraprat, *J. Environ. Manage.*, 2012, **111**, 133-141.
52. A. Abeynaike, L. Wang, M. I. Jones and D. A. Patterson, *Asia-Pac. J. Chem. Eng.*, 2011, **6**, 231-243.
53. C. Rombaldi, J. L. de Oliveira Arias, G. I. Hertzog, S. S. Caldas, J. P. Vieira and E. G. Primel, *Anal. Bioanal. Chem.*, 2015, **407**, 4805-4814.
54. J. P. Morris, T. Backeljau and G. Chapelle, *Rev. Aquacult.*, 2018, **11**, 42-57.
55. Y. Hou, A. Shavandi, A. Carne, A. A. Bekhit, T. B. Ng, R. C. F. Cheung and A. E.-d. A. Bekhit, *Crit. Rev. Environ. Sci. Technol.*, 2016, **46**, 1047-1116.
56. United States Geological Survey. Mineral Commodity Summaries, January 2016 - Stone (Crushed).  
[, https://minerals.usgs.gov/minerals/pubs/mcs/2016/mcs2016.pdf](https://minerals.usgs.gov/minerals/pubs/mcs/2016/mcs2016.pdf), (accessed Jan 25 2019).
57. J. Paz-Ferreiro, D. Baez-Bernal, J. Castro Insua and M. I. Garcia Pomar, *Chemosphere*, 2012, **86**, 1117-1121.
58. Y. T. Kwon, C. Lee and J. H. Yun, *J. Clean Prod.*, 2009, **17**, 708-711.
59. C. H. Lee, D. K. Lee, M. A. Ali and P. J. Kim, *Waste Manage.*, 2008, **28**, 2702-2708.

60. A. M. Ramirez-Perez, M. Paradelo, J. C. Novoa-Munoz, M. Arias-Estevez, M. J. Fernandez-Sanjurjo, E. Alvarez-Rodriguez and A. Nunez-Delgado, *J. Hazard Mater.*, 2013, **248-249**, 122-130.
61. F. A. Vega, E. F. Covelo and M. L. Andrade, *J. Colloid Interface Sci.*, 2006, **298**, 582-592.
62. F. A. Vega, E. F. Covelo and M. L. Andrade, *J. Hazard Mater.*, 2009, **169**, 36-45.
63. S. J. Köhler, P. Cubillas, J. D. Rodríguez-Blanco, C. Bauer and M. Prieto, *Environ. Sci. Technol.*, 2007, **41**, 112-118.
64. C. A. McCauley, A. D. O'Sullivan, M. W. Milke, P. A. Weber and D. A. Trumm, *Water Res.*, 2009, **43**, 961-970.
65. C. A. McCauley, A. D. O'Sullivan, P. A. Weber and D. Trumm, *New Zeal. J. Geol. Geop.*, 2010, **53**, 211-226.
66. S. Peña-Rodríguez, A. Bermúdez-Couso, J. C. Nóvoa-Muñoz, M. Arias-Estévez, M. J. Fernández-Sanjurjo, E. Álvarez-Rodríguez and A. Núñez-Delgado, *J. Environ. Sci.*, 2013, **25**, 2476-2486.
67. B. Uster, A. D. O'Sullivan, S. Y. Ko, A. Evans, J. Pope, D. Trumm and B. Caruso, *Mine Water Environ.*, 2015, **34**, 442-454.
68. P. Cubillas, S. Köhler, M. Prieto, C. Chairat and E. H. Oelkers, *Chem. Geol.*, 2005, **216**, 59-77.
69. J. Xiong, Y. Qin, E. Islam, M. Yue and W. Wang, *Desalination*, 2011, **276**, 317-321.
70. Y. Yu, R. Wu and M. Clark, *J. Colloid Interface Sci.*, 2010, **350**, 538-543.
71. R. Bayer and H. Lutz, *Dry Mortars*, Wiley-VCH, 2013.

72. J. N. Murphy and F. M. Kerton, in *Fuels, Chemicals and Materials from the Oceans and Aquatic Sources* eds. F. M. Kerton and N. Yan, Wiley, 2017, ch. Characterization and utilization of waste streams from mollusc aquaculture and fishing industries, pp. 189-225.
73. M. Wei, A. J. Ruys, B. K. Milthorpe and C. C. Sorrell, *J. Mater. Sci.: Mater. Med.*, 2005, **16**, 319-324.
74. Health Canada, <https://www.canada.ca/en/health-canada/services/food-nutrition/food-safety/food-additives/lists-permitted/10-adjusting-agents.html>, (accessed June 18, 2019).
75. X. Jiang, G. Li and Z. Wu, World Academy of Science, *Engineering and Technology International Journal of Chemical and Molecular Engineering*, 2010, **4**, 304-309.
76. Environment Canada, 2001. *Canadian Environmental Protection Act, 1999, Priority Substances List Assessment Report – Road Salt*, Hull, Quebec.
77. M. S. Perchanok, D. G. Manning and J. J. Armstrong, *Highway deicers: Standards, practice and research in the Province of Ontario*, Research and Development Branch, Downsview, Ontario, 1991.
78. W. Fu and A. P. Mathews, *Enzyme Microb. Tech.*, 2005, **36**, 953-959.
79. B. Yun Yang and R. Montgomery, *Bioresource Technol.*, 2003, **90**, 265-273.
80. H. J. Lee, N. Y. Jung, S. H. Park, S. M. Song, S. I. Kang, J.-S. Kim and M. S. Heu, *J. Korean Soc. Food Sci. Nutr.*, 2015, **44**, 888-895.
81. Z. Fan, X. Yang, J.-q. Guan, J. Zhang, L. Qiao and X.-y. Chang, *Shipin Gongye Keji*, 2015, **36**, 254-258.

82. J. Liu, Y. Zhang, Y. Liu, H. Liu and D. Xing, *Guangdong Huagong*, 2012, **39**, 24-26.
83. 김병익, *Preparation method of snow removing materials by using oyster shell*.  
South Korea Pat., KR201328694B1, 2013.
84. Cryotech, <http://www.cryotech.com/commercial>, (accessed June 23, 2019).
85. Daniel G. Strawn, Hinrich L. Bohn and G. A. O'Connor, *Soil Chemistry*, John Wiley & Sons, Incorporated, Chichester, West Sussex, 4 edn., 2015.
86. D. C. Montgomery, *Design and Analysis of Experiments*, John Wiley and Sons, Hoboken, NJ, United States of America, 8th edn., 2013.
87. U. G. K. Wegst, H. Bai, E. Saiz, A. P. Tomsia and R. O. Ritchie, *Nat. Mater.*, 2015, **14**, 23-36.
88. F. Nudelman and N. A. J. M. Sommerdijk, *Angew. Chem., Int. Ed.*, 2012, **51**, 6582-6596.
89. H. A. Lowenstam and S. Weiner, *On biomineralization*, Oxford University Press, 1989.
90. A. H. Heuer, D. J. Fink, V. J. Laraia, J. L. Arias, P. D. Calvert, K. Kendall, G. L. Messing, J. Blackwell, P. C. Rieke, D. H. Thompson, A. P. Wheeler, A. Veis and A. I. Caplan, *Science*, 1992, **255**, 1098-1105.
91. H.-L. Gao, S.-M. Chen, L.-B. Mao, Z.-Q. Song, H.-B. Yao, H. Cölfen, X.-S. Luo, F. Zhang, Z. Pan, Y.-F. Meng, Y. Ni and S.-H. Yu, *Nat. Commun.*, 2017, **8**, 287.
92. L.-B. Mao, H.-L. Gao, H.-B. Yao, L. Liu, H. Cölfen, G. Liu, S.-M. Chen, S.-K. Li, Y.-X. Yan, Y.-Y. Liu and S.-H. Yu, *Science*, 2016, **354**, 107-110.

93. Y.-Y. Kim, J. D. Carloni, B. Demarchi, D. Sparks, D. G. Reid, Miki E. Kunitake, C. C. Tang, M. J. Duer, C. L. Freeman, B. Pokroy, K. Penkman, J. H. Harding, L. A. Estroff, S. P. Baker and F. C. Meldrum, *Nat. Mater.*, 2016, **15**, 903-910.
94. F. Natalio, T. P. Corrales, M. Panthofer, D. Schollmeyer, I. Lieberwirth, W. E. G. Muller, M. Kappl, H. J. Butt and W. Tremel, *Science*, 2013, **339**, 1298-1302.
95. E. Loste, R. J. Park, J. Warren and F. C. Meldrum, *Adv. Funct. Mater.*, 2004, **14**, 1211-1220.
96. Y.-J. Han, L. M. Wysocki, M. S. Thanawala, T. Siegrist and J. Aizenberg, *Angew. Chem., Int. Ed.*, 2005, **44**, 2386-2390.
97. T. Y.-J. Han and J. Aizenberg, *Chem. Mater.*, 2008, **20**, 1064-1068.
98. F. Nudelman, E. Shimoni, E. Klein, M. Rousseau, X. Bourrat, E. Lopez, L. Addadi and S. Weiner, *J. Struct. Biol.*, 2008, **162**, 290-300.
99. I. C. Olson, A. Z. Blonsky, N. Tamura, M. Kunz, B. Pokroy, C. P. Romao, M. A. White and P. U. P. A. Gilbert, *J. Struct. Biol.*, 2013, **184**, 454-463.
100. L. Addadi, D. Joester, F. Nudelman and S. Weiner, *Chem. - Eur. J.*, 2006, **12**, 980-987.
101. J. Bai, *Advanced Fibre-Reinforced Polymer (FRP) Composites for Structural Applications*. Elsevier Science & Technology, Cambridge, United Kingdom, 2013.
102. S. Dashkovskiy, B. Suhr, K. Tushtev and G. Grathwohl, *Comput. Mater. Sci.*, 2007, **41**, 96-106.
103. V. J. Laraia and A. H. Heuer, *MRS Proceedings*, 1989, **174**, 125.
104. X.-X. Wang, L. Xie and R. Wang, *Biomaterials*, 2005, **26**, 6229-6232.

105. H.-B. Yao, J. Ge, L.-B. Mao, Y.-X. Yan and S.-H. Yu, *Adv. Mater.*, 2014, **26**, 163-188.
106. L. Li and C. Ortiz, *Nat. Mater.*, 2014, **13**, 501-507.
107. E. Loste and F. C. Meldrum, *ChemComm*, 2001, DOI: 10.1039/b101563j, 901-902.
108. C. Xiao, M. Li, B. Wang, M.-F. Liu, C. Shao, H. Pan, Y. Lu, B.-B. Xu, S. Li, D. Zhan, Y. Jiang, R. Tang, X. Y. Liu and H. Cölfen, *Nat. Commun.*, 2017, **8**, 1398.
109. C.-L. Chen, J. Qi, J. Tao, R. N. Zuckermann and J. J. DeYoreo, *Sci. Rep.*, 2014, **4**, 6266.
110. United Nations Sustainable Development Goals Knowledge Platform, <https://sustainabledevelopment.un.org/?menu=1300>, (accessed June 23, 2019).
111. B. E. Conway, *Electrochemical Supercapacitors: Scientific Fundamentals and Technological Applications*, Springer US, 1999.
112. J. R. Miller and P. Simon, *Science*, 2008, **321**, 651-652.
113. P. Simon and Y. Gogotsi, *Nat. Mater.*, 2008, **7**, 845-854.
114. M. Kaempgen, C. K. Chan, J. Ma, Y. Cui and G. Gruner, *Nano Lett.*, 2009, **9**, 1872-1876.
115. M. Armand, F. Endres, D. R. MacFarlane, H. Ohno and B. Scrosati, *Nat. Mater.*, 2009, **8**, 621-629.
116. G. P. Pandey and S. A. Hashmi, *J. Mater. Chem. A*, 2013, **1**, 3372-3378.
117. N. Guo, M. Li, Y. Wang, X. Sun, F. Wang and R. Yang, *ACS Appl. Mater. Interfaces*, 2016, **8**, 33626-33634.

118. F. B. Sillars, S. I. Fletcher, M. Mirzaeian and P. J. Hall, *Phys. Chem. Chem. Phys.*, 2012, **14**, 6094-6100.
119. M. Mirzaeian, Q. Abbas, A. Ogwu, P. Hall, M. Goldin, M. Mirzaeian and H. F. Jirandehi, *Int. J. Hydrogen Energy*, 2017, **42**, 25565-25587.
120. Y. J. Kang, S.-J. Chun, S.-S. Lee, B.-Y. Kim, J. H. Kim, H. Chung, S.-Y. Lee and W. Kim, *ACS Nano*, 2012, **6**, 6400-6406.
121. W. Lu, K. Henry, C. Turchi and J. Pellegrino, *J. Electrochem. Soc.*, 2008, **155**, A361-A367.
122. J. Jiang, D. Gao, Z. Li and G. Su, *React. Funct. Polym.*, 2006, **66**, 1141-1148.
123. A. Lewandowski and A. Swiderska, *Solid State Ionics*, 2004, **169**, 21-24.
124. T. E. Sutto, *J. Electrochem. Soc.*, 2007, **154**, P130-P135.
125. S. Nohara, H. Wada, N. Furukawa, H. Inoue, M. Morita and C. Iwakura, *Electrochim. Acta*, 2003, **48**, 749-753.
126. C. M. Yang, J. B. Ju, J. K. Lee, W. I. Cho and B. W. Cho, *Electrochim. Acta*, 2005, **50**, 1813-1819.
127. J. Nunes-Pereira, C. M. Costa and S. Lanceros-Mendez, *J. Power Sources*, 2015, **281**, 378-398.
128. P. Pal and A. Ghosh, *J. Power Sources*, 2018, **406**, 128-140.
129. X. Zhang, M. Kar, T. C. Mendes, Y. Wu and D. R. MacFarlane, *Adv. Energy Mater.*, 2018, **8**, n/a.
130. P. F. R. Ortega, J. P. C. Trigueiro, G. G. Silva and R. L. Lavall, *Electrochim. Acta*, 2016, **188**, 809-817.
131. S. Ketabi and K. Lian, *Electrochim. Acta*, 2013, **103**, 174-178.

132. R. L. Lavall, S. Ferrari, C. Tomasi, M. Marzantowicz, E. Quartarone, M. Fagnoni, P. Mustarelli and M. L. Saladino, *Electrochim. Acta*, 2012, **60**, 359-365.
133. Y. Gong, D. Li, C. Luo, Q. Fu and C. Pan, *Green Chem.*, 2017, **19**, 4132-4140.
134. N. Yadav, M. K. Singh, N. Yadav and S. A. Hashmi, *J. Power Sources*, 2018, **402**, 133-146.

## **Chapter 2 Enzymatic processing of mussel shells to produce biorenewable calcium carbonate in seawater**

**See Appendix A for additional data.**

A version of this chapter has been accepted for publication.

Jennifer N. Murphy, Kelly Hawboldt\* and Francesca M. Kerton\*

Enzymatic Processing of Mussel Shells to Produce Biorenewable Calcium Carbonate in Seawater. *Green Chem.*, 2018, **20**, 2913-2920.

### **2.1 Introduction**

Green chemistry has played a key role in the field of renewable feedstocks, an area of research that has been growing rapidly over the last two decades. The transformation of biomass into chemicals, fuels and materials, leading to the development of biorefineries, is of great interest to many.<sup>1</sup> Biological or chemical catalysis is often used for these transformations.<sup>2, 3</sup> Using by-products and waste streams from a process as a starting material for another process to make a second product can enhance overall sustainability. In recent years, researchers have explored waste streams in the food industry, isolating valuable organic molecules (e.g. limonene, amino acids) and biopolymers (e.g. pectin, collagen).<sup>4,5</sup> The isolation of inorganic compounds (i.e. biominerals) has not been explored to as large an extent despite the importance of such materials in the global chemical supply chain. An exception is the isolation of silica in various forms from rice husk.<sup>6-9</sup>

Ocean-sourced biomass is starting to gain attention in the development of renewable chemicals,<sup>10-14</sup> as the strain on land space to provide food versus biomaterials and energy increases. The fact that oceans cover 71% of the planet, makes our oceans and the fishing

and aquaculture industries a suitable place to ‘fish’ for new sources of chemicals and chemical products. Aquaculture has been highlighted by the United Nations Food and Agriculture Organization as an important method for sustainable protein production and thus global aquaculture ventures have grown significantly in size over the past twenty years.

In terms of materials relevant to this research, total world mollusc production worldwide from wild capture and aquaculture sources was nearly 18.5 million tonnes in 2013.<sup>15</sup> Mussels accounted for 10% of all molluscs produced in 2013 and around 95% of these were produced via aquaculture. As mussel shells are typically 95-99% calcium carbonate ( $\text{CaCO}_3$ ), continued growth in this sector globally will lead to significant quantities of biorenewable calcium carbonate becoming available from waste streams.  $\text{CaCO}_3$  is a versatile and widely used raw material obtained from quarrying activities. For example, it is used as a pigment in the paper and coatings industries, in food and health products such as antacids, and in water treatment and construction.<sup>16,17</sup> Shells are comprised of two polymorphs of  $\text{CaCO}_3$ , calcite and aragonite. The desirable properties of biogenic aragonite, known as nacre (mother of pearl), and calcite has led many researchers to pursue the syntheses of these biominerals using biomimetic strategies.<sup>18-21</sup> To use the calcium carbonate from waste mussel shells, the shells need to be cleaned of any organic matter, such as residual meat (protein) that is left behind on the mussel shell after processing (i.e. the posterior adductor muscle) or the entire mussel if the shell is damaged or too small for market. This organic matter not only decreases the purity of calcium carbonate but also

attracts vermin (birds, flies, rats) and causes a stench due to decomposition, which prevents waste mussel shells from being stored for lengthy periods of time.

To date, there have been very few studies on effective processes to clean mussel shells of residual meat. The primary process to 'clean' mollusc shells is to heat to high temperatures to 'burn' off the organic contents.<sup>22, 23</sup> Other processes include separating the meat from the shell via dissection or other means<sup>17, 24</sup>, and washing with water. Several groups have exploited waste mussel shells for their CaCO<sub>3</sub> (and sequentially CaO) in a broad range of applications ranging from cement and mortars to catalysts but details concerning the presence of residual protein or shell-cleaning were not provided.<sup>25-27</sup> There have been a few reports on enzymatic hydrolysis of mussel meat for food applications. Commercial proteases, Optimase and Protamex, have been used to hydrolyze mussel meat to yield protein hydrolysate,<sup>28</sup> but not to clean shells and use the mineral component. Optimal conditions using Protamex at pH 6.85 for the hydrolysis of mussel meat were an enzyme:substrate ratio of 4.5% at 51 °C for 3 h. These conditions resulted in a degree of hydrolysis of 26% and 65% protein recovery. A New Zealand patent has described the cleaning of waste mollusc shells using three protease solutions; Alcalase, Pepsin, and Papain. The pH was adjusted to acidic or basic, depending on which enzyme was used, with maximum reaction times of 2 h at temperatures ranging from 45-70 °C.<sup>29</sup> In these existing studies, the use of tap water or seawater as the medium was not explored only acidic or basic pH solutions, and whether the mussel was cooked or raw is not detailed.

In this chapter, an environmentally sustainable method to clean waste mussel shells of residual meat, produced at any point in processing of the mussel to extract product (e.g.

raw discards, and damaged cooked), using two industrially available food grade protease enzymes, Multifect PR 6L and Multifect PR 7L (herein referred to as 6L and 7L) is described. These enzymes were selected due to their availability on an industrial scale and stability.

This method produces two product streams (a protein hydrolysate and clean CaCO<sub>3</sub> rich shells), which could be used in further applications. It was hypothesized that a process which works using tap or seawater might lead to easier implementation at aquaculture processing plants. Because of the many factors that might interact and must be optimized including time, temperature, reaction medium and amount of enzyme solution, Design of Experiments (DoE) methodology was used in this research.

## **2.2 Results and Discussion**

Mussel and other mollusc shells have enormous potential as a source of biorenewable calcium carbonate. However, a sustainable process for the removal of residual meat must be developed in order to prevent problems upon storage (e.g. stench from decomposition, attraction of vermin). In order to evaluate the proposed processes, two methods were evaluated for determining meat removal efficacy (mass balance and TGA). After each experiment, the shells and any remaining meat were dried for one day at room temperature in air and then weighed. The wt% meat remaining was calculated based on the mass of meat remaining on the shell and the mass of the clean shells as outlined in **Equation 2.1**.

**Equation 2.1**

$$\text{wt\% meat remaining} = \left[ \frac{\text{mass of meat remaining}}{\text{mass of clean shells} + \text{mass of meat remaining}} \right] * 100\%$$

The wt% of meat remaining was also determined by TGA. A calibration curve was constructed using standards that were prepared using clean shells and adding dried meat at 0.5, 1.0, 2.5, 5.0, 7.5 and 10 wt% and ground in the mixer mill. The mass percent losses were calculated from 100-600 °C and each sample was run in triplicate; excellent linearity was achieved (**Figure 2.1**,  $R^2 = 0.9975$ ). The calibration curve shows TGA is a good analytical method to quantify the amount of meat remaining on mussel shells. Shell-cleaning experiments were evaluated using both TGA and the manual meat removal and weighing approach, and the data were in agreement. However, TGA is more time consuming than weighing samples and residues after cleaning. Furthermore, the mass balance method could be easily used for quality control at a mollusc food production site. Therefore, for all results from initial screening studies through to experimental designs, the samples were inspected for residual meat and weighed to obtain wt% values as a measure of efficacy.

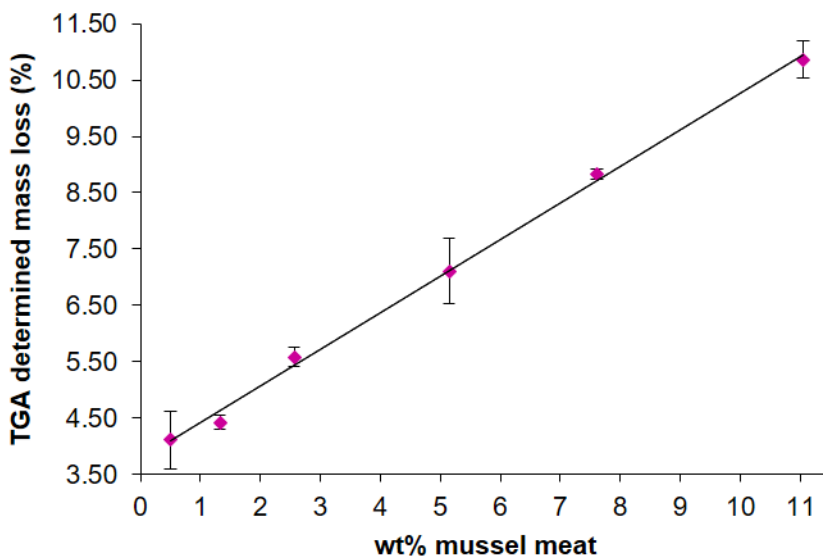


**Figure 2.1** Calibration curve for TGA analysis of mussel shells after enzymatic cleaning. One standard deviation shown with error bars.  $y=0.6511x + 3.7592$ .  $R^2=0.9975$ .

### 2.2.1 Initial Screening of Biocatalytic Process Conditions

In mussel aquaculture during harvesting and processing a significant amount of raw mussels are discarded as waste, including those with damaged shells and those that are too small. Therefore, reaction conditions were screened for treatment of raw shell-on mussels. In these exploratory experiments, four reaction media were studied; deionized water (DI), Tris-H buffer solution, natural seawater (NS), and synthetic seawater (SS). The medium is a critical part of this research for several reasons including cost, training, and environmental considerations. Many processing plants are next to the ocean and already have ocean wells, making natural seawater a very attractive option because it is abundant, easily accessed and cheap. The use of buffers or other media containing additives requires chemical and safety training and have higher costs. Deionized water was also screened as a neutral and non-saline option for comparison, and because for future use of the protein hydrolysate by-

product stream, saline contamination may be problematic. The amount of enzyme solution, time, and temperature were also taken into consideration. In later optimization studies, municipal tap water was used in place of deionized water and no significant differences were seen between the two.

In initial screening studies, very small volumes of enzyme solution were used at low temperatures (23-35 °C) and neither 6L or 7L were successful in fully cleaning the shells in any reaction media (**Table 2.1**), however overall 7L outperformed 6L in terms of meat removal (e.g. **Table 2.1**, entries 2 and 3). This suggests that the exopeptidase, even though it has a lower protease activity label as a commercial product, is more effective at digesting mussel meat than the endopeptidase. Noticing that natural seawater led to similar quantities of meat removal compared with deionized water (**Table 2.1**, entries 2-5) led to the exploration of higher enzyme loadings (2 - 6 µL/g) of 7L at 35.0 and 60.0 °C in seawater (**Table 2.1**, entries 6-10).

Increasing the loading of 7L from 1.2 µL/g to 4.0 µL/g at 35.0 °C for 4 h made no difference in the amount of meat remaining (**Table 2.1**, entries 4 and 6). However, increasing the loading to 6.0 µL/g removed nearly all the meat from shells at 35.0 °C in just 3 h (**Table 2.1**, entry 7). As expected, increasing the temperature to 60.0 °C with loadings of 7L up to 6.0 µL/g (**Table 2.1**, entries 9-10), led to increased activity of the enzyme and more complete hydrolysis of the mussel meat. Synthetic seawater has a slightly higher salinity than the natural seawater. This enhanced salinity led to an increased activity for 7L (**Table 2.1**, entry 11) and gave similar efficiencies at lower enzyme loadings compared with a reaction in nature seawater (**Table 2.1**, entry 7).

The activity of the endopeptidase, 6L, was also screened under a range of initial conditions by measuring the wt% meat remaining after treatment. Increasing the loading of 6L from 1.2  $\mu\text{L/g}$  to 2.0  $\mu\text{L/g}$  in a range of mediums at 35.0 °C (**Table 2.1**, entries 12, 14, and 16) increased hydrolysis but removed less residual meat than 7L under similar conditions (**Table 2.1**, entry 11). Raising the temperature to 55.0 °C under the same conditions (**Table 2.1**, entries 13 and 15) improved the activity of 6L, therefore, loading or temperature were not increased any further. At 55.0 °C, using 2.0  $\mu\text{L/g}$  6L in deionized water, shells were cleaned completely with no residual meat present (**Table 2.1**, entry 17). Use of Tris-H buffer with 6L gave comparable results to using deionized water under the same conditions, completely cleaning the shells of any meat at 55.0 °C (**Table 2.1**, entries 17 and 19).

**Table 2.1** Data for exploratory experiments on biocatalytic cleaning of raw shell-on blue mussels.

Entry	Enzyme	Enzyme loading ( $\mu\text{L/g}$ )	Medium <sup>a</sup>	Temperature ( $^{\circ}\text{C}$ )	Time (h)	Wt% Meat remaining
1	7L	1.2	DI	35.0	4	4.2
2	7L	1.2	DI	25.0	4	2.9
3	6L	1.2	DI	25.0	4	9.37
4	7L	1.2	NS	35.0	4	4.1
5	7L	1.2	NS	25.0	4	2.8
6	7L	4.0	NS	35.0	3	4.0
7	7L	6.0	NS	35.0	3	0.56
8	7L	2.0	NS	60.0	4	3.7
9	7L	4.0	NS	60.0	4	0.21
10	7L	6.0	NS	60.0	4	0.35
11	7L	2.0	SS	35.0	2	0.67
12	6L	2.0	NS	35.0	2	5.67
13	6L	2.0	NS	55.0	2	0.60
14	6L	2.0	SS	35.0	2	2.63
15	6L	2.0	SS	55.0	2	0.23
16	6L	2.0	DI	35.0	4	1.44
17	6L	2.0	DI	55.0	4	0
18	6L	2.0	Tris-H	35.0	4	1.7
19	6L	2.0	Tris-H	55.0	4	0
20	7L	4.0	Tris-H	45.0	4	0
21	7L	6.0	Tris-H	45.0	4	0

<sup>a</sup> DI, distilled water; NS, natural seawater; SS, synthetic seawater; Tris-H, trishydroxymethane buffer (pH=8.5).

7L was also successful in cleaning the shells completely with Tris-H buffer as the reaction medium but at higher enzyme loadings compared with 6L (**Table 2.1**, entries 20-21).

Based on these exploratory experiments, 6L was chosen for optimizing the process for removing residual meat from raw mussels. There were two main reasons for this selection.

Firstly, a buffer solution was not required to completely remove the meat so deionized water or seawater could be used. This reduces the cost of materials and would require less experience/safety training for persons carrying out the cleaning process if implemented at an aquaculture site. Also, less enzyme solution was needed to digest raw mussel meat in comparison to 7L and 6L is commercially available at a lower cost (mL/mL) than 7L.

It was also important to investigate the ability of the protease enzymes to digest cooked mussels because mussels are likely to be cooked, frozen, canned or bottled for export to meet global demands for protein. In a food processing setting, the majority of the waste would be cooked mussels, not raw. In this screening study, enzymatic hydrolysis was performed on cooked mussel meat removed from the shell (**Table 2.2**).

**Table 2.2** Data for exploratory experiments on biocatalytic digestion of cooked blue mussel meat, removed shells.<sup>a</sup>

Entry	Enzyme	Temperature (°C)	Time (h)	Percent digested (%)
1 <sup>b</sup>	6L	35.0	2	84.0
2 <sup>b</sup>	6L	55.0	2	85.9
3 <sup>b</sup>	6L	35.0	4	88.9
4 <sup>b</sup>	6L	55.0	4	89.5
5 <sup>b</sup>	7L	35.0	2	86.0
6 <sup>b</sup>	7L	55.0	2	73.6
7 <sup>b</sup>	7L	35.0	4	100
8 <sup>b</sup>	7L	55.0	4	83.0
9 <sup>b</sup>	7L	25.0	4	96.7
10 <sup>c</sup>	7L	35.0	2	76.6
11 <sup>c</sup>	7L	55.0	2	54.2
12 <sup>c</sup>	7L	35.0	4	79.6
13 <sup>c</sup>	7L	55.0	4	60.8
14 <sup>c</sup>	7L	25.0	4	97.2

<sup>a</sup> For these reactions, approximately 12.0 g of cooked mussel meat, temperatures 25.0-55.0 °C and 1.2 µL/g of enzyme solution were used; b. Reaction carried out in deionized water; c. Reaction carried out in natural seawater.

6L hydrolysed cooked mussel meat with the same efficacy, independent of time or temperature with 84-89.5% of meat hydrolysed (**Table 2.2**, entries 1-4) in deionized water. This contrasts with the same experiments performed using 7L (**Table 2.2**, entries 5-8) that gave a larger range of hydrolysis (73.6-100%) of cooked meat. Interestingly, the performance of 7L was better at lower temperatures (**Table 2.2**, entries 5 and 6) and when the processing time was increased to 4 h at 35.0 °C, 100% of the meat was hydrolysed (**Table 2.2**, entry 7). The results with 7L were so impressive at 35.0 °C it prompted the investigation of what would happen if the heat was turned off in the incubator. The cooked mussel meat was nearly 97% hydrolyzed at room temperature (**Table 2.2**, entry 9). Continuing with 7L, it was investigated whether natural seawater would be suitable for the hydrolysis of cooked meat (**Table 2.2**, entries 10-14), as it had been a suitable medium for cleaning shells of raw mussels. Disappointingly, regardless of enzyme used, only 54-80% hydrolysis of the cooked meat could be achieved in seawater. However, it is worth noting that at room temperature in natural seawater 97% of the meat was hydrolysed by 7L, which is comparable to data for deionized water (**Table 2.2**, entries 9 and 14). This key result prompted optimization studies for the hydrolysis of cooked mussel meat at ambient temperature using 7L and seawater.

### **2.2.2 Experimental Designs for Optimization of Shell Cleaning**

In order to further optimize conditions, a Design of Experiments (DoE) approach was used and the selection of the levels for the different factors studied was based on data from the exploratory experiments. Enzymes are sensitive to high temperatures, so this process needed to be carried out under mild reaction conditions to ensure the enzyme did not

denature but needed to be sufficient so that the shells were cleaned of residual meat. Reactions performed without heating (room temperature) showed that 6L performed poorly with raw shell-on mussels but superbly at 55.0 °C, therefore the temperature was not increased any higher during optimization. Additionally, higher temperatures would be less cost effective at aquaculture and shellfish processing plants. Because of how well 7L digested cook mussel meat at low temperatures, the optimization for cooked mussels without heating was done using 7L. The enzyme concentration range and incubation times were initially selected based on exploratory experiments. However, if the reaction time was insufficient at producing clean shells the design was modified. For example, initial experiments with 7L had shorter reaction times (up to 6 h) and this model was built upon to achieve a modified model with longer reaction times (10 h) to ensure the shells were clean. The hydrolysis mediums were chosen based on the exploratory experiments that showed raw whole mussel could be cleaned in seawater (**Table 2.1**). The optimization was performed without the use of Tris-H, as a buffer free process would be easier to perform at seafood processing sites, which are often in remote rural communities.

#### **2.2.2.1 Optimization of shell cleaning process for raw, shell-on mussels using Multifect PR 6L**

**Table 2.3** Factors and levels studied for optimization of shell cleaning process using Multifect PR 6L to remove meat from raw mussels

<b>Factor</b>	<b>Name</b>	<b>Low Actual</b>	<b>High Actual</b>	<b>Low Coded</b>	<b>High Coded</b>
X1	Temperature	35 °C	55 °C	-1	+1
X2	Enzyme Loading	1.0 µL/g	2.0 µL/g	-1	+1
X3	Time	2 hours	4 hours	-1	+1
X4	Medium	Natural seawater	Tap water	-1	+1

The effects of temperature (X1), amount of 6L enzyme solution (X2), time (X3) and aqueous medium (X4) on the shell cleaning efficacy were investigated (

**Table 2.3**). Each variable was studied at two levels, low (-1) and high (+1). This  $2^4$  factorial design was run in triplicate for a total of 55 experiments including 4 center points (**Appendix A**). Wt% meat remaining was the measured response (Y) for the experimental design. The model, which required a square root transform, was tested to determine the significant parameters via the analysis of variance (ANOVA) with a significance level of 5% using Design Expert 10 software. ANOVA showed that there were just two significant effects, temperature (X1) and time (X3) with p-values of  $< 0.0001$  and  $0.0025$ , respectively.

**Figure 2.2** shows a three-dimensional plot of the model obtained based on temperature and time when seawater was used at the highest enzymes loading ( $2.0 \mu\text{L/g}$ ) of 6L. It shows that wt% meat remaining decreases as temperature (X1) and time (X3) increase. Further experiments were not performed as the shells were cleaned fully and did not require further optimization or higher order models. From these experiments, it is concluded that the mussel meat from 20 g of raw mussels can be hydrolyzed to yield clean shells using 6L in seawater or tap water for 4 h at  $55.0 \text{ }^\circ\text{C}$  using just 10-20  $\mu\text{L}$  of enzyme solution.

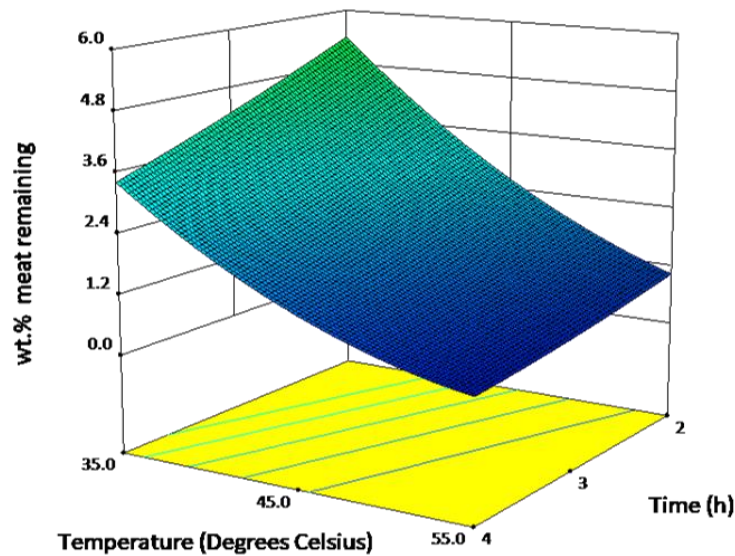


**Figure 2.2** Response surface of wt% meat remaining based on temperature and time for removal of raw protein from mussel shells using Multifect PR 6L.

#### 2.2.2.2 Optimization of shell cleaning process for cooked, shell-on mussels using Multifect PR 7L

A different design of experiments approach was used for optimizing the process to remove cooked protein from mussel shells using 7L. An I-optimal custom design (a response surface method) with 4 replicate points and 8 center points for a total of 24 experiments (see **Appendix A**). This response surface method has two numeric factors (amount of enzyme solution and time) and one categorical factor (reaction medium). The effects of amount of enzyme solution (Z1), time (Z2), and aqueous medium (Z3) on the shell cleaning efficacy for cooked mussels were investigated. Like the design for 6L, each variable was studied at two levels, low (-1) and high (+1). Amount of enzyme solution was investigated at 30 and 60  $\mu\text{L}$ ; time was investigated at 2 and 10 h; medium was investigated for natural seawater and synthetic seawater. Once again, the response (Y), was the wt% meat

remaining after enzymatic hydrolysis. This model required a log transform and was tested via the ANOVA with a significance level of 5% using Design Expert 10 software. ANOVA showed there were two significant effects, amount of 7L solution (Z1) and time (Z2) with p-values of 0.0196 and <0.0001, respectively. This contrasts with the model obtained for removing meat from raw mussels using 6L, where the two significant effects were temperature and time, and the amount of enzyme was not significant. **Figure 2.3** is a three-dimensional plot of the model obtained for this process in terms of the two most significant parameters studied (amount of enzyme solution and time) when natural seawater was used. This model shows that wt% meat remaining decreases as amount of 7L solution (Z1) and time (Z2) increase. As with the experimental design for 6L with raw mussels, further development of this 7L catalyzed cleaning process was not needed as the shells were fully cleaned of meat and did not require further optimization or higher order models. From these experiments, it is concluded that the cooked mussel meat from 20 g of cooked mussels can be cleaned using 7L in seawater or synthetic seawater for 10 h at room temperature using 60  $\mu$ L of enzyme solution. Although this reaction time is quite long, a process based on this might be suitable for overnight treatment of waste mussels in a seafood processing plant especially as it can be performed at room temperature (25 °C).

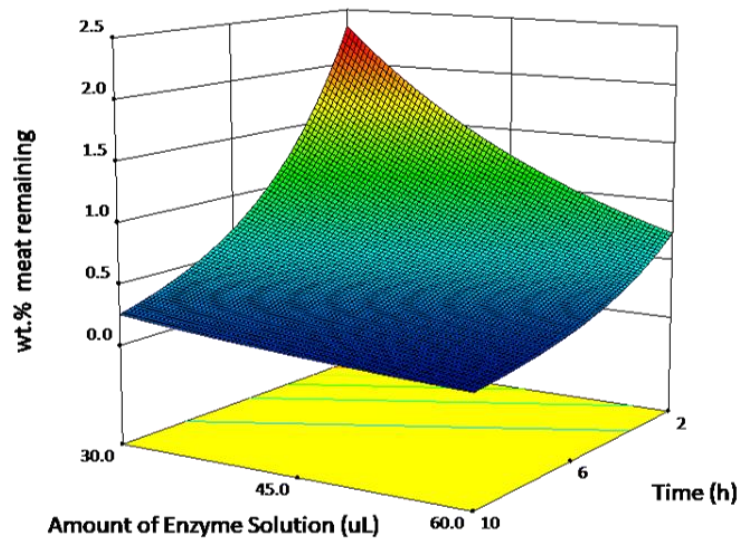


**Figure 2.3** Response surface of wt% meat remaining based on the amount of enzyme solution and time for the removal of cooked protein from mussel shells using Multifect PR 7L.

As previously mentioned, the New Zealand patent by Frude describes the cleaning of waste mollusc shells using three protease solutions; alcalase, pepsin, and papain. The pH was adjusted to acidic or basic, depending on which enzyme was used, with maximum reaction times of 2 h at temperatures of 45-70 °C.<sup>29</sup> Our work also uses protease enzymes, Multifect PR 6L and Multifect PR 7L and our optimal conditions had longer reaction times (4-10 h). However, this research showed that natural seawater and lower temperatures (including no heating) can be used for the hydrolysis of raw or cooked mussels to yield clean shells and protein hydrolysate. On average, whole mussels used were 50% shell by weight, therefore ~10 g of protein is hydrolyzed for each optimized reaction in our work. 1.0-2.0 µL/g 6L cleaned the shells of raw mussels and 6.0 µL/g 7L efficiently cleaned the shells of cooked

mussels. This corresponds to enzyme:substrate ratios of 0.1-0.2% and 0.6%, which are significantly lower than previously reported studies on mussel protein hydrolysis.<sup>28,29</sup>

The protein hydrolysate from blue mussels was freeze dried and was used in a palatability trial for aquarium fish. The freeze-dried mussel hydrolysate was fed to zebrafish in the laboratory over 24 months. Further characterization of the by-product streams (biorenewable calcium carbonate and protein hydrolysate) are ongoing.

### **2.3 Conclusions**

In the mussel aquaculture industry, the shellfish are either exported raw or are processed to yield other products (frozen, canned etc.). The waste shells produced represent a valuable by-product if the residual meat left on the shell can be removed. An enzymatic process that cleans the shell by-product in an environmentally friendly, cost-effective, and safe manner by using seawater, mild temperatures, and eliminating the use of acids and bases was developed. Mussel shells with raw protein attached were efficiently cleaned using 1.0-2.0  $\mu\text{L/g}$  6L in seawater or tap water for 4 h at 55.0 °C. Mussel shells with cooked protein attached were efficiently cleaned using 6.0  $\mu\text{L/g}$  7L in seawater or synthetic seawater for 10 h at 25.0 °C. For both processes developed, the models obtained show no interactions between factors. These processes employ low enzyme loadings (0.1-0.6%) and assuming the most significant ongoing cost in cleaning the shells is the enzyme, the cost of cleaning 20 g of mussels is less than 0.1 US cents. The cleaned shells have a variety of possible applications from wastewater treatment to alternatives to road salt. Further, the residual protein stream is a possible fishmeal source. By utilizing all by-product streams, a truly sustainable process can be developed. The biorenewable calcium carbonate can be

employed without further treatment, however, depending on the application, additional processing for higher purity calcium carbonate may be required. Extensions of this work are working towards new and exciting uses for the biorenewable calcium carbonate from the mussel shells produced and developing models for scale up of the enzymatic process.

## **2.4 Experimental**

### **2.4.1 General Considerations**

All mussels (eastern blue mussel, *Mytilus edulis*) were purchased from the same grocery store (Sobeys, Merrymeeting Road, St. John's, NL) and were of Newfoundland origin. Mussels were minimally pretreated after purchase. Beards (adhesive material mussels use to move around rocks etc.) were removed if visible but often they were inside the mussel and not noticed until the end of the experiment. When removing beards, some meat was also unavoidably removed. Synthetic seawater, 35 parts per thousand (ppt) or 35 g/L, was made using sea salts purchased from Sigma Aldrich. Natural seawater was collected from Middle Cove Beach, NL (47° 39' 2.16" N, -52° 41' 44.52" W), filtered and stored in a refrigerator. The salinity of the natural seawater was measured using an ATI Orion model 835 dissolved oxygen meter and was found to be 25 ppt. A Tris-H buffer (pH=8.5) was prepared by mixing 110.0 mL of 0.2 M tris(hydroxymethyl)aminomethane and 22.0 mL of 0.2 M hydrochloric acid and diluting to a total volume of 410.0 mL. Two hydrolase solutions were supplied by DuPont (Industrial Bioscience Division) and used as is. The first, Multifect PR 6L (6L), is an alkaline serine endopeptidase from *Bacillus licheniformis* with an activity of 2440 ELU/mL and the second, Multifect PR 7L (7L), is an exopeptidase from *Bacillus amyloliquefaciens* with an activity of 100 ELU/mL. A Qmax 4500 incubator

was used to maintain constant temperatures for biocatalytic reactions. An automated pipette was used to measure the amount of enzyme solution required. Shell and dried meat samples for thermogravimetric analyses (TGA) were ground using a SPEX Sample Prep 8000M mixer mill in a stainless-steel vial equipped with 2, 1/4" stainless steel balls for 12 min. TGA was carried out using a TA Instruments Q500 under high resolution dynamic mode. Samples were heated at a rate of 5.0 °C min<sup>-1</sup> under a N<sub>2</sub> atmosphere (50 mL min<sup>-1</sup>) from 25-600 °C and under air from 600-800 °C (50 mL min<sup>-1</sup>).

#### **2.4.2 Enzymatic Treatment of Whole Raw Mussels**

Whole live mussels were opened by hand by inserting a spatula and tearing the adductor that connects the two sides of the shell. The intact shell halves were placed into a 250 mL Erlenmeyer flask. Approx. 20 g of mussel were used for each experiment with the specified enzyme loadings from 1.2-6.0 μL/g (volume of enzyme solution per gram of mussel meat). The required amount of medium (deionized water, buffer solution, natural seawater or synthetic seawater) was added so that the mussels were fully immersed. The capped flasks were placed in a Qmax 4500 incubator set to the desired temperature (25-60 °C) and shaken at a platform speed of 160 rpm for 2-4 h. Afterwards the protein hydrolysate was decanted and heated to 80 °C to deactivate the enzyme. The protein hydrolysate was centrifuged to remove larger particles before being freeze dried. Shells were rinsed in distilled water before air drying for one day and then stored before analysis.

It is worth noting that even though each reaction starts with ~20 g of mussels, the relative mass of meat and shell, individually, are not known with certainty until the shells are clean and can be weighed. However, on average the mass of meat was approximately 50% of the

whole mussel, or about 10 g. Therefore, unless otherwise stated, 10 g of mussel meat was used to calculate the enzyme loadings.

### **2.4.3 Enzymatic Treatment of Whole Cooked Mussel Meat and Shell**

Treatment of whole cooked mussels followed the same procedure as raw mussels except the mussels were previously steamed for approx. 1 min. Reaction times were varied from 2-10 h.

### **2.4.4 Enzymatic Treatment of Cooked Mussel Meat**

6L or 7L (12  $\mu$ L), 12 g of meat [cooked (steamed for 1 min), removed from shell], and deionized water (25 mL) were added to a 250 mL Erlenmeyer flask. The mixture was heated for 2 or 4 h to the specified temperature in an incubator while rotating at 160 rpm. The aqueous mixture was filtered, the residual meat isolated and weighed while still wet.

## **2.5 References**

1. M. Aresta, A. Dibenedetto and F. Dumeignil, *Biorefinery From Biomass to Chemicals and Fuels*, De Gruyter, Berlin, Germany, 2012.
2. A. J. J. Straathof, *Chem. Rev.*, 2014, **114**, 1871-1908.
3. M. Besson, P. Gallezot and C. Pinel, *Chem. Rev.*, 2014, **114**, 1827-1870.
4. L. A. Pfaltzgraff, M. De Bruyn, E. C. Cooper, V. Budarin and J. H. Clark, *Green Chem.*, 2013, **15**, 307-314.
5. C. S. K. Lin, L. A. Pfaltzgraff, L. Herrero-Davila, E. B. Mubofu, S. Abderrahim, J. H. Clark, A. A. Koutinas, N. Kopsahelis, K. Stamatelatou, F. Dickson, S.

- Thankappan, Z. Mohamed, R. Brocklesby and R. Luque, *Energy Environ. Sci.*, 2013, **6**, 426-464.
6. K. Kaviyarasu, E. Manikandan, J. Kennedy, M. Jayachandran and M. Maaza, *Adv. Mater. Lett.*, 2016, **7**, 684-696.
  7. Y. Liu, Z. Wang, H. Zeng, C. Chen, J. Liu, L. Sun and W. Wang, *Mater. Lett.*, 2015, **142**, 280-282.
  8. T. C. Luan and T. C. Chou, *Ind. Eng. Chem. Res.*, 1990, **29**, 1922-1927.
  9. C. Real, M. D. Alcalá and J. M. Criado, *J. Am. Ceram. Soc.*, 1996, **79**, 2012-2016.
  10. I. S. Arvanitoyannis and A. Kassaveti, *Int. J. Food Sci. Technol.*, 2008, **43**, 726-745.
  11. F. M. Kerton, Y. Liu, K. W. Omari and K. Hawboldt, *Green Chem.*, 2013, **15**, 860-871.
  12. F. M. Kerton, in *Chemical Process Technology For A Sustainable Future*, eds. T. M. Letcher, J. L. Scott and D. A. Paterson, Royal Society of Chemistry Publishing, Cambridge, UK, 2014.
  13. N. Yan and X. Chen, *Nature*, 2015, **524**, 155-157.
  14. F. M. Kerton and N. Yan, *Fuels, Chemicals and Materials from the Oceans and Aquatic Sources*, Wiley, 2017.
  15. Food and Agriculture Organization of the United Nations, Fisheries and Aquaculture Department, <http://www.fao.org/fishery/statistics/en>, (accessed February 22, 2016).
  16. Industrial Minerals Association of North America, <http://www.ima-na.org/>, (accessed March 18, 2018).

17. K. Tekin, *Energy & Fuels*, 2015, **29**, 4382-4392.
18. S. Weiner and L. Addadi, *J. Mater. Chem.*, 1997, **7**, 689-702.
19. H.-B. Yao, J. Ge, L.-B. Mao, Y.-X. Yan and S.-H. Yu, *Adv. Mater.*, 2014, **26**, 163-188.
20. Y.-Y. Kim, J. D. Carloni, B. Demarchi, D. Sparks, D. G. Reid, M. E. Kunitake, C. C. Tang, M. J. Duer, C. L. Freeman, B. Pokroy, K. Penkman, J. H. Harding, L. A. Estroff, S. P. Baker and F. C. Meldrum, *Nat. Mater.*, 2016, **15**, 903-910.
21. L.-B. Mao, H.-L. Gao, H.-B. Yao, L. Liu, H. Coelfen, G. Liu, S.-M. Chen, S.-K. Li, Y.-X. Yan, Y.-Y. Liu and S.-H. Yu, *Science*, 2016, **354**, 107-110.
22. P. Ballester, I. Mármol, J. Morales and L. Sánchez, *Cem. Concr. Res.*, 2007, **37**, 559-564.
23. M. C. Barros, P. M. Bello, M. Bao and J. J. Torrado, *J. Clean. Prod.*, 2009, **17**, 400-407.
24. D. Gallardi, K. Hobbs, T. Mills, C. Couturier, C. Parrish and H. Murray, *Aquaculture*, 2014, **430**, 149–158.
25. R. Rezaei, M. Mohadesi and G. R. Moradi, *Fuel*, 2013, **109**, 534-541.
26. A. M. Ramírez-Pérez, M. Paradelo, J. C. Nóvoa-Muñoz, M. Arias-Estévez, M. J. Fernández-Sanjurjo, E. Álvarez-Rodríguez and A. Núñez-Delgado, *J. Hazard. Mater.*, 2013, **248–249**, 122-130.
27. P. Lertwattanaruk, N. Makul and C. Siripattaraprat, *J. Environ. Manage.*, 2012, **111**, 133-141.
28. V. M. Silva, K. J. Park and M. D. Hubinger, *J. Food Sci.*, 2010, **75**, C36-C42.
29. M. J. Frude, *Method for removing excess meat from whole of crushed mollusk*

*shellfish waste*, New Zealand Pat., 555418, 2008.

## **Chapter 3 Wealth from waste: Blue mussels (*Mytilus edulis*) offer up a sustainable source of natural and synthetic nacre**

**See Appendix B for additional data.**

A version of this chapter has been accepted for publication.

Jennifer N. Murphy, Céline M. Schneider, Lilo K. Mailänder, Quentin Lepillet, Kelly Hawboldt, and Francesca M. Kerton\*

Wealth from waste: Blue mussels (*Mytilus edulis*) offer up a sustainable source of natural and synthetic nacre, *Green Chem.*, 2019, **21**, 3920-3929

### **3.1 Introduction**

With the United Nations projecting the global population to reach 9.7 billion by 2050,<sup>1</sup> there is growing concern regarding sustainable sources of dietary protein. Environmental scientists have shown that a shift towards pescatarian or Mediterranean diets using aquacultural methods to produce the seafood would not only lead to improved human health but would reduce greenhouse gas emissions,<sup>2, 3</sup> which are significant in the meat and dairy industries. Due to cultural considerations, proximity to the oceans and economics, it is unrealistic to expect everyone to transition their diets in this way. However, in regions where such changes are made, in terms of environmental sustainability (e.g. carbon

footprint), farming molluscs and other bivalves requires less inputs (e.g. they are filter feeders and do not need to be provided with feed) compared with finfish such as salmon. Therefore, growth in the production of molluscs in aquaculture industries around the world is anticipated.

A big part of our social responsibility is waste management, as such increased fish consumption and fish product commercialization will lead to increased amounts of by-products, which in the case of mollusc farming and processing includes large volumes of shells. **Chapter 2** described a biocatalytic method for producing clean (protein-free) mussel shells sourced as by-products from the Canadian aquaculture industry.<sup>4</sup> With a sustainable method for isolating the shells developed, it became important to characterize these materials in order to develop future applications for them. To date, waste shells have been valorized in a number of ways including building materials and wastewater treatment<sup>5, 6</sup> as a sustainable replacement of CaCO<sub>3</sub>, the most heavily exploited mineral on Earth.<sup>7</sup> However, high value applications of these materials have been explored to a lesser extent especially when compared with synthetic nacre.

Mollusc shells are 95-99.9% CaCO<sub>3</sub>, with the remaining percentages made of other minerals and an organic matrix composed of silk-fibroin like proteins, β-chitin and glycoproteins that act as a glue to hold crystals of CaCO<sub>3</sub> in place as well as controlling nucleation and polymorph type.<sup>8, 9</sup> Mollusc shells can consist of calcite, aragonite or a mixture of both polymorphs. If both polymorphs are present, they are always separated into two layers as demonstrated by *Mytilus californianus* (California mussels).<sup>10</sup> For another mollusc, *Atrina rigida*, the outer layer is composed of calcite prisms that can be >100 μm

long and up to 50  $\mu\text{m}$  in diameter that are surrounded in a layer of organic matrix.<sup>11</sup> The aragonite layer of mollusc shells, also known as nacre or ‘mother of pearl’, are generally composed of polygonal aragonite platelets that are 5-15  $\mu\text{m}$  in diameter and 0.5  $\mu\text{m}$  thick. The platelets are arranged in parallel laminae and stacked on top of each layer separated by a small layer of the interlamellar organic matrix.<sup>12</sup> Unlike man-made composites that contain fibres,<sup>13</sup> nacre is a natural composite material that has platelet reinforcement,<sup>8</sup> a microstructure that gives nacre a 3000-fold higher fracture resistance than geological aragonite.<sup>14, 15</sup> Nacre is one of the most widely studied structural motifs because of its interesting bulk material properties such as tensile strength, Young’s modulus and fracture toughness.<sup>8, 9</sup> Because nacre is mechanically strong with high bioactivity and biocompatible, it has been explored in bone implantation applications including drug delivery, bone cement and artificial bone substitute, including dental implants.<sup>9, 12, 16</sup> Therefore, there is significant potential in building up new materials using natural nacre, in addition to synthetic nacre, if it can be sourced in a sustainable fashion.

Many researchers have used nacre as inspiration to make other composite nacre mimetic materials by combining a synthetic ceramic component with a polymeric material that results in a material with improved fracture resistance, mechanical strength and toughness.<sup>17</sup> Others have tried to control the crystallization of  $\text{CaCO}_3$  using mixtures of  $\beta$ -chitin, silk-fibroin, and acidic proteins to form platelets of aragonite with very few succeeding to synthesize nacre-like layered structures.<sup>17</sup> Synthetic nacre-like materials have previously been made by a plethora of bottom up assembly techniques.<sup>18, 19</sup> I wondered if a method for easily separating the aragonite and calcite parts of *Mytilus edulis*

(blue mussel) could be developed to allow ready access to highly desirable biogenic nacre. The liberation of platelets of nacre could help scientists improve the mechanical properties of new composites by using the platelets from a renewable source instead of synthesizing new platelets and be completely tunable with respect to protein/polymer binder. In this chapter, comprehensive characterization data for Atlantic blue mussel, *Mytilus edulis*, shells (whole shells, calcite layer and nacre layer) are reported including solid-state NMR spectra and a simple method for separating the two polymorphs of  $\text{CaCO}_3$ . Furthermore, preliminary results on using the biogenic  $\text{CaCO}_3$  crystalline materials as seeds for growth of artificial calcite and nacre in the presence and absence of mussel protein hydrolysate are described. The approaches described herein can contribute to the circular economy, as by-product streams (shells and protein hydrolysate) from the seafood industry are being used.

### 3.2 Results and Discussion

Mussel shells, with protein residues removed using a biocatalytic method,<sup>4</sup> were heated at 120, 160 and 200 °C for 48 h and compared with those air-dried at room temperature. Upon heat treatment, the shells change color from blue-black to brown initially and at higher drying temperatures, the outer surface of the shell turns pale brown (**Figure 3.1 a**). Also, the shells became more brittle and easier to crush with increasing drying temperature. Shells were ground using either a mixer mill (stainless steel vials and balls) or mortar and pestle when required for subsequent analysis. ICP-MS of the ground shells showed contamination from the stainless-steel mixing vial (Appendix B, **Table B1**) and so heat-treated shells were ground using a mortar and pestle in most cases. At temperatures of 160 °C and higher, the inner layer of the shell began to separate from the outer shell when

crushed. Therefore, spectroscopic characterization could be performed on samples of the inner and outer layers in addition to the whole shell.

As discussed in **Chapter 1**, the different parts of the shell and their separation can be studied using IR spectroscopy. Carbonate ions,  $\text{CO}_3^{2-}$ , have four fundamental modes of stretching;  $\nu_1$ , symmetric C-O stretch,  $\nu_2$ ,  $\text{CO}_3^{2-}$  out of plane bending,  $\nu_3$ , C-O asymmetric stretch (doubly degenerate) and  $\nu_4$ , O-C-O planar bending (doubly degenerate).<sup>20</sup> The symmetry of the  $\text{CO}_3^{2-}$  in the solid phase of calcite and aragonite dictates which of these fundamental modes are infrared active, allowing us to distinguish easily between aragonite and calcite. The site symmetry of the  $\text{CO}_3^{2-}$  ion based on crystal data is  $D_3$  and  $C_s$  in calcite and aragonite respectively.<sup>21</sup> Therefore, based on the selection rules for the  $D_3$  and  $C_s$  point groups, we expect to see three of the fundamental modes,  $\nu_2$ ,  $\nu_3$ , and  $\nu_4$  for calcite and all fundamental modes for aragonite. IR spectra were collected on an ATR instrument where absorbance is measured. Using OPUS software, spectra were baseline corrected and converted to transmittance. These spectra were not used for quantification and the conversion from absorbance to transmittance did not affect the band shape or maxima of the bands. In ATR the IR radiation only penetrates a couple micrometres into the sample, so spectra were collected in triplicate and averaged to improve homogeneity.

Several IR spectra of mussel shells that have undergone heat treatment are shown in predominantly calcite and afford IR spectra similar to optical calcite and reagent grade  $\text{CaCO}_3$  (**Figure B2**). In these shells, a small quantity of aragonite is present based on the low intensity  $\nu_1$  band at  $1083\text{ cm}^{-1}$ , the symmetric stretch that is absent in calcite, and a shoulder within the  $\nu_2$  band at  $873\text{ cm}^{-1}$ .<sup>20</sup> After heating the shells for 48 h at  $160\text{ }^\circ\text{C}$ , the

shoulder of  $\nu_2$  becomes more defined and there is an increase in intensity of  $\nu_3$  from  $1395\text{ cm}^{-1}$  at  $25\text{ }^\circ\text{C}$  to  $1407\text{ cm}^{-1}$  as well as the appearance of the doubly degenerate  $\nu_4$  band of aragonite at  $700\text{ cm}^{-1}$ . Interestingly, after heat treatment at  $200\text{ }^\circ\text{C}$ , there are two distinct bands for the  $\nu_2$  stretch at  $873$  and  $860\text{ cm}^{-1}$ , respectively, and an even more intense  $\nu_3$  band at  $1409\text{ cm}^{-1}$ . IR spectra with higher resolution ( $2\text{ cm}^{-1}$ ), **Figure 3.1b-iv**, of mussel shells heated at  $220\text{ }^\circ\text{C}$  showed an even more intense  $\nu_4$  which may mean these changes in the IR spectra corresponded to changes in the relative amounts of calcite and aragonite as a result of heat treatment. In particular, it is evident that there is more aragonite present after heat treatment based on the appearance of additional bands that match literature values for aragonite.<sup>20, 22, 23</sup> This may seem counterintuitive as aragonite is known to convert to calcite at temperatures between  $300\text{-}500\text{ }^\circ\text{C}$ ,<sup>12</sup> and at temperatures above  $650\text{ }^\circ\text{C}$  both polymorphs will decompose to form calcium oxide (lime). In the current study, the apparent increase in aragonite levels is linked with the thermal decomposition of the organic matrix within the shell structure.

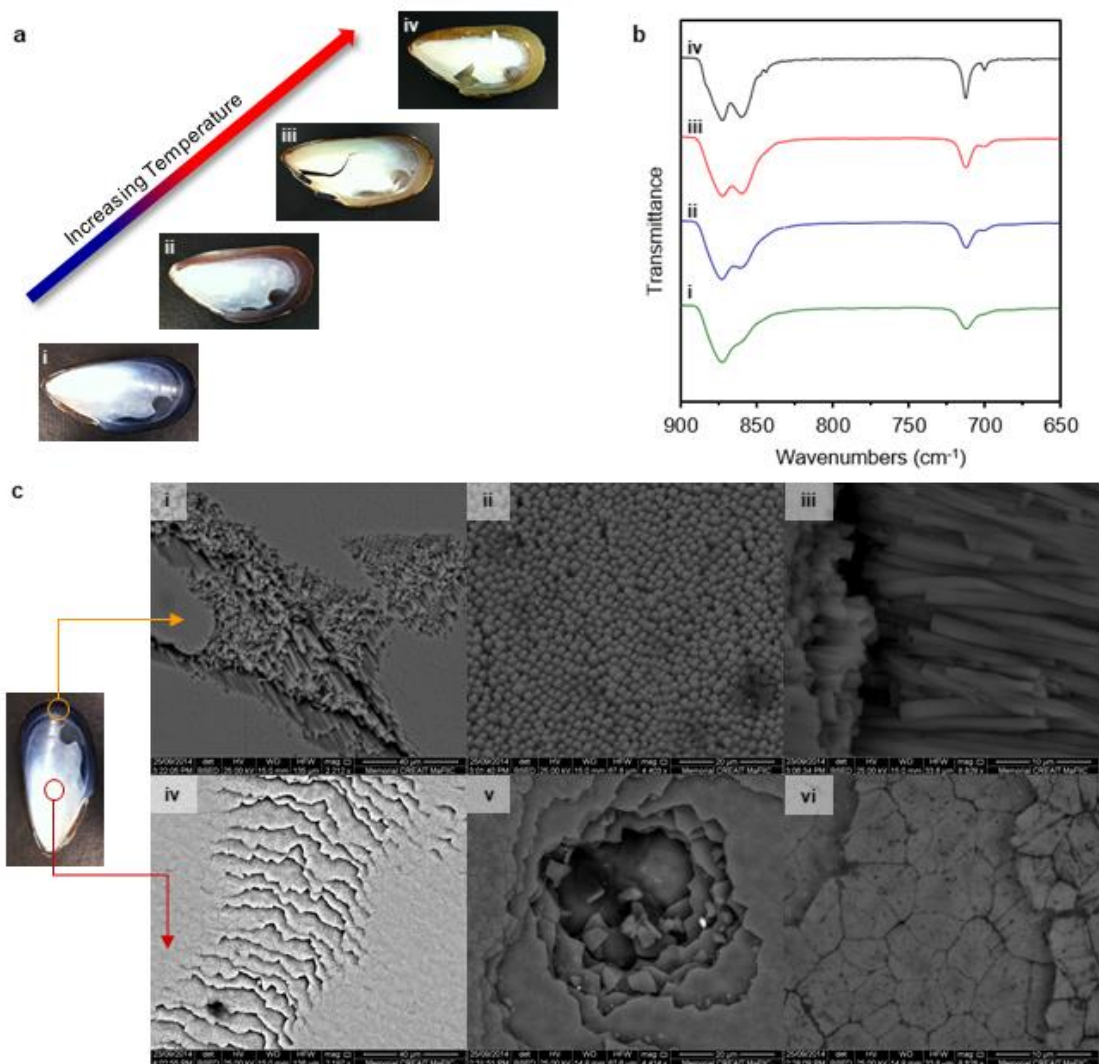


**Figure 3.1** a) Appearance of i) untreated blue mussel shells and shells heated at ii) 120 °C, iii) 160 °C, and iv) 200 °C for 48 h. b) Infrared spectra of i) untreated blue mussel shells and shells heated to ii) 160 °C iii) 200 °C and iv) 220 °C for 48 h. c) SEM micrographs (back-scatter detection) of blue mussel after heat treatment for 48 h at the noted temperature. Schematic of the inner and outer layer of mussel depicts where the micrographs were taken. The outer layer, i)-iii), after heating at 220 °C, 160 °C and 220 °C, respectively. The inner layer, iv)- vi), after heating at 220 °C, 160 °C and 160 °C, respectively.

Crystalline material within the many central (myostracal) layers in the shell is comprised of irregular spherulitic prismatic aragonite substructures with a thick coating of organic

matrix,<sup>28</sup> therefore removal of the matrix especially within this central portion of the shell (myostracum) leads to the different proportions of calcite:aragonite observed upon heating mussel shells at temperatures between 120 and 220 °C. Powder XRD data, discussed below, also provides evidence for varying ratios of aragonite and calcite upon heating the shells.

The morphology of heat-treated blue mussel shells was investigated using SEM. In the micrographs shown in **Figure 3.1c**, the shape and size of the aragonite and calcite crystals that make up the inner and outer layers of shells did not change when heated at temperatures up to 220 °C for 48 h. The inner layer is made up of polygonal plates 5-10 μm wide consistent with nacreous aragonite and the outer layer is made up of prismatic calcite with a diameter of approx. 2 μm and a length of 50 μm. In molluscs, calcite and aragonite crystallize from their (001) plane.<sup>28</sup> This makes it challenging to see the complete length of the prismatic calcite crystals via SEM. **Figure 3.1c** shows the prismatic calcite crystals from the fracture surface (side view). Biogenic aragonite of the nacreous layer has been seen in many other molluscs including *Unio treminalis*, *Haliotis rufescens*, and *Pinctada fucata*.<sup>10, 24-26</sup> **Figure 3.1c** shows the highly ordered layer structure of the nacreous inner layer of blue mussel shells. The layers of crystals can be seen, where plates of aragonite are arranged when stacked on top of each other. This arrangement is known to contribute to the enhanced strength of nacre.

As IR data suggested that some of the calcite had converted to aragonite upon heating, powder XRD (**Figure B3**) was used to confirm the increased presence of aragonite in the heated samples. A semi-quantitative phase composition analysis revealed the ratio of calcite:aragonite was 75:25 and 65:35 for untreated shells and shells heated at 200 °C for

48 h, respectively. The uncertainty of this method is +/- 5%. In general, as the drying temperature of the shells is increased, the amount of aragonite present increased. The ratios of calcite:aragonite can be of importance in some systems due to their difference in dissolution rate. For example, this discovery can lead to improvements where mollusc shells have been used in the area of soil amendment and waste water treatment where several  $M^{2+}$  cations are known to preferentially bind to aragonite over calcite and vice versa.<sup>6</sup>

Based on the initial results from heat treatment, heating the mussel shells at 220 °C (the maximum temperature of the oven) was investigated to see if there was any further increase in the amount of aragonite. Higher resolution IR spectra of these shells were very similar to shells treated at 200 °C (**Figure 3.1b** and Appendix B, **Figure B4**) with a more prominent  $\nu_4$  band at  $700\text{ cm}^{-1}$ . However, a very distinct physical change in the shells after heating at 220 °C for 48 h was observed; the inner shell and outer shell cleanly separated without any crushing, **Figure 3.2a**. This facile separation of  $\text{CaCO}_3$  polymorphs from a single shell has not been reported previously and is due to the significant reduction in organic matrix levels upon heating the shells. IR spectra of the outer and inner layer of the blue mussel shells, **Figure B4**, match with literature spectra of calcite and aragonite, respectively.<sup>20, 23, 27</sup> As other mollusc species are more widely harvested and eaten in other locations throughout the world, shells from eastern oysters, *Crassostrea virginica*, were heated at 220 °C for 48 h to see if a similar separation effect would occur. No shell separation occurred, and the oyster shells consisted only of calcite after heating at this temperature (**Figure B5**).

Powder XRD of the whole mussel shell dried at 220 °C for 48 h has a larger proportion of aragonite 45 wt% **Figure 3.1b**, i.e. a 10% increase upon increasing the drying temperature by 20 °C (**Figure B3**). The separated outer and inner shell were also subject to powder XRD as shown in **Figure 3.2b**, confirming the outer shell is indeed calcite and the inner shell aragonite with < 5 wt% of the other polymorph present. It is common for molluscs with both aragonite and calcite present to have an interlayer zone called the myostracum. SEM was used to study the cross section of the shell before and after heat treatment (**Figure B6**). A layer of myostracum which contains aragonite only<sup>28</sup>, can be seen on the micrograph of the outer layer, confirming small amounts of aragonite that are detected in the diffractogram of the outer prismatic layer. There was no identifiable prismatic calcite on the inner nacreous layer.

Solid-state <sup>1</sup>H NMR spectroscopy was used to investigate if any of the organic matrix, between the crystals of calcite and aragonite in the prismatic and nacreous layers was retained when the shell separated into two halves (**Figure 3.2** and **Table 3.1**). Comparison with shells not subjected to heat treatment was made. <sup>1</sup>H NMR experiments were performed at 20 kHz MAS on untreated mussel shells, whole shells after heat treatment, and the resulting inner and outer layers (**Figure 3.2c**). For the untreated mussel shells (**Figure B7**), resonances characteristic of the organic matrix overlap with the main broad resonance from -2 to 14 ppm. Each spectrum contains a resonance for water at chemical shifts ranging from 4.5-5.1 ppm. For the heat-treated whole shells and the calcite layer, the water resonance resulted from two distinct water environments. However, because the samples were spinning rapidly, spinning side bands were not observed so water resonances cannot be

identified based on if it is water on the surface of the material or if it can be assigned to co-crystallized water within the sample. Surprisingly, a resonance for the CH<sub>3</sub> protons of chitin or protein matrices as reported by others<sup>29, 30</sup> was not observed. The signal at 1.0-1.5 ppm in our spectra is from the rotor (**Figures B7 and B8**).

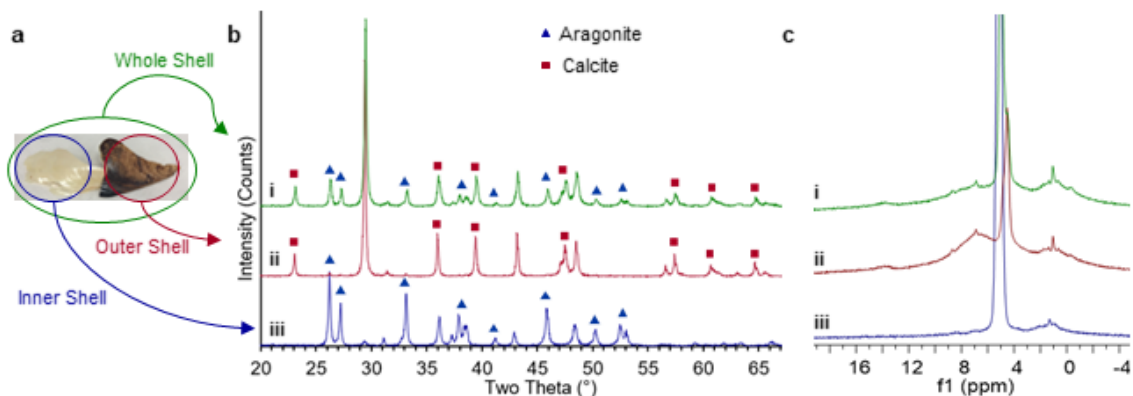


**Figure 3.2** a) Appearance of blue mussels after drying at 220 °C for 48 h. b) Powder XRD diffractograms for i) whole mussel shells treated at 220 °C for 48 h and the resulting ii) outer and iii) inner layer shell of the mussel. c) Normalized 600 MHz <sup>1</sup>H NMR spectra (20 kHz, relaxation delay 2 s, 16 scans) of i) whole mussel shells treated at 220 °C and the resulting ii) outer and iii) inner shell layer. Intensities of the signals are increased from the original spectra to show the peak at 13.8 ppm.

**Table 3.1** Summary of <sup>1</sup>H NMR data for nacreous molluscs

Mollusc Type	CaCO <sub>3</sub> Polymorphs	Heat Treatment	Water, δ ppm	HCO <sub>3</sub> <sup>-</sup> , δ ppm	Organic Matrix, δ ppm	Ref.
Mytilus edulis	Calcite & Nacre	None	4.8	None	6.9, 8.7	Our work
	Calcite & Nacre	220 °C, 48 h	4.5, 5.0	13.8	6.9, 8.7	
	Calcite	220 °C, 48 h	4.5, 4.8	13.8	6.9, 8.7	
	Nacre	220 °C, 48 h	5.1	None		
Perna canaliculus <sup>a</sup>	Calcite & Nacre	None	~5	14.5	None Defined	30
	Calcite & Nacre	250 °C, overnight	~5	None	None Defined	
Haliotis laevigata <sup>b</sup>	Nacre	None	5.2	14.4	None Defined	31

<sup>a</sup>Shells were ground to a fine powder before heat treatment <sup>b</sup>Nacre separated from the prismatic layer by sand blasting.

Two additional resonances at 6.9 and 8.7 ppm are observed that have not been reported by others to date. Previous reports of <sup>1</sup>H MAS NMR spectra of *Perna canaliculus* and *Haliotis laevigata* shells are similar to those presented in **Figure 3.2c** but without these two defined peaks overlapping with the broad signal. This is due to larger particle sizes of the crystalline material within our samples, which were obtained through gentle processing methods including enzymatic cleaning and grinding of the shells using a mortar and pestle. This hypothesis was confirmed, as when the shells were ground to a fine powder the resolution of <sup>1</sup>H NMR spectra diminished significantly and the sharp resonances at 6.9 and 8.7 ppm vanished. This is likely linked to a decrease in crystallinity as amorphous samples such as amorphous calcium carbonate have much broader resonances. Based on the polysaccharides and protein that make up the organic matrix of nacre, the signals at 6.9 and

8.7 ppm likely correspond to aromatic and amide protons respectively. Spectra of shells treated at 220 °C (**Figure 3.2c**) have the same line shape as those for shells without heat treatment but with a more intense water peak relative to the overlapping resonances from the organic matrix and an additional small broad resonance at 13.8 ppm. The decrease in intensity of the resonances from the organic matrix agrees with a decrease in combustible mass (i.e. organic content of the shells) determined by TGA.  $^1\text{H}$  NMR resonances of our work and others who have studied nacreous mollusc are summarized in **Table 3.1**. Jager *et al.* previously observed a resonance at 13.8 ppm in spectra of mollusc shells and assigned this to acidic bicarbonate hydrogens that result from an amorphous surface layer about 10 nm thick that coat the aragonite tablets in nacre in *Haliotis laevigata*.<sup>29, 31</sup> This signal was also observed in untreated *Perna canaliculus* (New Zealand green-lipped mussel).<sup>30</sup>  $^1\text{H}$  NMR spectra of amorphous calcium carbonate (ACC) did not reveal any acidic bicarbonate protons.<sup>32</sup> However, due to the similarity of the chemical shift of these protons compared with those of  $\text{KHCO}_3$  and  $\text{NaHCO}_3$  it is believed that the resonances in this region of  $^1\text{H}$  NMR spectra result from small amounts of  $\text{Ca}(\text{HCO}_3)_2$ .<sup>29, 32</sup> In this study, it is worth noting that these bicarbonate protons do not appear in the spectra of shells that have not been heat treated. Therefore, the bicarbonate protons present in the spectra of heat-treated shells cannot be in contact with the organic matrix, as their intensity should have decreased upon heat treatment because the amount of matrix is shown to also decrease via TGA data.

Spectra were obtained for the two separated components of the shell in order to determine if bicarbonate resonances were present in both the calcite and aragonite portions. Signals from the organic matrix in the outer layer of the shell, **Figure 3.2c**, remain and are the same

as those for the whole shell treated at 220 °C, including the broad acidic peak of bicarbonate hydrogen at 13.8 ppm. Interestingly, virtually all resonances for the protons of the organic matrix have vanished in the  $^1\text{H}$  MAS NMR spectrum of the inner aragonite portion of the shell, **Figure 3.2c**. This is likely because the concentration of the matrix is below the detection limit of this method. This observation agrees with previous studies that suggest the intercrystalline organic content being higher for the prismatic calcite layer<sup>11</sup> than the nacreous layer<sup>33</sup> of molluscs. As the untreated blue mussel shell contains more organic matrix, and hence its spectra exhibit the most intense  $^1\text{H}$  NMR signals, we can say with confidence that the acidic bicarbonate protons at 13.8 ppm appear as a result of heat treatment because they are not observed in the spectra of the untreated shells.



**Figure 3.3** Digital images of a) crushed nacre isolated from the inner layer of blue mussel shells and b) small flakes of nacre as a result of gentle grinding of nacre with a mortar and pestle.

$^{13}\text{C}$  CP MAS NMR spectra of the untreated mussel shell (**Figure B9**) provided additional data on the organic matrix in the shell as many others have seen for various nacre containing shells.<sup>24, 29, 30, 34</sup> When identical experiments were performed on the separated inner nacreous part of the shell, no  $^{13}\text{C}$  resonances were observed (**Figure B9**).  $^{13}\text{C}$  DE MAS NMR spectra of the inner nacreous portion exhibited a carbonate resonance at 171 ppm and no other signals whereas,  $^{13}\text{C}$  DE MAS NMR of the outer calcite-rich portion of the shell contained a carbonate peak at 169 ppm and some resonances from the organic matrix that were also seen in spectra of the untreated shells (**Figure B10** and **B11**). The inner nacreous layer of the shell also breaks apart into smaller pieces of nacre with minor compression, **Figure 3.3a** or grinding in a mortar and pestle resulting in small flaked aragonite/nacre, **Figure 3.3b**. Even though the shell has undergone heat treatment, the inner layer remains iridescent which confirms the microstructure of the nacre is preserved. While it seems counter intuitive to degrade nacre into platelets when so much research is focused towards making it, it may be even more advantageous towards the development of sustainable nacre-inspired composites. Already having the inorganic building blocks (nacre platelets), one needs a compatible biopolymer matrix to form a new composite by evaporation-induced self-assembly lamination technique like that used by Gao *et al.*<sup>19</sup> Depending on the application of the composite, i.e. construction, armor, biomedical, etc., the biopolymer matrix can theoretically be tunable to suit the need.

Due to the lack of organic matrix that remains as a result of heating, the presence nor absence of bicarbonate protons in the inner nacreous layer of the mussel shell cannot be confirmed because the resonances for the bicarbonate protons are enhanced via cross-

polarization with those of the matrix when present. Although more insight might be gained through further experimentation, no further NMR studies were performed at this time because 1) exceedingly large numbers of scans would be needed due to the small quantities of material available coupled with the fact that our probe is only capable using of a 3.2 mm rotor, and 2) the goal to show there was a decrease in the amount of organic matrix because of heat treatment was met. The NMR data suggest that the facile separation of the shell into two parts upon heat treatment results from decomposition of the organic matrix in between the prismatic calcite particles.

TGA of the mussel shells agrees with our NMR data. The temperature range we selected to measure the mass loss from the organic matrix was 585-615 °C. Representative TGA curves (Appendix B, **Figures B12-15**) show there was a clear mass loss in this region for the untreated shells (0.82 wt%) whereas for the shells heated to 220 °C for 48 h the mass loss was less (0.42 wt%). In previous research, the organic matrix of *Pinctada maxima* shells showed high thermal stability and underwent decomposition between 550-600 °C.<sup>12</sup> However, for some other mollusc shells the decomposition of the organic matrix occurs at lower temperatures: before 400 °C (*Perna canaliculus*)<sup>35</sup> or from 230-450 °C (*Pinctada maxima*).<sup>36</sup> Additionally for cockle shells, TGA showed a significant mass loss when aragonite changed to calcite from 400-500 °C releasing moisture (and organic matrix).<sup>37</sup> While there is no doubt that some organic matrix has been lost at temperatures below 585 °C, due to the varying amounts of aragonite in our shells, the mass loss in blue mussel shells before 550 °C could not be measured with confidence due to moisture that would be released along with organic matrix during polymorph conversion, and so chose to study the

mass loss event from 585-615 °C as shown in our TGA curves. Once the heat-treated shells were separated into the two components, the 0.42 wt% loss seen for the whole shell could be broken down into 0.40 wt% for the outer (calcite-rich) part whereas the inner shell only lost 0.02 wt% from 585-615 °C. These data therefore provide further evidence to support the conclusions made from solid-state NMR studies.

The surface area and particle size of ground mollusc shells influence their intended application.<sup>6</sup> BET surface area was determined for shells without treatment and shells dried at 220 °C for 48 h. Shell powders were sieved using 125 µm, 75 µm and 45 µm sieves. The BET surface area for shells dried at 220 °C were on average slightly higher (6.4 m<sup>2</sup>/g) than the surface area of the shells with no heat treatment (6.1 m<sup>2</sup>/g). These BET surface areas are higher than others reported in literature for any species of mussel shell that has not undergone calcination.<sup>35, 38-40</sup> This may be due to the biocatalytic cleaning method used in our research<sup>4</sup> because the protease enzyme may be hydrolyzing the proteins that make up the organic matrix on the surface layers of the blue mussel shells.

Higher temperatures for heat treatment of mussel shells were investigated (450-850 °C, 2 h). IR spectra (**Figure B16**) show no bands from aragonite in any of these samples and only bands typical for calcite were observed. This is because aragonite is converted to calcite above 500 °C.<sup>41</sup> The surface structure of the shells after the heat treatments was studied using SEM. When shells were heated at 450 °C for 2 h, **Figure B17**, the outer edges of the aragonite plates that make up the inner layer of the shell degraded and are no longer 'touching'. There was no significant change in the appearance of the calcite crystals. Their morphology appears the same as those treated for 2 h at 220 °C. However, heating the shells

at temperatures of 550 °C or higher for 2 h greatly affects the shape and size of both the aragonite and calcite crystals. As shown in Appendix B, **Figure B 17c-d**, it appears the shells have become calcined. The polygonal shaped aragonite plates have vanished and appear porous, and the calcite prismatic crystals have deteriorated considerably with the edges of the crystals rounding. After heating at 650 °C for 2 h, the inner and outer layers of the shell are unrecognizable from what they were and now appear porous (**Figure B17e-f**).  $\text{CaCO}_3$  thermally degrades to  $\text{CaO}$  after 650°C. From IR spectra, **Figure B16**, the shells still contain some  $\text{CaCO}_3$  after heating at these temperatures for 2 h but the intensity of bands decreases significantly compared with samples heated to 550 °C.

### **3.2.1 Preliminary Studies Towards Synthetic Nacre Using Mussel-Derived Additives**

Synthetic nacre-like materials have previously been made using a complicated assembly and mineralization approach using a chitosan matrix with a predesigned laminated structure.<sup>37</sup>  $^1\text{H}$  and  $^{13}\text{C}$  CP MAS NMR of freeze-dried mussel meat (Appendix B, **Figure B18** and **B19**) have some similarities to untreated mussel shells i.e. the organic matrix present in shells. This led to pursuing the synthesis of nacre using protein hydrolysate from previous shell cleaning experiments,<sup>4</sup> as the amino acid residues necessary to stabilize the formation of calcite or aragonite may be present. Two methods were used; a diffusion method and direct mixing method, as described in the experimental section. Synthetic  $\text{CaCO}_3$  products were analyzed by IR spectroscopy because it was easy to identify the polymorphs present based on the characteristic frequencies of calcite, aragonite and vaterite.<sup>23</sup> While IR spectroscopy was satisfactory for determining whether aragonite was present, it could not reveal if nacre was formed i.e. the morphology of the particles. SEM

images ultimately determined if nacre was present. Mixing and diffusion methods were both unsuccessful at growing aragonite below room temperature, regardless of addition of protein hydrolysate or mussel shells for seeding. For the control experiments (performed without protein hydrolysate or mussel shells for seeding) carried out below room temperature, primarily calcite formed (**Figure B20a**). Diffusion experiments at 50 °C led to a mixture aragonite and calcite for control experiments. Vaterite formed when protein hydrolysate and/or mussel shells were added under the same conditions (**Figure B20b**). The direct mixing method was more successful. The IR spectra of CaCO<sub>3</sub> samples for control reactions, **Figure 3.4a**, shows all three polymorphs were present. The presence of vaterite is confirmed by the presence of the following bands:  $\nu_4$  at 746 cm<sup>-1</sup>,  $\nu_2$  at 871 cm<sup>-1</sup> and an additional band in the asymmetric C-O stretch region,  $\nu_3$  at 1435 cm<sup>-1</sup>.<sup>23</sup> In another experiment, the presence of protein hydrolysate was shown to inhibit the formation of vaterite, and so only calcite and aragonite were formed, **Figure 3.4a-ii**. Aragonite was the primary polymorph formed at high temperatures when mussel shells were used for seeding in the absence of protein hydrolysate (**Figure B20c**), however, nacre was not formed.

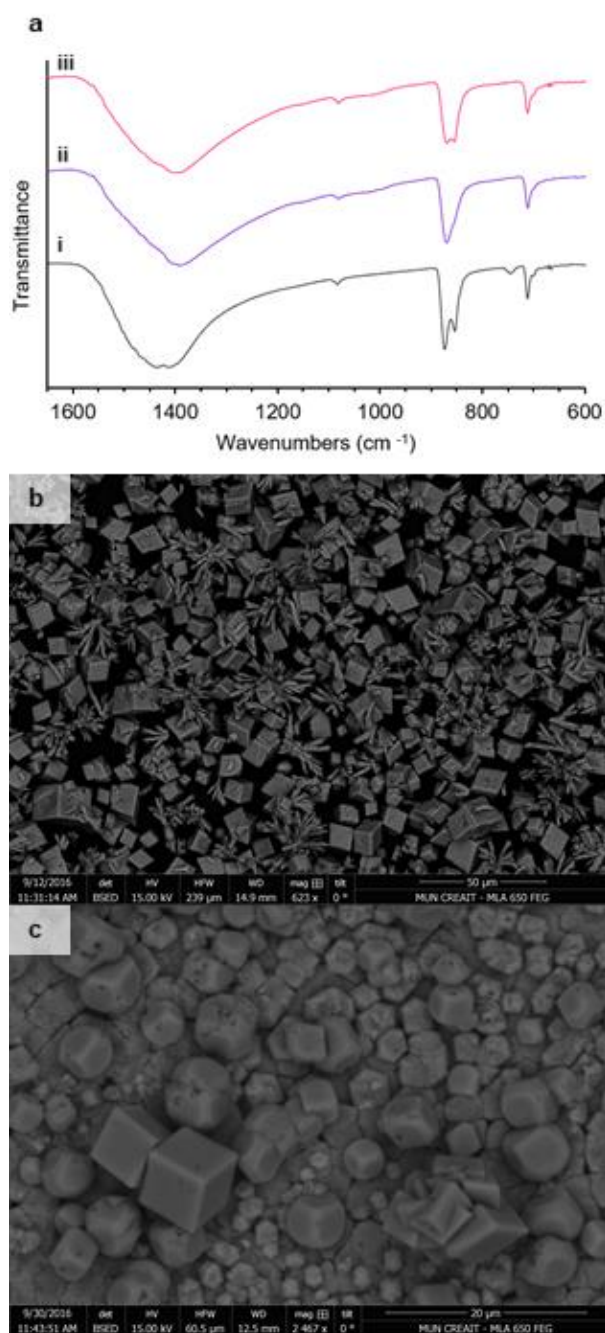


**Figure 3.4** a) IR spectra of synthetic CaCO<sub>3</sub> products from the direct mixing method using reaction conditions i) 0.8 M CaCl<sub>2</sub> and Na<sub>2</sub>CO<sub>3</sub> ii) 0.8 M CaCl<sub>2</sub> and Na<sub>2</sub>CO<sub>3</sub> with the addition of mussel protein hydrolysate and iii) 0.8 M CaCl<sub>2</sub> and Na<sub>2</sub>CO<sub>3</sub> with the addition of mussel protein hydrolysate and mussel shells for seeding nacre. b) SEM micrographs (back-scatter detector) of i) product from 0.8 M CaCl<sub>2</sub> and Na<sub>2</sub>CO<sub>3</sub> with the addition of mussel protein hydrolysate and mussel shells for seeding and ii) the shell surface after the reaction of i).

The most promising results towards the synthesis of nacre were achieved using the direct mixing method (2.5 h and 50 °C) as shown in **Figure 3.4**, where protein hydrolysate and mussel shells for seeding were both employed. In the IR spectra, there was an increase in the intensities of stretches corresponding to aragonite and no vaterite was observed. These results from IR spectroscopy were confirmed using powder XRD (**Figure B21**) and a semi-quantitative analysis confirmed there was indeed more aragonite when mussel shells were used for seeding. The amount of aragonite increased by 5 wt%. The resulting crystalline solid, displaced from the surface of the seed shell particles, showed no sign of nacre using SEM, **Figure 3.4b**. However, close examination of the shells used to seed the nacre growth show new platelets of nacre have grown along with large crystals of calcite, **Figure 3.4c**. The new growth of nacre can be seen on top of a nacreous portion of the shell. The synthetic nacre crystals are much smaller than the natural nacre crystals present in the original shell seeds used and are 1-5  $\mu\text{m}$  in diameter. These preliminary experiments show the use of mussel protein and mussel shell for ‘seeding’ are successful for growing nacre and inhibiting the growth of vaterite.

### **3.3 Conclusions**

For continued growth, aquaculture must be supported and developed in a sustainable and economical manner. The heat treatment of waste blue mussel shells can yield a variety of  $\text{CaCO}_3$  materials with differing ratios of calcite and aragonite. Powder XRD revealed untreated blue mussel shells have 25 wt% aragonite and heating the shells at 220 °C for 48 h increased the amount of aragonite by 20 wt%.  $^1\text{H}$  NMR data showed a decrease in the organic matrix content after heat treatment. This can be valuable for applications where

purity is a concern. Additionally, the outer prismatic calcite layer was liberated from the inner nacreous layer with ease. The nacre from the shell has the potential to be used as the inorganic building blocks in synthetic nacre-inspired materials that are strong and sustainable. After heating, organic matrix was present primarily in the prismatic calcite layer whereas in the nacreous layer it was undetectable by NMR with only about 0.02 wt% remaining by TGA. The removal of the organic matrix increases the purity of the iridescent aragonite and makes it less susceptible to allergic reactions if it were to be used as a more ethical and sustainable source of shimmer, in cosmetics for example. As an example of this, nacre was dyed with food dyes and incorporated it into a colourless builder gel used in nail salons. This makes for coloured nail enhancements with a natural shimmer from the nacre (Appendix B, **Figure B22**). In terms of materials chemistry, the inner nacreous layer of shell isolated must now be studied to determine how the partial removal of the organic matrix has affected the mechanical properties of the nacre and whether it is suitable for applications where nacre is employed, as well as what applications can be developed for this mother of pearl powder.

Inspired by the similarities of the organic matrix to mussel meat via NMR spectroscopy, the synthesis of nacre was carried out using protein hydrolysate from the enzymatic hydrolysis of mussel meat. This is an example of a use of waste mussel protein to produce a higher value material. As previously demonstrated, the use of freeze-dried mussel protein hydrolysate as a fish feed.<sup>4</sup> By sequentially adding in the protein hydrolysate to reaction mixtures of  $\text{Na}_2\text{CO}_3$  and  $\text{CaCl}_2$ , there was control over  $\text{CaCO}_3$  polymorph formation. Synthetic nacre was synthesized when protein hydrolysate and small pieces of mussel shells

were used for seeding. However, seeding poses challenges e.g. the synthetic nacre is difficult to collect from the shell surface. The isolation and analysis of the bulk properties of the synthetic nacre-like material synthesized is ongoing.

### **3.4 Experimental**

#### **3.4.1 Materials**

Waste mussels were provided by a local mussel processing plant, Green Seafoods Ltd., through collaboration with the Newfoundland Aquaculture Industry Association (NAIA). Shells were cleaned, removing any organic material, using industrially available food grade protease enzymes as previously described in **Chapter 2**.<sup>4</sup>

#### **3.4.2 Instrumentation**

Cleaned mussel shells were dried at 120, 160, 200 and 220 °C for 48 h for most studies. Selected samples were heated to 450-850 °C in a tube furnace under air. Samples that required a powdered form for analysis were ground using a stainless-steel mixer mill in a 65 mL stainless steel vial with two quarter inch stainless steel balls for 12 min. Infrared (IR) spectroscopy was performed using a Bruker Alpha FTIR spectrometer fitted with a single bounce diamond ATR accessory. Initial IR spectra were collected with a resolution of 4 cm<sup>-1</sup>. Subsequently, we increased the resolution to 2 cm<sup>-1</sup> for all samples that were heated above 200 °C to better distinguish the polymorphs present. All measurements were conducted in triplicates, averaged and plotted in Excel. Inductively coupled plasma mass spectrometry (ICP-MS) data were obtained using an ELAN DRC II ICPMS via an acid dissolution method using TraceMetal™ Grade HNO<sub>3</sub> (Fisher) and H<sub>2</sub>O<sub>2</sub>. Solid-state NMR

spectra were obtained at 298 K using a Bruker Avance II 600 spectrometer, equipped with a SB Bruker 3.2 mm MAS triple-tuned probe operating at 600.33 MHz for  $^1\text{H}$  and 150.97 MHz for  $^{13}\text{C}$  nuclei. Chemical shifts were referenced to tetramethylsilane (TMS) using adamantane as an intermediate standard for  $^{13}\text{C}$ . The samples were spun at 20 kHz in 3.2 mm zirconia rotors. Cross-polarization (CPMAS) spectra were collected with a Hartmann-Hahn match at 62.5 kHz and 100 kHz  $^1\text{H}$  decoupling, a contact time of 1 ms, a recycle delay of 1 s and 16k scans. Thermogravimetric analysis (TGA) was carried out using a TA Instruments Q500 TGA under high resolution dynamic mode. Samples were heated at a rate of  $5.0\text{ }^\circ\text{C min}^{-1}$  under a  $\text{N}_2$  atmosphere ( $50\text{ mL min}^{-1}$ ) from 25-800  $^\circ\text{C}$ . Scanning electron microscopy (SEM) images of large pieces of carbon coated shell were obtained using a FEI MLA 650 FEG under high vacuum ( $10^{-6}$  torr). The voltage of 15 kV and current of 10 mA at a working distance of 12.5-15 mm produced a 5.8 spot. An SDD was used for BSED. Powder X-ray diffraction (XRD) was performed using a Rigaku Ultima IV XRD equipped with  $\text{Cu K}\alpha$  radiation ( $\lambda=1.5406\text{ \AA}$ ) at 40 kV and 44 mA. The  $2\theta$  region was scanned from 0-100 $^\circ$  with a step size of 0.02 $^\circ$ . MDI JADE 2010 software was used to fit the XRD spectra using the whole fitting pattern approach as well as the semi-quantitative analysis of the polymorphs in the shell samples. Brunauer-Emmett-Teller (BET) surface area measurements were carried out using a TriStar II PLUS surface area analyzer from Micromeritics using  $\text{N}_2$  after degassing samples at 100  $^\circ\text{C}$  for 3 h.

### **3.4.3 Synthetic Nacre**

Synthetic  $\text{CaCO}_3$  was prepared by two methods; direct mixing and diffusion. In both cases, 0.8 M solutions of  $\text{CaCl}_2$  and  $\text{Na}_2\text{CO}_3$  were used. For the direct mixing method, 25 mL of

solution were heated or cooled to the reaction temperature before quickly being mixed together. In the instances where protein hydrolysate was used 25 mL of blue mussel protein hydrolysate, resulting from the enzymatic hydrolysis of 20 g of whole raw mussels (shell on) in 50 mL of distilled water,<sup>4</sup> was mixed with 25 mL of Na<sub>2</sub>CO<sub>3</sub> solution and heated or cooled to the desired temperature before being added to 25 mL of CaCl<sub>2</sub>. For seeding, small pieces of crushed, untreated mussel shell were used to seed CaCO<sub>3</sub> growth. For the diffusion method, 5 g of (NH<sub>4</sub>)<sub>2</sub>CO<sub>3</sub> was weighed into a petri dish and placed at the bottom of a desiccator. A petri dish containing 0.1 M CaCl<sub>2</sub> was placed in the desiccator, above the (NH<sub>4</sub>)<sub>2</sub>CO<sub>3</sub>. When protein hydrolysate or mussel shells were used, they were mixed with the CaCl<sub>2</sub> solution. At the end of the experiment, the precipitate and/or shells were suction filtered and washed with deionized water and ethanol.

#### **3.4.4 Nail Enhancements**

Cosmetic nail enhancements were prepared using a colourless builder gel (mixture of acrylates and photoinitiator) from Sally Beauty and Wilton food dyes were used to add colour.

#### **3.5 References**

1. World Population Prospects: *The 2017 Revision, Key Findings and Advance Tables*, P. D. Department of Economic and Social Affairs Report Working Paper No. ESA/P/WP/248, 2017.
2. D. Tilman and M. Clark, *Nature*, 2014, **515**, 518-522.

3. R. R. Gentry, S. D. Gaines, B. S. Halpern, H. E. Froehlich, B. S. Halpern, D. Grimm, P. Kareiva, M. Parke, M. Rust and B. S. Halpern, *Nat. Ecol. Evol.*, 2017, **1**, 1317-1324.
4. J. N. Murphy, K. Hawboldt and F. M. Kerton, *Green Chem.*, 2018, **20**, 2913-2920.
5. J. P. Morris, T. Backeljau and G. Chapelle, *Rev. Aquacult.*, 2018, **11**, 42-57.
6. J. N. Murphy, F. M. Kerton and in *Fuels, Chemicals and Materials from the Oceans and Aquatic Sources* eds. F. M. Kerton and N. Yan, Wiley, 2017, ch. Characterization and utilization of waste streams from mollusc aquaculture and fishing industries, pp. 189-225.
7. USGS, Mineral Commodity Summaries, January 2016 - Stone (Crushed).  
<https://minerals.usgs.gov/minerals/pubs/mcs/2016/mcs2016.pdf>, (accessed Jan 25 2019).
8. A. P. Jackson, J. F. V. Vincent and R. M. Turner, *Proc. R. Soc. Lond., B, Biol. Sci.*, 1988, **234**, 415-440.
9. F. Nudelman, *Semin. Cell Dev. Biol.*, 2015, **46**, 2-10.
10. S. Weiner and L. Addadi, *J. Mater. Chem.*, 1997, **7**, 689-702.
11. F. Nudelman, H. H. Chen, H. A. Goldberg, S. Weiner and L. Addadi, *Faraday Discuss.*, 2007, **136**, 9-25.
12. E. M. Gerhard, W. Wang, C. Li, J. Guo, I. T. Ozbolat, K. M. Rahn, A. D. Armstrong, J. Xia, G. Qian and J. Yang, *Acta Biomater.*, 2017, **54**, 21-34.
13. J. Bai, *Advanced Fibre-Reinforced Polymer (FRP) Composites for Structural Applications*. Elsevier Science & Technology, Cambridge, United Kingdom, 2013.

14. S. Dashkovskiy, B. Suhr, K. Tushtev and G. Grathwohl, *Comput. Mater. Sci.*, 2007, **41**, 96-106.
15. V. J. Laraia and A. H. Heuer, *MRS Proceedings*, 1989, **174**, 125.
16. X.-X. Wang, L. Xie and R. Wang, *Biomaterials*, 2005, **26**, 6229-6232.
17. H.-B. Yao, J. Ge, L.-B. Mao, Y.-X. Yan and S.-H. Yu, *Adv. Mater.*, 2014, **26**, 163-188.
18. L.-B. Mao, H.-L. Gao, H.-B. Yao, L. Liu, H. Cölfen, G. Liu, S.-M. Chen, S.-K. Li, Y.-X. Yan, Y.-Y. Liu and S.-H. Yu, *Science*, 2016, **354**, 107-110.
19. H.-L. Gao, S.-M. Chen, L.-B. Mao, Z.-Q. Song, H.-B. Yao, H. Cölfen, X.-S. Luo, F. Zhang, Z. Pan, Y.-F. Meng, Y. Ni and S.-H. Yu, *Nat. Commun.*, 2017, **8**, 287.
20. C. E. Weir and E. R. Lippincott, *J. Re. Nat. Stand. Sec. A*, 1961, **65A**, 173-183.
21. R. S. Halford, *J. Chem. Phys.*, 1946, **14**, 8-15.
22. N. Vagenas, *Talanta*, 2003, **59**, 831-836.
23. F. A. Anderson and L. Brečević, *Acta Chem. Scand.*, 1991, **45**, 1018-1024.
24. K. Takahashi, H. Yamamoto, A. Onoda, M. Doi, T. Inaba, M. Chiba, A. Kobayashi, T. Taguchi, T. A. Okamura and N. Ueyama, *ChemComm*, 2004, DOI: 10.1039/b315478e, 996-997.
25. B. Pokroy, A. N. Fitch and E. Zolotoyabko, *Cryst. Growth Des.*, 2007, **7**, 1580-1583.
26. X. Li, W.-C. Chang, Y. J. Chao, R. Wang and M. Chang, *Nano Lett.*, 2004, **4**, 613-617.
27. A. G. Xyla and P. G. Koutsoukos, *J. Chem. Soc., Faraday Trans. 1*, 1989, **85**, 3165-3172.

28. H. A. Lowenstam and S. Weiner, *On biomineralization*, Oxford University Press, 1989.
29. C. Jäger and H. Cölfen, *CrystEngComm*, 2007, **9**, 1237-1244.
30. I. Ben Shir, S. Kababya, I. Katz, B. Pokroy and A. Schmidt, *Chem. Mater.*, 2013, **25**, 4595-4602.
31. N. Nassif, N. Pinna, N. Gehrke, M. Antonietti, C. Jager and H. Colfen, *Proc. Natl. Acad. Sci. U.S A.*, 2005, **102**, 12653-12655.
32. H. Nebel, M. Neumann, C. Mayer and M. Epple, *Inorg. Chem.*, 2008, **47**, 7874-7879.
33. F. Nudelman, E. Shimoni, E. Klein, M. Rousseau, X. Bourrat, E. Lopez, L. Addadi and S. Weiner, *J. Struct. Biol.*, 2008, **162**, 290-300.
34. T. Asakura, M. Hamada, S.-W. Ha and D. P. Knight, *Biomacromolecules*, 2006, **7**, 1996-2002.
35. M. I. Jones, L. Y. Wang, A. Abeynaïke and D. A. Patterson, *Adv. App. Ceram.*, 2011, **110**, 280-286.
36. X. Bourrat, L. Francke, E. Lopez, M. Rousseau, P. Stempfle, M. Angellier and P. Alberic, *CrystEngComm*, 2007, **9**, 1205-1208.
37. J. Haslinda Shariffuddin, W. Chee Yean and S. Shariah Ghazali, *Materials Today: Proceedings*, 2018, **5**, 21718-21727.
38. C. Rombaldi, J. L. de Oliveira Arias, G. I. Hertzog, S. S. Caldas, J. P. Vieira and E. G. Primel, *Anal. Bioanal. Chem.*, 2015, **407**, 4805-4814.
39. P. Cubillas, S. Köhler, M. Prieto, C. Chairat and E. H. Oelkers, *Chem. Geol.*, 2005, **216**, 59-77.

40. K. Tekin, *Energy Fuels*, 2015, **29**, 4382-4392.
41. A. Abeynaike, L. Wang, M. I. Jones and D. A. Patterson, *Asia-Pac. J. Chem. Eng.*, 2011, **6**, 231-243.

## **Chapter 4 The synthesis of calcium acetate from raw and heat-treated blue mussel shell and its use as a de-icer**

**See Appendix C for additional data.**

A version of this chapter will be submitted for publication.

Jennifer N. Murphy, Kelly Hawboldt\* and Francesca M. Kerton\*

### **4.1 Introduction**

Mussel shells are a valuable source of  $\text{CaCO}_3$  (> 95%) and as such have been valorized in many areas where  $\text{CaCO}_3$  is used.<sup>1-3</sup> One area that mollusc shells have been underutilized is as a starting material for synthesis. This may be due to purity issues, as molluscs contain organic matter including silk fibroin-like proteins, acidic glycoproteins and  $\beta$ -chitin. Furthermore, studies have shown that there are also small amounts of other minerals present that leads to the presence of the following metals Pb, Hg, Cr, Mg and Fe.<sup>4, 5</sup> Barro *et al.* developed a plant in Spain to make high purity  $\text{CaCO}_3$  (> 95%) by calcining mussel shells up to 600 °C.<sup>6</sup> The resulting  $\text{CaCO}_3$  contained  $\text{MgCO}_3$  and organic carbon remained as the largest contaminants.

Calcium acetate ( $\text{Ca}(\text{CH}_3\text{COO})_2$ ) can be made by reacting  $\text{CaCO}_3$  or  $\text{CaO}$  with acetic acid ( $\text{CH}_3\text{COOH}$ ).  $\text{Ca}(\text{CH}_3\text{COO})_2$  can be used medicinally to treat high levels of phosphate in dialysis patients.<sup>7</sup>  $\text{Ca}(\text{CH}_3\text{COO})_2$  can also be used in the preparation of hydroxyapatite,<sup>8</sup>

which is used for biomedical applications such as bone and coatings of metal implants, and is an approved food additive in Canada.<sup>9</sup>

$\text{Ca}(\text{CH}_3\text{COO})_2$  can be used as an environmentally friendly de-icer in place of NaCl, however, it is currently not a commercial de-icer. A de-icer is a chemical, mainly salts, that are effective at removing ice or snow and preventing the formation of ice by reducing the freezing point of water.<sup>10</sup> In Canada and much of North America, the use of de-icing agents is critical to keep roadways safe and open during the winter months. The use of road salts minimizes traffic accidents, injuries and deaths during ice and snow conditions.<sup>11</sup> Road salt (mainly NaCl) has been used as a de-icing agent in Canada since the 1940s.<sup>12</sup> On average, 5 million tonnes of road salt are used each winter to keep roadways across the country safe. There are several concerns with the use of road salt regarding the environment, infrastructure, and human health. The use of road salts is linked to the salinization of fresh water and corrosion.<sup>13</sup>

NaCl is corrosive and non-degradable. Layers of differing densities can exist in lakes due to high salt concentrations and causes depletion of oxygen in deeper regions of lakes due to incomplete seasonal mixing. This improper mixing leads to the inability of the lake to distribute valuable nutrients to the lake as well and may lead to ecosystem changes. Prolonged chloride concentrations in excess of 250 mg/L is detrimental to aquatic life.<sup>14</sup> Increase in sodium concentrations increases the growth of blue-green algae which makes freshwater sources prone to algal blooms.

Acetate-based de-icers, such as biodegradable and non-corrosive calcium magnesium acetate ( $\text{CaMg}_2(\text{CH}_3\text{COO})_6$ ), can also affect the environment. The biodegradation of the

acetate ion causes a depletion of oxygen which can cause plant death. The harmful effects of any type of road salt are mainly observed in slow moving waterways where dilution is slow.<sup>15</sup> Acetate based de-icers also affect the integrity of concrete<sup>16</sup> but not to the same degree as chloride based de-icers.<sup>10</sup>

$\text{CaMg}_2(\text{CH}_3\text{COO})_6$  is 30 times the cost of rock salt and made from the reaction of dolomite ( $\text{CaCO}_3$  with at least 5%  $\text{MgCO}_3$ ) with  $\text{CH}_3\text{COOH}$ .<sup>17</sup> As a result,  $\text{CaMg}_2(\text{CH}_3\text{COO})_6$  is less commonly used on highways and its use is limited to environmentally sensitive regions including bridges.<sup>18</sup> However, the use of renewable feedstocks, such as by-products from the food industry, can make acetate-based de-icers cheaper. De-icers have been made from renewable sources of organic and inorganic materials.  $\text{CaMg}_2(\text{CH}_3\text{COO})_6$  and calcium magnesium propionate have been prepared via fermentation,<sup>18</sup>  $\text{Ca}(\text{CH}_3\text{COO})_2$  has been made using bamboo vinegar,<sup>19</sup> and a variety of de-icers have been made using degradation products from corn steep water.<sup>20</sup> These show organic materials can be sourced from fermentation of biomass and does not need to be sourced from oil resources.  $\text{Ca}(\text{CH}_3\text{COO})_2$  has previously been prepared using mollusc shells.<sup>21-24</sup>  $\text{Ca}(\text{CH}_3\text{COO})_2$  has been prepared using waste oyster shells and food-grade applications were targeted,<sup>23, 24</sup> and other researchers have targeted de-icing applications using waste oysters or clam shell powder.<sup>21</sup><sup>22</sup> There was a language barrier in understanding some of the literature; a patent from South Korea was translated from English but was still difficult to understand<sup>22</sup>, and the work of Lee *et al.* was mainly in Korean except for the abstract and tables of data.<sup>24</sup>

The objective of the research presented in this chapter was the synthesis of  $\text{Ca}(\text{CH}_3\text{COO})_2$  from waste blue mussel (BM) shells and to use this material as a de-icing agent.

$\text{Ca}(\text{CH}_3\text{COO})_2$  is currently not on the market as an anti-ice or de-icing agent. Few studies have been performed on calcium acetate as a de-icer,<sup>19</sup> but it has been reported that  $\text{Ca}(\text{CH}_3\text{COO})_2$  has a lower freezing point than NaCl (based on same molarity solutions), is an effective de-icer and is less corrosive than NaCl.<sup>19</sup> The use of mussel shells in the preparation of a bio-degradable road salt has the potential to change the outlook on NaCl use in rural communities where mussel processing occurs. Design of experiments (DoE) methodology is used herein to investigate three factors believed to be most influential to a green synthesis of calcium acetate using waste BM shells and to optimize the yield of  $\text{Ca}(\text{CH}_3\text{COO})_2$ . The  $\text{Ca}(\text{CH}_3\text{COO})_2$  products are characterized and experiments to test its de-icing capability are also presented.

## 4.2 Results

### 4.2.1 Ground Mussel Shell Contamination

Typically, when molluscs have been employed as catalysts, adsorbents, or amendments, they have been ground into a fine powder.<sup>3</sup> The use of ground mussel shells was tested for the synthesis of  $\text{Ca}(\text{CH}_3\text{COO})_2$ . Shells ground in the stainless-steel mixer mill had visible iron contamination. For example, the resultant mixture of mussel shells and acetic acid was black (**Figure 4.1a**), and even after filtering the  $\text{Ca}(\text{CH}_3\text{COO})_2$  solution was strongly coloured (**Figure 4.1b**), and iron filings were found on the stir bar after the reaction. Contamination from milling equipment is related to the materials the mill is made out of and its hardness.<sup>25</sup> Unfortunately, the agate and ceramic vials and balls for use in the mixer-mill within the Kerton group have restrictions that inhibit the use of materials greater than

5 mm in length and have limitations for hard materials. The agate vessel was used twice, using soft inner shell material, but this led to the vessel being damaged. Therefore, the synthesis of  $\text{Ca}(\text{CH}_3\text{COO})_2$  in this chapter was performed using manually crushed shells.

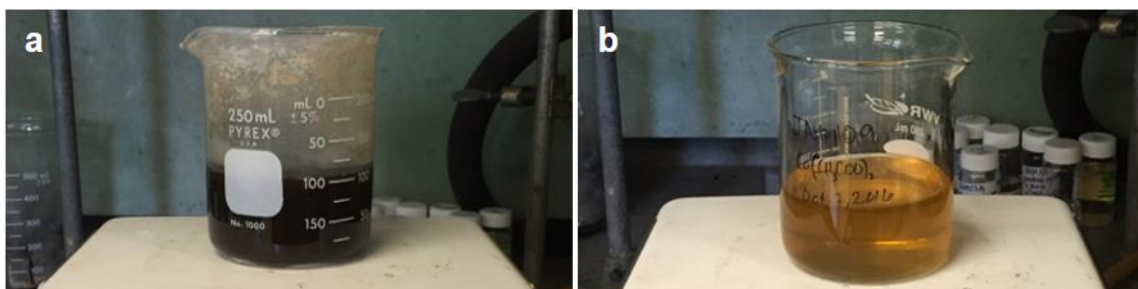


**Figure 4.1** Digital images of (a) the synthesis of  $\text{Ca}(\text{CH}_3\text{COO})_2$  using mussel shells that were ground in a stainless steel vial and (b) the resulting  $\text{Ca}(\text{CH}_3\text{COO})_2$  product after filtering.

#### 4.2.2 Exploratory Experimental Design for the Synthesis of Calcium Acetate

An introduction to Design of Experiments was described in **Chapter 1**. First a central composite circumscribed (CCC) design was used to investigate the effect of time, concentration of  $\text{CH}_3\text{COOH}$  ( $[\text{CH}_3\text{COOH}]$ ), and shell type on the yield of calcium acetate with the goal of maximizing the yield. **Table 4.1** shows the factors studied and their respective levels.

To study the effect of time, the gap between the levels was made large so any effect could be seen more clearly. The low level (-1), was 6 h and 24 h was used for the high level (+1). The axial points were 2.3 h ( $-\alpha$ ) and 27.7 h ( $+\alpha$ ), respectively. These levels were chosen because they were convenient for timing purposes. The high and low levels for  $[\text{CH}_3\text{COOH}]$  were chosen after reading related literature and patents, and based on the

requirement for sufficient solution levels to cover the shells in the flask. For [CH<sub>3</sub>COOH], the low level (-1) was 5% CH<sub>3</sub>COOH and the high level (+1) was 15% CH<sub>3</sub>COOH. The axial points were 2.9% CH<sub>3</sub>COOH (- $\alpha$ ) and 17.1% CH<sub>3</sub>COOH (+ $\alpha$ ), respectively. The molar concentrations of these solutions are 0.53, 0.88, 1.8, 2.6 and 3.0 mol/L, respectively. Molar [CH<sub>3</sub>COOH] observed in literature range from 0.5-10 mol/L.<sup>6, 21, 24</sup>

The effect of shell type was a categorical factor, unlike time and [CH<sub>3</sub>COOH] which are numerical and can be changed easily. Three shell types were studied; untreated shells, shells heated at 220 °C for 48 h, and calcined shells. These are denoted as RTC, HTC, and CC, respectively and stand for high temperature crushed, room temperature crushed and calcined crushed as they were broken up into small pieces of less than 2 cm. The HTC shells should afford higher yields because of its higher purity (i.e. less organic matrix) but RTC shells were explored as well because of potential environmental benefits (i.e. lower energy considerations) of using RTC shells as a source of CaCO<sub>3</sub>. The calcined shells were used to compare the reactivity of a CaO starting material (CC) with the two CaCO<sub>3</sub> starting materials (RTC and HTC). Volumes of CH<sub>3</sub>COOH were calculated based on the moles required to react with masses of shells assuming shells to be 100% CaCO<sub>3</sub> (or CaO in the case of CC).

**Table 4.1** Exploratory central composite circumscribed design factors and levels for the synthesis of calcium acetate from mussel shell materials.

Name	Factor	- $\alpha$	-1	0	+1	+ $\alpha$
A	% CH <sub>3</sub> COOH	2.9	5	10	15	17.1
B	Time (h)	2.3	6	15	24	27.7
C	Shell Type	-	RTC	HTC	CC	-

The yields for the 33 experiments of this design are found in **Appendix C**. Analysis of variance revealed all factors were significant in this exploratory design. There was an interaction between shell type and acetic acid and the square of acetic acid was significant as well, giving the model a quadratic shape. The analysis of variance and plots of the residuals are also found in **Appendix C**. Since this model was only used for exploratory experiments the model was not used for prediction, but it was used to develop another experimental design to optimize yield further for RTC and HTC shells.

For these exploratory experiments, the empirical models for the response (yield) in terms of the factors studied (time, % CH<sub>3</sub>COOH, and shell type) are plotted in three-dimensional diagrams (**Figure 4.2**, **Figure 4.3**, and **Figure 4.4**). **Figure 4.2** shows the model for the yield of Ca(CH<sub>3</sub>COO)<sub>2</sub> based on time and [CH<sub>3</sub>COOH] using CC shells. This shows that the yields of Ca(CH<sub>3</sub>COO)<sub>2</sub> are quite poor, around 50-60%, and do not change much with respect to time and [CH<sub>3</sub>COOH] variance. These results were surprising because CaO dissolves readily in water producing Ca(OH)<sub>2</sub> which is a stronger base than CaCO<sub>3</sub>. No powder XRD was performed on CC shells so some CaCO<sub>3</sub> may still be present. The yield of Ca(CH<sub>3</sub>COO)<sub>2</sub> increased as time increased but [CH<sub>3</sub>COOH] did not affect the yield. The maximum yield achieved with CC shells was 61% after 15 h using 10% CH<sub>3</sub>COOH. These results were surprising because CaO dissolves readily in water producing Ca(OH)<sub>2</sub> which is a stronger base than CaCO<sub>3</sub>.

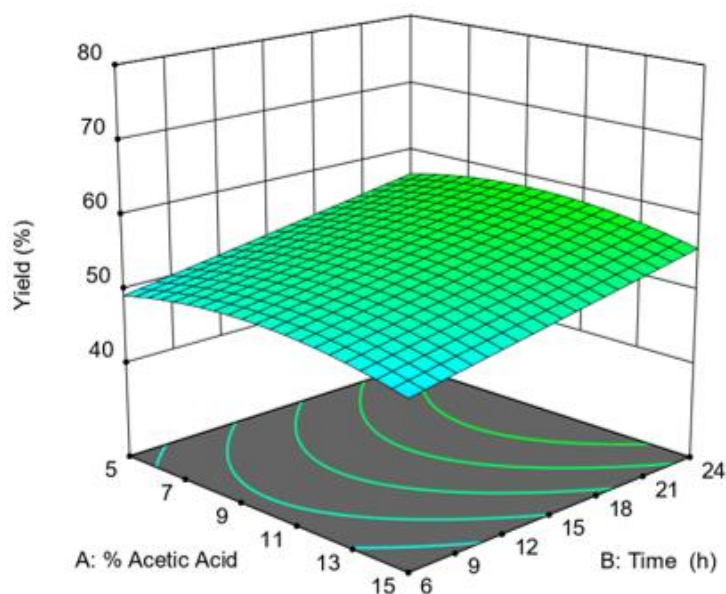


**Figure 4.2** The response surface plot of yield of  $\text{Ca}(\text{CH}_3\text{COO})_2$  based on concentration of acetic acid and time using calcined mussel shells (CC).

**Figure 4.3** shows the model of  $\text{Ca}(\text{CH}_3\text{COO})_2$  yield based on time and  $[\text{CH}_3\text{COOH}]$  using RTC shells. This figure shows that the yield of  $\text{Ca}(\text{CH}_3\text{COO})_2$  increases as time increases and as  $[\text{CH}_3\text{COOH}]$  decreases. Additionally, the  $\text{Ca}(\text{CH}_3\text{COO})_2$  yields achieved are higher than using CC shells. This was promising because RTC have not undergone any heat treatment and it would be more economical and sustainable to use these shells for the synthesis. The maximum yield achieved with RTC shells was 66% after 15 h using 2.9%  $\text{CH}_3\text{COOH}$ .

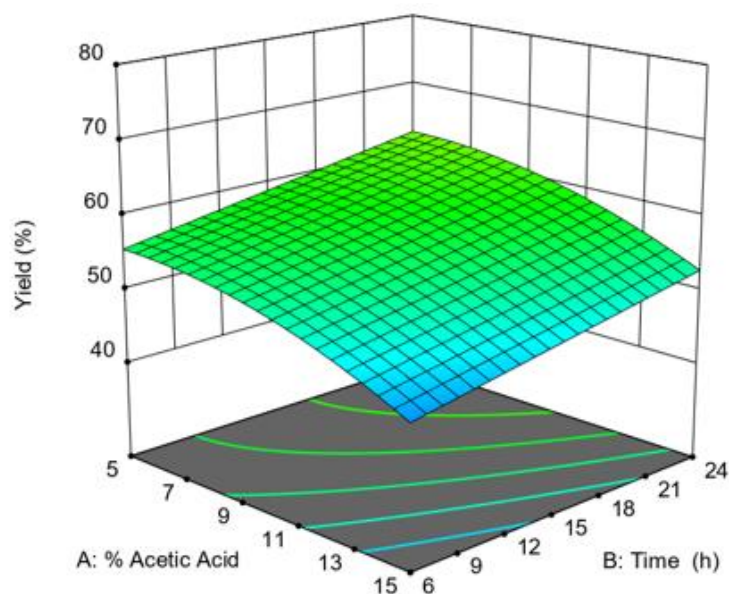


**Figure 4.3** The response surface plot of yield of calcium acetate based on concentration of acetic acid and time using raw mussel shells (RTC).

**Figure 4.4** shows the model of  $\text{Ca}(\text{CH}_3\text{COO})_2$  yield based on time and  $[\text{CH}_3\text{COOH}]$  using HTC shells. This figure shows that the yield of  $\text{Ca}(\text{CH}_3\text{COO})_2$  has the same trend as for RTC shells; the yield of  $\text{Ca}(\text{CH}_3\text{COO})_2$  increases as time increases and as  $[\text{CH}_3\text{COOH}]$  decreases. The modelled yield of  $\text{Ca}(\text{CH}_3\text{COO})_2$  is the highest for HTC shells if the three systems are compared. This is unsurprising as it was shown in **Chapter 3** that heat treatment degrades the organic matrix. The degradation increases the purity of the  $\text{CaCO}_3$  and increases the surface area of the shells. The maximum yield achieved with HTC shells was 77% after 15 h using 2.9%  $\text{CH}_3\text{COOH}$ .

The results of the initial exploratory experiments for the synthesis of  $\text{Ca}(\text{CH}_3\text{COO})_2$  from waste mussel shells afforded several conclusions that are important for the development of an optimized yield of  $\text{Ca}(\text{CH}_3\text{COO})_2$ . (1) Calcined shells (CC) produced the lowest yields

of  $\text{Ca}(\text{CH}_3\text{COO})_2$ , (2) RTC and HTC shells had the same trends with respect to time and  $[\text{CH}_3\text{COOH}]$ ; yield of  $\text{Ca}(\text{CH}_3\text{COO})_2$  increased with increasing time and decreasing  $[\text{CH}_3\text{COOH}]$  and (3) HTC shells gave the best yields of  $\text{Ca}(\text{CH}_3\text{COO})_2$ , most likely due to an increased surface area and purity. Because of the poor performance of CC shells and the lack of sustainability associated with calcining shells, the yield of  $\text{Ca}(\text{CH}_3\text{COO})_2$  was not optimized further using CC as a source of CaO. RTC shells were not used going forward because of the distinct advantage of the higher purity and surface area of HTC shells. Therefore, a new experimental design was developed focused on HTC shells only. To maximize the yield of  $\text{Ca}(\text{CH}_3\text{COO})_2$ , the path of steepest ascent in the model of yield must be followed. Therefore, the time must increase and the  $[\text{CH}_3\text{COOH}]$  must decrease.

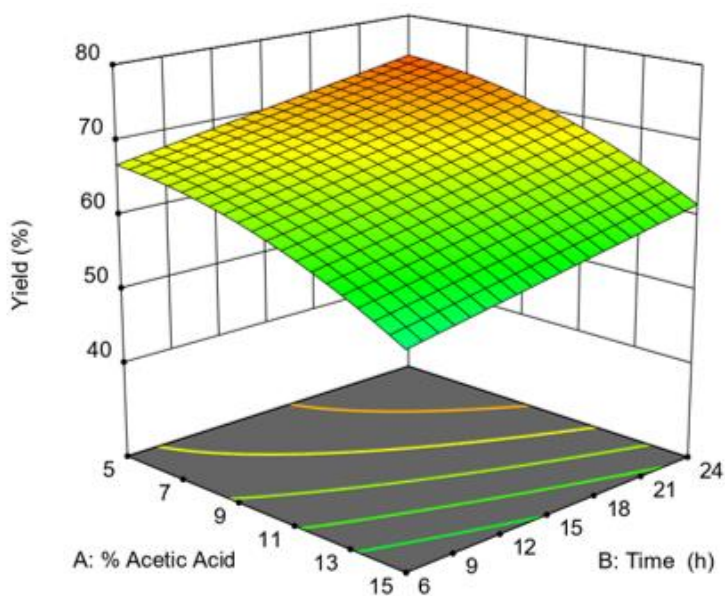


**Figure 4.4** The response surface plot of yield of  $\text{Ca}(\text{CH}_3\text{COO})_2$  based on concentration of acetic acid and time using heated mussel shells (HTC).

#### 4.2.3 Optimization of Calcium Acetate Yield using HTC shells

A custom RSM optimal design was used to optimize the yield in the fewest runs and  $\alpha$  values of time and  $[\text{CH}_3\text{COOH}]$  were chosen to be round figures and allow easy performance of experiments. The factors and levels for the custom RSM design are shown in **Table 4.2**. The molar  $[\text{CH}_3\text{COOH}]$  for this design are 0.18, 0.53, 0.88, 1.2, and 1.6 mol/L, respectively. The results of this model as well as the analysis of variance and plots of the residuals for this model are found in **Appendix C**.

**Table 4.2** Custom RSM design factors and levels for the optimization of yield of calcium acetate using HTC shells.

Name	Factor	$-\alpha$	-1	0	+1	$+\alpha$
A	% $\text{CH}_3\text{COOH}$	1	3	5	7	9
B	Time (h)	16	20	24	28	32

The empirical models for the optimization of the response (yield) in terms of the factors studied (time, and  $[\text{CH}_3\text{COOH}]$ ) using HTC shells is plotted in a three-dimensional diagram, **Figure 4.5**. This shows the model of  $\text{Ca}(\text{CH}_3\text{COO})_2$  yield based on time and  $[\text{CH}_3\text{COOH}]$ , and shows that the  $\text{Ca}(\text{CH}_3\text{COO})_2$  yield increases as time and  $[\text{CH}_3\text{COOH}]$  increase. This contrasts with the exploratory experiments where the yield increases as the  $[\text{CH}_3\text{COOH}]$  decreased. However, at lower  $[\text{CH}_3\text{COOH}]$  the yields are still quite good and higher than those observed in the exploratory CCD experiments because of increased time. The highest  $\text{Ca}(\text{CH}_3\text{COO})_2$  yield achieved using HTC shells was very good, 93% after 32 h using 9%  $\text{CH}_3\text{COOH}$ . 90% yield was obtained after 24 h using 9%  $\text{CH}_3\text{COOH}$ . Therefore, a maximum  $\text{Ca}(\text{CH}_3\text{COO})_2$  yield is achieved at times greater than 24 h using 9%  $\text{CH}_3\text{COOH}$  and is a 16% yield improvement upon results from the exploratory model.  $\text{Ca}(\text{CH}_3\text{COO})_2$  yields may still have increased beyond 32 h, however, they were not explored because a >90% yield was deemed satisfactory. A yield of 90% was also found after 32 h using 1%  $\text{CH}_3\text{COOH}$ . While it is good that such a dilute solution can make  $\text{Ca}(\text{CH}_3\text{COO})_2$ , a significant amount of additional water is required at this concentration of  $\text{CH}_3\text{COOH}$  in comparison to 9%  $\text{CH}_3\text{COOH}$  and this is less environmentally friendly because clean water is a valuable resource.

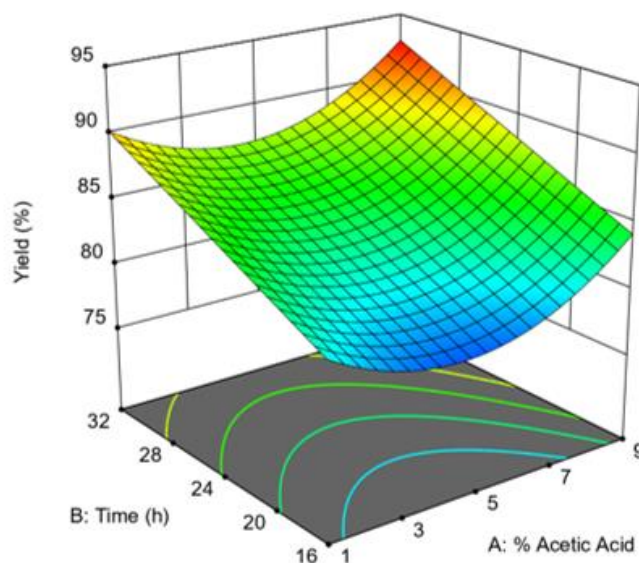


**Figure 4.5** The response surface plot of the optimization of  $\text{Ca}(\text{CH}_3\text{COO})_2$  yield based on concentration of acetic acid and time using heated mussel shells (HTC).

During experimentation for the synthesis of  $\text{Ca}(\text{CH}_3\text{COO})_2$ , anytime a concentration of 5%  $\text{CH}_3\text{COOH}$  was required, Heinz brand vinegar, i.e. food-grade vinegar, was used. This was trialed to demonstrate the ease of this synthesis and the relative safety associated with the starting materials. Anyone could make  $\text{Ca}(\text{CH}_3\text{COO})_2$  with vinegar and waste BM mussel shells and get a yield of 75-80% in 24 h. Whilst shipping would be more economical if glacial acetic acid was purchased because of the smaller volumes to be shipped – a full life cycle and cost analysis would need to be performed if this process was to be scaled up and performed commercially. Ideally, if there were a source of biomass in NL that could be fermented to produce  $\text{CH}_3\text{COOH}$  - that would be an avenue worth pursuing. It has been shown by others that bamboo vinegar can be used to make de-icer,<sup>19</sup> the concentration of  $\text{CH}_3\text{COOH}$  is low and this works well to produce  $\text{Ca}(\text{CH}_3\text{COO})_2$ .

#### 4.2.4 Characterization of Calcium Acetate

The  $\text{Ca}(\text{CH}_3\text{COO})_2$  products from using BM shells and optical calcite as  $\text{CaCO}_3$  starting material needed to be characterized as different hydrates and anhydrous forms of this salt exist. Optical calcite was used as a control experiment so that comparisons could be made between the product of the reaction prepared using pure  $\text{CaCO}_3$  compared with  $\text{CaCO}_3$  from HTC shells. Often calcium acetate is a monohydrate. **Figure 4.7** shows the overlay of IR spectra for  $\text{Ca}(\text{CH}_3\text{COO})_2$  products made using CC, RTC, HTC, and optical calcite in the  $400\text{--}1800\text{ cm}^{-1}$  region. From this spectra, it is concluded that each  $\text{CaCO}_3$  starting material is making the same form of  $\text{Ca}(\text{CH}_3\text{COO})_2$ . Through comparison with literature values for calcium acetate monohydrate ( $\text{Ca}(\text{CH}_3\text{COO})_2\cdot\text{H}_2\text{O}$ ) it is possible to confirm our product is indeed the monohydrate.<sup>26,27</sup> The hemihydrate has additional absorptions at  $1610\text{ cm}^{-1}$  and  $643\text{ cm}^{-1}$ , and the band at  $945\text{ cm}^{-1}$  would appear at  $947\text{ cm}^{-1}$ .<sup>26,27</sup> This is observed for  $\text{Ca}(\text{CH}_3\text{COO})_2$  made from CC shells (red) in **Figure 4.6**. It is likely that CaO starting material makes the hemihydrate rather than the monohydrate. This is further evidenced by the differences in bands in the  $2500\text{--}4000\text{ cm}^{-1}$  region where differences in water are seen, **Figure 4.7**. Several samples were tested to confirm this result. Additionally, the CC starting material may still contain some  $\text{CaCO}_3$  (i.e. incomplete calcination) and a mixture of the mono- and hemihydrate may be present. This was an additional reason why the CC shells were not pursued further as a starting material as they made a different product than what is desired and for all other analyses,  $\text{Ca}(\text{CH}_3\text{COO})_2$  made from CC shells is excluded.

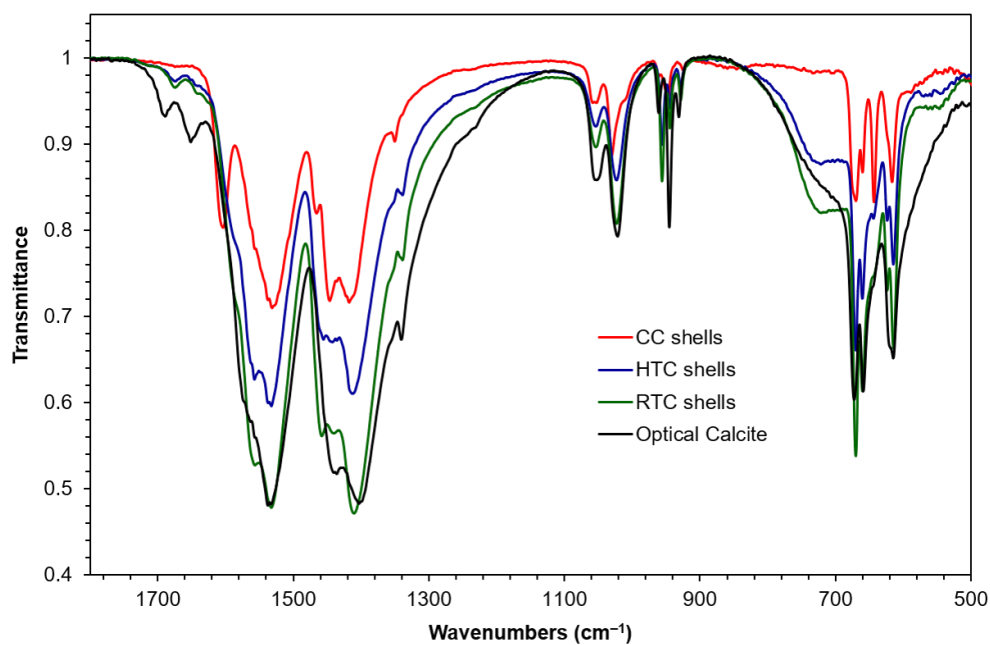


**Figure 4.6** Infrared spectra for  $\text{Ca}(\text{CH}_3\text{COO})_2$  products made using CC, RTC, HTC and optical calcite in the the 400-1800  $\text{cm}^{-1}$  region.

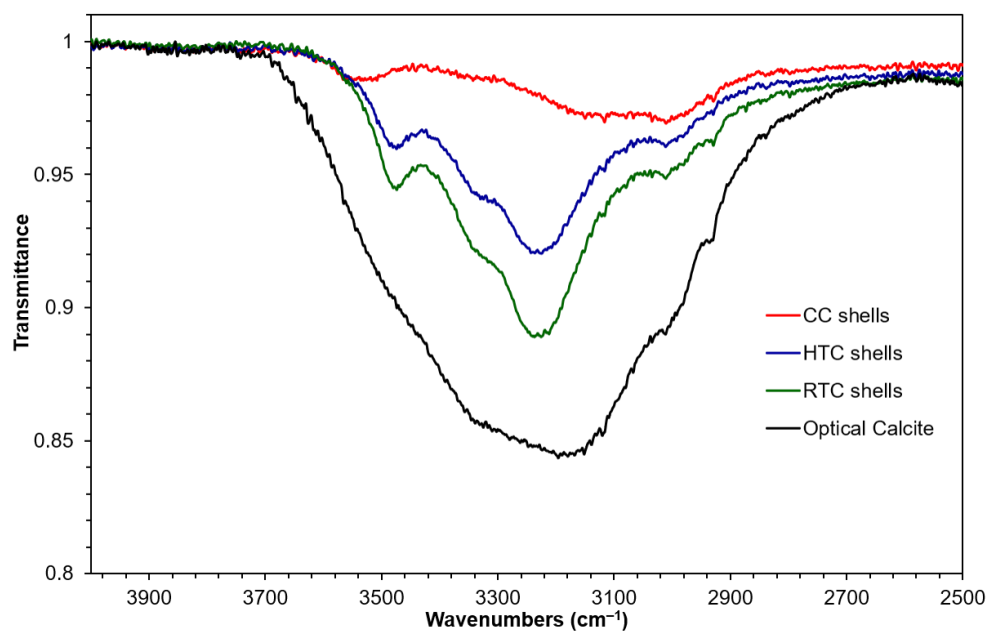


**Figure 4.7** Infrared spectra for  $\text{Ca}(\text{CH}_3\text{COO})_2$  products made using CC, RTC, HTC, and optical calcite showing the 2500-4000  $\text{cm}^{-1}$  region where there are clear differences in bands from water.

Thermogravimetric analysis (TGA), **Figure 4.8** and **Figure 4.9**, of  $\text{Ca}(\text{CH}_3\text{COO})_2$  from HTC and optical calcite confirmed what was observed by IR spectroscopy. The mass losses for  $\text{Ca}(\text{CH}_3\text{COO})_2$  from optical calcite and HTC starting materials show mass losses consistent with calcium acetate monohydrate,  $\text{Ca}(\text{CH}_3\text{COO})_2 \cdot \text{H}_2\text{O}$ , from herein referred to as monohydrate.<sup>26, 28, 29</sup> Water loss occurs in two steps of unequal masses, the first  $\frac{3}{4}$   $\text{H}_2\text{O}$  and the second  $\frac{1}{4}$   $\text{H}_2\text{O}$  from 85-215 °C. The mass losses totalled 10.2 and 10.3% for the monohydrate prepared from optical calcite and HTC, respectively, which is in good agreement with the theoretical mass loss of 10.2%. After a mass loss of acetone,  $\text{CH}_3\text{COCH}_3$ , produced via decomposition of the anion at 550 °C, the total mass loss for the monohydrate from optical calcite and HTC was 42.8 and 41.5 %, respectively. The  $\text{Ca}(\text{CH}_3\text{COO})_2 \cdot \text{H}_2\text{O}$  from optical calcite matches the theoretical value of 43.2 very well, whereas the mass loss due to acetone for HTC is slightly lower than expected. From **Figure 4.9**, which shows to the thermal analysis of  $\text{Ca}(\text{CH}_3\text{COO})_2 \cdot \text{H}_2\text{O}$  from HTC, there is an additional mass loss of 0.74% that is not present in the monohydrate from optical calcite. This mass loss is also present in the thermal analysis of mussel shells shown in **Chapter 3**. This mass loss is due to contamination of the monohydrate with organic matrix from the shell and is likely the reason why the mass losses of the monohydrate from HTC do not match the theoretical values perfectly. This is a limitation to the use of BM shells as a starting material to make chemicals where purity is a concern (i.e. pharmaceuticals).

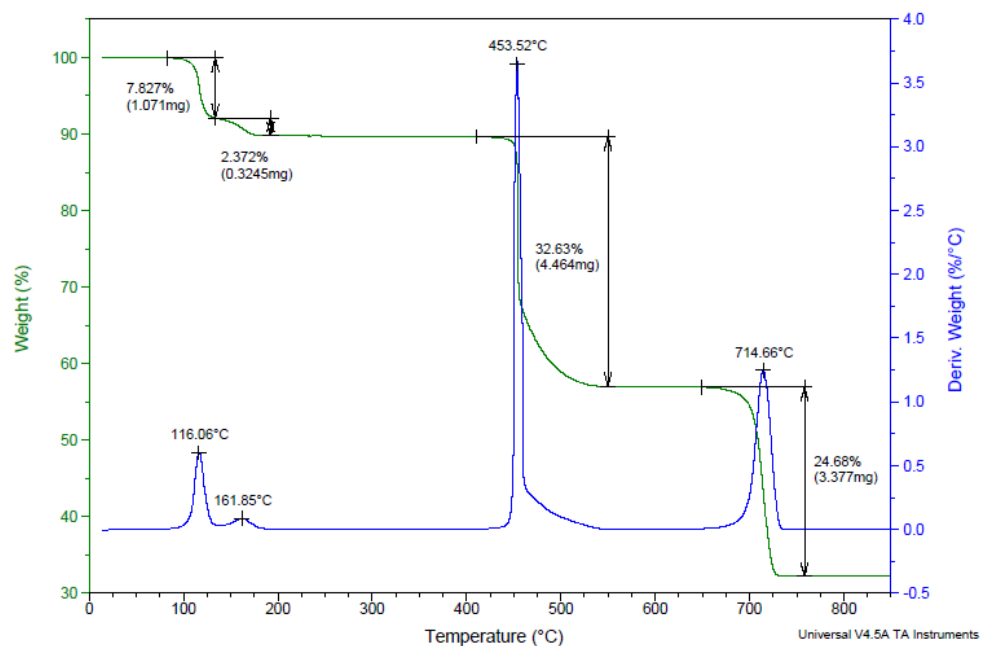


**Figure 4.8** Thermogravimetric analysis for calcium acetate monohydrate ( $\text{Ca}(\text{CH}_3\text{COO})_2 \cdot \text{H}_2\text{O}$ ) made using optical calcite.

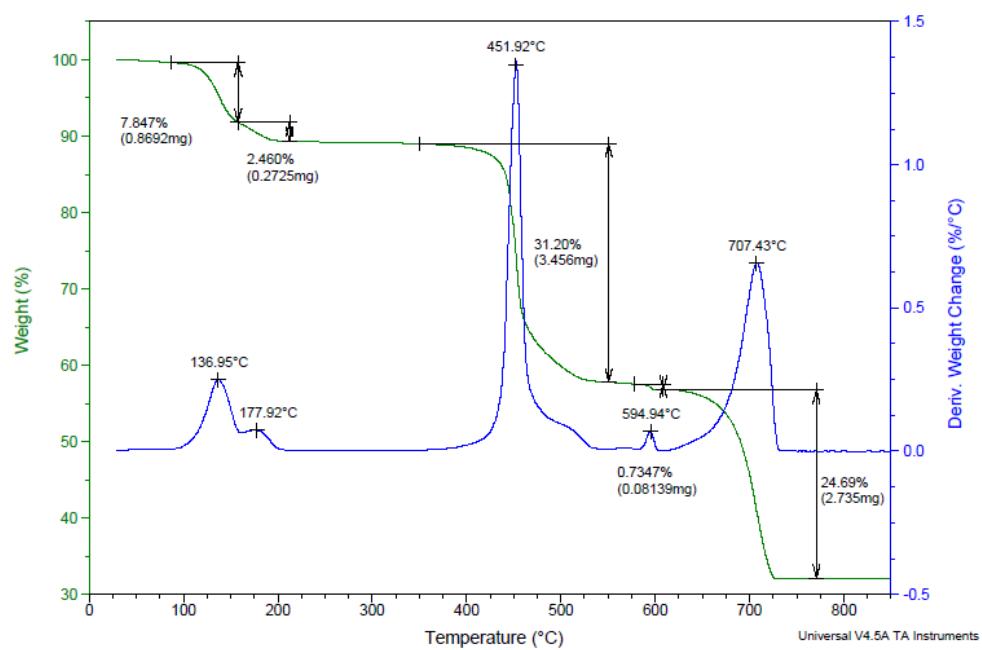


**Figure 4.9** Thermogravimetric analysis for calcium acetate monohydrate ( $\text{Ca}(\text{CH}_3\text{COO})_2 \cdot \text{H}_2\text{O}$ ) made using HTC shells.

The morphology of  $\text{Ca}(\text{CH}_3\text{COO})_2 \cdot \text{H}_2\text{O}$  is very different from  $\text{NaCl}$  which poses challenges to its use as a de-icer. Images from the crystallization of  $\text{Ca}(\text{CH}_3\text{COO})_2 \cdot \text{H}_2\text{O}$ , **Figure 4.10**, show it grows in tight bundles of thin crystalline needles with air gaps (which makes it light) that makes it difficult to use in de-icing applications especially in regions with high winds such as Newfoundland. Instead of going directly on the road,  $\text{Ca}(\text{CH}_3\text{COO})_2$  is applied as a brine or applied to the surface of adhesives (i.e. sand). Cryotech Inc., a company that sells similar de-icing and anti-ice agents, has a patented technology to make pellets with acetate de-icers to overcome the high dust challenges.<sup>17</sup> Scanning electron microscopy (SEM) images of a  $\text{Ca}(\text{CH}_3\text{COO})_2$  sample shows the tight needle organization in **Figure 4.11**, which is similar to what was observed for the calcite layer of BM shells. The prismatic orientation of  $\text{Ca}(\text{CH}_3\text{COO})_2 \cdot \text{H}_2\text{O}$  synthesized using HTC shells is different from commercial  $\text{Ca}(\text{CH}_3\text{COO})_2 \cdot \text{H}_2\text{O}$  and  $\text{Ca}(\text{CH}_3\text{COO})_2 \cdot \text{H}_2\text{O}$  prepared from butter clam shells.<sup>24</sup> I hypothesize that this may be due to the organic matrix controlling crystallization. It is well known that additives including macromolecules and amino acids can change the crystal shape of calcite.<sup>30-32</sup>



**Figure 4.10** Digital images of  $\text{Ca}(\text{CH}_3\text{COO})_2 \cdot \text{H}_2\text{O}$  made from BM shells that show its needle growth and fluffiness.

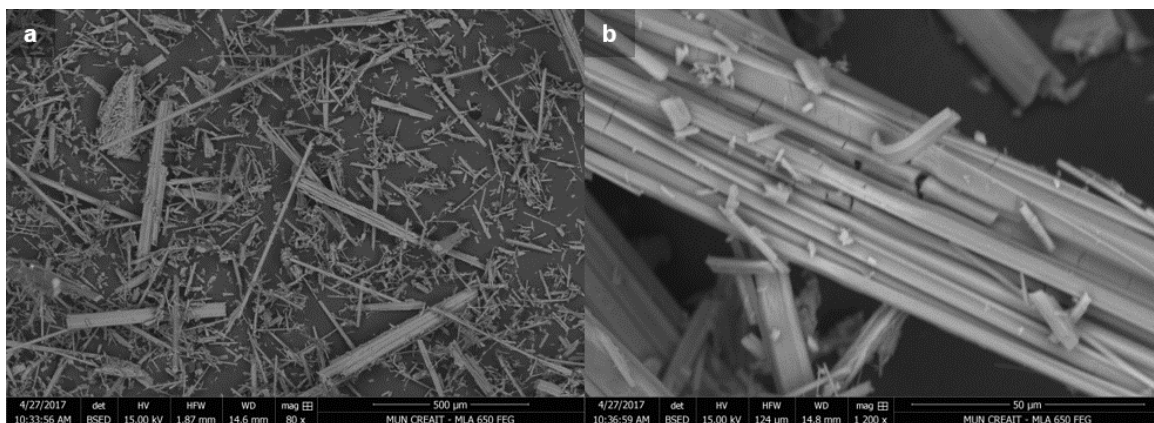


**Figure 4.11** Scanning electron micrographs (back-scattered) of calcium acetate monohydrate made from HTC shells at various magnifications.

The likely presence of organic matrix in the product as evidenced by TGA and differences in crystal shape between  $\text{Ca}(\text{CH}_3\text{COO})_2 \cdot \text{H}_2\text{O}$  from HTC compared to commercial  $\text{Ca}(\text{CH}_3\text{COO})_2 \cdot \text{H}_2\text{O}$  prompted an investigation into the diffraction of  $\text{Ca}(\text{CH}_3\text{COO})_2 \cdot \text{H}_2\text{O}$  from optical calcite in comparison to  $\text{Ca}(\text{CH}_3\text{COO})_2 \cdot \text{H}_2\text{O}$  from HTC shells. **Figure 4.12** shows the diffractograms for the two  $\text{Ca}(\text{CH}_3\text{COO})_2 \cdot \text{H}_2\text{O}$  products stacked along with a simulated powder spectrum from single crystals of  $\text{Ca}(\text{CH}_3\text{COO})_2 \cdot \text{H}_2\text{O}$ . Zoomed in regions of the diffractogram are shown in **Appendix C**. The peaks for the reflections in  $\text{Ca}(\text{CH}_3\text{COO})_2 \cdot \text{H}_2\text{O}$  made from optical calcite and HTC match with the simulated powder diffractogram from single crystals of  $\text{Ca}(\text{CH}_3\text{COO})_2 \cdot \text{H}_2\text{O}$ <sup>33</sup> and agree with observations from IR and TGA. There is no doubt that these products are calcium acetate monohydrate, however, the relative intensities of the reflections differ and there is a slight shift in peaks. This could have been corrected (i.e indexed or fitted) however it was not deemed necessary based on the supporting chemical characterization. The shift is most likely due to a raise or dip in the sample, from sample prep. Going from optical calcite to HTC, the 0–1 0 intensity

increases, and the 0 1 -2 intensity decreases. This suggests the  $\text{Ca}(\text{CH}_3\text{COO})_2 \cdot \text{H}_2\text{O}$  made from HTC crystallizes differently (i.e. preferentially from a different face).

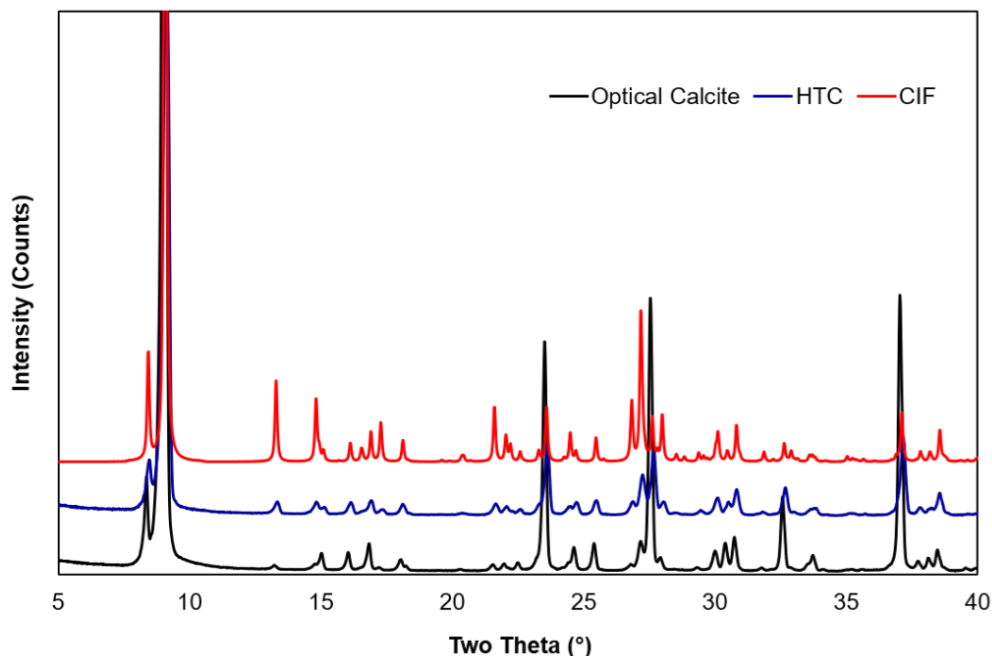


**Figure 4.12** Powder X-ray diffractograms of  $\text{Ca}(\text{CH}_3\text{COO})_2 \cdot \text{H}_2\text{O}$  made from optical calcite and HTC shells plotted with the simulated diffractogram from the crystallographic information file (CIF). CCDC 1122640.

#### 4.2.5 De-icing Experiments

De-icing experiments were carried out using  $\text{Ca}(\text{CH}_3\text{COO})_2 \cdot \text{H}_2\text{O}$  made from HTC shells to assess the efficacy of  $\text{Ca}(\text{CH}_3\text{COO})_2 \cdot \text{H}_2\text{O}$  as a de-icer. Others have already reported the successful use of  $\text{Ca}(\text{CH}_3\text{COO})_2 \cdot \text{H}_2\text{O}$  as a de-icer,<sup>19, 22</sup> but this  $\text{Ca}(\text{CH}_3\text{COO})_2 \cdot \text{H}_2\text{O}$  was made with a different mollusc source. Because of limitations of dealing with  $\text{Ca}(\text{CH}_3\text{COO})_2 \cdot \text{H}_2\text{O}$  in solid form (i.e. dust issues)  $\text{Ca}(\text{CH}_3\text{COO})_2 \cdot \text{H}_2\text{O}$  at various concentrations and applied as a brine was explored. Concentrations of  $\text{CaMg}_2(\text{CH}_3\text{COO})_6$

are typically 30% (m/v)<sup>14</sup>, therefore concentrations up to 30% of Ca(CH<sub>3</sub>COO)<sub>2</sub>·H<sub>2</sub>O were trialed. Experiments were performed at a single temperature one time but in a similar fashion to previous researchers.<sup>19</sup>

**Table 4.3** Data for de-icing experiments performed at different concentrations of calcium acetate brine applied to ice and reported as mass losses and gains at -16°C.

Concentration of Ca(CH <sub>3</sub> COO) <sub>2</sub> ·H <sub>2</sub> O	Percent loss or gain of water mass (%)
Blank – Distilled water	+ 10.7
15%	+ 6.45
20%	- 10.7
25%	- 13.2
30%	- 11.4

Based on de-icing experiments, calcium acetate melts ice, as shown in **Table 4.3**. However, the concentration used is very important. The blank experiment, where 10.0 mL of water was added to ice saw an increase of mass by 10.7%. A solution of 15% Ca(CH<sub>3</sub>COO)<sub>2</sub>·H<sub>2</sub>O was not suitable for de-icing as the mass of water (ice) increased (6.45%) after 15 minutes. Concentrations of 20-30% were successful, melting 10-13% of ice in 15 minutes at -16 °C. These concentrations compare well with common concentrations of liquid de-icing agents. For example, CaMg<sub>2</sub>(CH<sub>3</sub>COO)<sub>6</sub> is commonly administered at 25%, K(CH<sub>3</sub>COO) is 50%, MgCl<sub>2</sub> and CaCl<sub>2</sub> are 30%, and NaCl, if used as a brine is 23%.<sup>14</sup> Jiang *et al.* performed de-icing experiments at 0 °C using solid Ca(CH<sub>3</sub>COO)<sub>2</sub> prepared from distilled bamboo vinegar (0.478 mol/L) and Ca(OH)<sub>2</sub>.<sup>19</sup> There was no characterization of the reported of the Ca(CH<sub>3</sub>COO)<sub>2</sub>. After 1 h, 28% of ice was melted using 2 g of Ca(CH<sub>3</sub>COO)<sub>2</sub> on 100 g of ice. Additionally, in terms of moles, 41.5% of ice was melted after 1 h using 0.025 mol of Ca(CH<sub>3</sub>COO)<sub>2</sub>. It is difficult to compare this work with the work of others because a

$\text{Ca}(\text{CH}_3\text{COO})_2 \cdot \text{H}_2\text{O}$  brine at  $-16\text{ }^\circ\text{C}$  for 15 minutes was used. Regardless, both methods and  $\text{Ca}(\text{CH}_3\text{COO})_2$  compounds work as de-icing agents. The patent from South Korea reports 25-30% (m/v) of  $\text{Ca}(\text{CH}_3\text{COO})_2$  is used for de-icing but does not report the results.<sup>22</sup> This patent was translated from Korean and was difficult to understand.

### 4.3 Conclusions

Three starting materials sourced from waste BM shells were screened in the synthesis of calcium acetate. The three materials included; shells without heat treatment, shells heated to  $220\text{ }^\circ\text{C}$  for 48 h and shells calcined to yield CaO, denoted as RTC, HTC, and CC, respectively. Characterization data confirmed that the product of these reactions was a monohydrate. An exploratory CCD compared the yield of  $\text{Ca}(\text{CH}_3\text{COO})_2 \cdot \text{H}_2\text{O}$  with respect to shell type, concentration of  $\text{CH}_3\text{COOH}$ , and time. CC shells resulted in poor yields, regardless of time and  $\text{CH}_3\text{COOH}$  concentrations. RTC shells had better yields that increased as time increased and % $\text{CH}_3\text{COOH}$  decreased. HTC shells had the best yields and followed the same trend as RTC shells. The yield of  $\text{Ca}(\text{CH}_3\text{COO})_2 \cdot \text{H}_2\text{O}$  was optimized further using HTC shells using a custom optimal design with longer reaction times and low  $\text{CH}_3\text{COOH}$  concentrations. A maximum yield of 93% was reached after 32 h using 9%  $\text{CH}_3\text{COOH}$ . Other concentrations of  $\text{CH}_3\text{COOH}$  were still very successful and using food-grade white vinegar, an 85% yield of  $\text{Ca}(\text{CH}_3\text{COO})_2 \cdot \text{H}_2\text{O}$  was obtained after 24 h. The product monohydrate was characterized by IR spectroscopy, TGA and powder XRD. The  $\text{Ca}(\text{CH}_3\text{COO})_2 \cdot \text{H}_2\text{O}$  produced from BM shells HTC and RTC were the same as using pure  $\text{CaCO}_3$  in the form of optical calcite.  $\text{Ca}(\text{CH}_3\text{COO})_2$  made using CC shells was the hemihydrate. The morphology of  $\text{Ca}(\text{CH}_3\text{COO})_2 \cdot \text{H}_2\text{O}$  was prismatic like the outer calcite

layer of mussel shells (see **Chapter 3**). Powder XRD data suggest that the organic matrix is directing crystal growth because the reflection intensities of  $\text{Ca}(\text{CH}_3\text{COO})_2 \cdot \text{H}_2\text{O}$  produced using HTC differ from those for  $\text{Ca}(\text{CH}_3\text{COO})_2 \cdot \text{H}_2\text{O}$  prepared from optical calcite.

De-icing experiments showed that the  $\text{Ca}(\text{CH}_3\text{COO})_2 \cdot \text{H}_2\text{O}$  produced from waste BM melted 10-13 wt.% of ice in 15 minutes at concentrations of 20-30% (m/v) at  $-16^\circ\text{C}$ . This is very promising for progress towards a sustainable, non-corrosive and degradable de-icer; however, sustainability can be further improved is a renewable source of  $\text{CH}_3\text{COOH}$  was identified and used.

## **4.4 Experimental**

### **4.4.1 General Considerations**

Glacial acetic acid (99.9%) was purchased from Fisher Scientific and used without purification. Optical calcite was purchased in Colorado and is from Mexico. Blue mussels and Heinz brand vinegar were purchased at Sobeys, Merrymeeting Road, St. John's. Shells were cleaned, removing any organic material, using industrially available food grade protease enzymes as previously described in **Chapter 2**.<sup>34</sup> Cleaned mussel shells were dried at  $220^\circ\text{C}$  for 48 h (HTC) or calcined at  $750^\circ\text{C}$  for 4 h in a tube furnace under air (CC). A SPEX mixer mill equipped with a 65 mL stainless steel vial with two quarter inch stainless steel balls was used to grind shells for 12 min in initial experiments. Upon discovery of iron contamination in ground shells, experiments were performed using shells that were crushed to  $>2$  cm size flakes.

Infrared (IR) spectroscopy was performed using a Bruker Alpha FTIR spectrometer fitted with a single bounce diamond ATR accessory. IR spectra were collected with a resolution of  $2\text{ cm}^{-1}$ . All measurements were conducted in triplicates, averaged and plotted in Excel. Thermogravimetric analysis (TGA) was carried out using a TA Instruments Q500 under a  $\text{N}_2$  atmosphere ( $50\text{ mL min}^{-1}$ ) from 25-850 °C. Scanning electron microscopy (SEM) images were obtained using a FEI MLA 650 FEG under high vacuum ( $10^{-6}$  torr). The voltage of 15 kV and current of 10 mA at a working distance of 14.9 mm produced a 5.8 spot. An SDD was used for BSED. Powder X-ray diffraction (XRD) was performed using a Rigaku MiniFlex XRD equipped with  $\text{Cu K}\alpha$  radiation ( $\lambda=1.5406\text{ \AA}$ ). The  $2\theta$  region was scanned from  $0\text{-}50^\circ$  with a step size of  $0.02^\circ$ .

#### **4.4.2 Synthesis of Calcium Acetate**

Approximately 3 g of shells were weighed directly into an Erlenmeyer flask. The exact mass of shells was noted and the required volume of  $\text{CH}_3\text{COOH}$  was added. The size of the flask varied as the concentration and volume of  $\text{CH}_3\text{COOH}$  used was varied. For example, if 38 mL of 9%  $\text{CH}_3\text{COOH}$  was required, a 125 mL Erlenmeyer was used but if 341 mL of 1%  $\text{CH}_3\text{COOH}$  was required a 500 mL Erlenmeyer was used. All reactions were stirred magnetically at room temperature. Once the reaction was complete, the pH was tested with full range pH paper. If the pH paper did not indicate a neutral pH, small quantities of  $\text{NaOH}$  (3M) were added until the pH reached 7. The reaction mixture was gravity filtered and the calcium acetate solution was collected in a beaker. The solution was heated on a hot plate until most of the water evaporated. This was to speed up the crystallization of calcium acetate because it is very soluble in water. Once crystallization

was complete, samples were left at room temperature for three days to achieve constant mass before being weighed to calculate yields. This was preferred over drying in an oven so that the products remained monohydrates. Any unreacted shells, as the residue from the filtration step, were kept for another project (**Chapter 5**).

#### **4.4.3 De-icing Experimental Procedure**

Experiments were performed at a single temperature but in a similar fashion to previous researchers.<sup>19</sup> Ice was prepared by placing 50.0 mL of water in a 250.0 mL Erlenmeyer flask and placing the flask in the freezer at  $-16\text{ }^{\circ}\text{C}$ .  $\text{Ca}(\text{CH}_3\text{COO})_2$  solutions in concentrations of 15, 20, 25, and 30% (m/v) were prepared to a final volume of 10.0 mL. These m/v concentrations correspond to molar concentrations of 0.85, 1.1, 1.4, and 1.7 mol  $\text{L}^{-1}$ . The  $\text{Ca}(\text{CH}_3\text{COO})_2$  solutions were chilled at  $5\text{ }^{\circ}\text{C}$  for 1 h prior to adding the brine to the ice. The brine was added to the ice and remained in the freezer (at  $-16\text{ }^{\circ}\text{C}$ ) for 15 min after which any liquid was decanted, the mass of ice left over was recorded, and percent of ice removed was calculated.

#### **4.5 References**

1. Y. Hou, A. Shavandi, A. Carne, A. A. Bekhit, T. B. Ng, R. C. F. Cheung and A. E.-d. A. Bekhit, *Crit. Rev. Environ. Sci. Technol.*, 2016, **46**, 1047-1116.
2. J. N. Murphy and F. M. Kerton, in *Fuels, Chemicals and Materials from the Oceans and Aquatic Sources* eds. F. M. Kerton and N. Yan, Wiley, 2017, ch. Characterization and utilization of waste streams from mollusc aquaculture and fishing industries, pp. 189-225.

3. J. P. Morris, T. Backeljau and G. Chapelle, *Rev. Aquacult.*, 2018, **11**, 42-57.
4. N. Seco-Reigosa, S. Pena-Rodriguez, J. C. Novoa-Munoz, M. Arias-Estevez, M. J. Fernandez-Sanjurjo, E. Alvarez-Rodriguez and A. Nunez-Delgado, *Environ. Sci. Pollut. Res.*, 2013, **20**, 2670-2678.
5. A. M. Ramirez-Perez, M. Paradelo, J. C. Novoa-Munoz, M. Arias-Estevez, M. J. Fernandez-Sanjurjo, E. Alvarez-Rodriguez and A. Nunez-Delgado, *J. Hazard. Mater.*, 2013, **248-249**, 122-130.
6. M. C. Barros, P. M. Bello, M. Bao and J. J. Torrado, *J. Clean Prod.*, 2009, **17**, 400-407.
7. M. L. Mai, M. Emmett, M. S. Sheikh, C. A. Santa Ana, L. Schiller and J. S. Fordtran, *Kidney Int.*, 1989, **36**, 690-695.
8. M. Wei, A. J. Ruys, B. K. Milthorpe and C. C. Sorrell, *J. Mater. Sci.: Mater. Med.*, 2005, **16**, 319-324.
9. Health Canada, <https://www.canada.ca/en/health-canada/services/food-nutrition/food-safety/food-additives/lists-permitted/10-adjusting-agents.html>, (accessed June 18, 2019).
10. K. Wang, D. E. Nelsen and W. A. Nixon, *Cem. Concr. Compos.*, 2006, **28**, 173-188.
11. Environment Canada, 2001. *Canadian Environmental Protection Act, 1999, Priority Substances List Assessment Report – Road Salt*, Hull, Quebec.
12. M. S. Perchanok, D. G. Manning and J. J. Armstrong, *Highway deicers: Standards, practice and research in the Province of Ontario*, Research and Development

Branch, Downsview, Ontario, 1991.

13. S. S. Kaushal, *Environ. Sci. Technol.*, 2016, **50**, 2765-2766.
14. M. Fischel, Evaluation of Selected Deicers Based on a Review of the Literature, Report No. CDOT-DTD-R-2001-15, Denver, CO, 2001.
15. D. M. Ramakrishna and T. Viraraghavan, *Water, Air, Soil Pollut.*, 2005, **166**, 49-63.
16. M. C. Santagata and M. Collepardi, *Cem. Concr. Res.*, 2000, **30**, 1389-1394.
17. Cryotech, <http://www.cryotech.com/commercial>, (accessed June 23, 2019).
18. W. Fu and A. P. Mathews, *Enzyme Microb. Tech.*, 2005, **36**, 953-959.
19. X. Jiang, G. Li and Z. Wu, *World Academy of Science, Engineering and Technology International Journal of Chemical and Molecular Engineering*, 2010, **4**, 304-309.
20. B. Yun Yang and R. Montgomery, *Bioresource Technol.*, 2003, **90**, 265-273.
21. J. Liu, Y. Zhang, Y. Liu, H. Liu and D. Xing, *Guangdong Huagong*, 2012, **39**, 24-26.
22. 김병억, *Preparation method of snow removing materials by using oyster shell*, South Korea Pat., KR201328694B1, 2013.
23. Z. Fan, X. Yang, J.-q. Guan, J. Zhang, L. Qiao and X.-y. Chang, *Shipin Gongye Keji*, 2015, **36**, 254-258.
24. H. J. Lee, N. Y. Jung, S. H. Park, S. M. Song, S. I. Kang, J.-S. Kim and M. S. Heu, *J. Korean Soc. Food Sci. Nutr.*, 2015, **44**, 888-895.
25. T. Di Nardo and A. Moores, *Beilstein J. Org. Chem.*, 2019, **15**, 1217-1225.

26. N. H. Tennent and T. Baird, *Stud. Conserv.*, 1985, **30**, 73-85.
27. A. W. Musumeci, R. L. Frost and E. R. Waclawik, *Spectrochim. Acta A*, 2007, **67**, 649-661.
28. D. Asmi and I. M. Low, *Ceram. Int.*, 2008, **34**, 311-316.
29. A. T. Pemberton, D. B. Magers and D. A. King, *J. Chem. Ed.*, 2019, **96**, 132-136.
30. Y.-Y. Kim, J. D. Carloni, B. Demarchi, D. Sparks, D. G. Reid, Miki E. Kunitake, C. C. Tang, M. J. Duer, C. L. Freeman, B. Pokroy, K. Penkman, J. H. Harding, L. A. Estroff, S. P. Baker and F. C. Meldrum, *Nat. Mater.*, 2016, **15**, 903-910.
31. L.-B. Mao, H.-L. Gao, H.-B. Yao, L. Liu, H. Cölfen, G. Liu, S.-M. Chen, S.-K. Li, Y.-X. Yan, Y.-Y. Liu and S.-H. Yu, *Science*, 2016, **354**, 107-110.
32. H.-L. Gao, S.-M. Chen, L.-B. Mao, Z.-Q. Song, H.-B. Yao, H. Cölfen, X.-S. Luo, F. Zhang, Z. Pan, Y.-F. Meng, Y. Ni and S.-H. Yu, *Nat. Commun.*, 2017, **8**, 287.
33. E. A. Klop, A. Schouten, P. van der Sluis and A. L. Spek, *Acta Crystallogr. C*, 1984, **40**, 51-53.
34. J. N. Murphy, K. Hawboldt and F. M. Kerton, *Green Chem.*, 2018, **20**, 2913-2920.

## **Chapter 5 Absorbent self-assembling calcite material from the prismatic layer of waste *Mytilus edulis* shells**

**See Appendix D for additional data.**

A version of this chapter is in preparation for submission to *Matter*.

Jennifer N. Murphy, Céline M. Schneider, Kelly Hawboldt, and Francesca M. Kerton\*

### **5.1 Introduction**

Nature's ability to create sophisticated structures with impressive mechanical properties drives a broad field of biomimetic materials research.<sup>1</sup> The most abundant biomineral found in nature is  $\text{CaCO}_3$  where it serves a number of structural, protection, and mechanical functions in freshwater and marine organisms.<sup>2,3</sup> Biomineralized crystals differ structurally from geological and synthetic crystals and are difficult to simulate.<sup>4</sup> The morphology and growth of  $\text{CaCO}_3$  materials can be controlled biomimetically<sup>5-8</sup> and by other anthropogenic means.<sup>9-11</sup> Many have drawn inspiration from mollusc shells (>95%  $\text{CaCO}_3$ ) for materials synthesis and attempted to mimic natural  $\text{CaCO}_3$  prisms or nacre. Nacre is by far the more studied structural motif. Over the last three decades, nacre-inspired materials research has come a long way<sup>12</sup> and there are now many methods to synthesize nacre-layer materials for use as a biomaterial in orthopedic and tissue engineering applications<sup>13</sup>, as well as armour<sup>14</sup>, and electronics.<sup>15</sup> The study of prismatic calcite in molluscs is becoming more popular and

understanding its formation is also valuable.<sup>16</sup> For example, prismatic-type  $\text{CaCO}_3$  thin films<sup>17</sup> like the prismatic calcite layer of molluscs and flexible calcite needles that resemble spicules from *Sycon sp.*,<sup>8</sup> a calcareous sponge have recently been reported.

Natural materials are appealing for applications in the environment, such as oil spill remediation, and are potentially more economic than high performance absorbent materials made from polymers and various carbons.<sup>18</sup> While mollusc shells are a great source of inspiration to scientists, taking advantage of the ocean based biorefinery<sup>19,20</sup> to create new  $\text{CaCO}_3$  materials from mollusc shells may be valuable, as aquaculture production increases globally to produce sustainable animal protein.<sup>21</sup> To date, waste mollusc shells have been utilized in many areas where  $\text{CaCO}_3$  is traditionally used including in building materials, catalysis and waste water treatment.<sup>22,23</sup>

It is important for researchers to consider the use of renewable feedstocks and green synthetic routes in their preparation of new materials. In this chapter, a new morphology of biogenic calcite prepared from waste *Mytilus edulis* shells is reported. This  $\text{CaCO}_3$  material is produced alongside calcium acetate, which can be used as a dietary supplement to increase calcium levels as well as a treatment for hyperphosphatemia (too much phosphate in the blood).<sup>24</sup> It can be made quite simply at room temperature in aqueous media using food grade white vinegar. The self-assembling calcite (SAC) contains the same components of the strong, highly ordered prismatic calcite layer found in shells, but is soft and absorbent, and forms a hierarchical architecture composed of calcite crystals in a nest-like formation. While absorbent sponges made from renewable materials have been reported they are typically carbon materials prepared via pyrolysis (a high temperature process),<sup>18,</sup>  
<sup>25</sup> this inorganic sponge is a first and uses a material sourced from aquaculture waste and

transformed at room temperature. We also report the application of SAC towards absorption of crude oil and dyes from water.

## 5.2 Results

### 5.2.1 Preparation of SAC

This material was discovered while working on the synthesis of calcium acetate in **Chapter 4**. An overview of the preparation of self-assembling calcite (SAC) from blue mussel (BM) shells is shown in **Figure 5.1**. The cleaned shells<sup>26</sup> are heated to 220 °C for 48 h, **Figure 5.1a**. Heat treatment decreases the amount of organic matrix in the BM shells and allows easy separation of the inner nacreous aragonite layer from the outer prismatic calcite layer, as described in **Chapter 3**. The heat-treated shells, denoted BMH, are reacted with 5% CH<sub>3</sub>COOH to make what are termed ‘prepped shells’, **Figure 5.1b**. This step is important in the preparation of SAC. In fact, SAC cannot be made directly in a single step from BM shells upon CH<sub>3</sub>COOH treatment. The prepped shells undergo a second reaction with 5% CH<sub>3</sub>COOH to produce a mixture of calcium acetate, SAC, and unreacted shell material, **Figure 5.1c**. The difference in buoyancy between SAC and the remaining shells makes their separation simple. The calcium acetate and SAC are decanted from the remaining shells. Then, the calcium acetate solution is decanted from the SAC as shown in **Figure 5.1d**. Finally, SAC is rinsed with water to remove residual calcium acetate, and washed in absolute ethanol, **Figure 5.1e**. Moist SAC has a sponge-like texture and large amount of water within the agglomerates. Therefore, solvent exchange with ethanol assists in the drying process. Once the SAC is dried, **Figure 5.1f**, it is ready for use and has a candy floss (cotton candy) texture. Typically, SAC agglomerates are very spherical in shape (**Figure**

**5.1g)** and are homogeneous with no pieces of shell within them. It is also important to note that SAC is produced alongside calcium acetate monohydrate, **Figure 5.1h**, which is itself a useful compound for nutritional calcium supplementation. Oven-dried SAC can absorb 10 times its mass in liquid water. No absorption of moisture from air was observed when the SAC was stored in a humidity chamber over a period of a week at 20 °C, as no mass increase was observed.

Others have isolated calcite from mollusc shells. Individual prisms of calcite from molluscs *Atrina rigida* and *Pinna nobilis* have been liberated previously in dilute sodium hypochlorite solutions.<sup>16, 27, 28</sup> However, there have been no reports of a nest-like microstructure such as we present here. To support my observations regarding SAC formation from BM, control experiments were performed with alternate sources of CaCO<sub>3</sub> and other organic acids to try to synthesize SAC from BM. Three additional CaCO<sub>3</sub> sources were evaluated: reagent-grade CaCO<sub>3</sub>, aragonite from BM, and calcite from BM as per the outlined procedure. A small amount of SAC was formed when using the calcite from BM alone and no SAC formed using lab-grade CaCO<sub>3</sub> or aragonite from BM alone. This suggests that SAC yields are increased when whole BM shells are used. The myostracum<sup>3</sup>, a small layer that connects the inner nacreous aragonite and outer prismatic calcite layer of BM shells, is composed of aragonite and holds the prismatic calcite in its natural organized manner. Therefore, the myostracum must react with CH<sub>3</sub>COOH first in order for prisms of calcite to be liberated. This because aragonite has a higher dissolution rate than calcite.<sup>29</sup> Therefore, the aragonite (myostracum and nacre) preferentially forms calcium acetate, leaving the calcite available to form SAC. It should be noted that in this process the base

(CaCO<sub>3</sub>) is present in excess relative to the acid (CH<sub>3</sub>COOH), and therefore not all of the CaCO<sub>3</sub> present will react. SEM images show that during this first stage some of the calcite has reacted with CH<sub>3</sub>COOH because the prisms are slightly degraded compared to natural shells. The preferential reaction of aragonite could also be because calcite prisms in molluscs have been known to be coated in a thick layer of organic matrix, and this is likely protecting the calcite from dissolution to some degree. Several weak organic acids were explored as an alternative to acetic acid but none resulted in the formation of the SAC. For SAC to form and be separated easily, the calcium carboxylate by-product formed must be soluble. Oxalic, propanoic, citric and oleic acid (5%) were tested. Calcium oxalate and citrate have low solubility in water so the products could be seen precipitating very quickly and no SAC was produced. Oleic acid (5% in ethanol) did not result in the formation of SAC, even when some water was added to try to drive the reaction via hydrophobic interactions. Propanoic acid was the most suitable for making SAC because calcium propanoate has a high solubility in water and propanoic acid has a similar pKa to CH<sub>3</sub>COOH, however, none was formed. Gentle agitation (a shaker or rotating platform - not a magnetic stirrer) is imperative for the formation of SAC from waste BM shells. SAC did not form in control experiments using magnetic stirring.



**Figure 5.1** Overview of the preparation and purification of SAC. Digital images of BMH shells (a), the appearance of BMH shells after being treated with 5%  $\text{CH}_3\text{COOH}$ , washed with distilled water and dried (b), the result of treating b with 5%  $\text{CH}_3\text{COOH}$  is a mixture of SAC, residual BMH shells and calcium acetate (c), SAC is collected via simple decantation (d) and washed in ethanol (e) before being dried in a vacuum oven to get pure SAC (free of residual calcium acetate) (f). Some SAC is very spherical (g) and it is produced alongside calcium acetate monohydrate (h).

### 5.2.2 Characterization of SAC

IR spectra (Appendix D, **Figure D1**) of SAC contain bands at  $1388\text{ cm}^{-1}$ ,  $870\text{ cm}^{-1}$ , and  $712\text{ cm}^{-1}$  and these correspond to the  $\nu_3$ ,  $\nu_2$ , and  $\nu_4$  bands of calcite.<sup>30</sup> These match with the outer prismatic calcite layer of the BM shell and there are no bands corresponding to aragonite, the other polymorph present in the BM shell that makes up the inner nacreous layer. Therefore, this confirms aragonite from the shells preferentially reacts with the acetic acid to form calcium acetate during the preparation of SAC. Powder XRD of SAC (**Figure D2**) confirmed the absence of aragonite and the only crystalline phase present is calcite. The morphology of SAC was investigated using SEM and compared to the prismatic layer

of BM shells, **Figure 5.2**. In the micrographs of SAC at differing scales, shown in **Figure 5.2b-c**, some of the prismatic calcite is hundreds of  $\mu\text{m}$  in length. This is common with the prismatic calcite layer of mollusc shells.<sup>16</sup> However, there is a key difference with SAC from the prismatic calcite from molluscs and that is the nest-like structure of the SAC. Individual calcite crystals in a mollusc shell are surrounded by a layer of organic matrix making the prisms highly organized along the direction of crystal growth and in close contact with one another.<sup>3</sup> From fitting the BET isotherm, **Figure D4**, the surface area of supercritically dried SAC was  $37\text{ m}^2/\text{g}$ . This surface area is  $\sim 9$  times greater than the surface area of ground BMH shells. **Figure 5.3** shows that SAC is much more voluminous than ground BMH shells where 0.5 g of SAC and 0.5 g of ground BMH shells are compared side by side. This surface area is higher than any reported for ground mollusc that contains  $\text{CaCO}_3$ .<sup>31-34</sup>

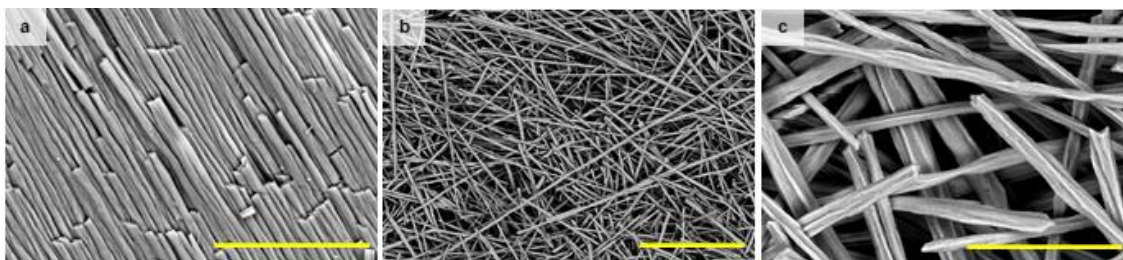


**Figure 5.2** Comparison of prismatic calcite from BMH shells and SAC. a) FESEM (BSED) image of the outer prismatic calcite layer of BMH shells after heating the shells at  $220\text{ }^\circ\text{C}$  for 48 h b-c Select FESEM images of SAC showing the microstructure composed of calcite crystals in a nest-like formation at different scales. Scale bars:  $30\text{ }\mu\text{m}$  (a),  $100\text{ }\mu\text{m}$  (b),  $20\text{ }\mu\text{m}$  (c).

NMR spectroscopy, elemental analysis and TGA were used to assess the purity of SAC. From NMR it is certain the SAC is free of calcium acetate. If calcium acetate were present

it would present as a sharp resonance in the  $^1\text{H}$  NMR spectrum because of its increased mobility compared to the solid calcite. The mass loss for the organic matrix is camouflaged in the TGA because there is overlap with the loss of  $\text{CO}_2$  from the calcite at  $600\text{ }^\circ\text{C}$ , **Figure D5**. There was a small mass loss at  $440\text{ }^\circ\text{C}$  that was also seen in the TGA of the outer layer of the BM shell that is very likely organic matrix. Mass losses corresponding to calcium acetate were not observed. Elemental analysis for SAC (C: 11.73 H:  $<0.2$  N:  $<0.2$ ) matches well with the theoretical values for  $\text{CaCO}_3$  (C: 12.00 H: 0 N: 0) so it is free of impurities such as calcium acetate, however it does rule out the presence of organic matrix.



**Figure 5.3** Visual comparison between BMH shells and SAC. Digital images of (a) 0.5 g of powdered BMH shells and (b) 0.5 g of SAC.

### 5.2.3 $^1\text{H}$ MAS NMR of SAC

It was curious as to how the calcite prisms became ‘loosened’ from the shell structure and then recombined to make nest like agglomerates of calcite. Perhaps the organic matrix that is present in the mussel shell was acting as a ‘glue’ that is still present in solution and helping the prisms recombine. Surprisingly,  $^1\text{H}$  MAS NMR spectra of SAC are identical to those of the outer prismatic layer of the BM shell, Appendix D, **Figure D6**, containing

peaks that are from the organic matrix as well as small broad peak at 13.8 ppm that corresponds to bicarbonate protons.<sup>35, 36</sup> This provides evidence of organic matrix being present in the SAC, however further studies are needed to determine if the matrix coats the prisms of calcite (like in mollusc shells) or is entangled in the SAC nests.

To further prove the <sup>1</sup>H NMR signal was from the organic matrix, a considerable amount of water insoluble organic matrix from BM shells was isolated. The inner nacreous layer reacted to make calcium acetate as shown by SEM, **Figure D7**, to reveal the outer prismatic layer. Large sheets of insoluble organic matrix were easily removed from the shell at this stage, **Figure D7**, and the remaining shell becomes flexible. The <sup>1</sup>H MAS and <sup>13</sup>C CP MAS NMR spectra, **Figures D8** and **D9**, have several peaks that match with untreated BM shell presented in **Chapter 3**. These spectra are representative, proving organic matrix is present in the SAC.

#### **5.2.4 Dye Adsorption Studies**

Due to the increased surface of SAC in comparison to ground BM shells and its ability to absorb water, its use in treating water contaminated with crystal violet as well as a fabric dye, readily available to the public, was investigated. The textile industry and wastewater from dyeing processes is one of the main sources of pollution in the World.<sup>37, 38</sup> Dyes are designed to be chemically resistant and withstand exposure to UV radiation, perspiration and common cleaning protocols (soap, water, bleach etc.).<sup>39</sup> This resistance can make dyes troublesome to remove from wastewater yet a discharge of untreated effluent directly affects microorganisms, flora, and fauna as a result of water transparency and dissolved oxygen content.<sup>40</sup> Chemical oxidation methods to degrade dyes have been successful<sup>38, 41</sup>,

however, there is limited information known regarding the effects dye degradation products will have on the environment and research toward physio-adsorption of dyes is still going on.<sup>42-44</sup> Mollusc shells have been previously used as a biosorbent for aqueous dyes.<sup>45, 46</sup> SAC could be used in a batch process whereby dye is adsorbed and then desorbed using methanol so that the dye and absorbent could potentially be recycled and used again. To this end, some preliminary experiments were performed. The adsorption of crystal violet was studied at two concentrations, 0.01 and 0.1 mg/mL (limited by the strong absorption of crystal violet in the UV-vis region). After 48 h SAC adsorbs 0.1 and 1.0 wt.%, respectively from the 0.01 and 0.1 mg/mL crystal violet solutions, and led to significant reductions in concentration, **Figure 5.4a**. After desorption there is maximum removal of up to 86% and 50% for 0.01 and 0.1 mg/mL, respectively. The adsorption of fabric dye was studied using a 5 mg/mL solution with 10 mg of SAC. SAC adsorbed 20-24 wt% and was strongly coloured, **Figure 5.4b**. The dye can be removed by heating, **Figure 5.4b**, as well as using a 50/50 methanol and water mixture. Representative spectra of crystal violet and fabric dye in H<sub>2</sub>O and 50/50 methanol and water, as well as calibration curves can be found in **Figures D10 and D11**. Using the methanol solution, 36-82% of the dye can be desorbed. We note that this desorption process needs further optimization in the future as all of the dye can be desorbed by adding more methanol.

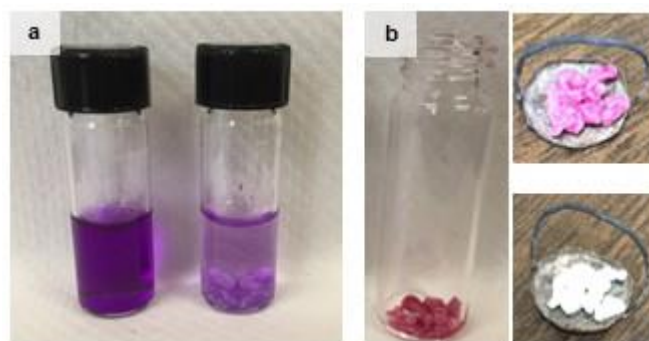


**Figure 5.4** Aqueous dye adsorption by SAC. Digital images of crystal violet (0.1 mg/mL) before and after adsorption for 48 h (a) and SAC stained with fuschia fabric dye after 24 h and before and after heat treatment at 500 °C for 10 minutes to desorb the dye (b). Dyes can also be desorbed in a MeOH/H<sub>2</sub>O solution.

### 5.2.5 Oil Recovery

For SAC to be a reliable material for practical oil clean up applications it must absorb and desorb oil with ease and be recyclable. The absorption capacity was studied over 10 cycles, in triplicate. **Figure 5.5** shows a cycle of absorption and desorption. SAC absorbed oil and stayed in the oil layer. The collection of oil-soaked SAC was simple. It was easily weighed and washed using small amounts of CHCl<sub>3</sub>. Oil absorption capacity (%), calculated by  $[(W - W_o)/W_o \times 100 (\%)]$  where  $W_o$  and  $W$  are the weight of SAC before and after absorption, respectively, as a function of cycle is shown in **Figure 5.5e**. After each desorption, the SAC was heated in an oven overnight. The average oil absorption capacity varies slightly between cycles and may be attributed to uneven drying of the SAC between runs. As a result of this systematic error in our processing, increases and decreases in oil absorption capacity were observed between cycles. Despite this, through 10 cycles, the oil absorption capacity is consistent. The lowest recorded oil absorption capacity for an individual experiment was 861% and the highest was 1130%. Within uncertainty, all the data points

are the same with an overall average of 978% +/- 84.3% from the 30 experiments. Also, some pieces of SAC were small and were lost during sample manipulation within the desorption process. Therefore, further optimization is needed but these studies are very promising. For comparison purposes, we tried absorbing crude oil with powdered BMH shells. However, the shell material could not be recovered as it did not agglomerate. Therefore, powdered BMH shells are unsuitable for oil recovery and do not have the excellent absorbent properties demonstrated by SAC.

High performance sponges have been made with carbonaceous materials<sup>47-50</sup>, such as carbon nanotubes, graphene, and polymers.<sup>51-56</sup> While some of these sponges can be made under mild conditions<sup>52</sup> they often require complicated procedures using harsh solvents,<sup>47</sup> high temperatures (i.e. pyrolysis)<sup>57</sup> and high vacuum<sup>49</sup> to achieve high porosity. The preparation of SAC technically requires heating as well as it is made using heat treated BMH shells, however 220 °C is much lower than pyrolysis temperatures.<sup>58</sup> The use of renewable materials to make absorbent sponges includes bacterial cellulose,<sup>59</sup> cotton,<sup>18</sup> and waste paper.<sup>25</sup> Of these, the most renewable is the bacterial cellulose grown by fermentation<sup>59</sup> which gives a sponge material that can absorb 100-300 times its weight in a variety of solvents and oils, but the absorption of crude oil was not studied. SAC is prepared in a simple manner, in aqueous media at room temperature using a waste material of the food industry so does not compete with crop space or paper/materials production.

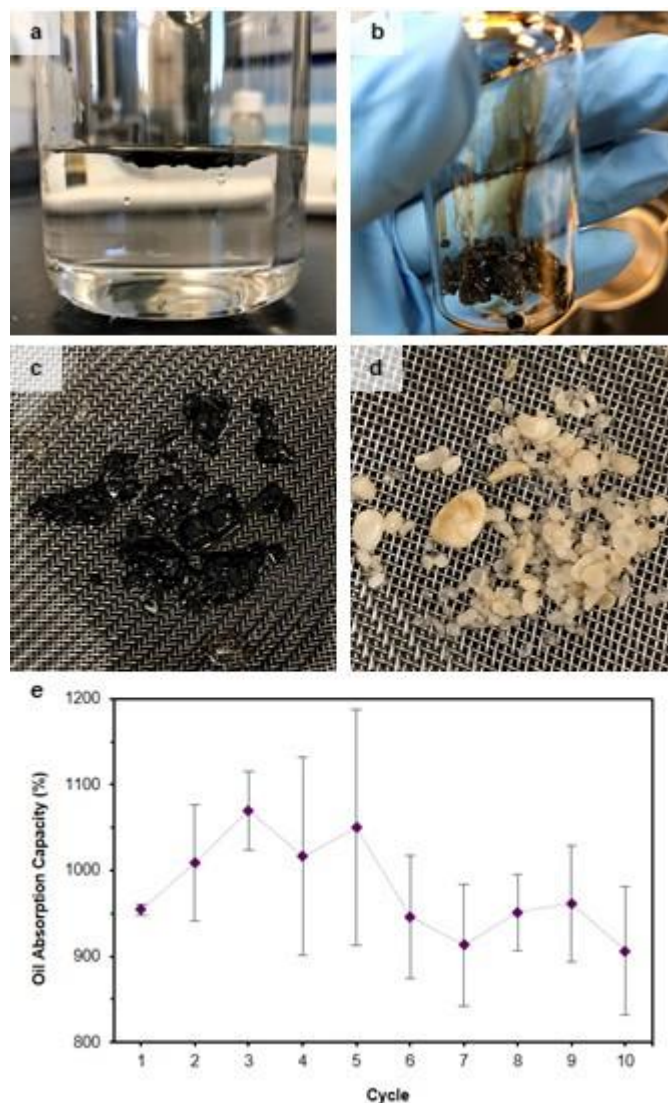


**Figure 5.5** Typical cycle of SAC crude oil absorption. Digital images of SAC added to a thin film of crude oil (a) is easily separated by a simple filtration (b) and collected for weighing (c) and finally cleaned with small volumes of  $\text{CHCl}_3$  before drying and repeating the cycle. SAC absorbs crude oil consistently over 10 cycles (e) as the oil absorption capacity is statistically the same over ten cycles. Error bars represent one standard deviation of each cycle.

### 5.3 Conclusions

In summary, an absorbent calcite material produced from waste BM shells was prepared and characterized. Results show the material is held together with residual naturally occurring organic matrix 'glue' to form a nest-like morphology. SAC is soft and deformable with a texture like candy floss (cotton candy). SAC can absorb 1-24 wt% of common dyes from water, and the dye and SAC are recoverable via complete desorption in methanol. Most impressively, SAC has an absorption capacity of 978% +/- 84.3% for crude oil and shows good recyclability over 10 re-uses. SAC is the first inorganic sponge for oil remediation. While there are several absorbent sponges made from renewable sources such as cotton and wastepaper, they still compete for land space or other important industries. It is environmentally and economically favourable to use BM waste as a raw material to make SAC because it does not compete for valuable cropland or materials production processes (e.g. recycled paper products) because it sourced from aquaculture waste. SAC is an efficient and safe absorbent for crude oil and textile dyes that shows good recyclability. These results demonstrate how a natural structure can be modified in a sustainable fashion to yield a higher value material as well as the synergistic effects of an ocean-based material aiding our oceans when in need. In addition to our absorbency studies; because of the biocompatibility of calcite, SAC may be of value in biomedical applications and the preparation of new composite materials.

## 5.4 Experimental

### 5.4.1 Materials

Blue mussels were purchased from a local grocery store or donated by processing plants in NL. Shells were cleaned, removing any organic material, using industrially available food grade protease enzymes as previously described.<sup>26</sup> Shells used without heat treatment or crushing are termed BMR (blue mussel, raw) and shells heated to 220 °C and then crushed are termed BMH (blue mussel, heated). Heinz brand vinegar was used for the 5% v/v CH<sub>3</sub>COOH. Sea Salts and crystal violet were purchased from Sigma Aldrich. Light crude oil provided by Husky Energy (Newfoundland). CH<sub>3</sub>CH<sub>2</sub>OH (absolute) was purchased from Commercial Alcohols. CHCl<sub>3</sub> (ACS grade) was purchased from ACP Chemicals. Oleic acid (tech. 90%), Citric acid (anhydrous, ACS, >99.5%), and oxalic acid (anhydrous, 98%) were purchased from Alfa Aesar. Propionic acid was purchased from Fisher Scientific. Fuschia-colored fabric dye (RIT brand) was purchased was purchased from a local craft supplier. All chemicals were used as received.

### 5.4.2 Characterization

Infrared spectroscopy (IR) was performed using a Bruker Alpha FTIR spectrometer fitted with a single bounce diamond ATR accessory. IR spectra were collected with a resolution of 2 cm<sup>-1</sup>. All measurements were conducted in triplicates, averaged and plotted in Excel. Solid-state NMR spectra were obtained at 298 K using a Bruker Avance II 600 spectrometer, equipped with a SB Bruker 3.2 mm MAS triple-tuned probe operating at 600.33 MHz for <sup>1</sup>H and 150.97 MHz for <sup>13</sup>C nuclei. Chemical shifts were referenced to tetramethylsilane (TMS) using adamantane as an intermediate standard for <sup>13</sup>C. The

samples were spun at 20 kHz in 3.2 mm zirconia rotors. Cross-polarization (CPMAS) spectra were collected with a Hartmann-Hahn match at 62.5 kHz and 100 kHz  $^1\text{H}$  decoupling, a contact time of 1 ms, a recycle delay of 1 s and 16k scans. Thermogravimetric analysis (TGA) was carried out using a TA Instruments Q500 TGA under high resolution dynamic mode. Samples were heated at a rate of  $5.0\text{ }^\circ\text{C min}^{-1}$  under a  $\text{N}_2$  atmosphere ( $50\text{ mL min}^{-1}$ ) from 25-800  $^\circ\text{C}$ . Scanning electron microscopy (SEM) images of carbon coated materials were obtained using a FEI MLA 650 FEG under high vacuum ( $10^{-6}$  torr). The voltage of 10-15 kV and current of 10 mA at a working distance of 10.5-14.4 mm produced a 5.8 spot. A SDD was used for BSED. Powder X-ray diffraction (XRD) was performed using a Rigaku Ultima IV XRD equipped with  $\text{Cu K}\alpha$  radiation ( $\lambda=1.5406\text{ \AA}$ ) at 40 kV and 44 mA. The  $2\theta$  region was scanned from 0-100 $^\circ$  with a step size of 0.02 $^\circ$ .  $\text{N}_2$  gas adsorption isotherms were collected on a Micrometrics Tristar II 3020 instrument with the sample maintained at 77 K using  $\text{N}_2(\text{l})$ . Before measurements, samples were super-critically dried with  $\text{CO}_2(\text{l})$  and were not activated. UV-vis was performed on a dual-beam Thermo Scientific Evolution 300 UV-vis spectrophotometer equipped with a xenon lamp, using quartz cuvettes with a 1 cm pathlength. Elemental analysis was performed by Guelph Chemical Laboratories Ltd.

#### **5.4.3 Preparation of Self Assembled Calcite (SAC)**

Aqueous  $\text{CH}_3\text{COOH}$  (75.0 mL) and BMH shells (5.0 g,  $\sim 0.050\text{ mol CaCO}_3$ ) were combined in a 250 mL Erlenmeyer flask and placed on a VWR Mini Shaker rotating at 180 rpm for 24 h. The resulting colourless  $\text{Ca}(\text{CH}_3\text{COO})_2$  solution was decanted for subsequent crystallisation and the remaining shells (2.5 g) were rinsed 3 times with distilled water and

left to air dry. The residual shells from several preparations of  $\text{Ca}(\text{CH}_3\text{COO})_2$  were combined and then used in a subsequent reaction after air-drying for 5 days. Residual shells (6.6 g,  $\sim 0.066$  mol  $\text{CaCO}_3$ ) and  $\text{CH}_3\text{COOH}$  (75 mL) were combined in a 250 mL Erlenmeyer flask and placed on a shaker rotating at 180 rpm for 25 h. After this time, there were spherical-shaped masses with a sponge-like texture (self-assembled calcite, SAC) floating within the solution. SAC was decanted with the solution of  $\text{Ca}(\text{CH}_3\text{COO})_2$ . Residual shell could be used in later preparations of SAC. SAC (200 mg) was with small amounts (10 mL) of distilled water. SAC (200 mg) was further purified by gently agitating it on the shaker in distilled water (25 mL) and exchanging the water frequently. SAC (200 mg) was further washed with ethanol (25 mL) and dried in a vacuum oven overnight at 60 °C. SAC was characterized using IR, Powder XRD, SSNMR spectroscopy, TGA, BET, Elemental Analysis, and SEM. On average, 200 mg of SAC was prepared.

#### **5.4.4 Isolation of insoluble organic matrix**

Aqueous  $\text{CH}_3\text{COOH}$  (75.0 mL) and BMR shells (10.0 g,  $\sim 0.100$  mol  $\text{CaCO}_3$ ) were combined in a 250 mL Erlenmeyer flask and placed on the bench top, unagitated for 24 h. At this stage, large sheets of insoluble organic matrix were removed from the shell. The organic matrix was cleaned by washing with distilled water several times before drying overnight between two sheets of filter paper.

#### **5.4.5 Dye Adsorption/Desorption**

The method of detection used for this study was UV-vis spectroscopy. Calibration curves for the two dyes were constructed using distilled  $\text{H}_2\text{O}$  and 50:50 distilled  $\text{H}_2\text{O}:\text{CH}_3\text{OH}$  to

assess adsorption and desorption of the dyes onto the SAC. SAC (10 mg) was added to dye solutions (2.00 mL) of fabric dye (RIT, 5 mg/mL) and crystal violet (0.01 and 1.0 mg/mL) for 24-48 h period. After this time, UV-vis was performed and the mass of dye remaining in solution was determined. The dye-adsorbed SAC was dried overnight at ambient temperatures. CH<sub>3</sub>OH (2.00 mL) dye-adsorbed SAC and left to stand for 24 h. The mass of dye desorbed was determined once again by UV-vis spectroscopy. Dye could also be removed by heating the dye-adsorbed SAC at 500 °C for 10 minutes and the SAC re-used.

#### **5.4.6 Oil Recovery**

Synthetic seawater (35.0 parts per thousand, prepared using Sigma Aldrich Sea Salts in a volumetric flask) and crude oil were cooled to 7 °C using a circulating chiller. In a 100 mL beaker, oil (~2 g) was dropped onto the surface of the synthetic seawater (50 mL) to make a thin film. Approx. 50 mg of SAC was added to the beaker. After 1 min, the mixture was filtered through a metal mesh colander to separate the oil-soaked SAC from the synthetic seawater. The oil-soaked SAC was weighed, and the mass of oil absorbed was calculated. The SAC was then washed with 3 × CHCl<sub>3</sub> (10 mL) and then dried in an oven overnight at 70 °C. This process was repeated in triplicate for 10 cycles to study the recyclability of SAC for oil recovery. Small amounts of SAC were lost during the cleaning process and it was reweighed at the start of each cycle.

## 5.5 References

1. U. G. K. Wegst, H. Bai, E. Saiz, A. P. Tomsia and R. O. Ritchie, *Nat. Mater.*, 2015, **14**, 23-36.
2. F. Nudelman and N. A. J. M. Sommerdijk, *Angew. Chem., Int. Ed.*, 2012, **51**, 6582-6596.
3. H. A. Lowenstam and S. Weiner, *On biomineralization*, Oxford University Press, 1989.
4. A. H. Heuer, D. J. Fink, V. J. Laraia, J. L. Arias, P. D. Calvert, K. Kendall, G. L. Messing, J. Blackwell, P. C. Rieke, D. H. Thompson, A. P. Wheeler, A. Veis and A. I. Caplan, *Science*, 1992, **255**, 1098-1105.
5. H.-L. Gao, S.-M. Chen, L.-B. Mao, Z.-Q. Song, H.-B. Yao, H. Cölfen, X.-S. Luo, F. Zhang, Z. Pan, Y.-F. Meng, Y. Ni and S.-H. Yu, *Nat. Commun.*, 2017, **8**, 287.
6. L.-B. Mao, H.-L. Gao, H.-B. Yao, L. Liu, H. Cölfen, G. Liu, S.-M. Chen, S.-K. Li, Y.-X. Yan, Y.-Y. Liu and S.-H. Yu, *Science*, 2016, **354**, 107-110.
7. Y.-Y. Kim, J. D. Carloni, B. Demarchi, D. Sparks, D. G. Reid, Miki E. Kunitake, C. C. Tang, M. J. Duer, C. L. Freeman, B. Pokroy, K. Penkman, J. H. Harding, L. A. Estroff, S. P. Baker and F. C. Meldrum, *Nat. Mater.*, 2016, **15**, 903-910.
8. F. Natalio, T. P. Corrales, M. Panthofer, D. Schollmeyer, I. Lieberwirth, W. E. G. Muller, M. Kappl, H. J. Butt and W. Tremel, *Science*, 2013, **339**, 1298-1302.
9. E. Loste, R. J. Park, J. Warren and F. C. Meldrum, *Adv. Funct. Mater.*, 2004, **14**, 1211-1220.

10. Y.-J. Han, L. M. Wysocki, M. S. Thanawala, T. Siegrist and J. Aizenberg, *Angew. Chem., Int. Ed.*, 2005, **44**, 2386-2390.
11. T. Y.-J. Han and J. Aizenberg, *Chem. Mater.*, 2008, **20**, 1064-1068.
12. H.-B. Yao, J. Ge, L.-B. Mao, Y.-X. Yan and S.-H. Yu, *Adv. Mater.*, 2014, **26**, 163-188.
13. E. M. Gerhard, W. Wang, C. Li, J. Guo, I. T. Ozbolat, K. M. Rahn, A. D. Armstrong, J. Xia, G. Qian and J. Yang, *Acta Biomater.*, 2017, **54**, 21-34.
14. L. Li and C. Ortiz, *Nat. Mater.*, 2014, **13**, 501-507.
15. E. Loste and F. C. Meldrum, *ChemComm*, 2001, DOI: 10.1039/b101563j, 901-902.
16. F. Nudelman, H. H. Chen, H. A. Goldberg, S. Weiner and L. Addadi, *Faraday Discuss.*, 2007, **136**, 9-25.
17. C. Xiao, M. Li, B. Wang, M.-F. Liu, C. Shao, H. Pan, Y. Lu, B.-B. Xu, S. Li, D. Zhan, Y. Jiang, R. Tang, X. Y. Liu and H. Cölfen, *Nat. Commun.*, 2017, **8**, 1398.
18. H. Bi, Z. Yin, X. Cao, X. Xie, C. Tan, X. Huang, B. Chen, F. Chen, Q. Yang, X. Bu, X. Lu, L. Sun and H. Zhang, *Adv. Mater.*, 2013, **25**, 5916-5921.
19. F. M. Kerton, Y. Liu, K. W. Omari and K. Hawboldt, *Green Chem.*, 2013, **15**, 860-871.
20. N. Yan and X. Chen, *Nature*, 2015, **524**, 155-157.
21. R. R. Gentry, S. D. Gaines, B. S. Halpern, H. E. Froehlich, B. S. Halpern, D. Grimm, P. Kareiva, M. Parke, M. Rust and B. S. Halpern, *Nat. Ecol. Evol.*, 2017, **1**, 1317-1324.

22. J. N. Murphy and F. M. Kerton, in *Fuels, Chemicals and Materials from the Oceans and Aquatic Sources* eds. F. M. Kerton and N. Yan, Wiley, 2017, ch. Characterization and utilization of waste streams from mollusc aquaculture and fishing industries, pp. 189-225.
23. J. P. Morris, T. Backeljau and G. Chapelle, *Rev. Aquacult.*, 2018, **11**, 42-57.
24. M. L. Mai, M. Emmett, M. S. Sheikh, C. A. Santa Ana, L. Schiller and J. S. Fordtran, *Kidney Int.*, 1989, **36**, 690-695.
25. H. Bi, X. Huang, X. Wu, X. Cao, C. Tan, Z. Yin, X. Lu, L. Sun and H. Zhang, *Small*, 2014, **10**, 3544-3550.
26. J. N. Murphy, K. Hawboldt and F. M. Kerton, *Green Chem.*, 2018, **20**, 2913-2920.
27. F. Marin and G. Luquet, *Comptes Rendus Palevol*, 2004, **3**, 469-492.
28. B. Pokroy, A. N. Fitch and E. Zolotoyabko, *Adv. Mater.*, 2006, **18**, 2363-2368.
29. S. J. Koehler, P. Cubillas, J. D. Rodriguez-Blanco, C. Bauer and M. Prieto, *Environ. Sci. Technol.*, 2007, **41**, 112-118.
30. C. E. Weir and E. R. Lippincott, *J. Re. Nat. Stand. Sec. A*, 1961, **65A**, 173-183.
31. M. I. Jones, L. Y. Wang, A. Abeynaïke and D. A. Patterson, *Adv. App. Ceram.*, 2011, **110**, 280-286.
32. C. Rombaldi, J. L. de Oliveira Arias, G. I. Hertzog, S. S. Caldas, J. P. Vieira and E. G. Primel, *Anal. Bioanal. Chem.*, 2015, **407**, 4805-4814.
33. K. Tekin, *Energy Fuels*, 2015, **29**, 4382-4392.
34. A. Abeynaïke, L. Wang, M. I. Jones and D. A. Patterson, *Asia-Pac. J. Chem. Eng.*, 2011, **6**, 231-243.

35. I. Ben Shir, S. Kababya, I. Katz, B. Pokroy and A. Schmidt, *Chem. Mater.*, 2013, **25**, 4595-4602.
36. C. Jäger and H. Cölfen, *CrystEngComm*, 2007, **9**, 1237-1244.
37. S. S. Muthu, *Sustainable innovations in textile chemistry and dyes*, Springer, Singapore, 2018.
38. N. Chahbane, D.-L. Popescu, D. A. Mitchell, A. Chanda, D. Lenoir, A. D. Ryabov, K.-W. Schramm and T. J. Collins, *Green Chem.*, 2007, **9**, 49-57.
39. H. Zollinger, *Color chemistry: Syntheses, properties and applications of organic dyes and pigments*, Wiley, Weinheim, 3rd edn., 2003.
40. F. Duarte, V. Morais, F. J. Maldonado-Hódar and L. M. Madeira, *Chem. Eng. J.*, 2013, **232**, 34-41.
41. L. L. Tang, A. D. Ryabov and T. J. Collins, *ACS Catal.*, 2016, **6**, 3713-3718.
42. V. S. Mane, I. Deo Mall and V. Chandra Srivastava, *J. Environ. Manage.*, 2007, **84**, 390-400.
43. P. N. Nguyet, Y. Hata, N. Maharjan, T. Watari, M. Hatamoto and T. Yamaguchi, *Environ. Technol.*, 2018, DOI: 10.1080/09593330.2018.1534000, 1-10.
44. S. Mondal, M. K. Purkait and S. De, *Advances in dye removal technologies*, Springer, Singapore, 2018.
45. D. Suteu, D. Bilba, M. Aflori, F. Doroftei, G. Lisa, M. Badeanu and T. Malutan, *Clean: Soil, Air, Water*, 2012, **40**, 198-205.
46. M. El Haddad, A. Regti, M. R. Laamari, R. Slimani, R. Mamouni, S. E. Antri and S. Lazar, *J. Taiwan Inst. Chem. Eng.*, 2014, **45**, 533-540.

47. X. Gui, J. Wei, K. Wang, A. Cao, H. Zhu, Y. Jia, Q. Shu and D. Wu, *Adv. Mater.*, 2010, **22**, 617-621.
48. E. A. Daza, S. K. Misra, J. Scott, I. Tripathi, C. Promisel, B. K. Sharma, J. Topczewski, S. Chaudhuri and D. Pan, *Sci. Rep.*, 2017, **7**, 41880.
49. H.-W. Liang, Q.-F. Guan, L.-F. Chen, Z. Zhu, W.-J. Zhang and S.-H. Yu, *Angew. Chem., Int. Ed.*, 2012, **51**, 5101-5105, S5101/5101-S5101/5113.
50. H. Bi, X. Xie, K. Yin, Y. Zhou, S. Wan, R. S. Ruoff and L. Sun, *J. Mater. Chem. A*, 2014, **2**, 1652-1656.
51. N. Leventis, C. Chidambareswarapattar, A. Bang and C. Sotiriou-Leventis, *ACS Appl. Mater. Interfaces*, 2014, **6**, 6872-6882.
52. G. Hayase, K. Kanamori, M. Fukuchi, H. Kaji and K. Nakanishi, *Angew. Chem., Int. Ed.*, 2013, **52**, 1986-1989.
53. J. Ge, L.-A. Shi, Y.-C. Wang, H.-Y. Zhao, H.-B. Yao, Y.-B. Zhu, Y. Zhang, H.-W. Zhu, H.-A. Wu and S.-H. Yu, *Nat. Nanotechnol.*, 2017, **12**, 434.
54. G. Wang and H. Uyama, *Sci. Rep.*, 2016, **6**, 21265.
55. D. H. Kim, M. C. Jung, S.-H. Cho, S. H. Kim, H.-Y. Kim, H. J. Lee, K. H. Oh and M.-W. Moon, *Sci. Rep.*, 2015, **5**, 12908.
56. C. Ruan, K. Ai, X. Li and L. Lu, *Angew. Chem., Int. Ed.*, 2014, **53**, 5556-5560.
57. Y. Yang, Z. Tong, T. Ngai and C. Wang, *ACS Appl. Mater. Interfaces*, 2014, **6**, 6351-6360.
58. J.-L. Wertz and O. Bédué, *Lignocellulosic Biorefineries*, EPFL Press, New York, 2013.

59. Z.-Y. Wu, C. Li, H.-W. Liang, J.-F. Chen and S.-H. Yu, *Angew. Chem., Int. Ed.*, 2013, **52**, 2925-2929.

## **Chapter 6 Bio-renewable calcite as an inorganic filler in ionic liquid gel polymer electrolytes for supercapacitors**

**See Appendix E for additional data.**

A version of this chapter is in preparation for a manuscript.

Jennifer N. Murphy Tiago C. Mendes, Mega Kar, Francesca M. Kerton and Douglas R. MacFarlane

### **6.1 Introduction**

With the global abuse of fossil fuels to power modern civilization leading to limited resources and climate change, a global shift towards sustainable and renewable resources is more urgent than ever.<sup>1</sup> Energy systems play a large role in our lives, so electrical storage systems, such as batteries and electrochemical capacitors (ECs), are at the forefront for renewable energy.<sup>2</sup> ECs or supercapacitors are high power density charge storage devices with a much longer cycle life compared to rechargeable batteries that stems from the electrostatic process at the electrode-electrolyte interface.<sup>3,4</sup> They are used in a broad range of applications ranging from portable electronics to electric vehicles and even heavy machinery. ECs are safer during rapid charging and discharging compared to batteries. While often used in a circuit accompanying a battery, ECs can replace batteries in applications where high delivery or uptake, or power is required.<sup>2</sup> However, the energy

storage capacity is lower than batteries and research toward increasing this metric is gaining popularity. In order to improve the performance of ECs there are two components of the device that can be altered, the electrode material and the electrolyte. Energy density is directly proportional to the square of the potential,  $E = \frac{1}{2} CV^2$ , where C is capacitance and V is potential. Aqueous electrolytes are limited to a potential of approximately 2 V.<sup>5</sup> While the maximum potential of 2.7 V for organic electrolytes is much higher than aqueous electrolytes, their flammability and toxicity make organic electrolytes hazardous.<sup>6</sup> Therefore, investigating electrolytes with higher operating potentials while also being inherently more safe is attractive for clean energy applications. Ionic Liquids (ILs) have high conductivities and wider electrochemical windows than organic and aqueous electrolytes and have been explored as electrolytes in supercapacitors to increase the maximum cell voltage, thereby increasing the maximum energy density.<sup>6-9</sup> ILs are chemically and thermally stable and their non-flammability and negligible volatility make them inherently safer than organic electrolytes.

ILs are much more viscous than organic and aqueous electrolytes, however, a leakage risk still exists for ECs. The construction of a safe and secure electrochemical device hinges on removing this risk of leakage. ILs have been used to make gel polymer electrolytes, a combination of polymer and IL where the IL is entrapped in the polymer, making a solid-state electrolyte/separator with additional mechanical and interfacial stability than typical electrolytes.<sup>10-14</sup> Solid electrolytes reduce leaking of ECs and helps to maintain good electrode-electrolyte contact.<sup>15, 16</sup> Ionic liquid-based gel polymer electrolytes (ILGPEs) have been synthesized using a plethora of ionic liquids and polymer combinations and used in lithium batteries and electrochemical supercapacitors.<sup>17-20</sup> Research has shown the

chemical, mechanical stability and conductivity of ILGPEs can be improved further with the addition of passive inorganic fillers (one that is not involved in the conduction process) such as ceramics (ie. SiO<sub>2</sub>) and zeolites because they disturb crystal packing of the polymer and the electrolyte (IL) can move more freely.<sup>11, 17, 21-23</sup> These fillers can also act as a diluent and reduce the cost of the ILGPE.

Many reports have focused on the renewability of the carbon electrode material through the conversion of biomass to porous carbon for electrodes for ECs.<sup>8, 24, 25</sup> To my knowledge, the sustainability of an inorganic or ceramic filler component that can be used in order to improve stability or mechanical properties of the ILGPE and reduce the cost, has not been considered. In the previous chapter (**Chapter 5**), the discovery and characterization of a unique biorenewable self-assembling calcite (SAC) material that was prepared from waste blue mussel shells was presented. Unlike the hard and brittle calcite that makes up mussel shells, this expanded calcite is soft and compressible with a texture similar to candy floss. In the current chapter, the addition of this sustainable inorganic filler into ILGPEs made with 1-ethyl-3-methylimidazolium bis(trifluoromethylsulfonyl)imide [EMIM][NTf<sub>2</sub>] and Poly vinylidene fluoride-co-hexafluoropropylene (PVdF-co-HFP) is described. The effects of the addition of the calcite on the ILGPE were investigated using electrochemical impedance spectroscopy (EIS), infrared spectroscopy (IR), thermogravimetric analysis (TGA), differential scanning calorimetry (DSC) and scanning electron microscopy (SEM). Symmetric coin cell capacitors were fabricated using the ILGPE with and without calcite for direct comparison purposes. The performance of the ECs was studied by EIS, cyclic voltammetry (CV) and galvanostatic charge-discharge cycling.

## 6.2 Results and Discussion

Prior to adding in the SAC filler, the ratio of PVdF-co-HFP added to [EMIM][NTf<sub>2</sub>] was investigated in order to find an optimal ratio so that the resulting ILGPE was strong and flexible. [EMIM][NTf<sub>2</sub>]:PVdF-co-HFP ratios (by weight) investigated were 88:12, 84:16 80:20. ILGPEs with [EMIM][NTf<sub>2</sub>]:PVdF-co-HFP ratios of 88:12 and 84:16 were not rigid and tore very easily. The ILGPE with [EMIM][NTf<sub>2</sub>]:PVdF-co-HFP ratio of 80:20 was strong and flexible. Therefore, the effect of adding varying amounts (0.5-4 wt%) of SAC from mussel shells as a percentage of the total mass of [EMIM][NTf<sub>2</sub>]:PVdF-co-HFP with an 80:20 ratio of IL to polymer was studied. An ILGPE control, [EMIM][NTf<sub>2</sub>]:PVdF-co-HFP with an 80:20 ratio of IL to polymer but no calcite, was used for comparison purposes and is herein abbreviated as ILGPE-I.

### 6.2.1 Ionic Conductivity

The ILGPE films were 100-160 μm thick and this made ionic conductivity measurements difficult to obtain. The addition of a 0.5 and 1 wt% calcite had a negative effect on the conductivity and did not enhance the mechanical stability of the film. The best ILGPE film, with respect to being strong and flexible and easy to handle and a minimal decline in ionic conductivity was the ILGPE with an IL to polymer ratio of 80:20 and 2 wt% of calcite incorporated, here on abbreviated as ILGPE-II. Films with 4 wt% calcite PVdF-co-HFP (ILGPE-III) initially had good conductivity, however this film was difficult to handle (not rigid) and would tear very easily. Therefore, it was decided to move forward with ILGPE-I and -II for more in-depth characterization and fabrication of supercapacitors.

The ionic conductivity of the ILGPE-I and -II at 25 °C was 4.3 and 2.7 mS/cm, respectively. The ionic conductivities for these two films were measured in triplicate. An Arrhenius plot of the ionic conductivities can be found in Appendix E, **Figure E1**. There is a decrease in conductivity for the ILGPE-II as we expected because it has less IL than ILPGE-I. However, the ionic conductivity of ILGPE-II is still higher or on par with other ILGPEs containing imidazolium based ILs, with or without inorganic additives,<sup>7, 11, 20-22, 26</sup> especially considering there are no ionic conductivity boosting compounds added, such as metal salts, organic carbonates and/or sulpholane.<sup>23, 27-30</sup> Additionally, the ionic conductivity of 2.7 mS/cm for ILGPE-II is consistent with reports of polymer blend composite electrolytes used for Li ion batteries that contain powdered CaCO<sub>3</sub>.<sup>31, 32</sup>

### 6.2.2 ILGPE Characterization

**Figure 6.1a** shows IR spectra of three films, ILGPE-I, -II, and -III, respectively. All characteristic absorptions for calcite were masked by the [EMIM][NTf<sub>2</sub>] and PVdF-co-HFP except for one band at 710 cm<sup>-1</sup> which corresponds to the O-C-O bend of the CO<sub>3</sub><sup>2-</sup> in calcite.<sup>33</sup> The intensity of this band increases as more calcite is added and is absent in the control film, ILGPE-I. Thermogravimetric analysis of ILGPE-I and -II, **Figure 6.1b**, show the two films have near identical thermal stability, beginning to decompose at 350 °C. ILGPE-I and -II also have the same glass transition temperature, -95.0 °C, as determined by DSC, see **Appendix E**, which suggests the properties of the two films are the same. Surface morphologies of the ILGPEs were characterized by SEM. **Figure 6.2** shows representative images for the surface and edges of ILGPE-II. There are very clear porous

regions where the prismatic calcite is visible. The differences in rigidity of ILGPE-III and

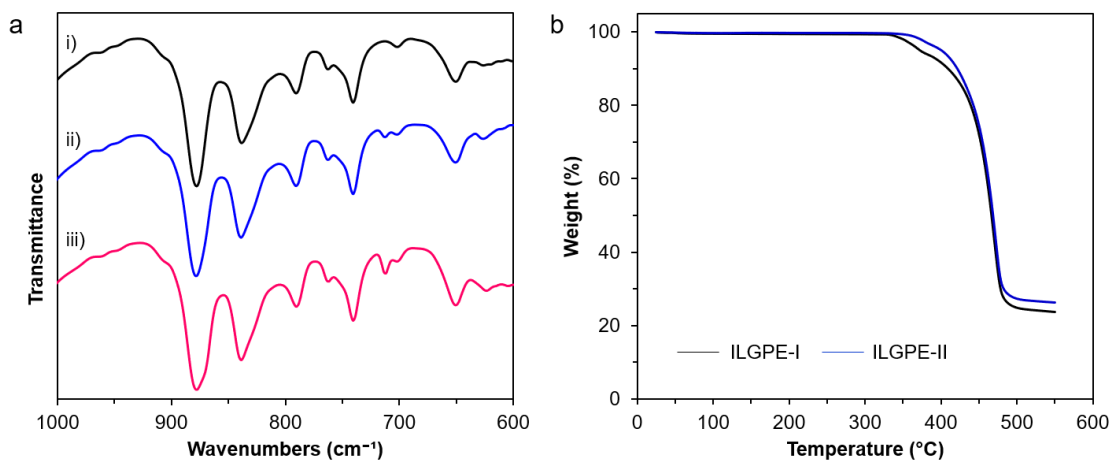


**Figure 6.1** a) FTIR spectra of ILGPEs to show the incorporation of calcite. i) ILGPE-I, ii) ILGPE-II, and iii) ILGPE-III. b) Thermogravimetric analysis of ILGPE-I and ILGPE-II.

ILGPE-II are shown in **Figure 6.2c** and **d**. ILGPE-III bends under its own weight whereas ILGPE-II remains straight (i.e. rigid). Cross section micrographs of ILGPE-I and -II are presented in **Appendix E**. The cross-section morphology is the same for both films. The calcite incorporation is homogenous, and crystals are directed along the plane of the film. That is, the calcite is aligned parallel to the surface and not pointing out of the film. The addition of calcite to the ILGPE changes the volume of the mixture. This means the amount of IL per film can be adjusted and decreases the cost of the electrolyte by 17%. Electrochemical measurements were performed to assess the performance of the ILGPE-II in comparison to ILGPE-I to see how the addition of calcite affects capacitance and cycling stability. ILGPE-I and -II were used in the fabrication of symmetric electrochemical

capacitors called Cell-I and -II, respectively and were subject to the same electrochemical testing.

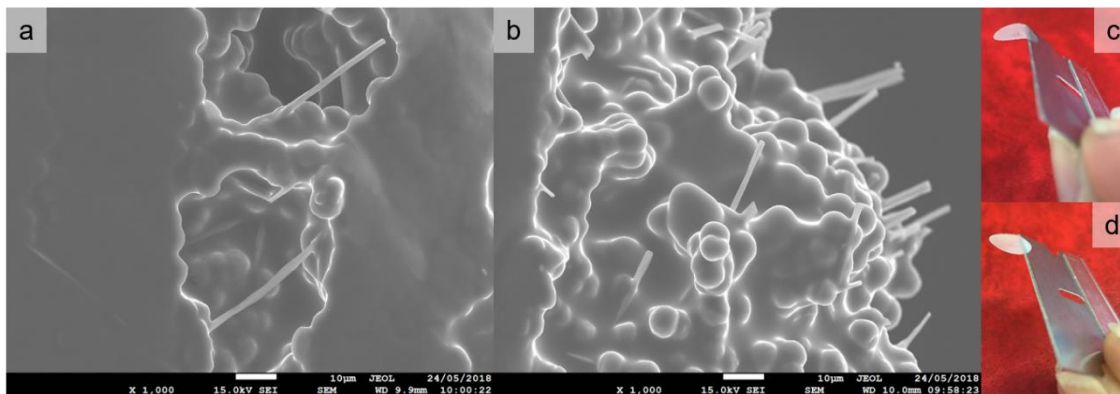


**Figure 6.2** SEM micrographs of a) porous region and b) edge region of ILGPE-II and digital images of c) ILGPE-III and d) ILGPE-II.

### 6.2.3 Electrochemical Measurements

Cyclic voltammetry was used to explore different operating potentials at a scan rate of 100 mV/s to determine the potential window Cell-I and -II. 30 cycles at each voltage were first performed to stabilize the supercapacitors. The results were very similar for both supercapacitors, with the results for Cell-II shown in **Figure 6.3a** and **3b** and results for Cell-I found in **Appendix E**. Above 3.5 V the voltammogram is no longer rectangle shaped and exhibits a sharp increase in voltage. This is likely due to partial decomposition of the IL at this high voltage and the current becomes partly faradaic. Even though the electrochemical window of the pure IL has been reported to be 4V,<sup>11</sup> many have reported a limitation to the electrochemical window when the ILs are incorporated in GPEs.<sup>26</sup>

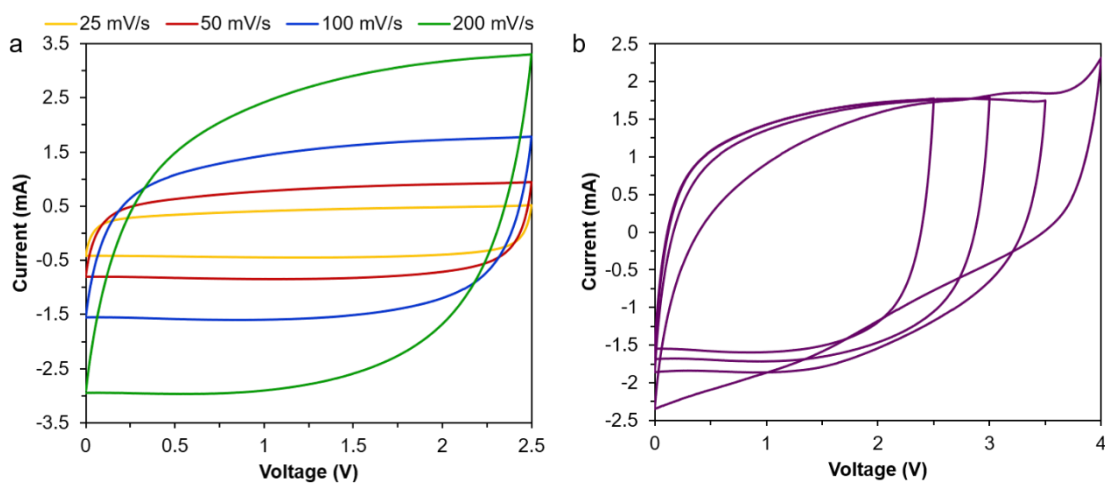


**Figure 6.3** Cyclic voltammograms of Cell II at a) different scan rates and b) different operating potentials at a scan rate of 100 mV/s.

**Figure 6.3a** shows that while an increase in current is observed from 25 to 200 mV/s, the rectangular shape becomes increasingly distorted as a result of the resistance of the device. The specific capacitance of Cell-I and -II as calculated from the CVs ( $C = 2(\Delta i/sm)$ , where  $i$  is current,  $s$  is the scan rate, and  $m$  is the mass of active carbon on one electrode) were very similar (Cell-I = 153, 146 133 and 109 F/g, and Cell-II= 147, 140, 129 and 114F/g at 25, 50, 100 and 200 mV/s, respectively).

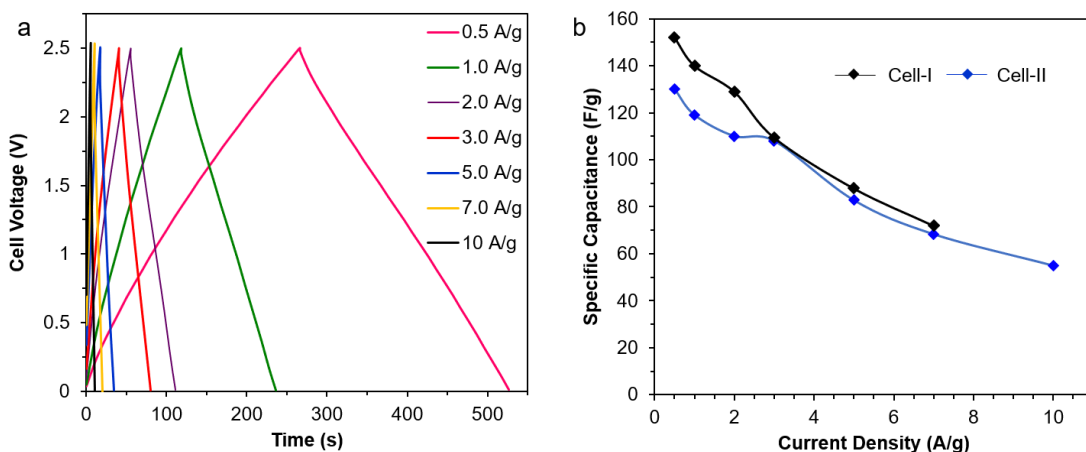


**Figure 6.4** a) Galvanostatic discharge curves for Cell II at various current densities and b) specific capacitance of Cell I (black) and Cell II (blue) as a function of current densities.

Galvanostatic charge-discharge curves of both supercapacitors at current densities ranging from 0.5-7 A/g have a symmetric triangle shape that is distinctive of double-layer capacitors with a high coulombic efficiency. This means that the charge coming out of the device is nearly 100% the charge that went into the device. **Figure 6.4a** shows the charge-discharge curve of Cell-II is very symmetric with nearly linear charge and discharge behavior. Specific capacitances as a function of current density for Cell-I and -II are shown in **Figure 6.4b**. The specific capacitances are calculated from the discharge capacity from galvanostatic cycling as per  $C = 2 (I\Delta t/mV)$ , where  $I\Delta t/m$  is the discharge capacity,  $m$  is the mass of active carbon on one electrode and  $V$  is the potential the device was charged to. highest specific capacitance for Cell-II was 130 F/g at a current density of 0.5 A/g, about 15% less that of Cell-I at the same current density. At 2 A/g, the specific capacitance of Cell-II was 110 F/g whereas the Cell-I was 129 A/g. The differences in capacitance between Cell-I and -II are expected due to the lower ionic conductivity of the ILGPE in Cell-II

because it contains less IL. However, at current densities beyond 2 A/g, the specific capacitance of Cell-I and Cell-II were nearly the same. Interestingly, at 10 A/g, Cell-I stopped working (failed to charge) while Cell-II, that contains ILGPE-II (the one with calcite) remained operational. It is normal for the specific capacitance to decrease with increase in current density as a result of the increasingly restricted movement of the ions into the nanoporous structure of the carbon material.

#### **6.2.4 Impedance Spectroscopy**

Charge transfer processes and ionic transport of the supercapacitors were investigated by EIS, **Figure 6.5a**. There are three parts of the Nyquist plot that are important for determining information about how the device charges and how ions interact at the electrolyte/electrode interface; i) where the EIS curve intercepts the real axis (X-axis) is used to estimate the value of the equivalent series resistance (ESR) of the device, ii) the diameter of the first semicircle provides an estimate of the charge transfer resistance ( $R_{CT}$ ) and iii) the behaviour of the curve at the lowest frequencies determines whether the device is a true capacitor. The equivalent series resistance (ESR) is 6.7  $\Omega$  and 4.6  $\Omega$  for Cell-II and -I, respectively. The charge transfer resistance ( $R_{CT}$ ) was found to be 46.9  $\Omega$  for the Cell-II and 57.4  $\Omega$  for the Cell-I. This significant difference of more than 10  $\Omega$  for the  $R_{CT}$  given the similarity of the ESR between the two films is evidence that Cell-II has better charge transfer and ion diffusion than the Cell-I under these conditions, adding to its stability and rate capability. Both supercapacitors have a near vertical line along the imaginary axis (Y-axis) at the lowest frequencies, further confirming capacitive behaviour. The differences in

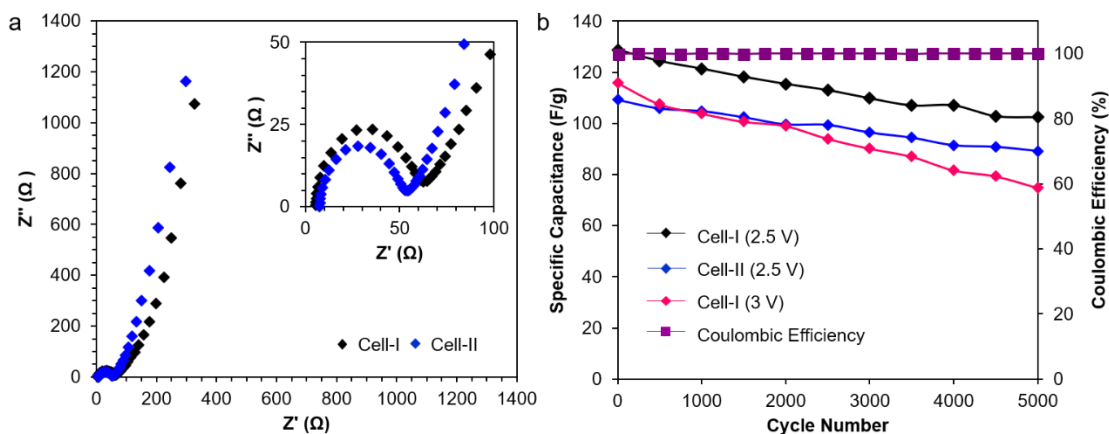


**Figure 6.5** a) Nyquist plot for Cell I (black) and Cell II (blue). Inset: Magnified high frequency region. b) Cyclic stability of Cell I and Cell II at a current density of 2 A/g. Data in black and blue shows the respective cells charging to 2.5 V and data in pink shows Cell I charging to 3.0 V. Secondary axis shows Coulombic efficiency (purple) for Cell II over 5000 cycles.

charge transfer resistance between Cell-I and -II led to the investigation of differences in the stiffness between ILGPE-I and -II. Dynamic mechanical analysis (DMA) was performed on the ILGPEs to determine if there were any differences in the shear measurement mode (deformation of shape). An oscillatory force (stress) is applied to the materials and the resulting displacement (strain) is measured. The storage modulus relates to the energy stored in a material and the loss modulus relates to energy that is dissipated as heat. According to DMA results, **Appendix E**, at 25 °C, the storage modulus, loss modulus and tan delta for the ILGPE-I and -II were 8.22 MPa, 0.924, 0.122 and 2.80 MPa, 0.654, and 0.233, respectively. The storage modulus is a measure of stiffness of the material; therefore, ILGPE-I is about 3 times stiffer than ILGPE-II. The needle like morphology of the calcite provides an entangled semi-rigid network within the electrolyte material that has a certain degree of flexibility and compliance, thus improving the

mechanical properties of the gel. The softness and ease which ILGPE-II can be compressed may account for superior electrolyte-electrode contact which would result in better charge transfer and ion diffusion exhibited by Cell-II by EIS.

Galvanostatic cycling (**Figure 6.5b**) the supercapacitors revealed that Cell-II devices were more stable at 2.5 V as compared to 3 V. Cell-II at 2.5 V and 2 A/g showed excellent stability, dropping just 18.5% in specific capacitance with coulombic efficiency remaining >99% after 5000 cycles. Charging to 3 V at a current density of 2 A/g Cell-II was not as stable, with a 35.5% decrease in the specific capacitance despite high coulombic efficiency. Cell-I was as stable as Cell-II having high coulombic efficiency and a 20.5% decrease in specific capacitance after 5000 cycles. This shows that by incorporating the calcite into the ILGPE films has not decreased the stability or lifetime of the device.

The Ragone plot (**Figure 6.6**) of a supercapacitor is used to show the relationship of energy density to power density. Energy (E) density and power (P) density were calculated using  $E = \frac{1}{2} C_{\text{cell}} V^2$  and  $P = E/\Delta t$  where  $C_{\text{cell}}$  is the specific capacitance of the whole cell, V is the cell potential and  $\Delta t$  is the time it takes for the supercapacitor to discharge. The highest energy density occurs at the lowest current density and the highest power density occurs at the highest current density. The power and energy density of Cell-I and Cell-II were very similar, meaning the inorganic calcite filler did not have a detrimental effect on the most critical criteria for the supercapacitor. In fact, because Cell-II could be studied at a current density of 10 A/g (in terms of the mass of the electrode material), it has a higher power density than Cell-I.

Cell-I had a high energy density of 33.0 Wh/kg at a power density of 0.385 kW/kg. At a higher power density of 5.51 kW/kg, the energy density remained high at 15.6 Wh/kg. Cell-II had a high energy density of 28.2 Wh/kg at a power density of 0.391 kW/kg. Cell-II had the highest power density of 8.81 kW/kg at a still very high energy density of 8.1 Wh/kg. Cell-II is superior to a closely related supercapacitor system that contains an ILGPE made up of EMIM TFSI:PVdF-HFP:Zeolite (70:28:2) that had its highest power density of 2.73 kW/kg at the same 10 A/g.<sup>11</sup> This is likely due to differences in the amount of polymer in the ILGPE and surface area of active carbon.

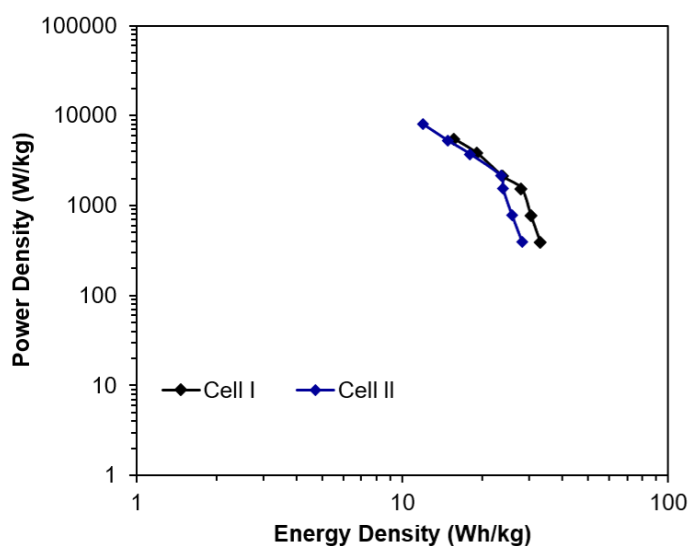


**Figure 6.6** Ragone plot for Cell I (black) and Cell II (blue) charging from 0-2.5 V. Charge/discharge current density is 0.5-10 A/g.

In this chapter, comparisons are only made between and focus on the two supercapacitors fabricated with and without calcite described herein. This is because it is difficult to compare the current systems with those in the literature when there are many differences in the structures and fabrications of the cells and experimental measurements performed,

including mass of active material, electrolyte (IL), thickness of the electrolyte etc. The power and energy density of Cell-I and -II were not dramatically different and are both within standards of what is typical of an electrochemical supercapacitor.<sup>2</sup>

### **6.3 Conclusions**

In summary, the addition of biorenewable calcite into the ILGPE resulted in films that are free standing, flexible and mechanically strong. Both ILGPEs were thermally stable up to 350 °C and had a maximum cell potential of 3.5 V. When part of a symmetric coin cell capacitor, it was shown that ILGPE-II did not affect the stability or lifetime of the device. In some instances, calcite proved beneficial. Cell-II had a smaller  $R_{CT}$  and better retention of specific capacitance (81.5%) after 5000 cycles in comparison to Cell-I. Neither the electrochemical window nor capacitance behavior were altered by the addition of biorenewable calcite. The specific capacitance, energy density of Cell-II was very similar to Cell-I, and still well within the standards for activated carbon supercapacitors. Cell-II had higher power density (able to withstand higher current density) than Cell-I. The maximum energy density and power density of Cell-II were 28 Wh/kg and 8.1 kW/kg at 0.5 and 10 A/g, respectively. This research is promising for the development of solid-state electrolytes for supercapacitors like ILGPEs because biorenewable calcite has enhanced the mechanical stability of ILGPEs and decreased the cost. The small volume of calcite added allowed 1-2 more ILGPE-containing symmetric coin cells to be prepared per standard batch of ILGPE-II in comparison to ILGPE-I. This biorenewable inorganic additive, that would have ended up in a landfill, decreased the cost of the supercapacitor by up to 17%. ILGPE-II, which contained calcite, was more mechanically stable and better

suitable for a supercapacitor in my opinion because it was compressible (a characteristic of the calcite material itself) and was not as stiff as ILGPE-I, and thus may have also led to better electrolyte and electrode contacts within the device

## **6.4 Experimental**

Experiments within this chapter were primarily performed at Monash University and were funded through an NSERC Michael Smith Foreign Study Supplement.

### **6.4.1 Materials**

1-ethyl-3-methylimidazolium bis(trifluoromethylsulfonyl)imide [EMIM][NTf<sub>2</sub>] (99.9%) was purchased from Solvionic. Acetone was purchased from Univar (>99.5%). Polyvinylidene fluoride-co-hexafluoropropylene (PVdF-co-HFP), Polyvinylidene fluoride (PVdF) powder, Vulcan XC-72R (carbon black) and N-methyl-2-pyrrolidone (NMP) were purchased from Sigma Aldrich. TF-B520, the activated carbon for the electrodes, was purchased from MTI corporation. All chemicals were used without further purification.

### **6.4.2 Preparation of ILGPEs**

Initial screening showed the minimum amount of PVdF-co-HFP needed to make stable, fully solid films was 20 wt%. Therefore, the films reported herein all have an [EMIM][NTf<sub>2</sub>]: PVdF-co-HFP ratio of 4:1. PVdF-co-HFP was dissolved in acetone at 50 °C with stirring before adding the [EMIM][NTf<sub>2</sub>]. The clear colourless solution was stirred and heated until approximately half of the solvent evaporated. At this point, if the film was to include calcite, calcite would be added and stirred vigorously with continued heating. The wt% of calcite added was relative to the combined mass of [EMIM][NTf<sub>2</sub>] and PVdF-

co-HFP. The films were cast onto a large glass plate 1000  $\mu\text{m}$  doctor blade when there was very little solvent left and dried in a vacuum oven overnight at 60  $^{\circ}\text{C}$ . The resulting films were between 100-160  $\mu\text{m}$  thick and cut into spheres with a 9.72 mm diameter for supercapacitor fabrication.

### **6.4.3 Preparation of Electrodes**

Electrodes were prepared using 80% TF-B520 (activated carbon), 10% Vulcan XC-72R (carbon black) and 10% PVdF powder (binder) by weight. The PVdF was dissolved in a minimal amount of NMP. The carbon materials were ground in an agate mortar and pestle very vigorously before being added to the clear colourless PVdF solution. The black mixture remained viscous and was stirred at room temperature for 20 h before being cast onto an aluminium foil current collector using a 100  $\mu\text{m}$  doctor blade. The film was dried in a vacuum oven at 110  $^{\circ}\text{C}$  for 24 h before being cut into 6.35 mm disks. The disks were dried further in a vacuum oven before being transferred to an argon glovebox for supercapacitor fabrication. The mass of active carbon materials on each electrode was 0.3 mg.

### **6.4.4 Electrochemical Measurements**

The ionic conductivity of the ILGPEs were measured by AC impedance spectroscopy using an MTZ-35 BioLogic instrument. Films were loaded into a barrel cell equipped with two stainless steel electrodes with surface area of 4.15  $\text{cm}^2$ . The temperature of the barrel cell was controlled with a Eurotherm 2204e temperature controller. The conductivity was measured from 25-80  $^{\circ}\text{C}$  in 10  $^{\circ}\text{C}$  increments from 30  $^{\circ}\text{C}$  with a hold of 5 minutes before

the measurement commenced at frequencies ranging from 1.0 Hz to 10 MHz using a signal voltage of 0.1 V.

To make the supercapacitors, the ILGPEs were employed as the electrolyte separator and as such were sandwiched between two symmetric electrodes with a diameter of 6.35 mm. The electrodes were made with commercially available carbon materials using the slurry coating method onto aluminium foil. The coin cell supercapacitors were fabricated in an argon glove box. Galvanostatic charge-discharge tests were performed using a NEWARE battery testing system from 0-3 V at current densities ranging from 0.5-7 A/g. 5000 cycles of the devices at 2.5 V with a current density of 2 A/g were completed to assess the stability and lifetime of the supercapacitors. Specific capacitances from galvanostatic testing were calculated using  $C = 2(I\Delta t/m\Delta V)$  where  $I$  is the constant discharge current,  $\Delta t$  is the discharging time,  $m$  is the mass of one electrode, and  $\Delta V$  is the voltage drop upon discharging. Energy density ( $E$ ) and power density ( $P$ ) were then calculated using  $E = [C(\Delta V)^2]/8$  and  $P = E/\Delta t$  where  $E$ ,  $C$ ,  $\Delta V$ ,  $P$  and  $\Delta t$  are the specific energy, specific capacitance, potential window, specific power and discharge time, respectively. A multichannel potentiostat from Princeton Applied Research VMP2 was used to perform electrochemical measurements on the fabricated supercapacitors. Cyclic voltammetry (CV) and electrochemical impedance spectroscopy (EIS) was performed using a two-electrode setup at room temperature. The CV experiments were conducted at scan rates of 25, 50, 100 and 200 mV/s and voltages ranging from 0-4.0 V. The EIS was measured in a frequency range of 1 MHz to 0.01 Hz. Specific capacitance was calculated from the CVs according to  $C = i/s$  where  $i$  is the average current and  $s$  is the scan rate.

### 6.4.5 Characterization of ILGPEs

Thermogravimetric Analysis (TGA) was performed with a Mettler Toledo TGA/DSC 1STARe at a heating rate of 10 °C min<sup>-1</sup> from 25-550 °C under flow of N<sub>2</sub> (50 mL min<sup>-1</sup>). A DSC Q100 was used for differential scanning calorimetry (DSC) experiments where the films were first cooled to -150 °C (with a 2-minute isothermal hold) and then heated to 100 °C (with a 2-minute isothermal hold). The heating and cooling rates were both 10 °C min<sup>-1</sup>. Three cycles were performed and the first was discarded. Fourier transform infrared spectra were obtained using a Bruker Equinox IFS 55 infrared spectrophotometer in attenuated total reflectance over 64 scans with a resolution of 4 cm<sup>-1</sup>. Dynamic mechanical analysis was performed using a Perkin Elmer DMA 800. Films were cooled to -130 °C rapidly and the heated to 30 °C at a rate of 5 °C per minute. Scanning electron microscopy (SEM) images from Memorial University were obtained using a FEI MLA 650 FEG under high vacuum (10<sup>-6</sup> torr). The voltage ranged from 5-10 kV and current of 10 mA at working distances ranging from 8.4-10.5 mm.

### 6.5 References

1. M. Armand and J. M. Tarascon, *Nature*, 2008, **451**, 652-657.
2. P. Simon and Y. Gogotsi, *Nat. Mater.*, 2008, **7**, 845-854.
3. B. E. Conway, *Electrochemical Supercapacitors: Scientific Fundamentals and Technological Applications*, Springer US, 1999.
4. J. R. Miller and P. Simon, *Science*, 2008, **321**, 651-652.
5. M. Kaempgen, C. K. Chan, J. Ma, Y. Cui and G. Gruner, *Nano Lett.*, 2009, **9**, 1872-1876.

6. M. Armand, F. Endres, D. R. MacFarlane, H. Ohno and B. Scrosati, *Nat. Mater.*, 2009, **8**, 621-629.
7. G. P. Pandey and S. A. Hashmi, *J. Mater. Chem. A*, 2013, **1**, 3372-3378.
8. N. Guo, M. Li, Y. Wang, X. Sun, F. Wang and R. Yang, *ACS Appl. Mater. Interfaces*, 2016, **8**, 33626-33634.
9. F. B. Sillars, S. I. Fletcher, M. Mirzaeian and P. J. Hall, *Phys. Chem. Chem. Phys.*, 2012, **14**, 6094-6100.
10. Y. J. Kang, S.-J. Chun, S.-S. Lee, B.-Y. Kim, J. H. Kim, H. Chung, S.-Y. Lee and W. Kim, *ACS Nano*, 2012, **6**, 6400-6406.
11. W. Lu, K. Henry, C. Turchi and J. Pellegrino, *J. Electrochem. Soc.*, 2008, **155**, A361-A367.
12. J. Jiang, D. Gao, Z. Li and G. Su, *React. Funct. Polym.*, 2006, **66**, 1141-1148.
13. A. Lewandowski and A. Swiderska, *Solid State Ionics*, 2004, **169**, 21-24.
14. T. E. Sutto, *J. Electrochem. Soc.*, 2007, **154**, P130-P135.
15. S. Nohara, H. Wada, N. Furukawa, H. Inoue, M. Morita and C. Iwakura, *Electrochim. Acta*, 2003, **48**, 749-753.
16. C. M. Yang, J. B. Ju, J. K. Lee, W. I. Cho and B. W. Cho, *Electrochim. Acta*, 2005, **50**, 1813-1819.
17. J. Nunes-Pereira, C. M. Costa and S. Lanceros-Mendez, *J. Power Sources*, 2015, **281**, 378-398.
18. M. Mirzaeian, Q. Abbas, A. Ogwu, P. Hall, M. Goldin, M. Mirzaeian and H. F. Jirandehi, *Int. J. Hydrogen Energy*, 2017, **42**, 25565-25587.
19. P. Pal and A. Ghosh, *J. Power Sources*, 2018, **406**, 128-140.

20. X. Zhang, M. Kar, T. C. Mendes, Y. Wu and D. R. MacFarlane, *Adv. Energy Mater.*, 2018, **8**, n/a.
21. P. F. R. Ortega, J. P. C. Trigueiro, G. G. Silva and R. L. Lavall, *Electrochim. Acta*, 2016, **188**, 809-817.
22. S. Ketabi and K. Lian, *Electrochim. Acta*, 2013, **103**, 174-178.
23. R. L. Lavall, S. Ferrari, C. Tomasi, M. Marzantowicz, E. Quartarone, M. Fagnoni, P. Mustarelli and M. L. Saladino, *Electrochim. Acta*, 2012, **60**, 359-365.
24. Y. Gong, D. Li, C. Luo, Q. Fu and C. Pan, *Green Chem.*, 2017, **19**, 4132-4140.
25. N. Yadav, M. K. Singh, N. Yadav and S. A. Hashmi, *J. Power Sources*, 2018, **402**, 133-146.
26. P. Tamilarasan and S. Ramaprabhu, *Energy*, 2013, **51**, 374-381.
27. A. Lewandowski and A. Swiderska, *Solid State Ionics*, 2003, **161**, 243-249.
28. J. P. Tafur and A. J. Fernandez Romero, *J. Membr. Sci.*, 2014, **469**, 499-506.
29. J. P. T. Guisao and A. J. F. Romero, *Electrochim. Acta*, 2015, **176**, 1447-1453.
30. G. P. Pandey, Y. Kumar and S. A. Hashmi, *Solid State Ionics*, 2011, **190**, 93-98.
31. S. S. Zhang, K. Xu and T. R. Jow, *J. Power Sources*, 2005, **140**, 361-364.
32. H. Y. Liu, L. L. Liu, C. L. Yang, Z. H. Li, Q. Z. Xiao, G. T. Lei and Y. H. Ding, *Electrochim. Acta*, 2014, **121**, 328-336.
33. A. G. Xyla and P. G. Koutsoukos, *J. Chem. Soc., Faraday Trans. 1*, 1989, **85**, 3165-3172.

## **Chapter 7 Conclusions and Future Work**

### **7.1 Conclusions**

In **Chapter 1**, the concepts of green chemistry and the ocean-based refinery were introduced. Mollusc aquaculture is increasing worldwide, and it is our social responsibility to make sure it increases in a sustainable manner and manage waste in such a way that the economy is benefited without harming the environment. A large hurdle for utilizing waste mussels is the residual meat attached to the shell and the stench it causes when stored for long periods of time, not to mention the eutrophication risk. The primary way in which residual protein has been removed to date is by heating shells to high temperatures and washing with large amounts of fresh water. Characterization data had shown that mollusc shells contain one or both of the following polymorphs of  $\text{CaCO}_3$ , calcite and aragonite. Also, if they were both present, it was reported that they were separated into two layers; an outer prismatic layer and an inner nacreous layer. As the shells are  $>95\%$   $\text{CaCO}_3$ , many applications have been explored where mined  $\text{CaCO}_3$  has been replaced with the shells including amendment of acidic soils, treatment of acid mine drainage, water treatment, and to make  $\text{CaO}$  for catalysis and materials applications.

In **Chapter 2**, an enzymatic process that cleans the shell by-product in an environmentally friendly, cost-effective, and safe manner by using seawater, mild temperatures, without the use of acids and bases was presented. A Design of Experiments (DoE) approach to optimize the shell-cleaning protocol and used two industrially available food grade protease enzymes, Multifect PR 7L and Multifect PR 6L. Mussel shells with raw protein attached were efficiently cleaned using 1.0-2.0  $\mu\text{L/g}$  Multifect PR 6L in seawater or tap water for 4

h at 55.0 °C. Mussel shells with cooked protein attached were efficiently cleaned using 6.0 μL/g Multifect PR 7L in seawater or synthetic seawater for 10 h at 25.0 °C. These processes employ low enzyme loadings (0.1-0.6%) and assuming the most significant ongoing cost in cleaning the shells is the enzyme, the cost of cleaning 20 g of mussels is less than 0.1 US cents. This method yields two streams that can be valorized. The cleaned shells have a variety of possible applications from wastewater treatment to alternatives to road salt, and the residual protein stream is a possible fishmeal source. This chapter was the critical first step toward biorefining waste from mussel aquaculture.

In **Chapter 3**, the heat treatment of blue mussel shells yielded a variety of CaCO<sub>3</sub> materials with differing ratios of calcite and aragonite. Powder XRD revealed untreated blue mussel shells have 25 wt% aragonite and heating the shells at 220 °C for 48 h increased the amount of aragonite by 20 wt%. <sup>1</sup>H NMR data showed a decrease in the organic matrix content after heat treatment. Additionally, the outer prismatic calcite layer was liberated from the inner nacreous layer with ease. After heating, organic matrix was present primarily in the prismatic calcite layer whereas in the nacreous layer it was undetectable by NMR with only about 0.02 wt% remaining by TGA. The removal of the organic matrix increases the purity of the iridescent aragonite and makes it less susceptible to allergic reactions if it were to be used as a more ethical and sustainable source of shimmer/glitter, in cosmetics for example. The organic matrix and freeze-dried mussel meat had similarities via NMR spectroscopy which inspired an attempt to synthesize nacre using the protein hydrolysate produced via the enzymatic hydrolysis of mussel meat and described in the previous chapter. By sequentially adding in the protein hydrolysate to reaction mixtures of Na<sub>2</sub>CO<sub>3</sub> and CaCl<sub>2</sub>,

there was control over  $\text{CaCO}_3$  polymorph formation. Synthetic nacre was synthesized when protein hydrolysate and small pieces of mussel shells were used for seeding. While this worked quite well, the seeding technique poses challenges because the synthetic nacre cannot be easily collected from the shell surface.

In **Chapter 4**, three starting materials sourced from waste blue mussel shells in the synthesis of calcium acetate,  $\text{Ca}(\text{CH}_3\text{COO})_2$ , were screened. The three materials included; shells without heat treatment, shells heated to  $220\text{ }^\circ\text{C}$  for 48 h and shells calcined to yield  $\text{CaO}$ , denoted as RTC, HTC, and CC, respectively. An exploratory central composite design compared the yield of  $\text{Ca}(\text{CH}_3\text{COO})_2$  with respect to shell type, concentration of  $\text{CH}_3\text{COOH}$ , and time. CC shells gave poor yields regardless of time and  $\text{CH}_3\text{COOH}$  concentrations. RTC shells gave better yields that increased as time increased and  $\text{CH}_3\text{COOH}$  concentration decreased. HTC shells gave the best yields and followed the same trends relative to process conditions as RTC shells. The yield of  $\text{Ca}(\text{CH}_3\text{COO})_2\cdot\text{H}_2\text{O}$  was optimized further using HTC shells using a custom optimal design with longer reaction times and lower  $\text{CH}_3\text{COOH}$  concentrations. A maximum yield of 93% was reached after 32 h using 9%  $\text{CH}_3\text{COOH}$ . Other concentrations of  $\text{CH}_3\text{COOH}$  were still very successful and using food-grade white vinegar, an 85% yield of  $\text{Ca}(\text{CH}_3\text{COO})_2\cdot\text{H}_2\text{O}$  was obtained after 24 h. The crystalline product, a monohydrate, was characterized by IR spectroscopy, TGA and powder XRD. The  $\text{Ca}(\text{CH}_3\text{COO})_2\cdot\text{H}_2\text{O}$  produced from BM shells HTC and RTC was the same as that prepared using pure  $\text{CaCO}_3$ . In contrast,  $\text{Ca}(\text{CH}_3\text{COO})_2$  made using CC shells was the hemihydrate. De-icing experiments showed that the  $\text{Ca}(\text{CH}_3\text{COO})_2\cdot\text{H}_2\text{O}$  produced from waste BM melted 10-13 wt% of ice in 15 min at concentrations of 20-30%

(m/v) at  $-16\text{ }^{\circ}\text{C}$ . This is very promising for progress towards a sustainable, non-corrosive and degradable de-icer; however, sustainability can be further improved if a renewable source of  $\text{CH}_3\text{COOH}$  was identified and used. While carrying out this project, an unusual by-product formed which ended up being the focus of **Chapter 5**.

In **Chapter 5**, the preparation and characterization of an absorbent, high surface area calcite material produced from waste blue mussel shells was presented. This material was isolated while making calcium acetate in **Chapter 4**. The sponge-like material was discovered by chance and was very peculiar. It was concluded that its formation was dependent on both aragonite and calcite being present to react with  $\text{CH}_3\text{COOH}$  at the same time. The aragonite from the myostracum (that is holding together the prismatic calcite) dissolves and the prisms of calcite are liberated. The prisms are known to be coated in a thick layer of organic matrix and recombined to create a new nest-like morphology of calcite with gentle agitation. The presence of the organic matrix was proved with solid state NMR as the spectra for the self assembling calcite (SAC) contains the same resonances as spectra for raw blue mussel shells. SAC is soft and deformable with a texture like candy floss (cotton candy). It can adsorb 1-24 wt% of common dyes from water, and the dye and SAC are recoverable via complete desorption in methanol. SAC has an absorption capacity of 978% +/- 84.3% for crude oil and shows good recyclability over 10 re-uses. SAC may be the first inorganic sponge for oil remediation. This chapter demonstrated how a natural structure can be modified in a sustainable fashion to yield a higher value material as well as the synergistic effects of an ocean-based material aiding our oceans when in need.

The last project was funded by a Michael Smith Foreign Study Supplement and was carried out in Melbourne at Monash University under the supervision of Prof. Doug MacFarlane. In **Chapter 6**, the preparation of ionic liquid gel polymer electrolytes (ILGPEs) and their use in supercapacitors is described. SAC was incorporated into the ILGPEs as an inorganic filler and determined the optimal filler amount was 2 wt% based on the mass of the other ILGPE components. The properties of the ILGPE with 2 wt.% SAC with an ILGPE that did not have SAC were compared. The ILGPEs that contained 2 wt% SAC were free standing, flexible and mechanically strong. Both ILGPEs were thermally stable up to 350 °C and had a maximum cell potential of 3.5 V. It was shown that the addition of SAC did not affect the stability or lifetime of symmetric coin cell capacitors fabricated using ILGPEs. In some ways, calcite proved beneficial. The capacitor that contained SAC had a smaller charge transfer resistance and better retention of specific capacitance (81.5%) after 5000 cycles in comparison to the cell without SAC. The specific capacitance and energy density of the two cells were very similar and well within the standard ranges expected for activated carbon supercapacitors. The cell containing SAC had superior power density than the cell without SAC because it was able to withstand higher current density. This research is promising for the development of solid-state electrolytes for supercapacitors like ILGPEs because biorenewable calcite has enhanced the mechanical stability of ILGPEs and decreased the cost. The addition of SAC as an inorganic additive, that would have ended up in a landfill, decreased the cost of the supercapacitor by up to 17%.

## 7.2 Future Work

Being the first student to work on this project in the Kerton group, there are many areas where this research can be expanded and explored. With respect to **Chapter 2**, the protein hydrolysate resulting from the enzymatic hydrolysis should to be characterized. The scale up of this process is on-going in the Hawboldt group (Department of Process Engineering, Memorial University).

The heat treatment of the shells in **Chapter 3** had some interesting results, namely the increase in aragonite, that may be advantageous if mussel shells were used to treat acid mine drainage (AMD) from tailing ponds in Newfoundland. Aragonite has a different dissolution rate to calcite,<sup>1, 2</sup> as was noticed in **Chapter 5** when making SAC. This has proven to be advantageous for the removal of toxic  $M^{2+}$  metals such as cadmium.<sup>2</sup> This led to the pursuit of the treatment of acid mine drainage to see if there was indeed a difference with metal removal between raw and heat treated mussel shells. If this were the case, then shells could theoretically be tunable for the types of metals present in an AMD system.

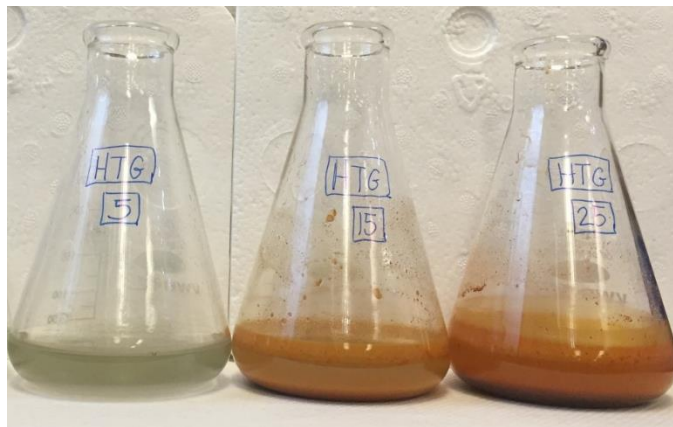


**Figure 7.1** Digital image of different loading of HTG shells added to the AMD solution after 1 h of stirring. Left 5 g/L, middle 15 g/L, and right 25 g/L.

To this end, in preliminary studies, a test solution containing several metal cations based on data from Dr. Penny Morrill (Department of Earth Sciences, Memorial University) for a tailing pond near a gold and copper mine in Baie Verte, NL. The resulting acid mine drainage (AMD) solution had a pH of 1.3 and with metal concentrations as shown in **Table 7.1**. I used shell loadings of 5, 15 and 25 g/L. The treatment of this AMD solution was tested with the same shell materials as **Chapter 4**; shells without heat treatment, and shells heated to 220 °C for 48 h that were ground to a fine powder using the 65 mL stainless steel vial and 2, ¼ inch stainless steel balls for 8 minutes (denoted as RTG and HTG). When the shell materials were added to the AMD solution, the highest loadings led to quite dramatic colour changes in the AMD samples as precipitates formed. As shown in **Figure 7.1**, the lowest shell loading did not produce significant quantities of precipitate, the middle loading of 15 g/L produced dark orange solids, and the highest shell loading of 25 g/L looked visibly similar to the 15 g/L experiment but with more solids produced and a more intense colour. After 1 h, the pH of the AMD solution treated with 15 g/L of RTG and HTG was 5.9 and 6.3, respectively, and their respective solutions were analyzed by ICP-MS.

**Table 7.1** shows the concentration of metal cations after remediation with RTG and HTG shells. As discussed in **Chapter 3**, RTG shells have a higher portion of calcite and HTG shells have a higher portion of aragonite. While both shell materials are quite satisfactory at removing metals, considering the moderate shell loading and short amount of time, there were metals that each material in these initial studies appears to be better at removing. RTG shells were better at removing sulfur (in the form of sulfate) and iron, whereas HTG shells were better at removing copper, zinc, and cadmium. Neither material was very good at

removing manganese, nickel or cobalt, and both materials were good at removing aluminium and chromium. Both shell materials led to an increase in magnesium and calcium levels, which was expected because they are both present in the mussel shell.

**Table 7.1** Concentration of elements present in AMD solution before and after being treated with 15 g/L RTG and HTG shells.

<b>Metal (units)</b>	<b>AMD solution</b>	<b>RTG</b>	<b>HTG</b>
Mg (ppm)	135	152	153
Al (ppb)	14,793	432	460
S (ppm)	2,546	962	1,270
Ca (ppm)	251	840	1,180
Cr (ppb)	12.6	< DL	< DL
Mn (ppb)	2,218	2,183	2,151
Fe (ppb)	852,107	511,207	536,800
Co (ppb)	75.8	70.0	69.7
Ni (ppb)	128	117	113
Cu (ppb)	304	4.03	< DL
Zn (ppb)	846	330	267
Cd (ppb)	215	148	113

Based on these preliminary results, it would be worth studying different mixtures of mussel-sourced calcite and aragonite in treating AMD solutions. In **Chapter 3**, the two polymorphs were separated, therefore, custom mixtures of calcite and aragonite could be used to target specific metals present in solution.

The inner nacreous layer isolated in **Chapter 3** needs to be studied further to determine how the partial removal of the organic matrix has affected the mechanical properties of the nacre and whether it is suitable for applications where nacre is employed. The nacre from the shell has the potential to be used as the inorganic building blocks in synthetic nacre-

inspired materials that are strong and sustainable.<sup>3</sup> The interesting delamination of eastern blue mussel shells was interesting and it may be worth while for others who work with molluscs to see if this occurs in different species. Having only reported the results of heat treatment of eastern blue mussels and eastern oyster, western blue mussels (from research study period in Australia) were investigated and do delaminate after heat treatment at 220 °C for 48 h as well. Another area that may benefit from this delamination knowledge is archaeology.

In terms of further studies towards synthetic nacre using bio-sourced templates and stabilizers, other seeding techniques could be trialed. For example, instead of using pieces of the mussel shell (described in **Chapter 3**), one could try using just a couple of platelets of nacre that were liberated from the inner layer of the shell. If nacre continues to grow, synthetic nacre could be grown and isolated easily.

From **Chapter 4**, although preliminary studies were successful using calcium acetate monohydrate towards de-icing, more stringent de-icing experiments as per standard methods should be performed.<sup>4</sup> This would mean testing the de-icing efficacy at different temperatures over several time periods.

While SAC has been fully characterized (**Chapter 5**) it would be interesting to investigate how changing the scale of the process changes the size of the SAC formed. It might also be possible to control the size of the calcite prisms that make up SAC. For example, if SAC was disassembled by grinding (i.e. the agglomerations broken down) and the resulting calcite prisms were put back into aqueous solution, would it reform smaller SAC agglomerates? This could also be explored with loose prisms of calcite by adding in a

designer biopolymer matrix. Further directions worth pursuing towards the applications of SAC are biomedical applications and new composite materials.

Lastly, the organic matrix from blue mussel shells was isolated in **Chapter 5** by simple means in 5% CH<sub>3</sub>COOH. The sheets of insoluble macromolecules are currently under investigation as a sustainable substrate for surface-enhanced Raman spectroscopy (SERS) to detect aromatic thiols.<sup>5</sup> This research is being conducted in collaboration with Dr. Christa Brosseau at Saint Mary's University.

### 7.3 References

1. P. Cubillas, S. Köhler, M. Prieto, C. Chairat and E. H. Oelkers, *Chem. Geol.*, 2005, **216**, 59-77.
2. S. J. Köhler, P. Cubillas, J. D. Rodríguez-Blanco, C. Bauer and M. Prieto, *Environ. Sci. Technol.*, 2007, **41**, 112-118.
3. H.-L. Gao, S.-M. Chen, L.-B. Mao, Z.-Q. Song, H.-B. Yao, H. Cölfen, X.-S. Luo, F. Zhang, Z. Pan, Y.-F. Meng, Y. Ni and S.-H. Yu, *Nat. Commun.*, 2017, **8**, 287.
4. C. C. Chappelow, A. D. McElroy, R. R. Blackburn, D. Darwin, F. G. De Noyelles and C. E. Locke, *Handbook of Test Methods for Evaluating Chemical Deicers*, National Research Council, Washington, D.C., November 1992.
5. T. P. Lynk, O. J. R. Clarke, N. Kesavan and C. L. Brosseau, *Sensors and Actuators B Chemical*, 2018, **257**, 270-277.

## Appendix A

**Table A1** Experimental data for 2<sup>4</sup> factorial design with center points using Multifect 6L to clean raw, shell-on mussels. Optimization of temperature, time, amount of enzyme solution, and reaction medium to yield the minimum meat residue.

Run	Temperature (°C) (X1)	Enzyme Loading (µL/g) (X2)	Time (h) (X3)	Medium <sup>a</sup> (X4)	Wt% Meat Remaining (Response)
1	35.0	1.0	4	NS	2.3
2	55.0	2.0	4	NS	0
3	35.0	2.0	2	NS	5.3
4	35.0	2.0	2	TW	12.6
5	55.0	2.0	4	NS	0
6	35.0	1.0	2	TW	8.4
7	35.0	1.0	2	TW	6.4
8	35.0	2.0	4	NS	6.4
9	55.0	1.0	4	TW	0.15
10	35.0	2.0	2	NS	9.1
11	35.0	2.0	4	TW	2.5
12	55.0	1.0	2	TW	0.91
13	35.0	2.0	2	TW	1.3
14	35.0	1.0	4	TW	2.7
15	55.0	2.0	2	NS	0.13
16	35.0	1.0	4	NS	0.93
17	35.0	2.0	2	NS	3.1
18	35.0	2.0	4	TW	1.4
19	55.0	2.0	2	TW	0
20	55.0	2.0	4	TW	0
21	45.0	1.5	3	NS	3.1
22	55.0	2.0	2	TW	0.21
23	35.0	1.0	4	NS	5.1
24	55.0	2.0	2	NS	0.8
25	55.0	1.0	2	TW	0.82
26	35.0	1.0	2	TW	1.2
27	55.0	1.0	4	TW	0.71
28	35.0	2.0	2	TW	0.91
29	35.0	1.0	2	NS	5.1
30	35.0	1.0	2	NS	8.1
31	55.0	1.0	2	TW	1.9

32	55.0	1.0	2	NS	0.52
33	55.0	2.0	4	NS	0.44
34	35.0	1.0	4	TW	6.4
35	55.0	1.0	4	NS	0.32
36	55.0	1.0	4	TW	0
37	55.0	2.0	4	TW	0.08
38	55.0	1.0	4	NS	0.52
39	55.0	1.0	4	NS	0
40	35.0	2.0	4	NS	0.94
41	55.0	1.0	2	NS	1.2
42	45.0	1.5	3	TW	2.1
43	35.0	1.0	2	NS	6.8
44	45.0	1.5	3	TW	3.4
45	35.0	2.0	4	TW	3.8
46	55.0	2.0	2	NS	0.92
47	35.0	2.0	4	NS	3.7
48	55.0	2.0	4	TW	0.11
49	35.0	1.0	4	TW	3.2
50	55.0	1.0	2	NS	1.8
51	45.0	1.5	3	NS	2.5
52	55.0	2.0	2	TW	0.62

---

<sup>a</sup>NS=natural seawater and TW=tap water

**Table A2 and Design Summary:** Analysis of variance and partial sum of squares for the 2<sup>4</sup> factorial design using Multifect 6L to clean raw, shell on mussels.

Source	Sum Squares	of df	Mean Square	F Value	p-value > F	Prob
Model	26.07	2	13.04	46.11	5.47 E-12	significant
X1- Temperature	23.21	1	23.21	82.09	4.80 E-12	
X3-Time	2.86	1	2.86	10.12	0.0026	
Residual	13.86	49	0.28			
Lack of Fit	2.51	15	0.17	0.50	0.9233	not significant
Pure Error	11.35	34	0.33			
Cor Total	39.93	51				

<b>Std. Dev.</b>	0.53	<b>R-Squared</b>	0.6530
<b>Mean</b>	1.33	<b>Adj R-Squared</b>	0.6388
<b>C.V. %</b>	40.05	<b>Pred R-Squared</b>	0.6078
<b>PRESS</b>	15.66	<b>Adeq Precision</b>	14.713
<b>-2 Log Likelihood</b>	78.80	<b>BIC</b>	90.650
<b>AICc</b>	85.30		

The model has a square root transform with a constant, k=0.0126.

Final equation in terms of coded factors for the use of Multifect 6L to clean raw, shell on mussels:

$$\text{Sqrt (wt. \% meat remaining + 0.01)} = 1.33 - 0.69(X1) - 0.24(X3)$$

Residual Diagnostics for the model resulting from the 2<sup>4</sup> factorial design with center points using Multifect 6L to clean raw, shell-on mussels are shown in Figures A1-A3.

The analysis of variance (ANOVA) gave two significant effects, temperature (X1) and time (X3), for the 2<sup>4</sup> factorial design for the optimization of cleaning raw, shell on mussels with Multifect 6L. As shown in **Figure A4**, when temperature and time are increased, the less residual meat that remains. Ultimately meaning, at higher temperature and longer reaction times, we get cleaner mussel shells.

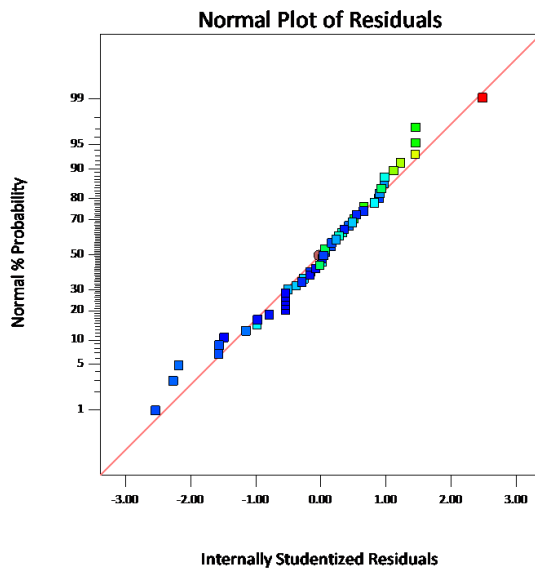


**Figure A1** Normal Plot of residuals for the model developed from the  $2^4$  factorial design used to optimize the use of Multifect 6L to clean raw, shell on mussel.

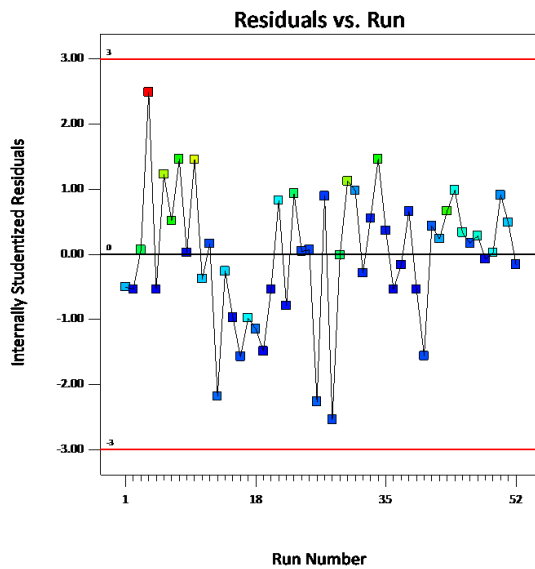


**Figure A2** Residuals vs. run for the model developed from the  $2^4$  factorial design used to optimize the use of Multifect 6L to clean raw, shell on mussel.

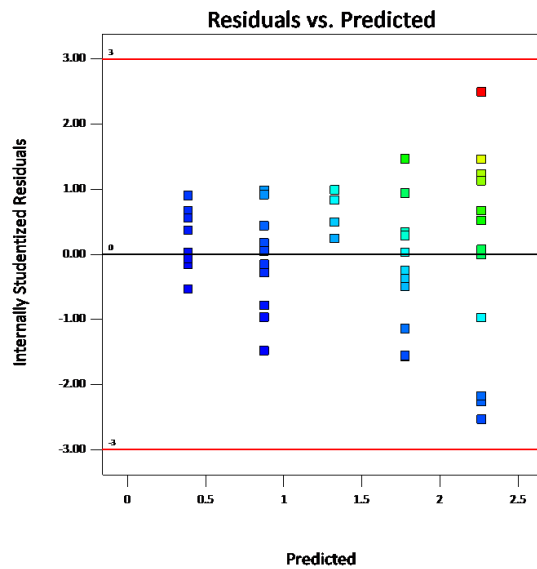


**Figure A3** Residuals vs. predicted for the model developed from the  $2^4$  factorial design used to optimize the use of Multifect 6L to clean raw, shell on mussel.

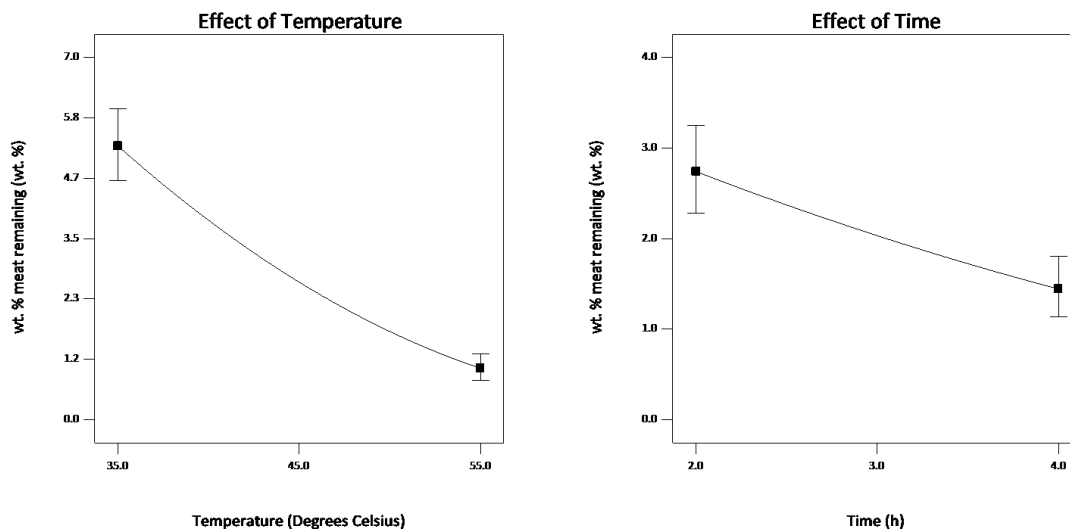


**Figure A4** One factor plots for the  $2^4$  factorial design for the optimization of reaction conditions with respect to temperature, amount of enzyme solution, time and medium for the cleaning of raw, shell on mussels using Multifect 6L. The effect of temperature (X1), left and the effect of time (X3), right.

**Table A3** Experimental data for the I-optimal custom design (a response surface method) with 4 replicate points and 8 center points using Multifect 7L to clean cooked, shell-on mussels. Optimization of time, amount of enzyme solution, and reaction medium to yield the minimum meat residue.<sup>a</sup>

Run	Enzyme Loading ( $\mu\text{L/g}$ ) (Z1)	Time (h) (Z2)	Medium <sup>b</sup> (Z3)	Wt% Meat Remaining (Response)
1	3.0	2	NS	1.5
2	4.5	6	NS	0.28
3	4.5	6	SS	0.25
4	6.0	2	NS	1.1
5	4.5	6	NS	0.2
6	6.0	10	NS	0
7	6.0	10	SS	0
8	4.5	6	SS	0.23
9	4.5	6	NS	0.2
10	3.0	2	SS	1.7
11	3.0	10	NS	0.12
12	3.0	10	NS	0.86
13	4.5	6	SS	0.24
14	3.0	2	NS	1.7
15	3.0	10	SS	0.13
16	4.5	6	NS	0.23
17	6.0	10	NS	0.09
18	6.0	2	NS	0.62
19	4.5	6	SS	0.17
20	3.0	2	SS	0.48
21	6.0	2	SS	0.58
22	6.0	2	SS	2.28
23	3.0	10	SS	0.95
24	6.0	10	SS	0.22

<sup>a</sup>All reactions performed at room temperature; <sup>b</sup>NS = natural seawater (salinity, 25 ppt) and SS = synthetic seawater (salinity, 35 ppt)

**Table A4 and Design Summary:** Analysis of variance and partial sum of squares for the I-optimal custom design using Multifect 7L to clean cooked, shell on mussels.

Source	Sum Squares	of df	Mean Square	F Value	p-value > F	Prob
Model	24.09	2	12.05	14.64	0.0001	significant
Z1-Enzyme Loading	5.25	1	5.25	6.38	0.0196	
Z2-Time	18.84	1	18.84	22.90	< 0.0001	
Residual	17.28	21	0.82			
Lack of Fit	5.22	7	0.75	0.87	0.5548	not significant
Pure Error	12.06	14	0.86			
Cor Total	41.38	23				

<b>Std. Dev.</b>	0.91	<b>R-Squared</b>	0.5823
<b>Mean</b>	-1.14	<b>Adj R-Squared</b>	0.5426
<b>C.V. %</b>	79.28	<b>Pred R-Squared</b>	0.4061
<b>PRESS</b>	24.57	<b>Adeq Precision</b>	10.340
<b>-2 Log Likelihood</b>	60.23	<b>BIC</b>	69.76
<b>AICc</b>	67.43		

The model has a natural log transform with a constant,  $k=0.0126$ .

Final equation in terms of coded factors for the use of Multifect 7L to clean cooked, shell on mussels:

$$\ln(\text{wt. \% meat remaining} + 0.01) = -1.14 - 0.57(Z1) - 1.09(Z2)$$

Residual Diagnostics for the model resulting from the I-optimal design with center points using Multifect 7L to clean cooked, shell-on mussels are shown in **Figures A5-A6**.

The analysis of variance (ANOVA) gave two significant effects, time (Z1) and amount of enzyme solution (Z2), for the I-optimal design for the optimization of cleaning cooked, shell on mussels with Multifect 7L. As shown in **Figure A8**, when time and amount of enzyme solution are increased, the less residual meat that remains. Ultimately meaning, the longer reaction times and the higher the enzyme solution loading, the cleaner mussel shells.

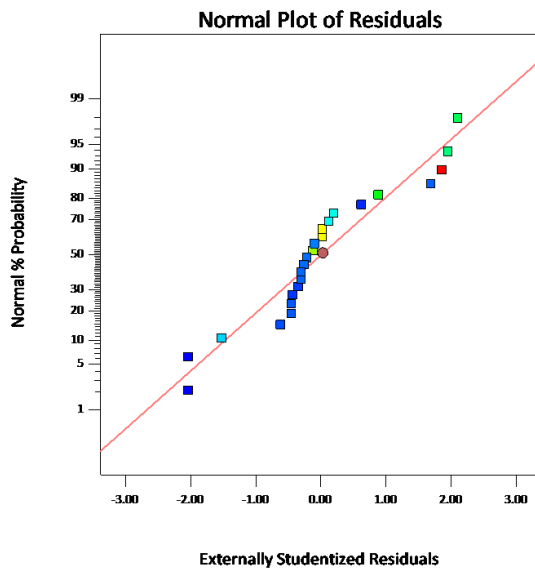


**Figure A5** Normal Plot of residuals for the model developed from the I-optimal design used to optimize the use of Multifect 7L to clean cooked, shell on mussel.

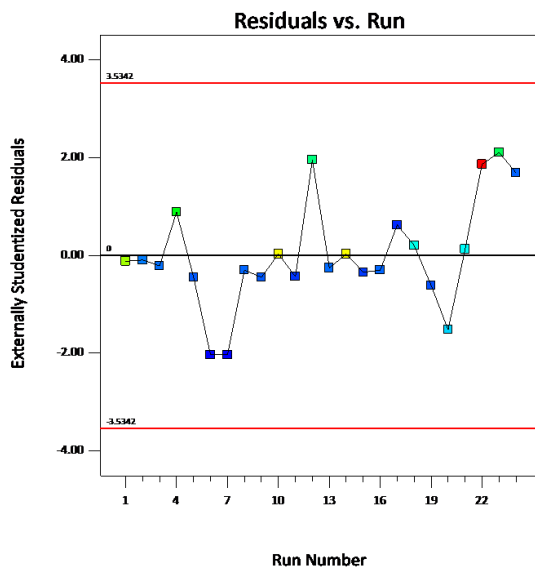


**Figure A6** Residuals vs. run for the model developed from the I-optimal design used to optimize the use of Multifect 7L to clean cooked, shell on mussel.

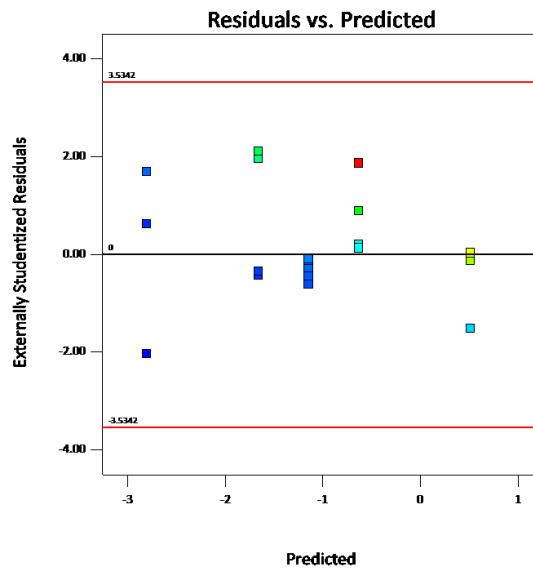


**Figure A7** Residuals vs. predicted for the model developed from the I-optimal design used to optimize the use of Multifect 7L to clean cooked, shell on mussel.

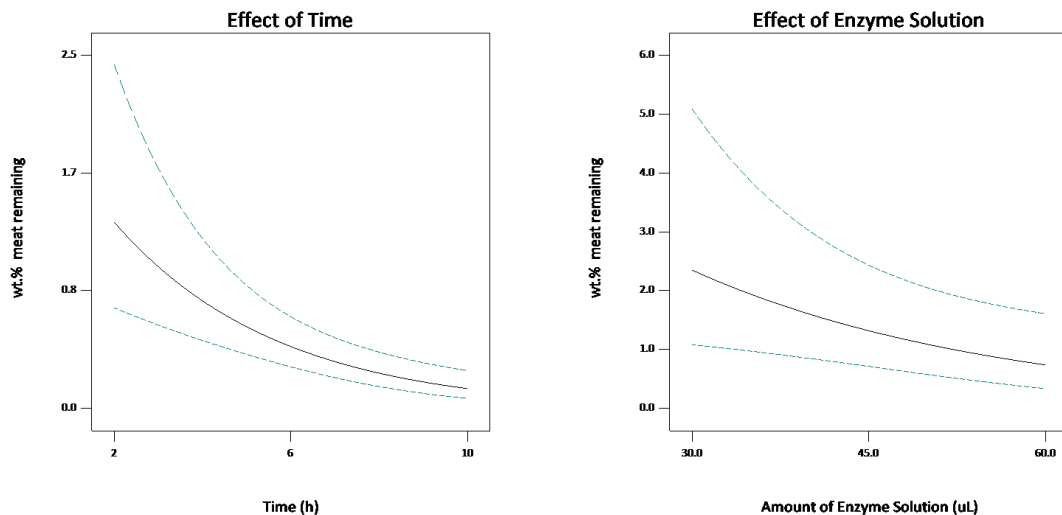


**Figure A8** One factor plots for the I-optimal design for the optimization of reaction conditions with respect to time, amount of enzyme solution, and medium for the cleaning of cooked, shell on mussels using Multifect 7L. The effect of time (Z1), left, and the effect of the amount of enzyme solution (Z2), right.

## Appendix B

**Table B1** Selected ICP-MS analytes for untreated blue mussel shells and mussel shells heated at 220 °C for 48 h. Units are in ppm.

Analyte (LOD)	Untreated (Mixer Mill) <sup>a</sup>	220 °C, 48 h (Mixer Mill)	Untreated (Mortar & Pestle) <sup>b</sup>	220 °C, 48 h (Mortar & Pestle) <sup>b</sup>
<b>Li (0.001)</b>	1.588	1.242	0.873	0.994
<b>Ca (0.182)</b>	353442.0	386784.4	345618.0	367614.3
<b>Cl (4.031)</b>	4572.6	1861.50	619.25	553.31
<b>Cr (0.004)</b>	7.526	3.132	1.770	1.191
<b>Fe (0.142)</b>	3434.395	112.692	<80.2	<99.91
<b>Mn (0.001)</b>	37.547	1.699	1.222	2.011
<b>Co (0.000)</b>	<0.15	<0.16	<0.13	<0.15
<b>Cu (0.004)</b>	158.99	188.603	157.654	164.724
<b>As (0.001)</b>	0.445	0.456	0.155	<0.41
<b>Sr (0.0003)</b>	809.453	894.522	798.713	827.754
<b>Ag (0.0002)</b>	<0.15	<0.14	<0.12	<0.15
<b>Cd (0.000)</b>	<0.29	<0.29	<0.25	<0.31
<b>Hg (0.000)</b>	<0.15	<0.15	<0.13	<0.16
<b>Pb (0.000)</b>	0.462	0.117	0.117	<0.08
<b>Ba (0.0001)</b>	11.972	3.738	1.960	1.725

<sup>a</sup> Mussel shells were ground in a mixer mill equipped in a 65 mL stainless steel vial with two quarter inch stainless steel balls for 12 min. <sup>b</sup>Mussel shells were ground using a mortar and pestle.

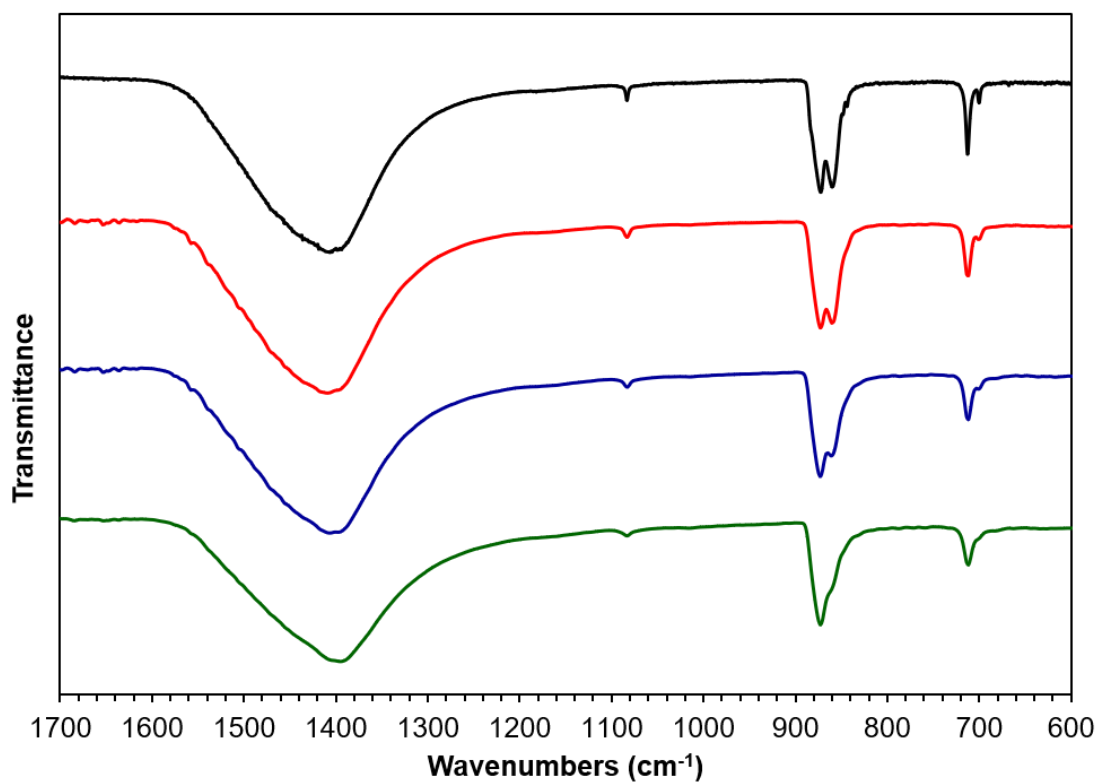


**Figure B1** Infrared spectra of untreated mussel shells (green) and mussel shells heated to 160 °C (blue), 200 °C (red) and 225 °C (black) for 48h.

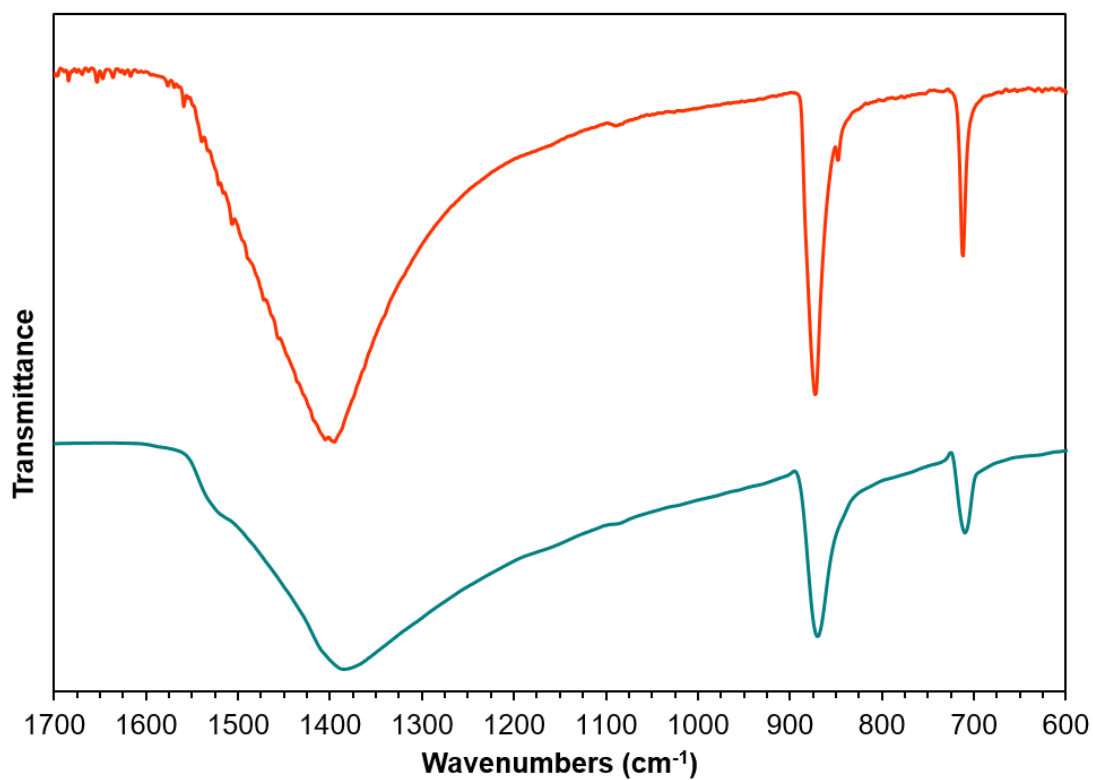


**Figure B2** Infrared spectra of optical calcite sourced from Mexico (orange) and reagent grade calcium carbonate from Sigma Aldrich (teal). Neither samples underwent heat treatment.

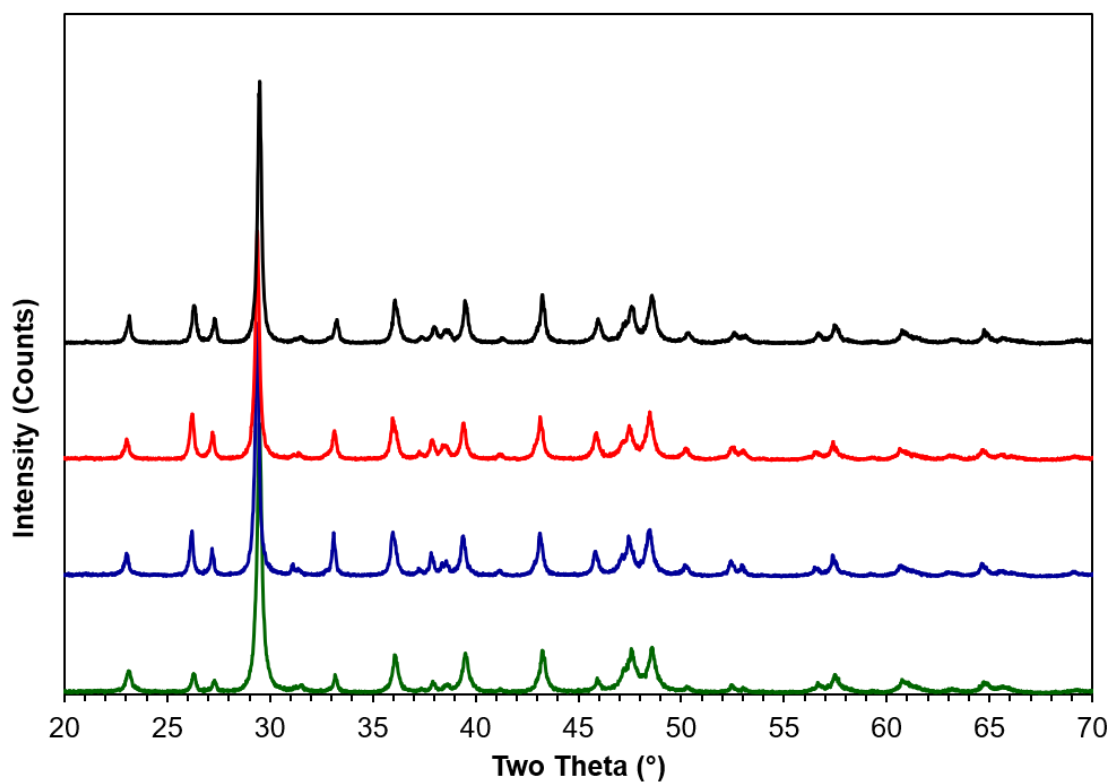


**Figure B3** Powder XRD diffractograms for untreated mussel shells (green) and mussel shells heated to 160 °C (blue), 200 °C (red) and 225 °C (black) for 48h.

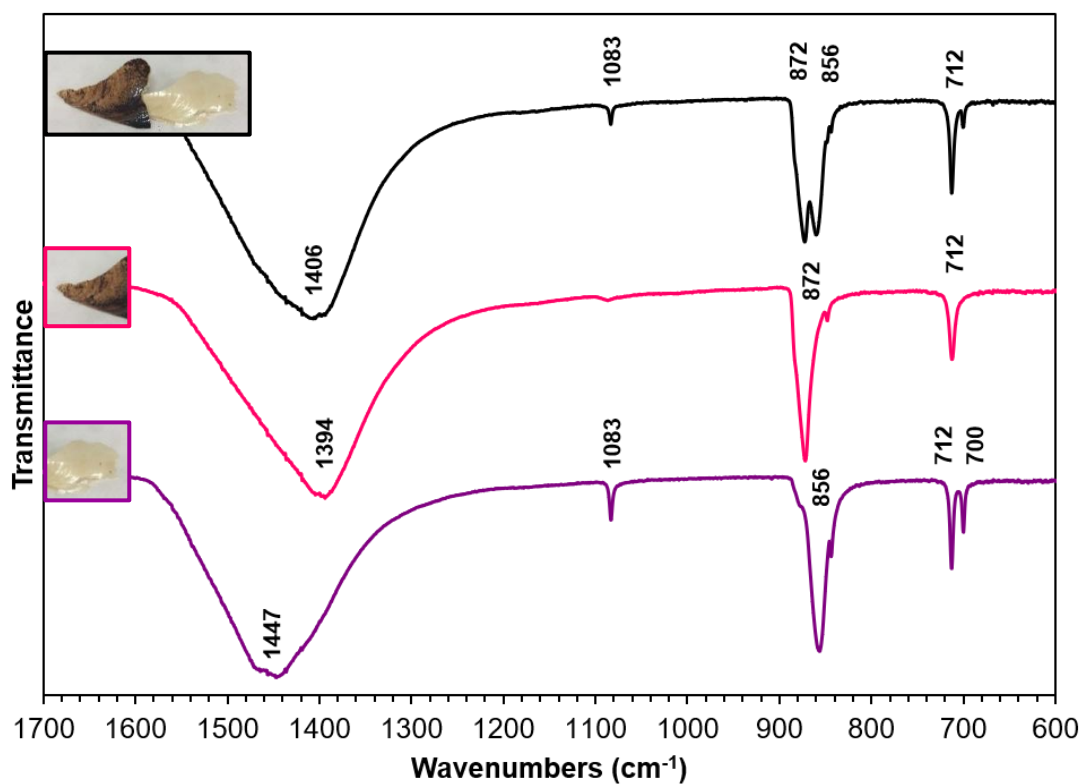


**Figure B4** Infrared spectra for whole mussel shells heated at 220 °C for 48h (black) and the resulting outer prismatic calcite layer (pink) and inner nacreous aragonite layer (purple) of the shell that cleanly separate as a result of heating.

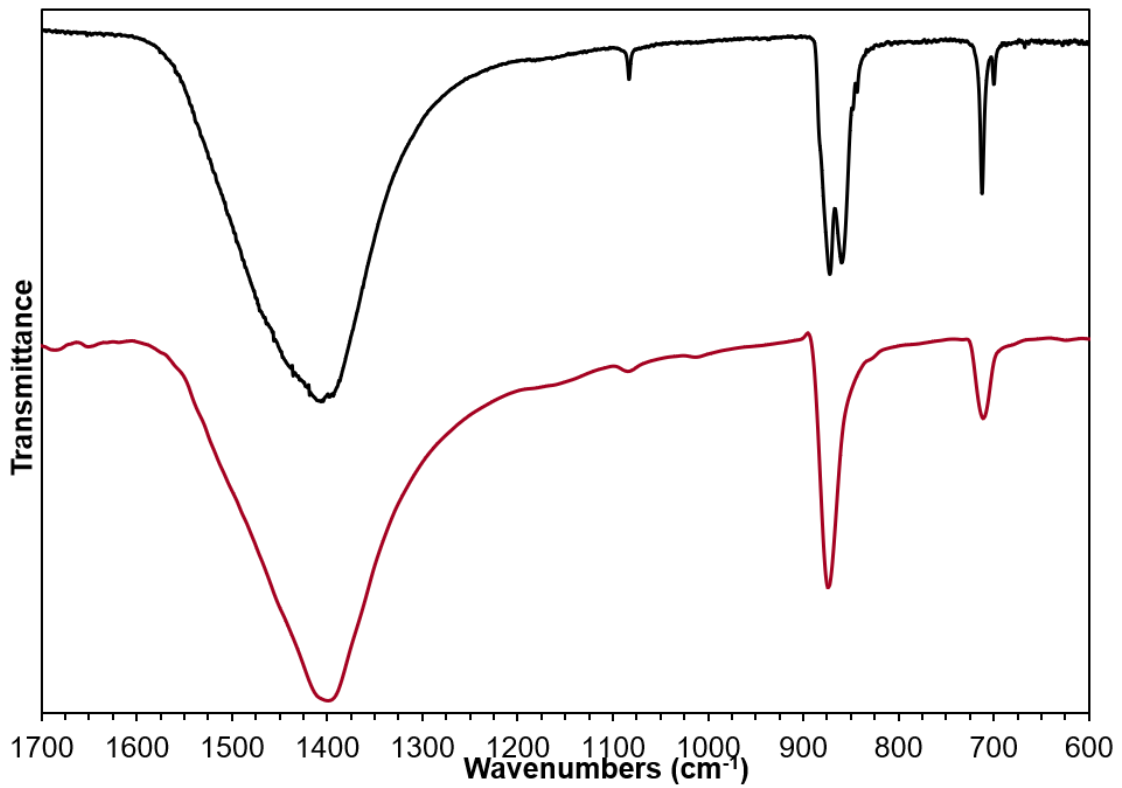


**Figure B5** Infrared spectra of blue mussel, *Mytilus edulis*, (black) and eastern oyster, *Crassostrea virginica*, (burgundy) shells treated at 220 °C for 48h.

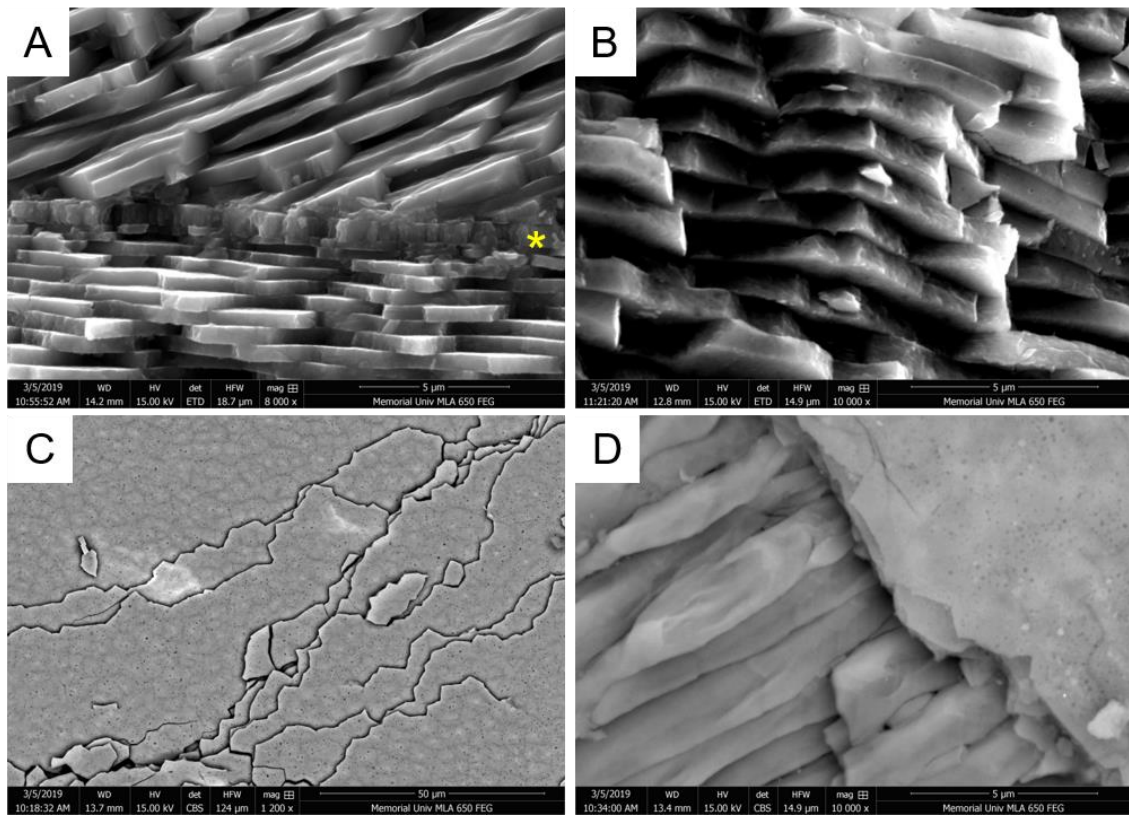


**Figure B6** SEM micrographs of A) the cross section of untreated blue mussel shells shows the outer prismatic calcite layer separated from the inner nacreous aragonite layer by the myostracum (denoted by a star), B) cross section of the inner nacreous layer that results from heating the blue mussel shell to 220 °C for 48 h, C) the back side of the inner nacreous layer of blue mussel shell, and D) the inside of the outer layer of the blue mussel shell (where it separates from the inner nacreous layer) that clearly shows some of the myostracum attached.

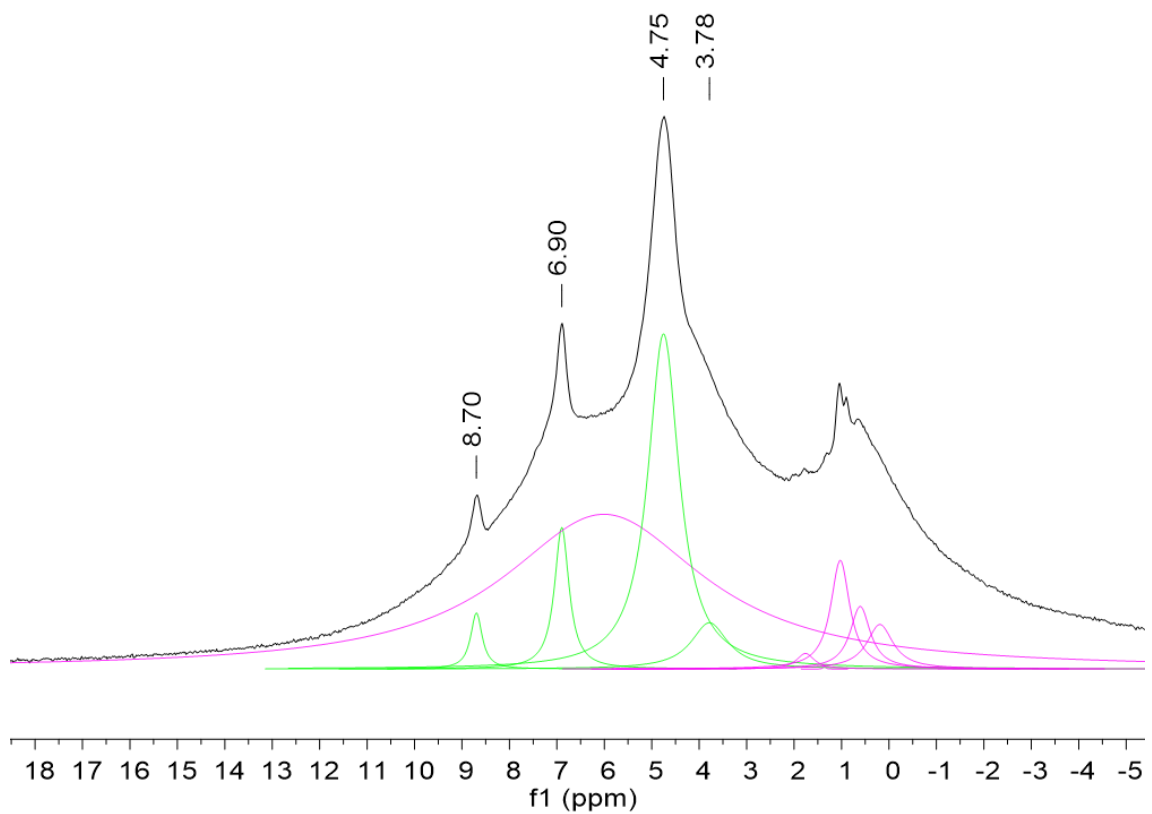


**Figure B7** Normalized 600 MHz  $^1\text{H}$  NMR spectra of untreated blue mussel shells that were ground with a mortar and pestle. 3.2 mm zirconia rotor and spinning at 20 kHz with a relaxation delay of 2s. 16 scans. This spectrum shows the deconvolution of peaks where the pink lines (that correspond to the zirconia rotor that is shown in Figure B8) are not part of the signal from the organic matrix in the blue mussel shell.

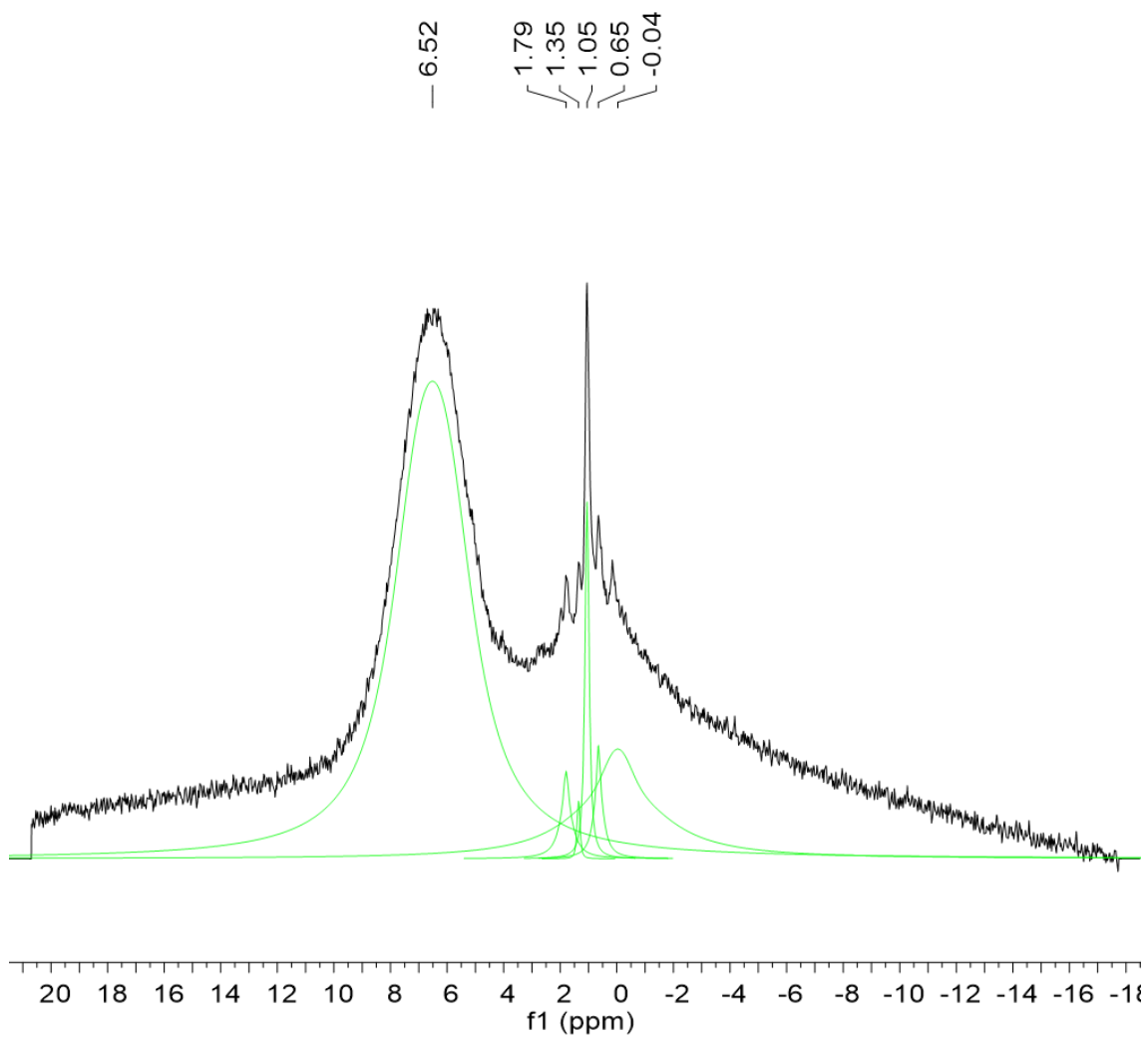


**Figure B8** Normalized 600 MHz  $^1\text{H}$  NMR spectra of empty 3.2 mm zirconia rotor. Spinning at 20 kHz with a relaxation delay of 2 s. 16 scans

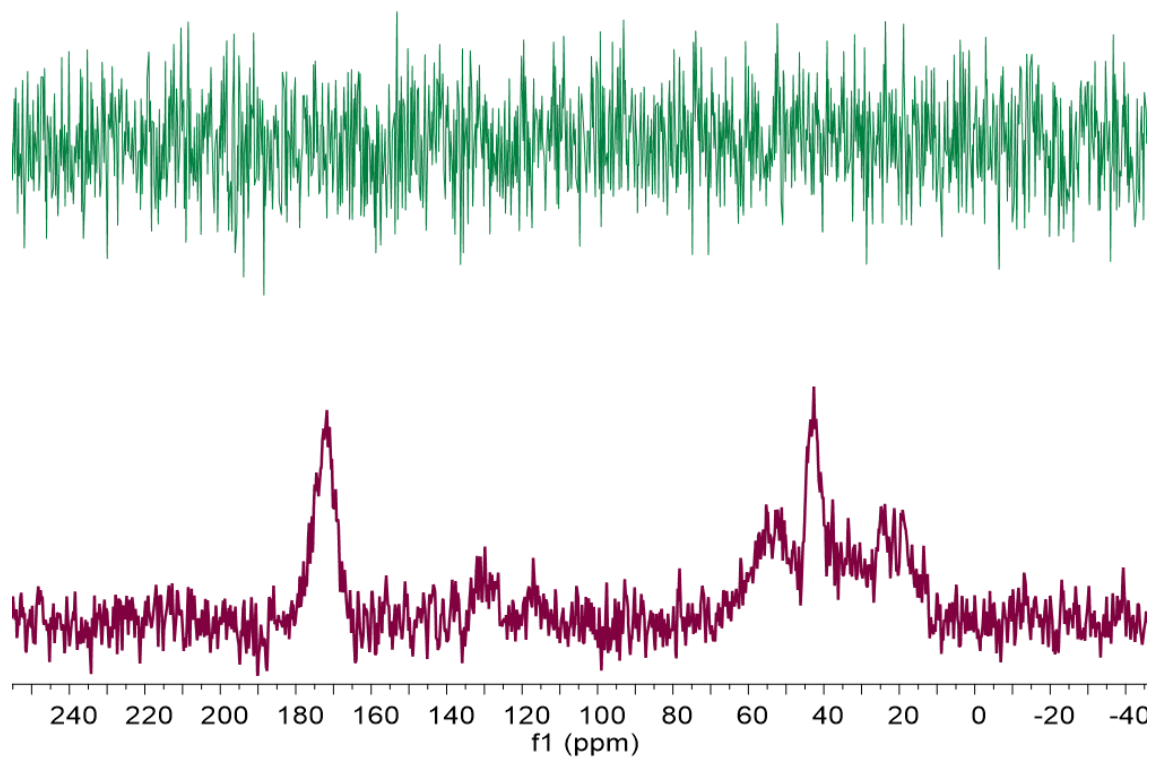


**Figure B9**  $^{13}\text{C}$  CP MAS NMR spectra of the inner nacreous layer of blue mussel (teal) that is a result of heating the shells to 220 °C for 48h and untreated mussel shells (purple). Acquisition of the two spectra had the same experimental conditions. 3.2 mm zirconia rotor spinning at 20 kHz with a contact time of 1 ms. Proton decoupling level of 100 kHz and a relaxation delay of 1 s. Hartmann-Hahn rf was matched to 62.5 kHz. 16k scans.

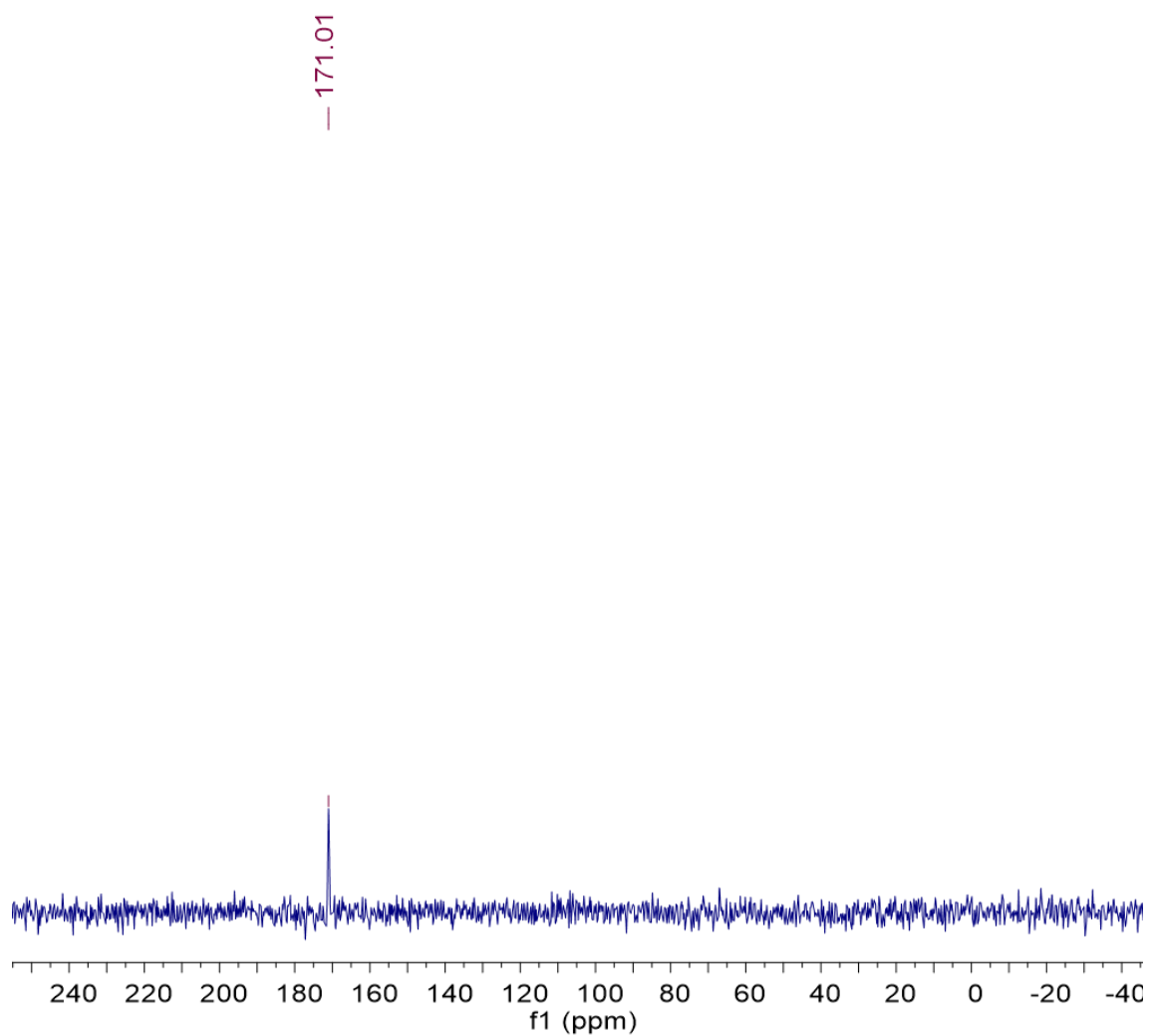


**Figure B10**  $^{13}\text{C}$  DE MAS NMR of the inner nacreous layer of blue mussel shells ground with a mortar and pestle. 3.2 mm zirconia rotor. Spinning at 20 kHz with a proton decoupling level of 100 kHz and a relaxation delay of 320 s. 60 scans.

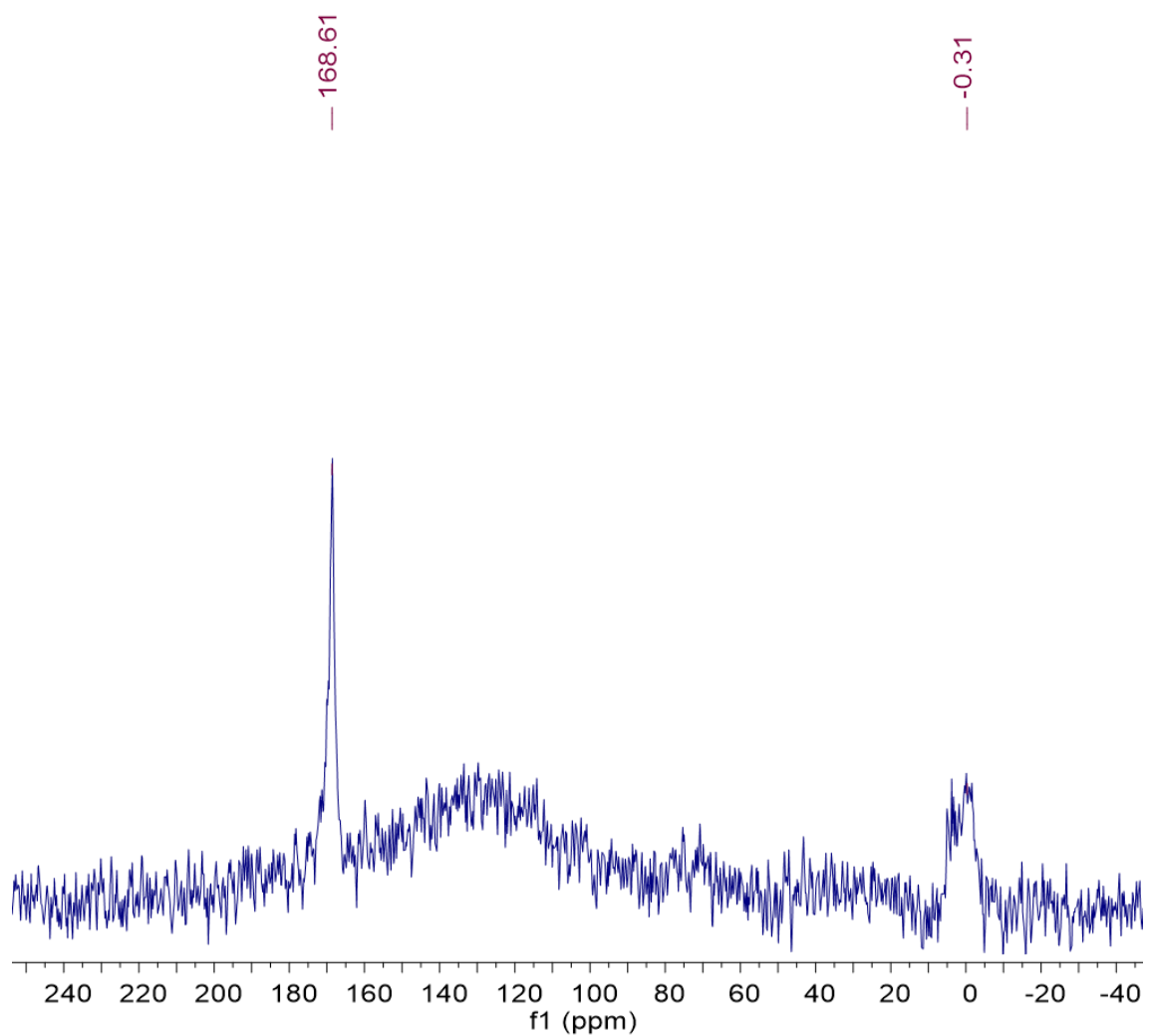


**Figure B11**  $^{13}\text{C}$  DE MAS NMR of the outer prismatic layer of blue mussel shells ground with a mortar and pestle. 3.2 mm zirconia rotor. Spinning at 20 kHz with a proton decoupling level of 100 kHz and a relaxation delay of 10 s. 8k scans.

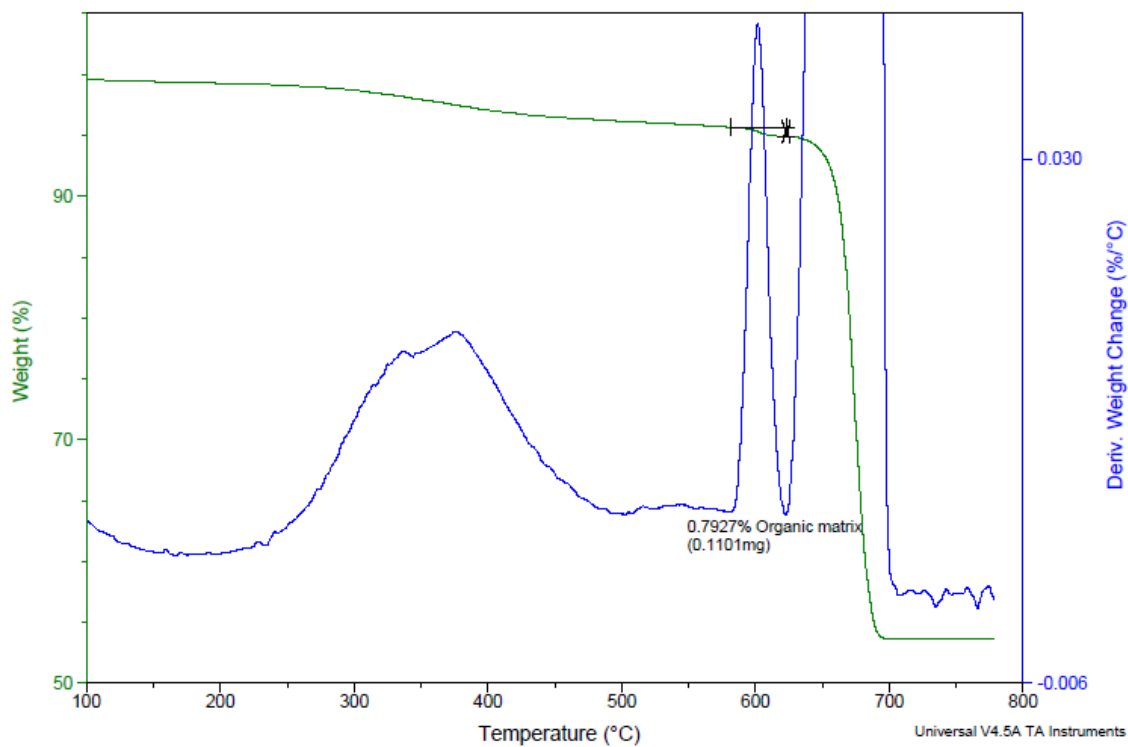


**Figure B12** Thermogravimetric analysis of untreated blue mussel shells.

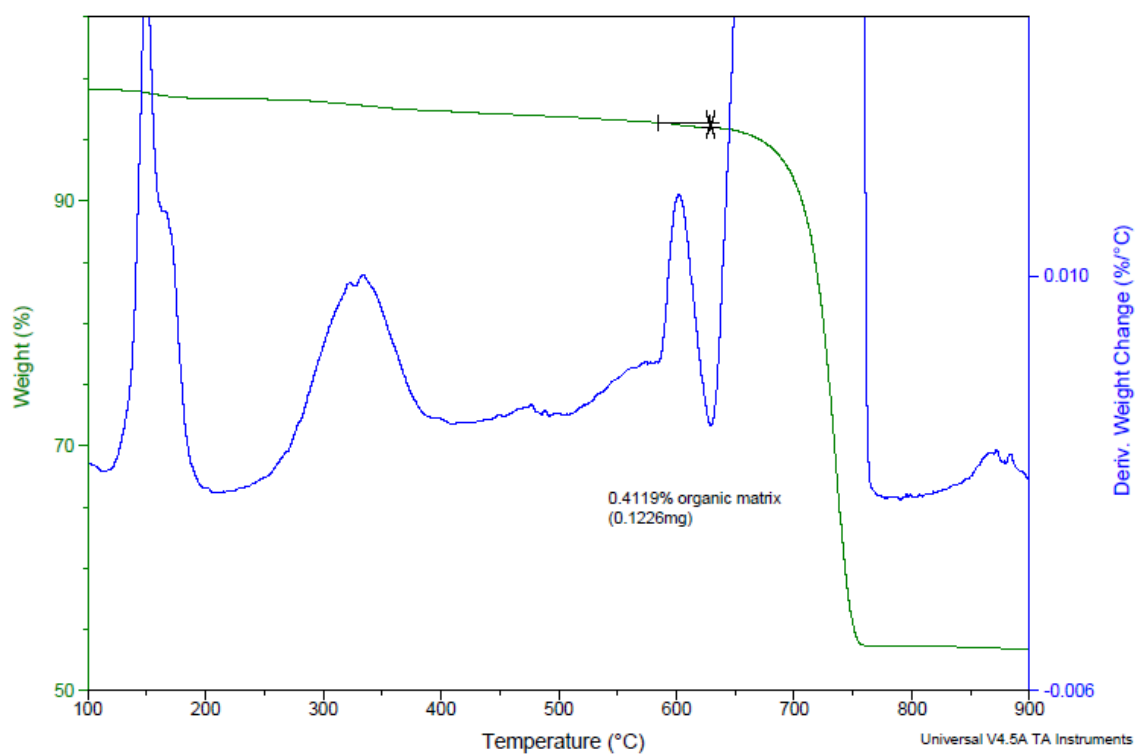


**Figure B13** Thermogravimetric analysis of blue mussel shells that have been heated to 220 °C for 48 h.

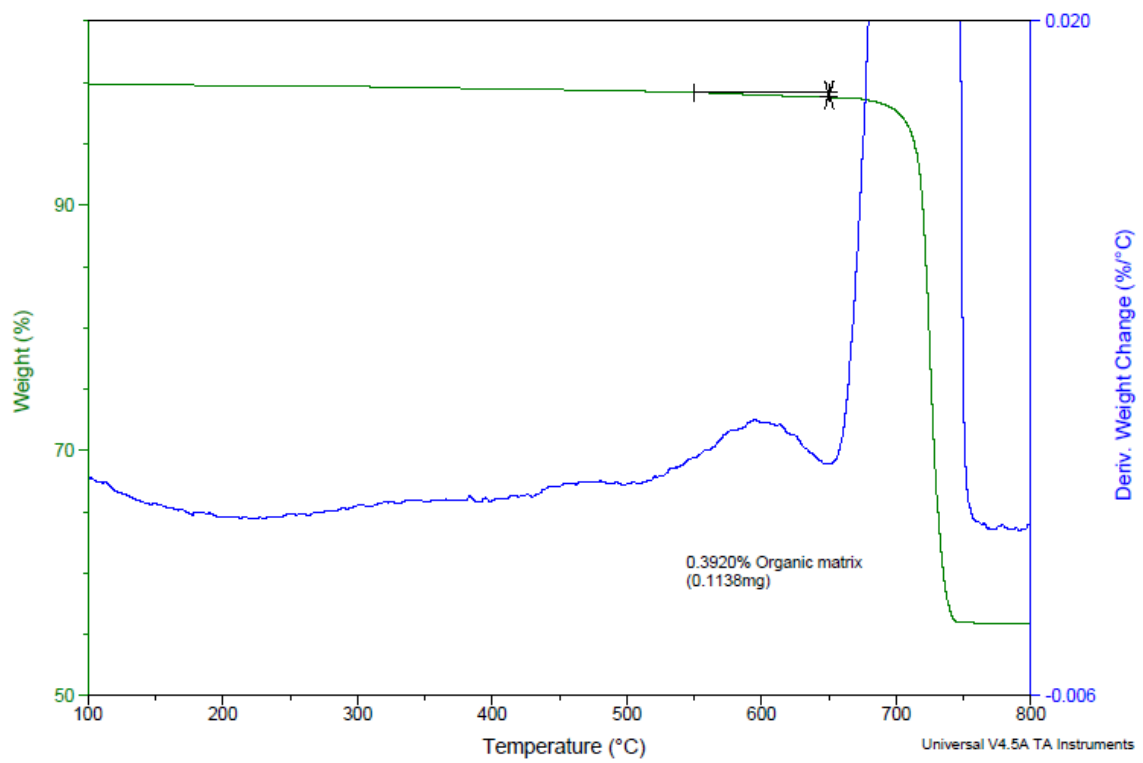


**Figure B14** Thermogravimetric analysis of the outer layer of blue mussel shells.

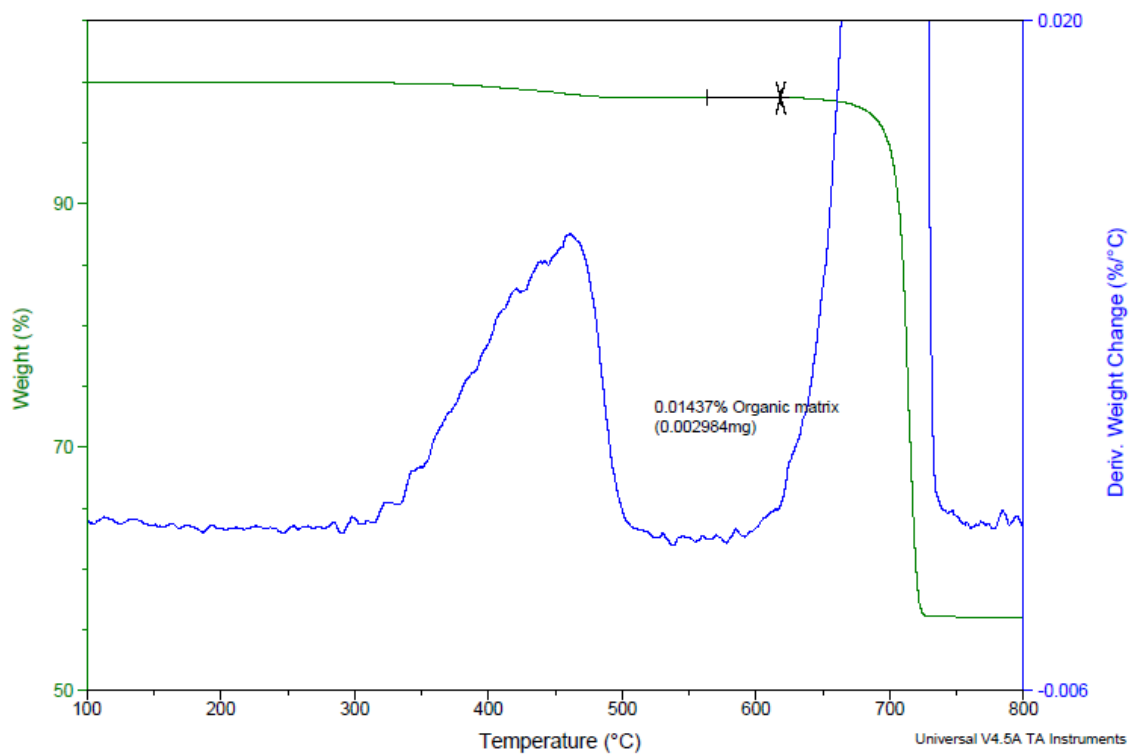


**Figure B15** Thermogravimetric analysis of the inner layer of blue mussel shells.

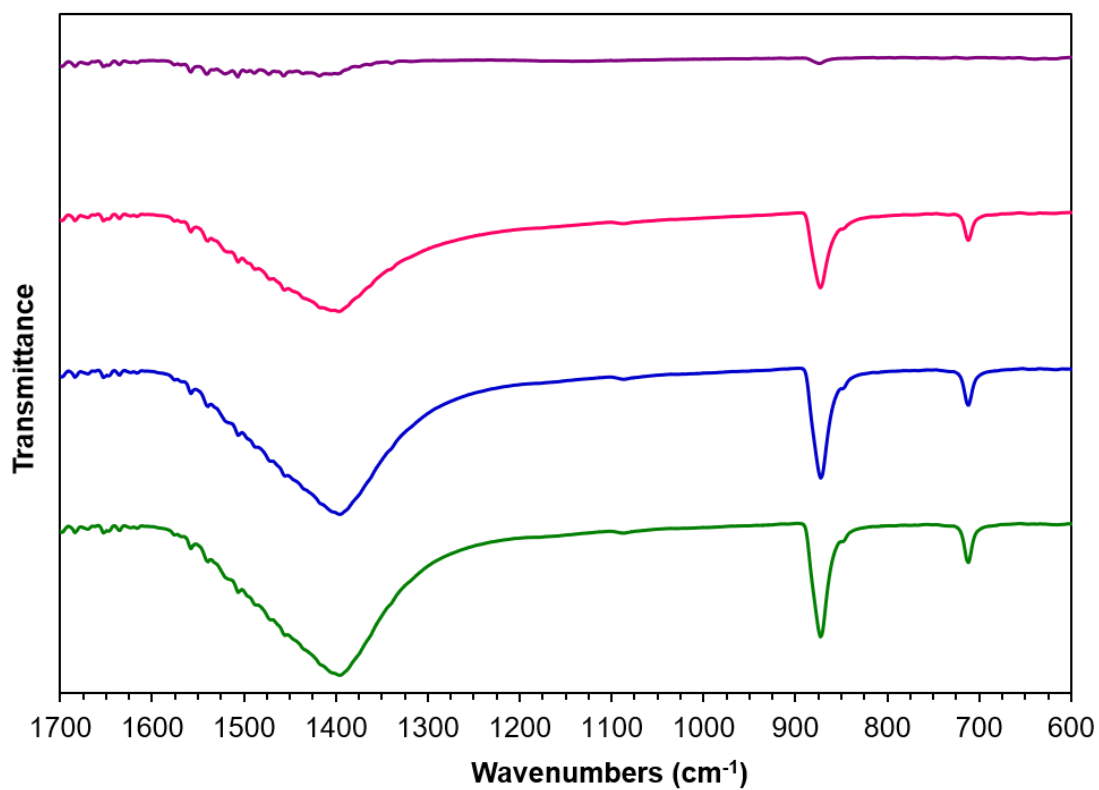


**Figure B16** Infrared spectra of blue mussels treated from 450 °C (green), 550 °C (blue), 650 °C (pink) and 750 °C (purple) for 2h.

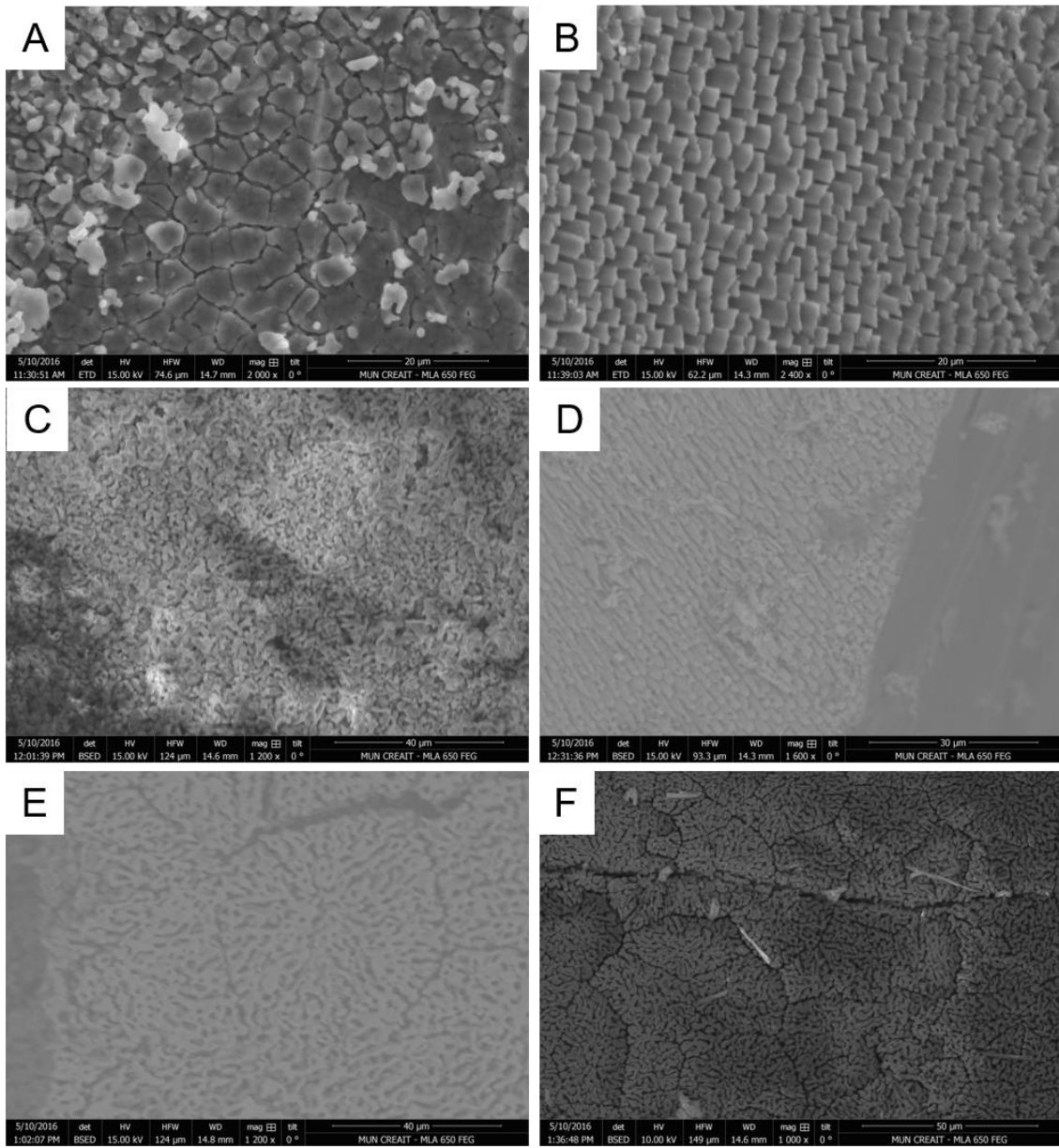


**Figure B17** SEM micrographs of A) the inner layer of blue mussel shell after heating to 450 °C, B) the outer layer of blue mussel shell after heating to 450 °C, C) the inner layer of blue mussel shell after heating to 550 °C, D) the outer layer of blue mussel shell after heating to 550 °C, E) the inner layer of blue mussel shell after heating to 650 °C and F) the inner layer of blue mussel shell after heating to 650 °C. Shells were heated for 2h at their respective temperatures.

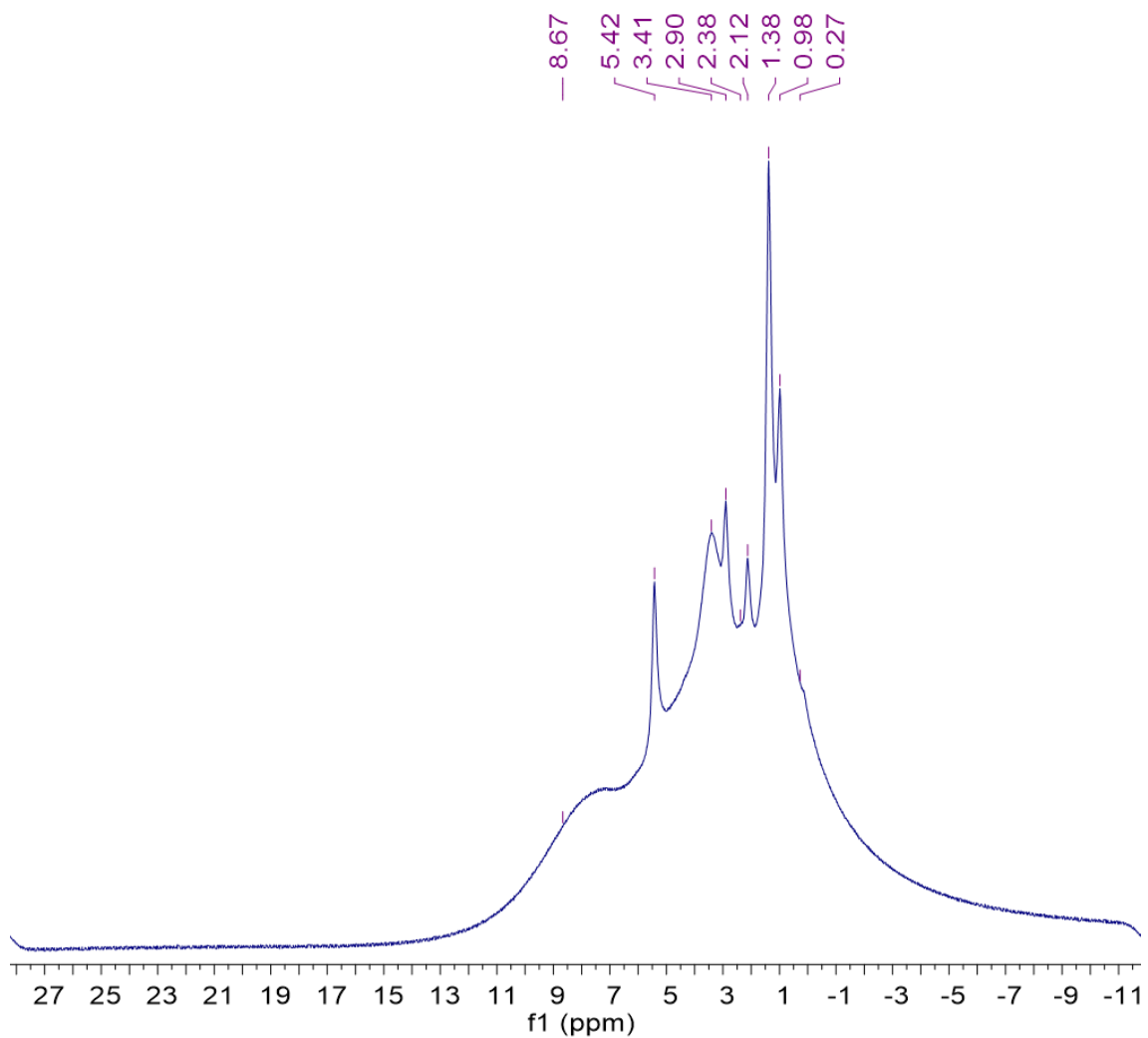


**Figure B18** Normalized 600 MHz  $^1\text{H}$  NMR spectra of freeze-dried blue mussel meat. 3.2 mm zirconia rotor and spinning at 20 kHz with a relaxation delay of 5s. 4 scans.

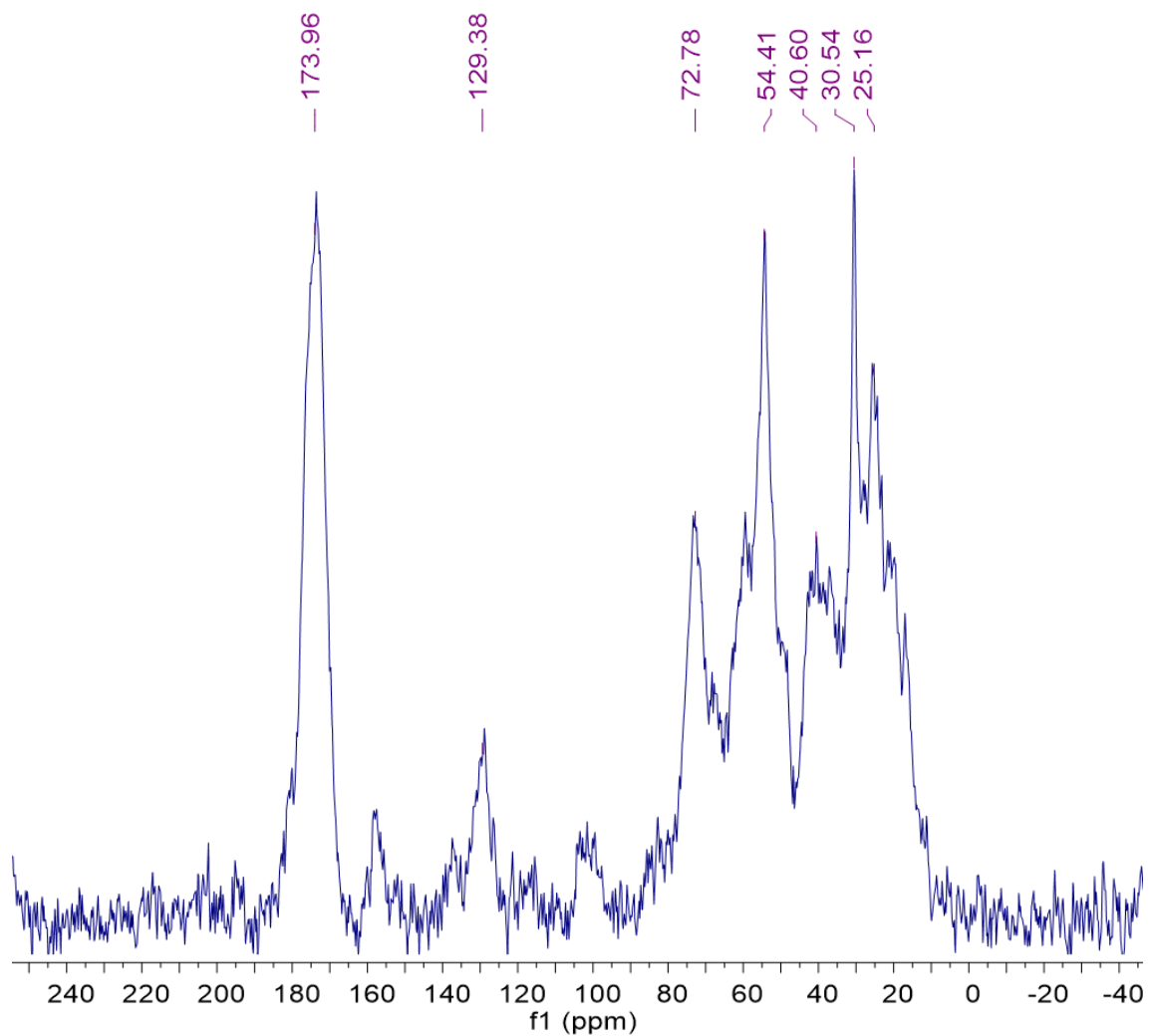


**Figure B19**  $^{13}\text{C}$  CP MAS NMR of freeze-dried blue mussel (*Mytilus edulis*) meat. 3.2 mm zirconia rotor spinning at 20 kHz with a contact time of 2 ms. Proton decoupling level of 100 kHz and a relaxation delay of 3 s. Hartmann-Hahn rf was matched to 62.5 kHz. 1k scans.

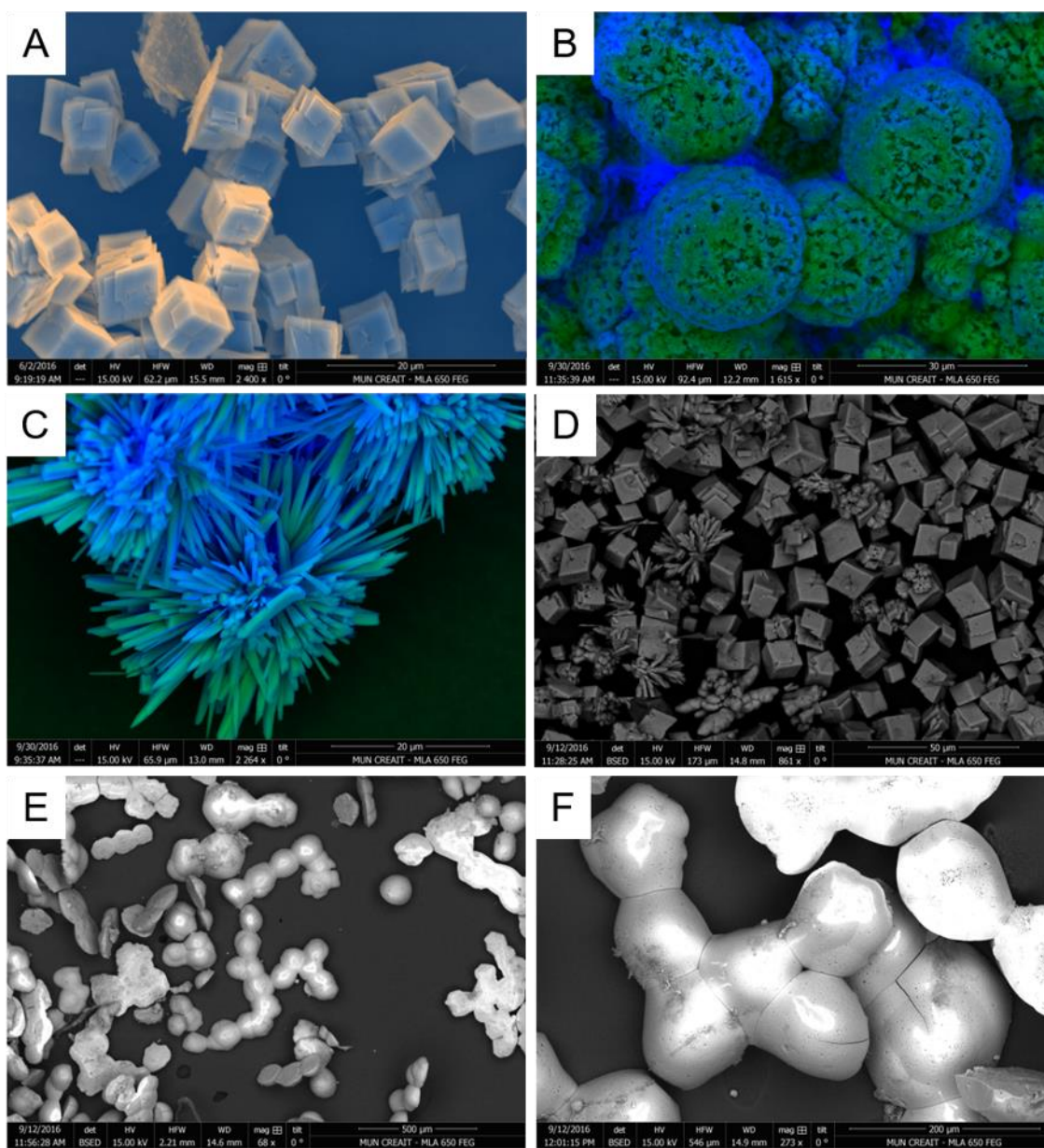


**Figure B20** Representative SEM micrographs of synthetic CaCO<sub>3</sub> products. A) calcite, B) vaterite, C) aragonite, D) mixture of calcite, aragonite and vaterite, E) vaterite with a unique formation, similar to nacre and F) zoomed in region of vaterite.

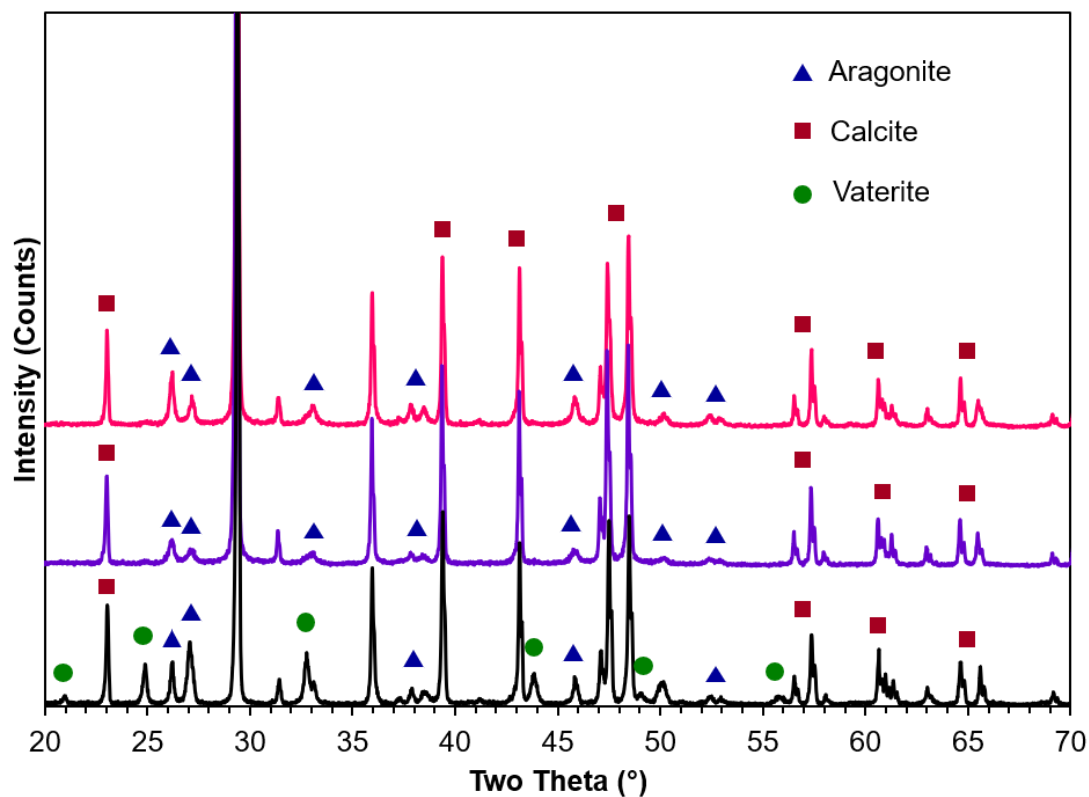


**Figure B21** Powder XRD diffractograms for synthetic  $\text{CaCO}_3$  products from reaction conditions 0.8 M  $\text{CaCl}_2$  and  $\text{Na}_2\text{CO}_3$  (black), 0.8 M  $\text{CaCl}_2$  and  $\text{Na}_2\text{CO}_3$  with the addition of mussel protein hydrolysate (purple) and 0.8 M  $\text{CaCl}_2$  and  $\text{Na}_2\text{CO}_3$  with the addition of mussel protein hydrolysate and mussel shells for seeding nacre (pink). Identification of polymorphs denoted by blue triangles for aragonite, red squares for calcite and green circles for vaterite.



**Figure B22** Examples of colour and texture of dyed nacre and its use in UV cure gel nail enhancements.

## Appendix C

**Table C1** Results from initial central composite circumscribed design to synthesize calcium acetate. Factors studied were time, concentration of CH<sub>3</sub>COOH and shell type. The response studied was the yield of calcium acetate.

Run	Time (h)	% CH <sub>3</sub> COOH	Shell Type	Yield (%)
8	2.3	10	HTC	55.1
10	2.3	10	RTC	57.4
11	6	5	HTC	62.6
16	6	15	CC	50.0
21	6	15	RTC	41.2
22	6	5	RTC	45.2
30	6	15	HTC	53.8
36	6	5	CC	56.7
2	15	17.1	RTC	48.6
3	15	2.9	HTC	77.4
4	15	10.0	CC	61.1
6	15	17.1	HTC	56.1
7	15	10.0	HTC	68.0
9	15	2.9	CC	35.5
12	15	10.0	RTC	56.4
17	15	17.1	CC	47.0
18	15	2.9	RTC	66.2
19	15	10	HTC	65.9
20	15	10	RTC	59.2
24	15	10	HTC	66.4
25	15	10	RTC	58.5
26	15	10	CC	57.5
27	15	10	RTC	56.0
28	15	10	HTC	69.5
31	15	10	RTC	57.2
35	15	10	HTC	67.7
37	15	10	CC	57.9
38	15	10	CC	59.3

39	15	10	CC	51.2
1	24	5	RTC	60.8
5	24	5	CC	58.1
15	24	15	RTC	49.2
23	24	15	HTC	62.7
29	24	15	CC	51.5
32	24	5	HTC	74.0
13	27.7	10	RTC	60.6
33	27.7	10	HTC	72.1
34	27.7	10	CC	56.9

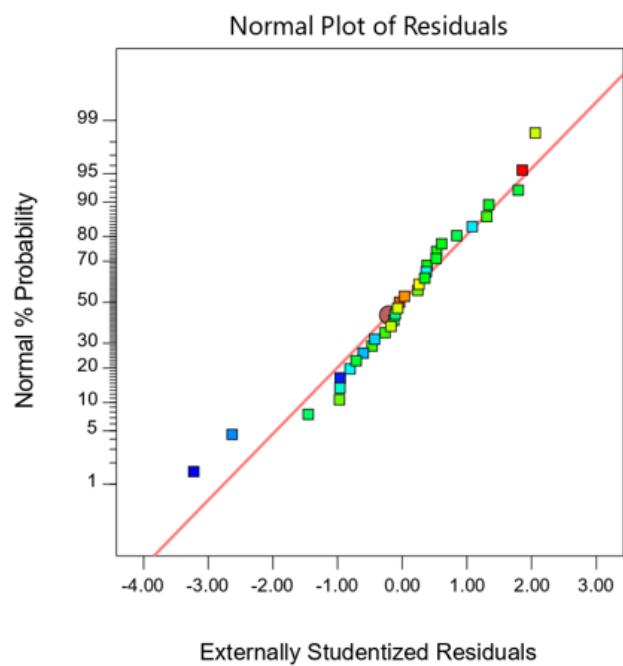


**Figure C1** Normal Plot of residuals for the model developed from the CCC design to synthesize calcium acetate using three shell types.

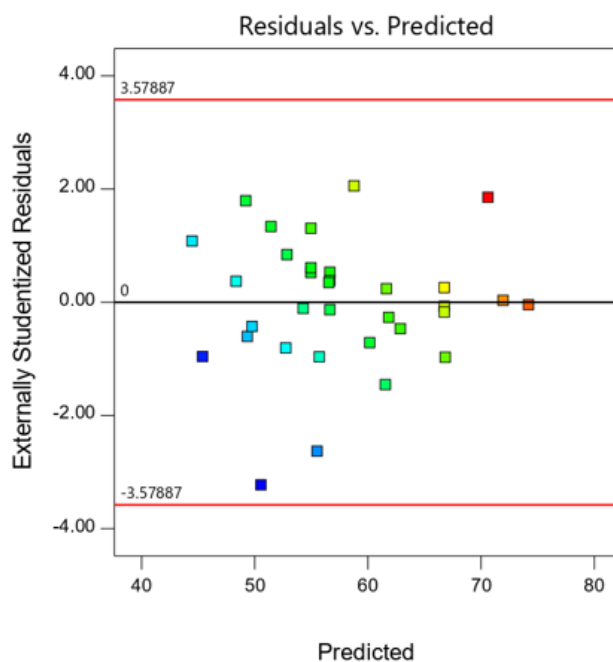


**Figure C2** Residuals vs. run for the model developed from the CCC design to synthesize calcium acetate using three shell types.

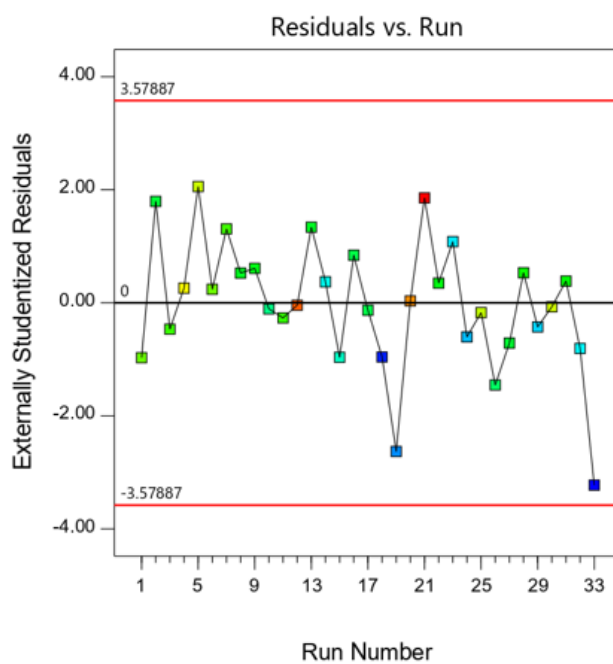


**Figure C3** Residuals vs. predicted for the model developed from the CCC design to synthesize calcium acetate using three shell types.

**Table C2** Analysis of variance for the initial central composite design for the synthesis of calcium acetate.

<b>Source</b>	<b>Sum of Squares</b>	<b>df</b>	<b>Mean Square</b>	<b>F-value</b>	<b>p-value</b>	
<b>Model</b>	1856.65	7	265.24	10.30	< 0.0001	significant
A-Acetic Acid Concentration	369.06	1	369.06	14.34	0.0009	
B-Time	324.40	1	324.40	12.60	0.0016	
C-Shell Type	893.94	2	446.97	17.36	< 0.0001	
AC	152.61	2	76.31	2.96	0.0699	
A <sup>2</sup>	116.64	1	116.64	4.53	0.0433	
<b>Residual</b>	643.50	25	25.74			
Lack of Fit	627.65	19	33.03	12.50	0.0024	significant
Pure Error	15.85	6	2.64			
<b>Cor Total</b>	2500.16	32				

<b>Std. Dev.</b>	5.07	<b>R<sup>2</sup></b>	0.7426
<b>Mean</b>	57.62	<b>Adjusted R<sup>2</sup></b>	0.6705
<b>C.V. %</b>	8.80	<b>Predicted R<sup>2</sup></b>	0.4316
		<b>Adeq Precision</b>	11.9011

**Table C3** Results from the custom design to synthesize  $\text{Ca}(\text{CH}_3\text{COO})_2 \cdot \text{H}_2\text{O}$  using HTC shells. Factors studied were time and concentration of  $\text{CH}_3\text{COOH}$ . The response studied was the yield of calcium acetate.

Run #	Time (h)	% $\text{CH}_3\text{COOH}$	Yield (%)
1	24	5.0	85.0
2	24	5.0	80.9
3	32	1.0	89.6
4	24	5.0	81.4
5	20	1.0	84.2
6	20	1.0	84.2
7	16	1.0	81.0
8	32	9.0	93.0
9	28	3.0	88.1
10	28	7.0	88.5
11	16	5.0	80.5
12	24	9.0	90.3
13	16	5.0	77.0
14	20	7.0	87.9
15	16	9.0	81.9
16	32	5.0	83.7
17	32	9.0	92.9
18	24	9.0	88.1
19	32	1.0	89.6

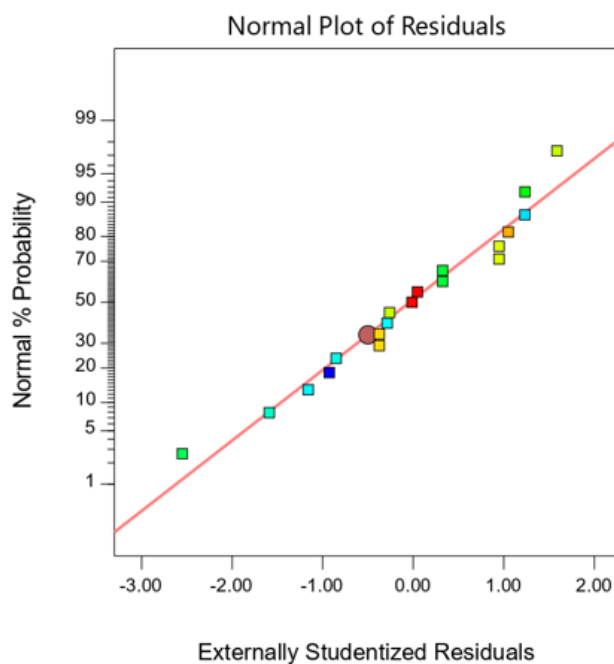


**Figure C4** Normal Plot of residuals for the model developed from the custom design to synthesize calcium acetate using HTC shells.

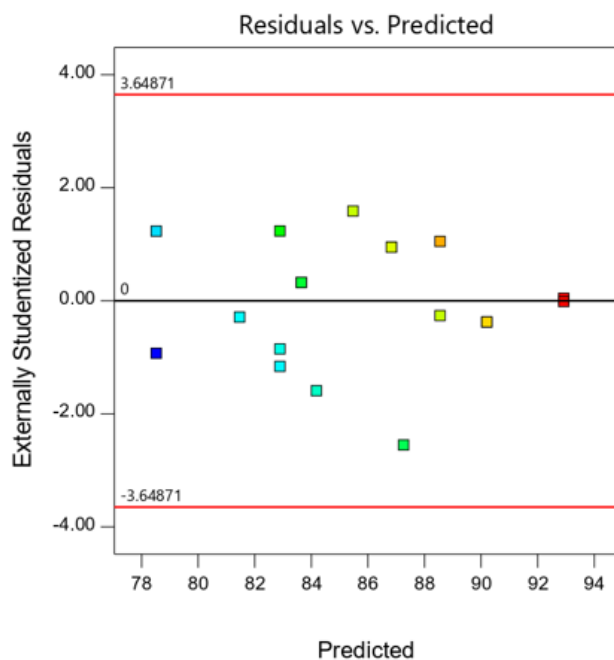


**Figure C5** Residuals vs. predicted for the model developed from the custom design to synthesize calcium acetate using HTC shells.

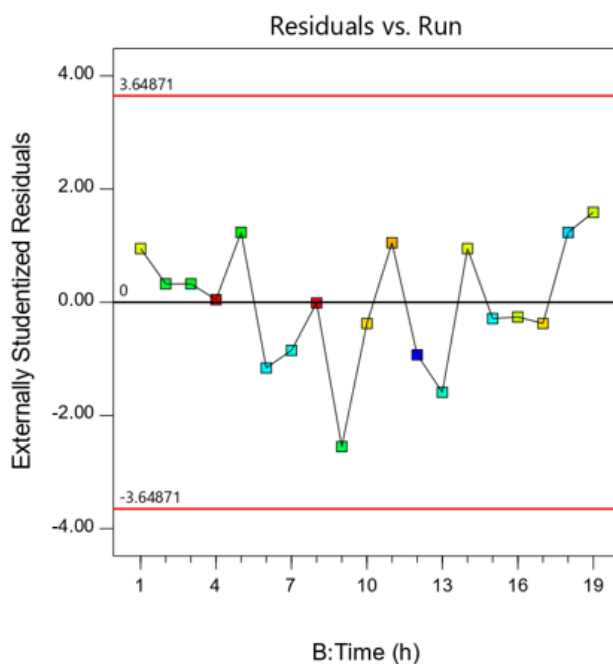


**Figure C6** Residuals vs. run for the model developed from the custom design to synthesize calcium acetate using HTC shells.

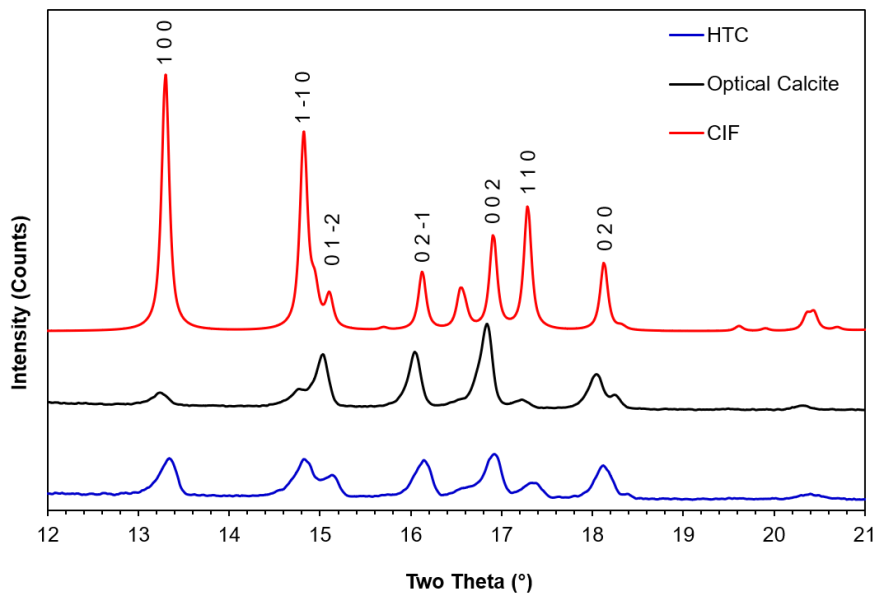
**Table D1 and Design Summary:** The analysis of variance for the custom design to optimize the synthesis of calcium acetate monohydrate using HTC shells.

Source	Sum of Squares	df	Mean Square	F-value	p-value	
<b>Model</b>	321.64	3	107.21	30.90	< 0.0001	significant
A-Acetic Acid Concentration	19.52	1	19.52	5.63	0.0315	
B-Time	189.57	1	189.57	54.63	< 0.0001	
A <sup>2</sup>	75.36	1	75.36	21.72	0.0003	
<b>Residual</b>	52.05	15	3.47			
Lack of Fit	33.49	7	4.78	2.06	0.1658	not significant
Pure Error	18.56	8	2.32			
<b>Cor Total</b>	373.69	18				

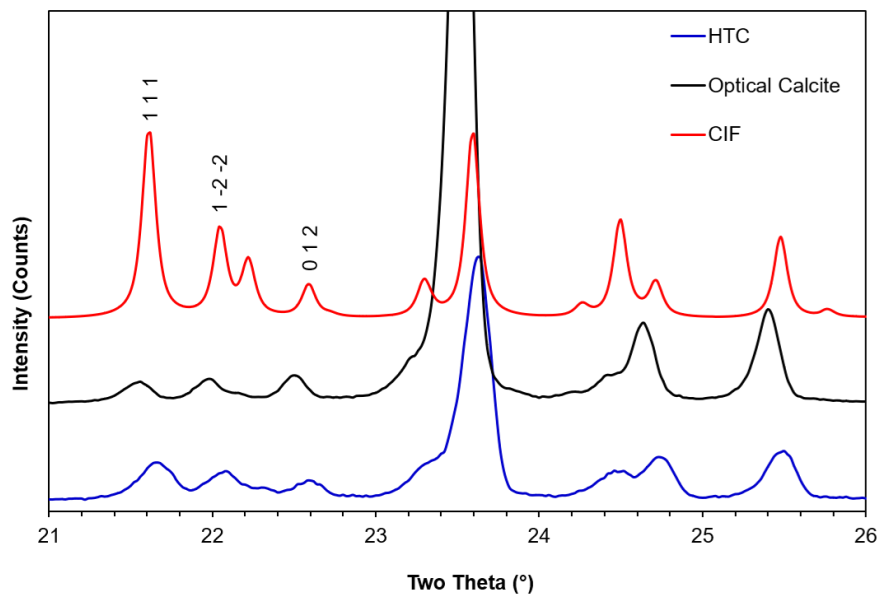
  

<b>Std. Dev.</b>	1.86	<b>R<sup>2</sup></b>	0.8607
<b>Mean</b>	85.71	<b>Adjusted R<sup>2</sup></b>	0.8329
<b>C.V. %</b>	2.17	<b>Predicted R<sup>2</sup></b>	0.7792
		<b>Adeq Precision</b>	16.8496

$$\text{Yield} = 82.89 + 1.36 A + 4.37 B + 4.30 A^2$$



**Figure C7** Powder X-ray diffractograms of  $\text{Ca}(\text{CH}_3\text{COO})_2 \cdot \text{H}_2\text{O}$  made from optical calcite and HTC shells plotted with the simulated diffractogram from the crystallographic information file (CIF) in the  $2\theta = 12-21^\circ$  range.



**Figure C8** Powder X-ray diffractograms of  $\text{Ca}(\text{CH}_3\text{COO})_2 \cdot \text{H}_2\text{O}$  made from optical calcite and HTC shells plotted with the simulated diffractogram from the crystallographic information file (CIF) in the  $2\theta = 21-26^\circ$  range.

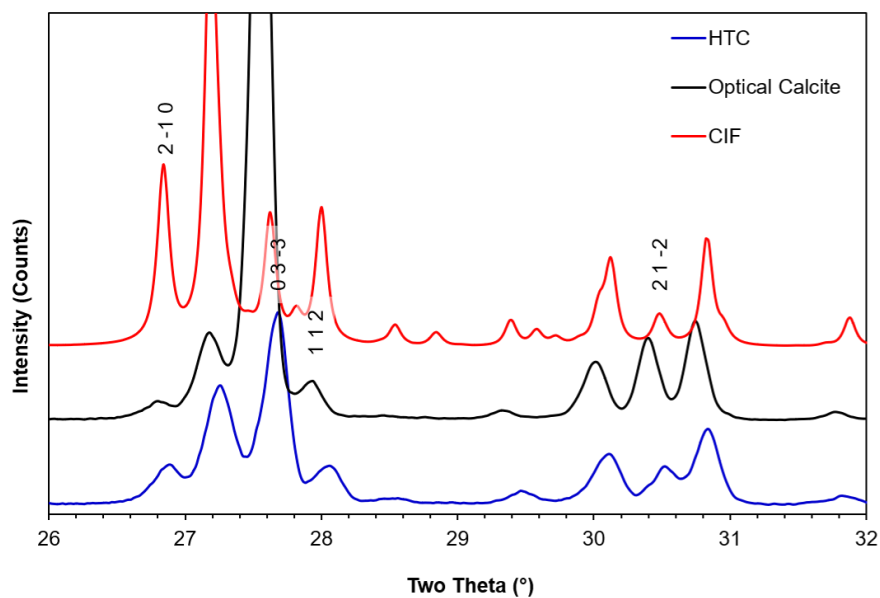


**Figure C9** Powder X-ray diffractograms of  $\text{Ca}(\text{CH}_3\text{COO})_2 \cdot \text{H}_2\text{O}$  made from optical calcite and HTC shells plotted with the simulated diffractogram from the crystallographic information file (CIF) in the  $2\theta = 26\text{-}32^\circ$  range.

## Appendix D

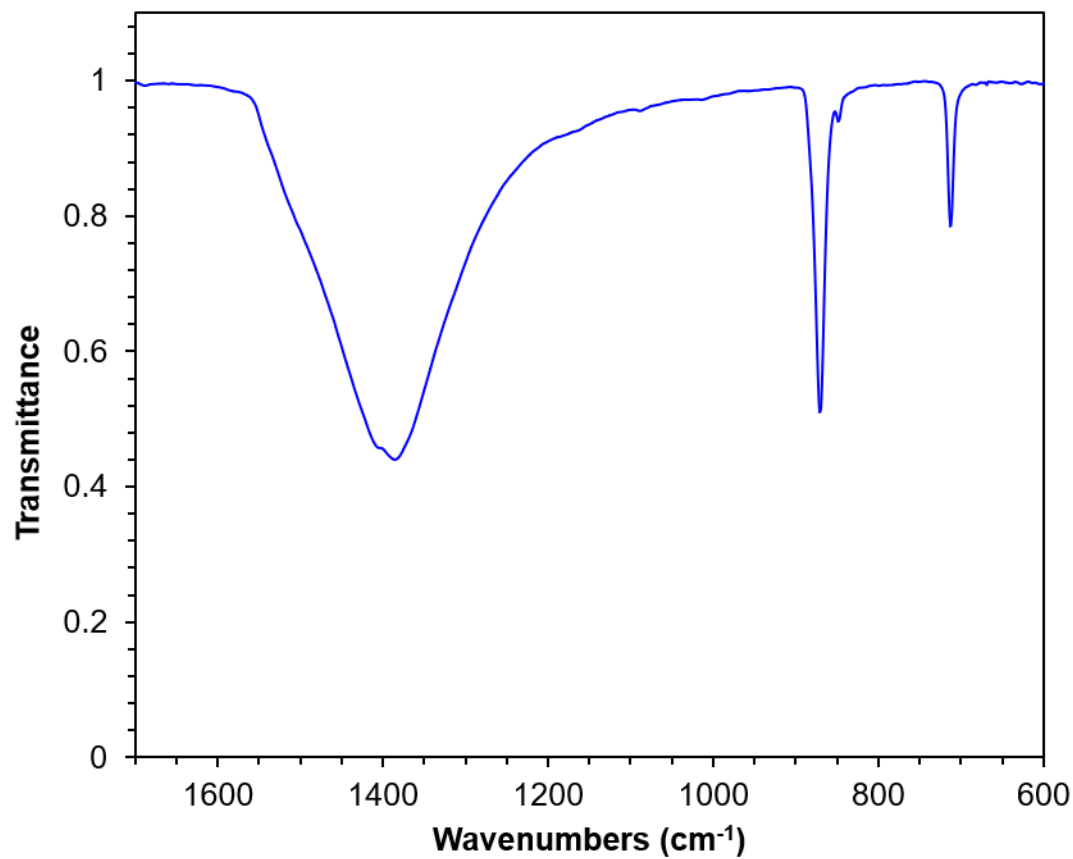


**Figure D1** Infrared spectrum of clean and dry self-assembled calcite (SAC).

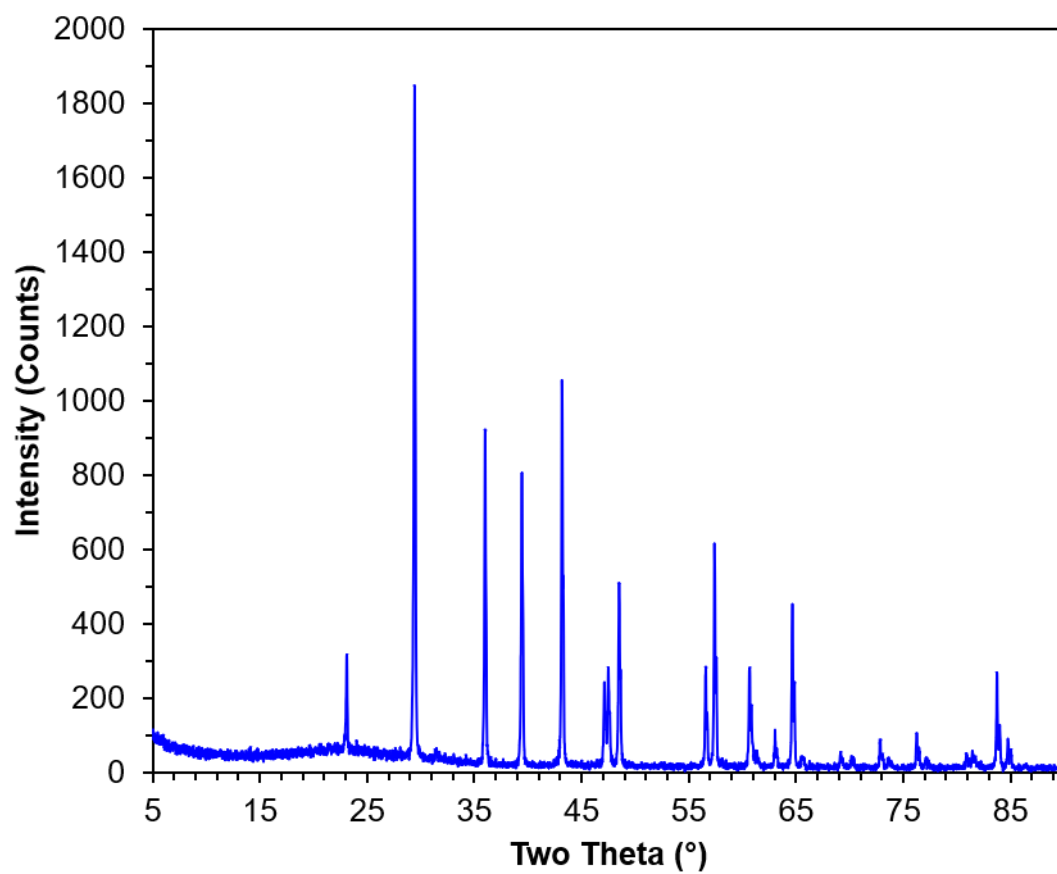


**Figure D2** Powder XRD diffractogram of clean and dry SAC.

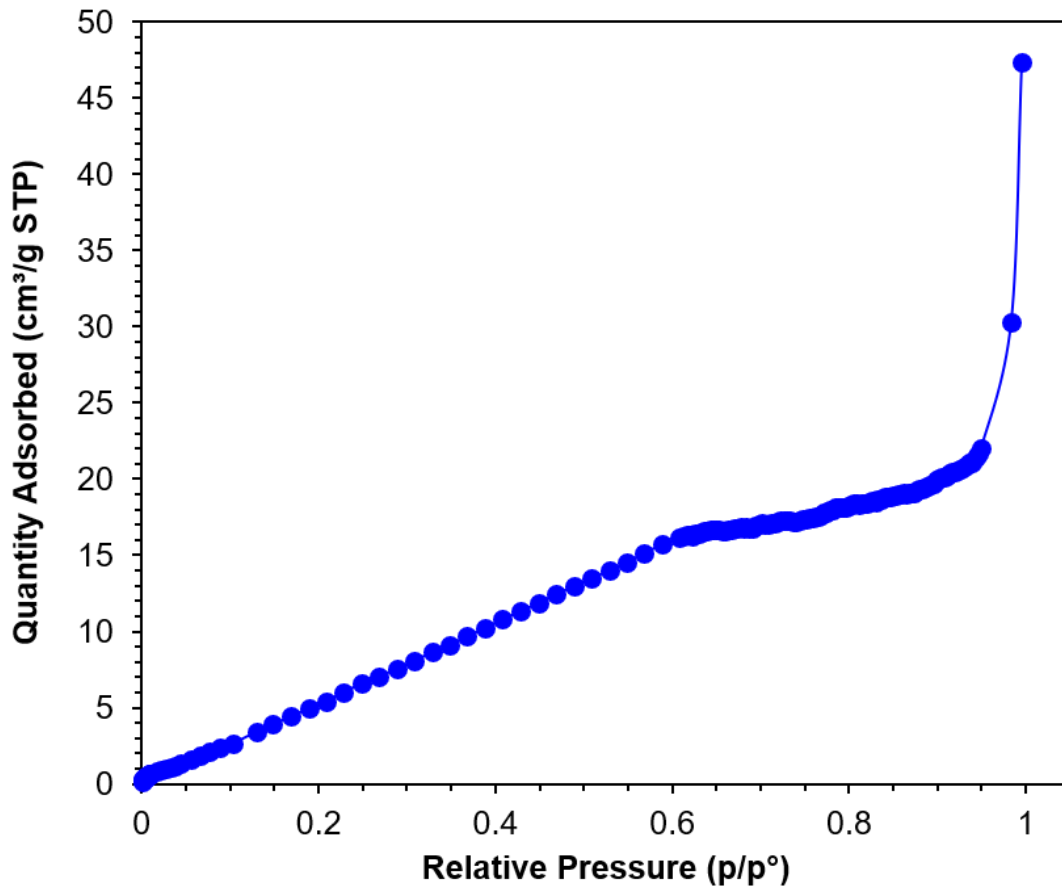


**Figure D3** Nitrogen adsorption isotherm for clean and dry SAC.

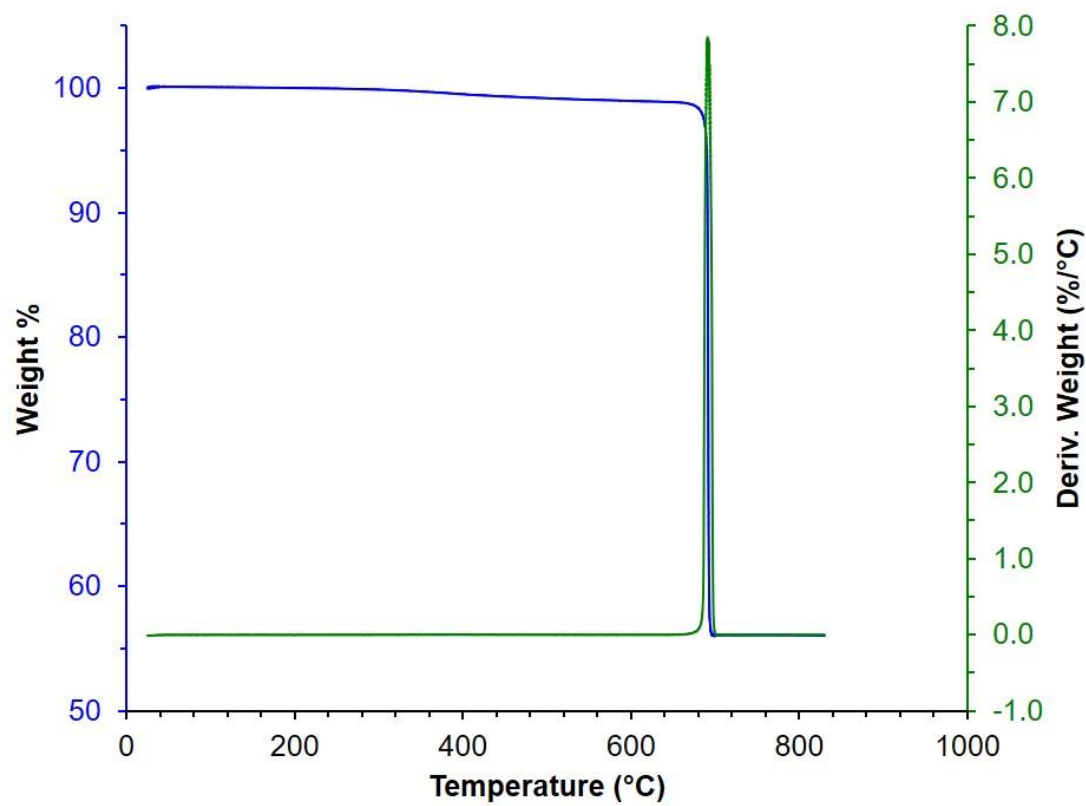


**Figure D4** Thermogravimetric analysis of SAC.

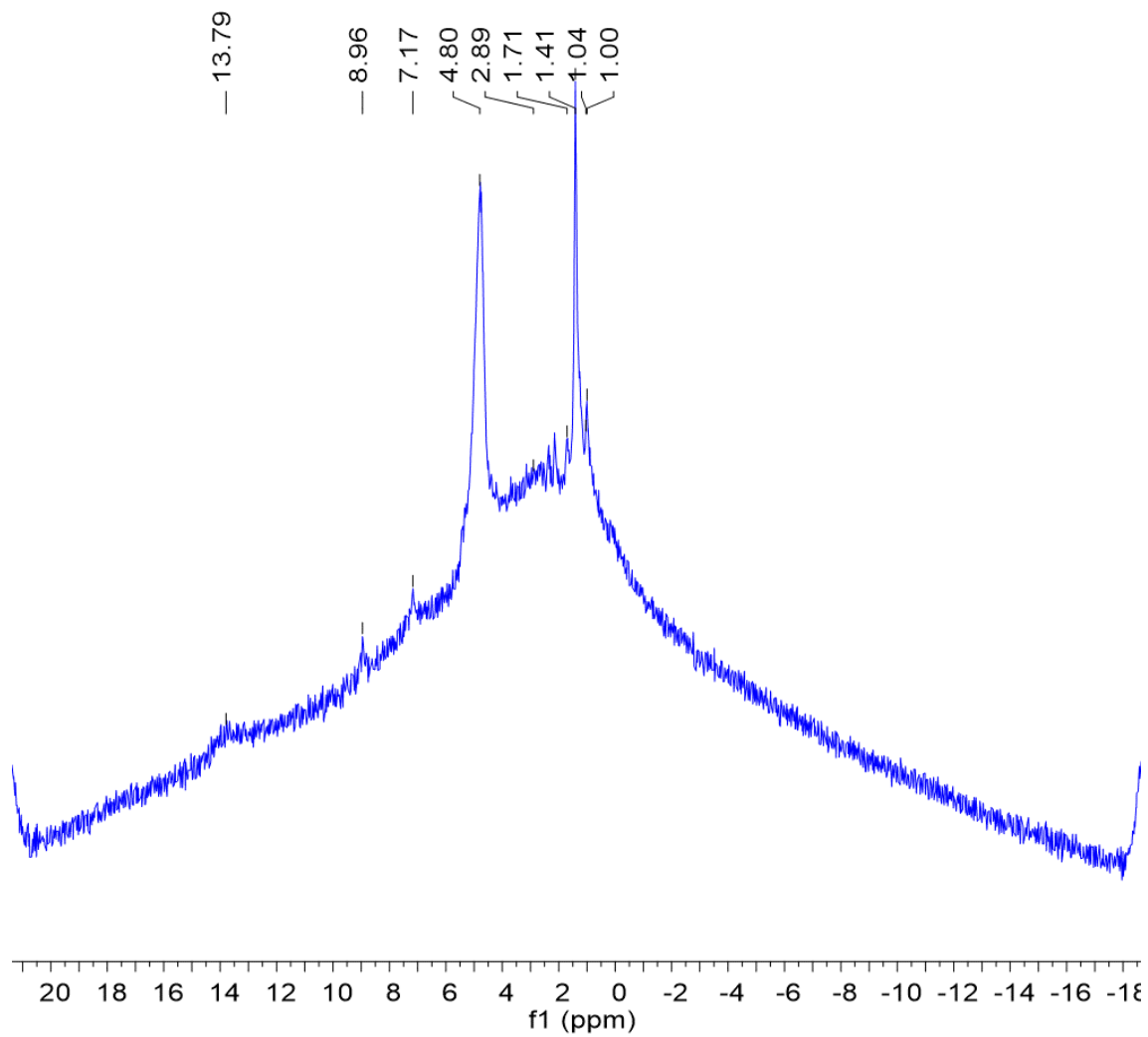


**Figure D5** Normalized 600 MHz  $^1\text{H}$  NMR spectra clean and dry SAC. 3.2 mm zirconia rotor and spinning at 20 kHz with a relaxation delay of 5s. 8scans. Peaks from 1.00-1.71 are from the rotor cap.

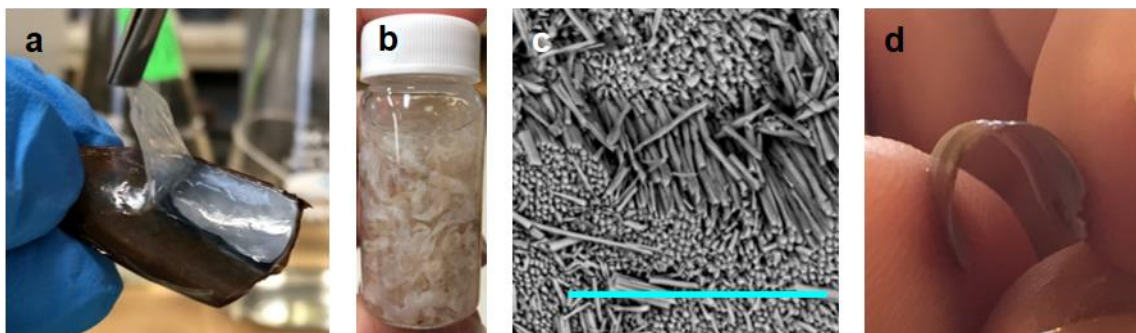


**Figure D6** Isolation and characterization of the insoluble matrix in *Mytilus edulis* shell. Digital images of the removal of (a) the insoluble matrix from the blue mussel shell and (b) a collection of many large sheets of the insoluble matrix in water. An SEM image (c) of an inner shell portion shows the inner nacre has reacted with 5%  $\text{CH}_3\text{COOH}$  and what is left is a flexible calcite portion of shell (d). Scale bar in (c) is 50  $\mu\text{m}$ .

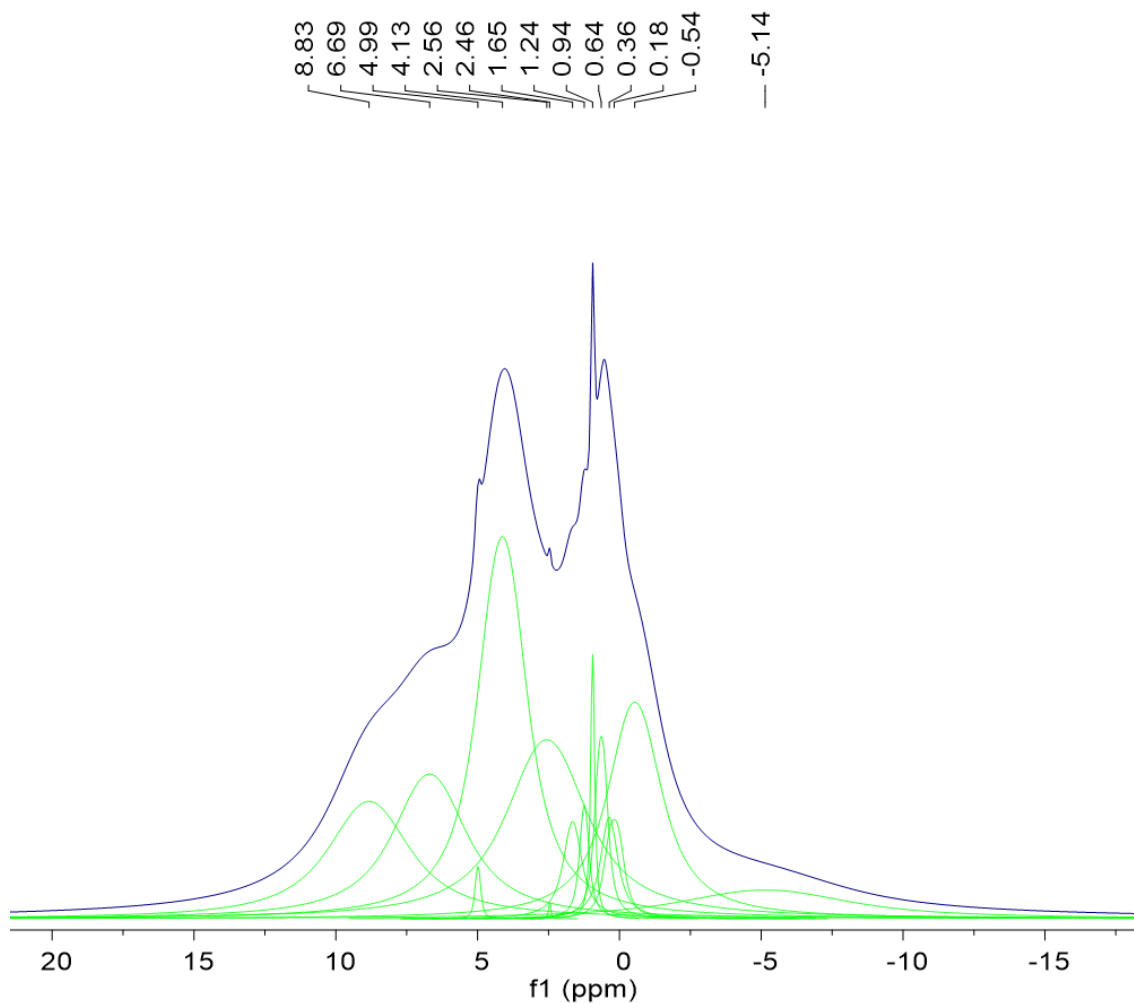


**Figure D7** Normalized 600 MHz  $^1\text{H}$  NMR spectra of the insoluble matrix from blue mussel shells. 3.2 mm zirconia rotor and spinning at 20 kHz with a relaxation delay of 2s. 16 scans. This spectrum shows the deconvolution of peaks.

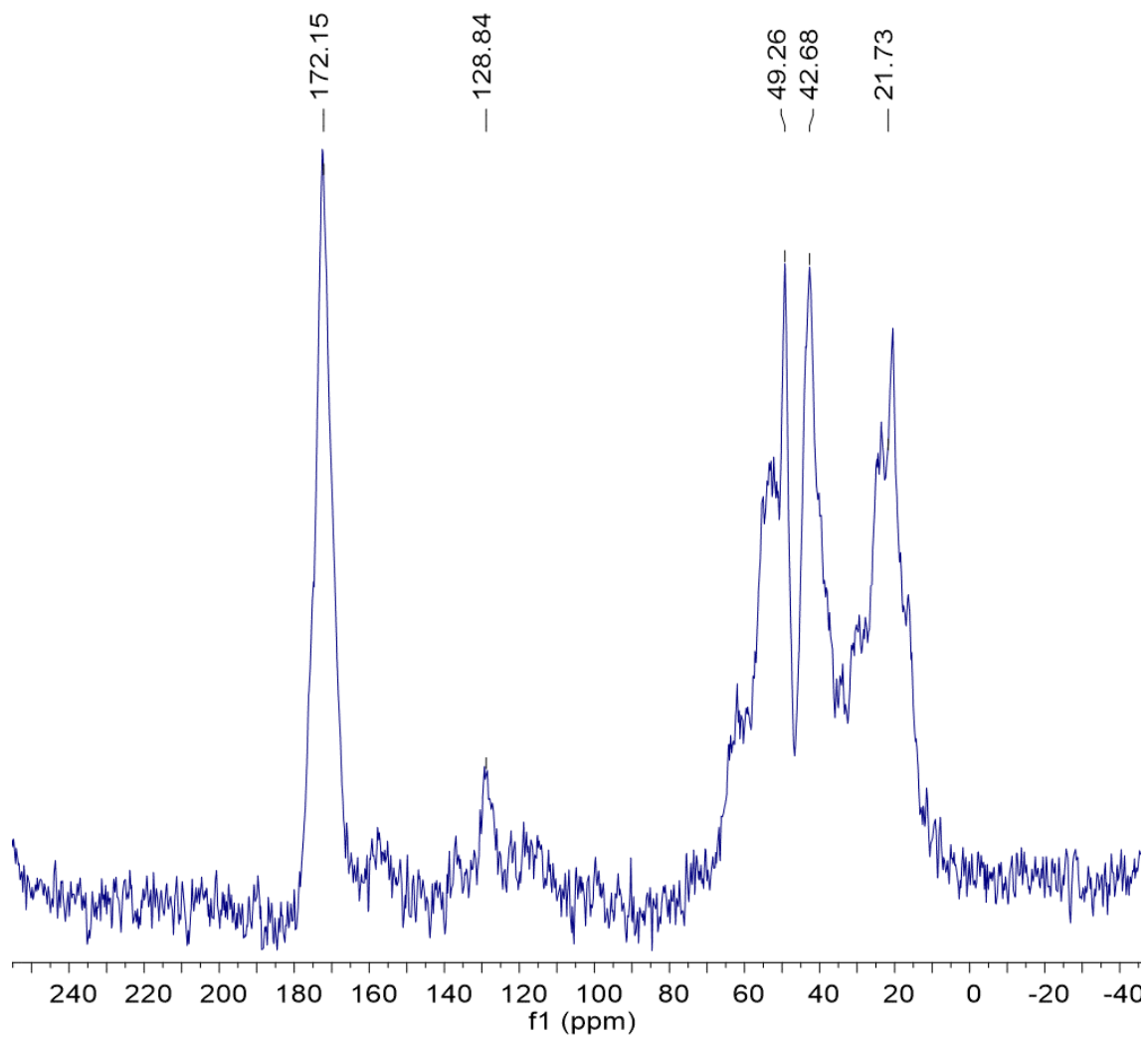


**Figure D8**  $^{13}\text{C}$  CP MAS NMR spectra of the insoluble matrix isolated from blue mussel shells. 3.2 mm zirconia rotor spinning at 20 kHz with a contact time of 1 ms. Proton decoupling level of 100 kHz and a relaxation delay of 1 s. Hartmann-Hahn rf was matched to 62.5 kHz. 1k scans.

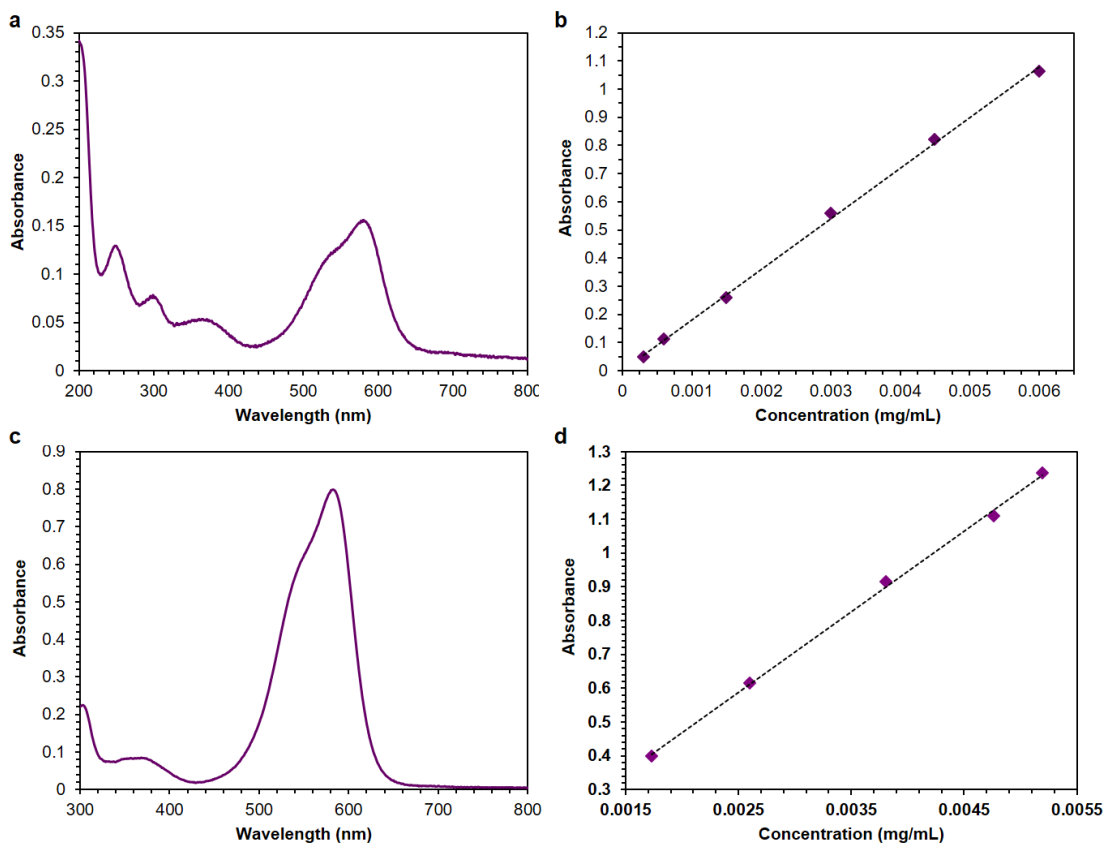


**Figure D9** UV-vis spectra and calibration curves for crystal violet. **(a)** UV-vis spectra of crystal violet in distilled water ( $\lambda_{\text{max}} = 580 \text{ nm}$ ) and **(b)** the resulting calibration curve where  $y = 179.23 x + 0.0025$  and  $R^2 = 0.9988$ . **(c)** UV-vis spectra of crystal violet in 50:50 distilled water and methanol ( $\lambda_{\text{max}} = 582 \text{ nm}$ ) and **(d)** the resulting calibration curve where  $y = 238.53 x - 0.0082$  and  $R^2 = 0.9987$ .

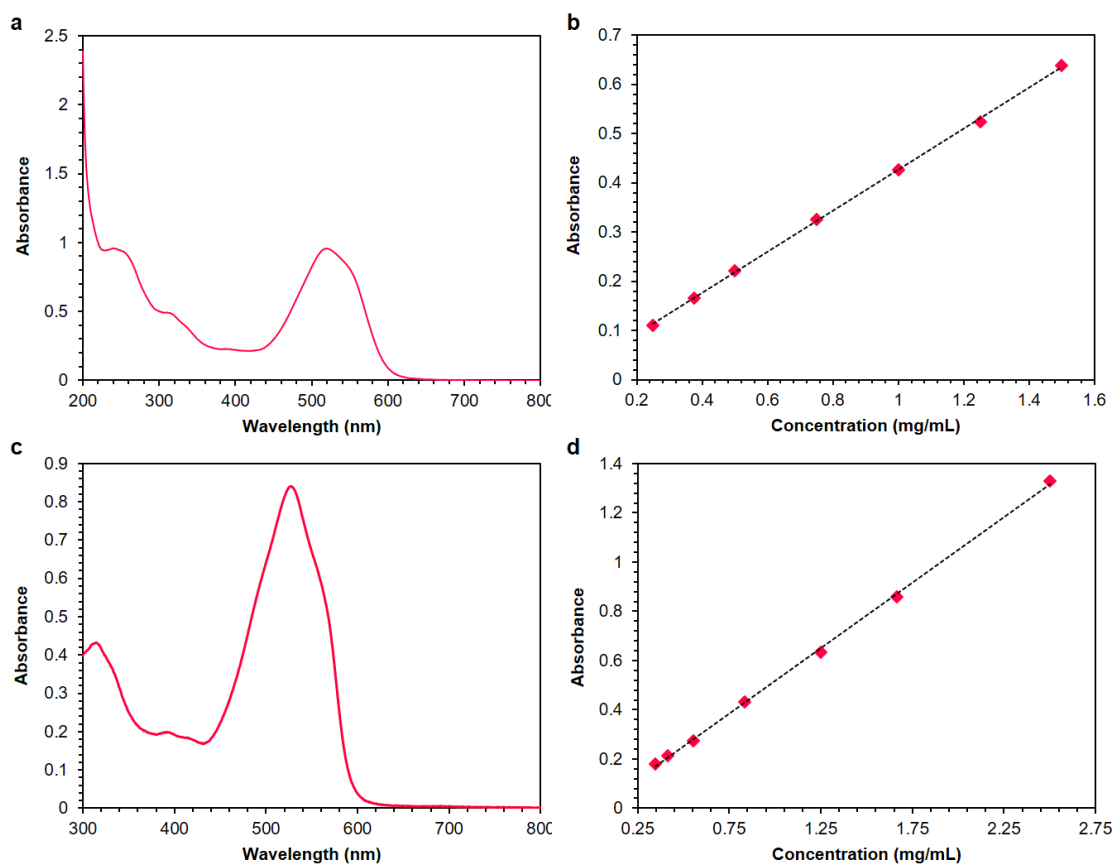


**Figure D10** UV-vis spectra and calibration curves for RIT brand fuchsia dye. **(a)** UV-vis spectra of RIT dye (fuchsia) in distilled water ( $\lambda_{\text{max}} = 522$  nm) and **(b)** the resulting calibration curve where  $y = 0.417x + 0.0092$  and  $R^2 = 0.9996$ . **(c)** UV-vis spectra of RIT dye in 50:50 distilled water and methanol ( $\lambda_{\text{max}} = 527$  nm) and **(d)** the resulting calibration curve where  $y = 0.532x - 0.015$  and  $R^2 = 0.9993$ .

## Appendix E

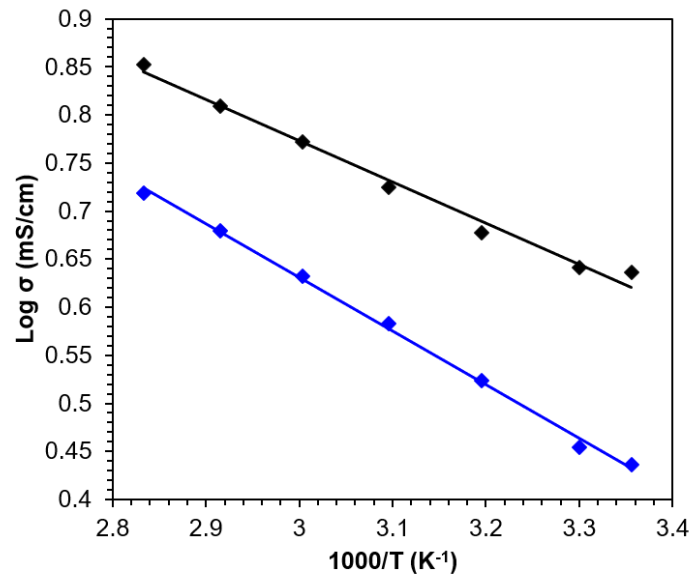


**Figure E1** Arrhenius plot for ILGPE-I (black) and ILGPE-II (blue).

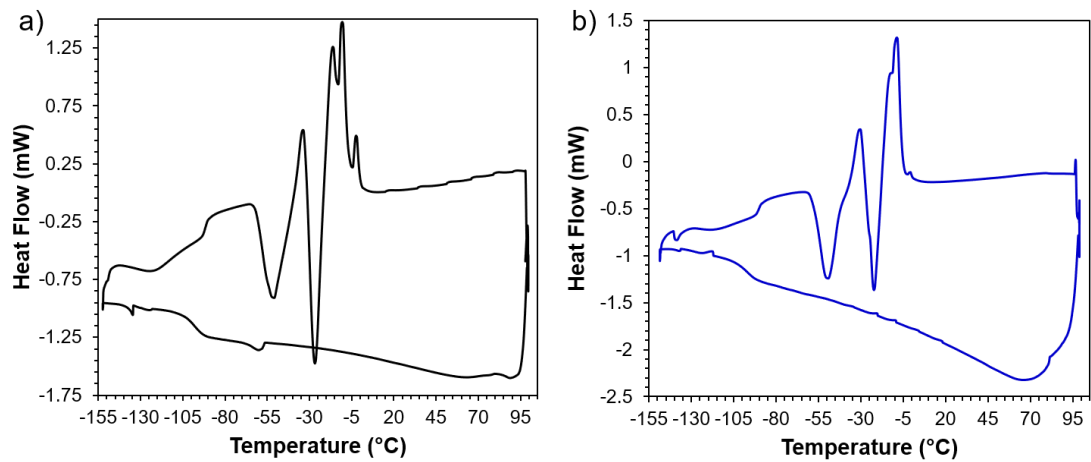


**Figure E2** DSC curves for a) ILGPE-I and b) ILGPE-II.

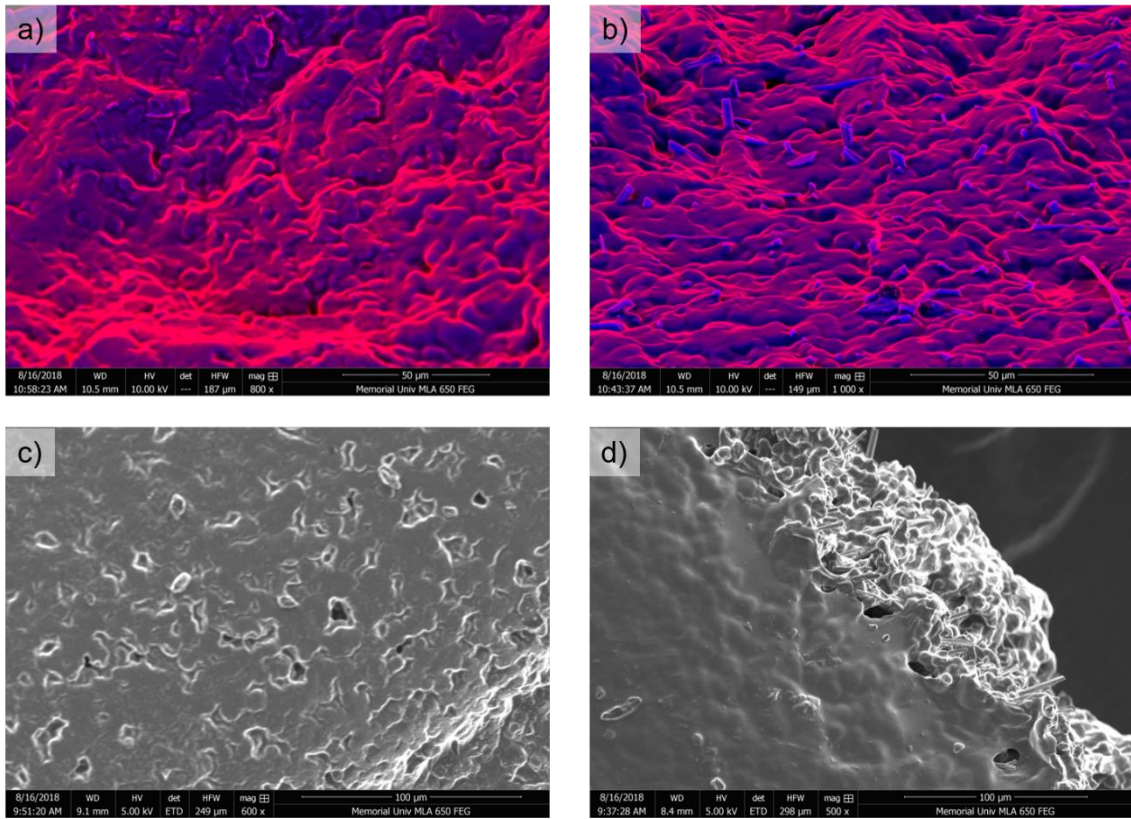


**Figure E3** SEM images of the cross section of a) ILGPE-I and b) ILGPE-II. Surface images of c) ILGPE-I and d) ILGPE-II

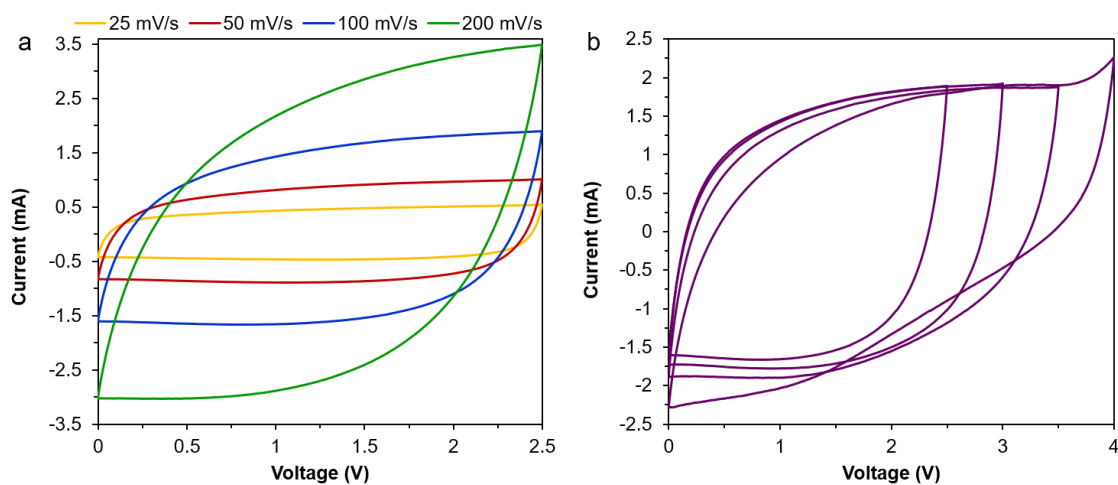


**Figure E4** Cyclic voltammograms of Cell I at a) different scan rates and b) different operating potentials at a scan rate of 100 mV/s.

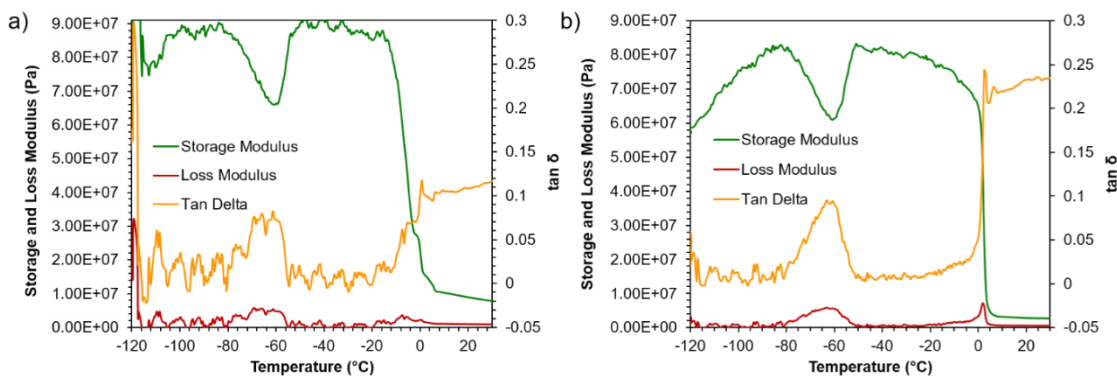


**Figure E5** Dynamic mechanical analysis of a) ILGPE-I and b) ILGPE-II.

